DISSERTATION

DEVELOPMENT OF *N*-ARYL PHENOXAZINES AS STRONGLY REDUCING ORGANIC PHOTOREDOX CATALYSTS

Submitted by

Blaine Gould McCarthy

Department of Chemistry

In partial fulfillment of the requirements

For the Degree of Doctor of Philosophy

Colorado State University

Fort Collins, Colorado

Spring 2020

Doctoral Committee:

Advisor: Garret Miyake

Jeffery Bandar
Amber Krummel
Susan James

ABSTRACT

DEVELOPMENT OF *N*-ARYL PHENOXAZINES AS STRONGLY REDUCING ORGANIC PHOTOREDOX CATALYSTS

N-aryl phenoxazines were identified as a new family of organic photoredox catalysts capable of effecting single electron transfer reductions from the photoexcited state. A number of phenoxazines bearing different *N*-aryl and core substituents were synthesized, characterized, and employed as catalysts. Spectroscopic and electrochemical characterization of these phenoxazines was used to establish structure-property relationships for the design of visible-light absorbing, strongly reducing organic photoredox catalysts. The application of phenoxazines as catalysts for organocatalyzed atom transfer radical polymerization (O-ATRP), a light-driven method for the synthesis of well-defined polymers, revealed the importance of several catalyst properties for achieving control over the polymerization. Investigation of the properties and catalytic performance of *N*-aryl phenoxazines has provided fundamental insight into the reactivity of organic excited state reductants and photophysical properties of organic molecules. The catalysts developed through this work provide sustainable alternatives to more commonly used precious-metal containing photoredox catalysts.

ACKNOWLEDGEMENTS

General Acknowledgements

I would like to thank my thesis committee - Prof. Garret Miyake, Prof. Jeffrey Bandar, Prof. Amber Krummel, and Prof. Susan James - for their guidance through the defense of this dissertation.

I am grateful to Prof. Eugene Chen who provided me with valuable guidance as a graduate student and during my transition to postdoctoral research.

I am grateful to my fellow graduate students and postdoctoral researchers who were a part of the Miyake lab at CU Boulder and CSU. Each of you uniquely inspired me, pushed me, and played an integral role in developing an intellectually-stimulating, exciting, and enjoyable group culture.

The work described herein would not have been possible without an excellent group of collaborators from the Damrauer and Musgrave groups at CU Boulder. It has been especially rewarding to grow alongside my peers Steven and Izzy who provided essential technical expertise and comedic relief during this endeavor.

I am grateful to my undergraduate research advisor, Prof. Chuck Jakobsche, for nurturing my interest in chemistry and laying the intellectual and experimental foundation for my graduate studies. I am also indebted to my former lab mates and a number of professors at Clark University who were an essential part of my journey.

I am grateful for the love and support of my family and friends prior to and throughout graduate school. I am particularly grateful to my parents David and Betsy who provided me with a natural appreciation for education and instilled in me a sense of duty to take care of others. I have

striven to conduct myself based on these principles in graduate school and will continue to do so in the future.

I am so grateful to have met my partner Ryan in graduate school. His love, support, and humor have carried me through the inherent challenges of research. Ryan, your voracious appetite for learning and ambition to grow in a multi-dimensional manner continues to inspire me.

If I could go back to the beginning of this journey, I would easily choose Garret to be my mentor again. Garret, I would not be where I am nor who I am without your guidance; I am truly grateful for everything that you have done for me. Your unwavering belief in me has altered the trajectory of my life.

Acknowledgements of Co-author Contributions and Funding Agencies

Chapter 2: This dissertation chapter contains the manuscript of an article [Pearson, R.M.[*]; Lim, C.-H.[*]; McCarthy, B.G.; Musgrave, C.; Miyake, G.M. "Organocatalyzed Atom Transfer Radical Polymerization Using *N*-Aryl Phenoxazines as Photoredox Catalysts" *Journal of the American Chemical Society*, **2016**, *138*, 11399–11407. [*]These authors contributed equally.]. R.M.P. proposed to study phenoxazines as catalysts for O-ATRP, synthesized the phenoxazines used as catalysts in this work, and performed initial key experiments to demonstrate the catalytic activity of phenoxazines in O-ATRP. C.-H.L. performed all density functional theory calculations under the advisement of C.B.M. and carried out spectroscopic and electrochemical catalyst characterization.

The work described in this chapter was supported by the University of Colorado Boulder, the Advanced Research Projects Agency-Energy (DEAR0000683), and the American Chemical Socity Petroleum Research Fund (56501-DNI7). Research reported in this publication was

supported by the National Institute of General Medical Sciences of the National Institutes of Health under Award Number R35GM119702. The content is solely the responsibility of the authors and does not necessarily represent the official views of the National Institutes of Health. BGM is supported by the University of Colorado Department of Chemistry and Biochemistry Marian Sharrah Fellowship. CBM was supported by NSF grant CHE-1214131. We gratefully acknowledge the use of XSEDE supercomputing resources (NSF ACI-1053575). The authors would like to thank Steven Satur (CU Boulder) for technical assistance.

Chapter 3: This dissertation chapter contains the manuscript of an article [McCarthy, B.G.; Pearson, R.M.; Lim, C.-H.; Sartor, S.M.; Damrauer, N.H.; Miyake, G.M. "Structure-Property Relationships for Tailoring Phenoxazines as Reducing Photoredox Catalysts" *Journal of the American Chemical Society*, **2018**, *140*, 5088–5101.]. C.-H.L. performed all density functional theory calculations. R.M.P. spearheaded the development of phenoxazine catalysts with modified core structures and aided with catalyst synthesis. S.M.S. and N.H.D. contributed intellectually through aiding with our interpretation and understanding of spectroscopic data to elucidate the nature of the excited states of these catalysts.

The work described in this chapter was supported by Colorado State University and the University of Colorado Boulder. Research reported in this publication was supported by the National Institute of General Medical Sciences (Award R35GM119702) of the National Institutes of Health. The content is solely the responsibility of the authors and does not necessarily represent the official views of the National Institutes of Health. Acknowledgement is made to the donors of The American Chemical Society Petroleum Research Fund for partial support of this research (56501- DNI7) and the Advanced Research Projects Agency-Energy (DE-AR0000683). B.G.M. and S.M.S. acknowledge support from NSF GRFPs. C.-H.L. acknowledges NIH's F32

postdoctoral fellowship support (F32GM122392). We gratefully acknowledge the use of XSEDE supercomputing resources (NSF ACI-1053575).

Chapter 4: This dissertation chapter contains the manuscript of an article [McCarthy, B.G.; Miyake, G.M. "Organocatalyzed Atom Transfer Radical Polymerization Catalyzed by Core Modified *N*-Aryl Phenoxazines Performed under Air" *ACS Macro Letters*, **2018**, *7*, 1016–1021.]. There were no co-authors on this work.

This work was supported by Colorado State University. Research reported in this publication was supported by the National Institute of General Medical Sciences (Award Number R35GM119702) of the National Institutes of Health. The content is solely the responsibility of the authors and does not necessarily represent the official views of the National Institutes of Health. B.M. is grateful for support from an NSF GRFP. We thank Max Kudisch and Bret Boyle for help with the design and 3D-printing of the photoreactor used in this work. We thank Daniel Corbin for MALDI training.

Chapter 5: This dissertation chapter contains the manuscript of an article [Sartor, S.M.; McCarthy, B.G.; Pearson, R.M.; Miyake, G.M.; Damrauer, N.H. "Exploiting Charge Transfer States for Maximizing Intersystem Crossing Yields in Organic Photoredox Catalysts" *Journal of the American Chemical Society*, **2018**, *140*, 4778–4781.]. S.M.S. performed all time-resolved spectroscopic experiments. R.M.P. performed all computational work.

An NSF GRFP supported S.M.S. and B.G.M. G.M.M. acknowledges support from CSU, CU Boulder, and grant R35GM119702 of the NIH. We gratefully acknowledge the use of XSEDE supercomputing resources (NSF TG-CHE170050).

DEDICATION

This dissertation is dedicated to my mentors.

TABLE OF CONTENTS

CHAPTER 1 – INTRODUCTION

Thesis Structure

The author of this thesis conducted research on diverse projects spanning polymer chemistry and catalysis, yet the focus of this dissertation is on progress made in one research area: the development of *N*-aryl phenoxazines as organic photoredox catalysts. This dissertation describes the first report of applying *N*-aryl phenoxazines as strongly reducing organic photoredox catalysts for organocatalyzed atom transfer radical polymerization (O-ATRP), the development of a family of core modified phenoxazine catalysts with varied properties, and the elucidation of catalyst structure-property relationships. Critical to the development of this family of catalysts was an emphasis on understanding the impacts of molecular structure on access to intramolecular charge transfer excited states, an endeavor that was enriched through collaboration with the Musgrave group and the Damrauer group at the University of Colorado, Boulder.

The overall structure of this thesis follows a journal-format style based on selected publications, with each chapter being modeled off of one published research article. The chapters include two first-author works that were published in the *Journal of the American Chemical Society* and *ACS Macro Letters*, as well as two supporting-author manuscripts published in the *Journal of the American Chemical Society* in collaboration with the Musgrave group and the Damrauer group. These journal articles detail the development of phenoxazines as excited state reductants and the application of phenoxazines as catalysts for O-ATRP, enabling the synthesis of well-defined polymers under robust conditions. The topics covered in this thesis are presented in four chapters with the following titles:

1. Organocatalyzed Atom Transfer Radical Polymerization Using *N*-Aryl Phenoxazines as Photoredox Catalysts
2. Structure-Property Relationships for Tailoring Phenoxazines as Reducing Photoredox Catalysts
3. Organocatalyzed Atom Transfer Radical Polymerization Catalyzed by Core Modified *N*-Aryl Phenoxazines Performed under Air
4. Exploiting Charge Transfer States for Maximizing Intersystem Crossing Yields in Organic Photoredox Catalysts

In addition to the topics covered in this dissertation, a full list of the works published by the author of this thesis during her doctoral research is included below:

1. Chen, D-F.; Boyle, B.M.; McCarthy, B.G.; Lim, C.-H.; Miyake, G.M. "Controlling Polymer Composition in Organocatalyzed Photoredox Radical Ring-Opening Polymerization of Vinylcyclopropanes" *Journal of the American Chemical Society*, **2019**, *141*, 13268–13277 (**DOI:** 10.1021/jacs.9b07230).

2. Sartor, S.M.; Lattke, Y.M.; McCarthy, B.G.; Miyake, G.M.; Damrauer, N.H. "Effects of Naphthyl Connectivity on the Photophysics of Compact Organic Charge-Transfer Photoredox Catalysts" *Journal of Physical Chemistry A*, **2019**, *123*, 4727–4736 (**DOI:** 10.1021/acs.jpca.9b03286).

3. Dolinski, N.D.; Page, Z.A.; Discekici, E.H.; Meis, D.; Lee, I.-H.; Jones, G.R.; Whitfield, R.; Pan, X.; McCarthy, B.G.; Shanmugam, S.; Kottisch, V.; Fors, B.P.; Boyer, C.; Miyake, G.M.; Matyjaszewski, K.; Haddleton, D.M.; Read de Alaniz, J.; Anastasaki, A.; Hawker, C.J. "What happens in the dark? Assessing the temporal control of photo-mediated controlled radical

polymerizations" *Journal of Polymer Science Part A: Polymer Chemistry*, **2019**, *57*, 268–273 (**DOI:** 10.1002/pola.29247).

4. McCarthy, B.G.; Miyake, G.M. "Organocatalyzed Atom Transfer Radical Polymerization Catalyzed by Core Modified *N*-Aryl Phenoxazines Performed under Air" *ACS Macro Letters*, **2018**, *7*, 1016–1021 (**DOI:** 10.1021/acsmacrolett.8b00497).

5. Sartor, S.M.; McCarthy, B.G.; Pearson, R.M.; Miyake, G.M.; Damrauer, N.H. "Exploiting Charge Transfer States for Maximizing Intersystem Crossing Yields in Organic Photoredox Catalysts" *Journal of the American Chemical Society*, **2018**, *140*, 4778–4781 (**DOI:** 10.1021/jacs.8b01001).

6. McCarthy, B.G.; Pearson, R.M.; Lim, C.-H.; Sartor, S.M.; Damrauer, N.H.; Miyake, G.M. "Structure-Property Relationships for Tailoring Phenoxazines as Reducing Photoredox Catalysts" *Journal of the American Chemical Society*, **2018**, *140*, 5088–5101 (**DOI:** 10.1021/jacs.7b12074).

7. Theriot, J.C.; McCarthy, B.G.; Lim, C.-H.; Miyake, G.M. "Organocatalyzed Atom Transfer Radical Polymerization: Perspectives on Catalyst Design and Performance" *Macromolecular Rapid Communications*, **2017**, *38*, 1700040–1700052 (**DOI:** 10.1002/marc.201700040).

8. Boyle, B.M.; French, T.A.; Pearson, R.M.; McCarthy, B.G.; Miyake, G.M. "3D-Printing Block Copolymer Photonic Crystals" *ACS Nano*, **2017**, *11*, 3052–3058 (**DOI:** 10.1021/acsnano.7b00032).

9. Lim, C.-H.; Ryan, M.D. ; McCarthy, B.G.; Theriot, J.C.; Sartor, S.M.; Damrauer, N.H.; Musgrave, C.; Miyake, G.M. "Intramolecular Charge Transfer and Ion Pairing in *N,N*-Diaryl Dihydrophenazine Photoredox Catalysts for Efficient Organocatalyzed Atom Transfer Radical

Polymerization" *Journal of the American Chemical Society*, **2017**, *139*, 348–355 (**DOI:** 10.1021/jacs.6b11022).

10. Pearson, R.M.; Lim, C.-H.; McCarthy, B.G.; Musgrave, C.; Miyake, G.M. "Organocatalyzed Atom Transfer Radical Polymerization Using *N*-Aryl Phenoxazines as Photoredox Catalysts" *Journal of the American Chemical Society*, **2016**, *138*, 11399–11407 (**DOI:** 10.1021/jacs.6b08068).

Motivations

Over the past decade, increased interest in the application of photoredox catalysis for organic synthesis has engendered the development of numerous light-driven transformations for the synthesis of small molecules and materials. This recent renaissance in photochemistry can be attributed to the unique benefits afforded by these methods, including the ability to use light to drive reactions under mild conditions and the ability to access open shell intermediates capable of undergoing mechanisms that compliment polar, two-electron modes of reactivity. Key to the development of these advances has been the use of transition metal photoredox catalysts (PCs), such as tris[2-phenylpyridinato-C^2,N]iridium(III), or $Ir(ppy)_3$, and tris(bipyridine)ruthenium(II), or $Ru(bpy)_3$, that exhibit desirable photophysical and redox properties.[1] For example, $Ir(ppy)_3$ absorbs visible-light to access a long-lived triplet excited state with an excited state reduction potential, E^{0*}, of -1.73 V versus the saturated calomel electrode (vs. SCE). The ability of $Ir(ppy)_3$ to absorb visible light is advantageous since the use of higher-energy ultraviolet (UV) light to drive reactions can lead to degradation of substrates. Access to a long-lived triplet excited state ($^3Ir(ppy)_3^*$) increases the probability of bimolecular collision of $^3Ir(ppy)_3^*$ with substrate, an event that is critical for productive chemistry. Moreover, the strong reduction potential of $^3Ir(ppy)_3^*$ enables reduction of functional groups such as sulfonyl chlorides, anhydrides, alkyl and aryl

halides, and aldehydes to generate reactive intermediates. Despite the synthetic utility of transition metal PCs such as $Ir(ppy)_3$, concerns about the long-term sustainability of compounds containing rare earth elements such as Ir and Ru has spawned the development of organic alternatives. Our group became interested in organic photoredox catalyst development to address these sustainability concerns, to investigate whether new catalyst motifs could unlock unprecedented reactivity, and to develop new light-driven transformations.

Over the past decade, several families of organic molecules have been explored as PCs including rhylene dyes, pyryliums, acridiniums, fluorescein, eosin y, rose bengal and rhodamine dyes.[2] The majority of these compounds are oxidizing in the photoexcited state and thus have been used directly as photooxidants or as ground state reductants via addition of a sacrificial electron donor. Comparatively, fewer reports have detailed the discovery or design of strongly reducing organic PCs. For example, at the inception of this research program, few organic catalysts capable of reducing aryl halides (E^0_{red} ~ -0.8 to -2.0 V vs. SCE[3]) from the photoexcited state (PC^*) or from the reduced form of the ground state had been studied (Figure 1.1). Thus, we envisioned that new families of organic excited state reductants would provide more sustainable alternatives to strongly reducing transition metal catalysts such as $Ir(ppy)_3$ and potentially exhibit unprecedented reactivity.

In addition to addressing the broad need for organic PCs, our group has been interested in the development of organocatalyzed transformations. At the beginning of this research program, we identified photoredox catalysis as a viable approach for the development of a metal-free atom transfer radical polymerization (ATRP), a commonly used controlled radical polymerization technique for the synthesis of polymers with targeted molecular weights and narrow molecular weight distributions. In the mechanism of traditional ATRP, a metal catalyst reduces the alkyl

halide group of the initiator or polymer chain end to generate radicals that react with monomer to grow the polymer chain. Notably, the reduction potential of the alkyl-halide bond of a typical ATRP initiator is approximately -0.6 to -0.8 V vs. SCE, rendering this a relatively challenging reduction by thermodynamic considerations. We hypothesized that an organic catalyst could be used to reduce alkyl halide initiators and mediate an organocatalyzed ATRP (O-ATRP) if it could access a sufficiently reducing photoexcited state. Our group first investigated the dye perylene[4] and later *N*,*N*-diaryl dihydrophenazines[5] as PCs for the development of O-ATRP methods. The latter were found to be superior catalysts for O-ATRP due to their ability to absorb visible light to access strongly reducing excited states (E^{0*} ~ -2.0 V vs. SCE). Building off of this work, we were inspired to explore the catalytic activity of *N*-aryl phenoxazines since they are structurally and electronically similar to *N*,*N*-diaryl dihydrophenazines.

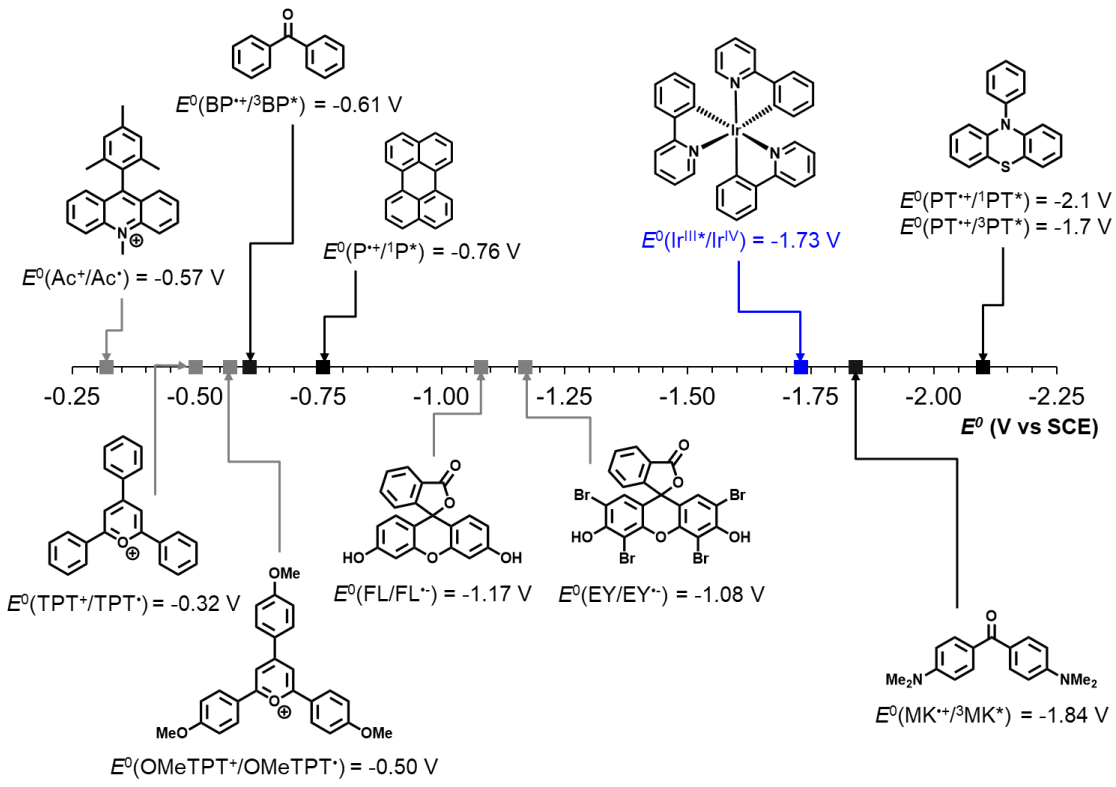

Figure 1.1. *Electrochemical series of the excited state reduction potentials (black squares) or ground state reduction potentials (grey squares) of organic PCs compared with the commonly used transition metal PC, $Ir(ppy)_3$ (blue square).*

Phenoxazine derivatives have been applied in a myriad of materials applications including as part of donor-acceptor-donor motifs for organic light emitting diodes (OLEDs)[6], dyes for dye-sensitized solar cells[7], and polymers for p-channel semiconductors and organic field transistors[8]. Interestingly, the phenoxazine heterocycle is present in a handful of compounds naturally produced by bacteria[9] and has been incorporated into synthetic antitumor[10], antifungal[11], and antimalarial[12] therapeutics. We hypothesized that *N*-aryl phenoxazines could serve as excited state reductants since these compounds absorb light efficiently, possess an electron-rich core, and form stable radical cations.[13] In 2016, we demonstrated that *N*-aryl phenoxazines catalyze O-ATRP to synthesize well-defined polymers (Chapter 2). After demonstrating the capability of *N*-aryl phenoxazines to reduce substrates from the photoexcited state, we aimed to design derivatives with tailored properties to broaden the utility of this catalytic platform. Modification of the 3- and 7-positions of the phenoxazine core with a number of aryl substituents was used to develop a family of core modified phenoxazines and establish catalyst structure-property relationships (Chapter 3). Excitingly, a number of these core modified phenoxazines were found to exhibit excellent performance in O-ATRP under robust reaction conditions, including in polymerizations conducted in the presence of air (Chapter 4). We continued to deepen our understanding of phenoxazine catalyst design through elucidating the photophysical processes of their excited states. These studies revealed the importance of accessing an intramolecular charge transfer excited state for achieving high triplet quantum yields (Chapter 5).

Through this work, a family of phenoxazine PCs with varied photophysical and redox properties have been developed. We envision that the diverse properties that these PCs exhibit will

open new avenues for organic photoredox catalysis such as the development of wavelength-selective chemistries through application of PCs with distinct absorption profiles and the development of highly selective reductions through the choice of PCs with tailored redox properties. Excitingly, some derivatives such as the phenoxazine shown in Figure 1.2 exhibit properties similar to that of $Ir(ppy)_3$, providing more sustainable alternatives to this commonly used transition metal PC.

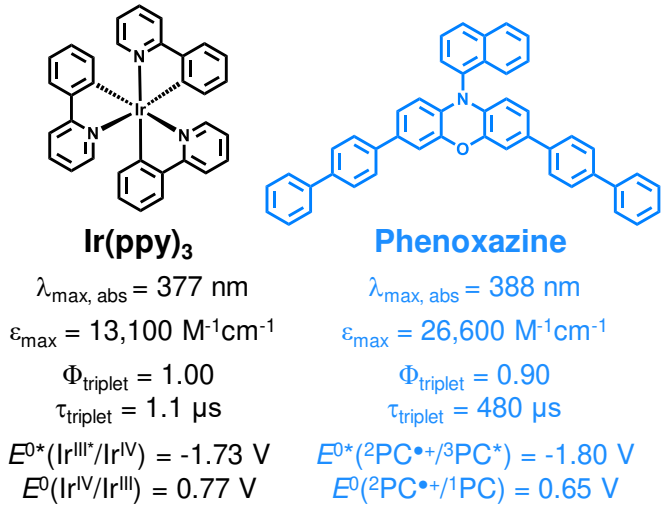

Figure 1.2. *Structures and properties of the commonly used excited state reductant $Ir(ppy)_3$ (black) and one of the phenoxazines developed through this work (blue).*

REFERENCES

(1) Prier, C. K.; Rankic, D. A.; MacMillan, D. W. C. *Chem. Rev.* **2013**, *113*, 5322–5363.

(2) Romero, N. A.; Nicewicz, D.A. *Chem. Rev.* **2016**, *116*, 10075–10166.

(3) Roth, H. G.; Romero, N. A.; Nicewicz, D. A. *Synlett* **2016**, *27*, 714–723.

(4) Miyake G. M.; Theriot, J. C. *Macromolecules* **2014**, *47*, 8255–8261.

(5) Theriot, J. C.; Lim, C-H.; Yang, H.; Ryan, M. D.; Musgrave, C. B.; Miyake, G. M. *Science* **2016**, *352*, 1082–1086.

(6) a) Okamoto, T.; Kozaki, M.; Doe, M.; Uchida, M.; Wang, G.; Okada, K. *Chem Mater.* **2005**, *17*, 5504–5511. b) Zhu, Y.; Kulkarni, A. P.; Wu, P.; Jenekhe, S. A. *Chem. Mater.* **2008**, *20*, 4200–4211. c) Park, Y.; Kim, B.; Lee, C.; Hyun, A.; Jang, S.; Lee, J.; Gal, Y.; Kim, T. H.; Kim, K.; Park, J. *J. Phys. Chem. C* **2011**, *115*, 4843–4850. d) Tanaka, H.; Shizu, K.; Adachi, C. *Chem. Commun.* **2012**, *48*, 11392–11394.

(7) a) Tian, H.; Yang, X.; Cong, J.; Chen, R.; Liu, J.; Hao, Y. *Chem. Commun.* **2009**, 6288–6290. b) Karlsson, K. M.; Jiang, X.; Eriksson, S. K.; Gabrielsson, E.; Rensmo, H.; Hagfeldt, A.; Sun, L. *Chem. Eur. J.* **2011**, *17*, 6415–6424. c) Chem, J. M.; Tian, H.; Bora, I.; Jiang, X.; Gabrielsson, E.; Karlsson, M.; Hagfedlt, A.; Sun, L. *J. Mater. Chem.* **2011**, *21*, 12462–12472. d) Tan, H.; Pan, C.; Wang, G.; Wu, Y.; Zhang, Y.; Zou, Y.; Yu, G.; Zhang, M. *Org. Electron.* **2013**, *14*, 2795–2801. e) Lee, W.; Bum, S.; Choi, J.; Jung, H.; Woo, h.; Hun, S.; Kim, B.; Jae, M.; Pil, J. *Dyes Pigm*. **2014**, *102*, 13–21. f) Tan, H.; Pan, C.; Wang, G.; Wu, Y.; Zhang, Y.; Yu, G.; Zhang, M. *Dyes Pigm.* **2014**, *101*, 47–54.

(8) a) Zhu, Y.; Babel, A.; Jenekhe, S. *Macromolecules* **2005**, *38*, 7983–7991. b) Yoon, H.; Lee, W.; Lee, J.; Lim, D.; Hwang, D.; Kang, I. *Bull. Korean Chem. Soc.* **2009**, *30*, 1237–1434.

(9) Waksman, S. A.; Katz, E.; Vining, L. C. *Pathology and Bacteriology* **1958**, *44*, 602–882.

(10) a) Ren, J.; Liu, D.; Tian, L.; Wei, Y.; Proksch, P.; Zeng, J.; Lin, W. *Bioorg. Med. Chem. Lett.* **2013**, *23*, 1297–1301. b) Tomoda, A.; Arai, S.; Ishida, R. *Bioorg. Med. Chem. Lett.* **2001**, *11*, 1057–1058. c) Kato, S.; Shirato, K. E.; Imaizumi, K.; Toyota, H.; Mizuguchi, J.; Odawara, M.; Che, X.; Akiyama, S.; Abe, A.; Tomoda, A. *Oncol. Rep.* **2006**, *15*, 843–848. d) Koshibu-Koizumi, M.; Akazawa, T.; Iwamoto, M.; Taskasaki, F.; Mizuno, R.; Kobayashi, A.; Abe, A.; Tomoda, M.; Hamatake, R.; Ishida, J. *Cancer Res. Clin. Oncol.* **2002**, *128*, 363–368.

(11) Frade, V. H. J.; Sousa, M.; Moura, J. C. V. P.; Goncalves, M. S. T. *Tetrahedron Lett.* **2007**, *48*, 8347–8352.

(12) Ge, J.; Arai, .; Yang, M.; Bakar, A.; Lu, .; Ismail, N. S. M.; Wittlin, S.; Kaiser, M.; Brun, R.; Charman, S. A.; Nguyen, T.; Morizzi, J.; Itoh, I.; Ihara, M. *ACS Med. Chem. Lett.* **2010**, *183*, 360–364.

(13) Gegiou, D.; Huber, J. R.; Weiss, K. *J. Am. Chem. Soc.* **1970**, *678*, 50–58.

CHAPTER 2 – ORGANOCATALYZED ATOM TRANSFER RADICAL POLYMERIZATION USING *N*-ARYL PHENOXAZINES AS PHOTOREDOX CATALYSTS

Overview

N-Aryl phenoxazines have been synthesized and introduced as strongly reducing metal-free photoredox catalysts in organocatalyzed atom transfer radical polymerization for the synthesis of well-defined polymers. Experiments confirmed quantum chemical predictions that, like their dihydrophenazine analogs, the photoexcited states of phenoxazine photoredox catalysts are strongly reducing and achieve superior performance when they possess charge transfer character. We compare phenoxazines to previously reported dihydrophenazines and phenothiazines as photoredox catalysts to gain insight into the performance of these catalysts and establish principles for catalyst design. A key finding reveals that maintenance of a planar conformation of the phenoxazine catalyst during the catalytic cycle encourages the synthesis of well-defined macromolecules. Using these principles, we realized a core substituted phenoxazine as a visible light photoredox catalyst that performed superior to UV-absorbing phenoxazines as well as previously reported organic photocatalysts in organocatalyzed atom transfer radical polymerization. Using this catalyst and irradiating with white LEDs resulted in the production of polymers with targeted molecular weights through achieving quantitative initiator efficiencies, which possess dispersities ranging from 1.13 to 1.31.

Introduction

Atom transfer radical polymerization (ATRP) is the most used controlled radical polymerization (CRP) for the synthesis of polymers with controlled molecular weight (MW),

dispersity (*Đ*), architecture, and composition.[1] Traditionally, metal catalysts have been employed to mediate the equilibrium between an alkyl halide and a carbon centered radical, produced by reduction of the halide, and deter bimolecular termination pathways.[2] Concerns about metal contamination of polymers intended for biomedical or electronic applications have motivated efforts to lower metal catalyst loadings and enhance purification methods.[3] Although CRPs exist that are mediated by organic catalysts and which thus entirely circumvent the issue of metal contamination,[4] organic catalysts capable of mediating an organocatalyzed ATRP (O-ATRP) are limited because of the required significant reducing power required to reduce alkyl bromides commonly used for ATRP (~ -0.6 to -0.8 V vs SCE).[5]

Photoredox catalysis presents a strategy to drive chemical transformations under mild conditions through the generation of reactive open-shell catalysts via photoexcitation.[6] Recently, work in this field has heavily focused on polypyridal ruthenium and iridium complexes because such metal complexes efficiently absorb visible light, possess sufficiently long excited state lifetimes as a result of metal to ligand charge transfer (MLCT), and have tunable redox properties. However, most photoredox catalysts (PCs) do not possess the reducing power to directly reduce an alkyl bromide through an outer sphere electron transfer mechanism. Commonly, supplemental sacrificial electron donors are required for alkyl bromide reduction through a reductive quenching pathway. The addition of sacrificial electron donors, however, introduces potential side-reactions[7] that impede the ability to synthesize polymers with low *Đ*.[8] Select strongly reducing iridium[9] or copper[10] PCs can directly reduce an alkyl bromide through an oxidative quenching pathway, and elimination of the sacrificial electron donor can facilitate the synthesis of well-defined polymers.[11] Light mediated CRPs further introduce spatial and temporal control as an attractive interactive feature for the incorporation of added synthetic complexity.[12] However, the concerns of metal con-

tamination and the sustainability of iridium or ruthenium metal PCs motivate the use of organic PCs.[14,13]

In accord with transition metal PCs, few organic PCs are able to directly reduce an alkyl bromide without the addition of a sacrificial electron donor.[14] Strongly reducing organic catalysts, including perylene,[15] *N*-aryl phenothiazines,[16] and *N*,*N*-diaryl dihydrophenazines[17] have been demonstrated as organic PCs capable of mediating O-ATRP (Figure 2.1). Continued progress in this field is required to further understand the mechanism of this polymerization to realize even more efficient PCs.

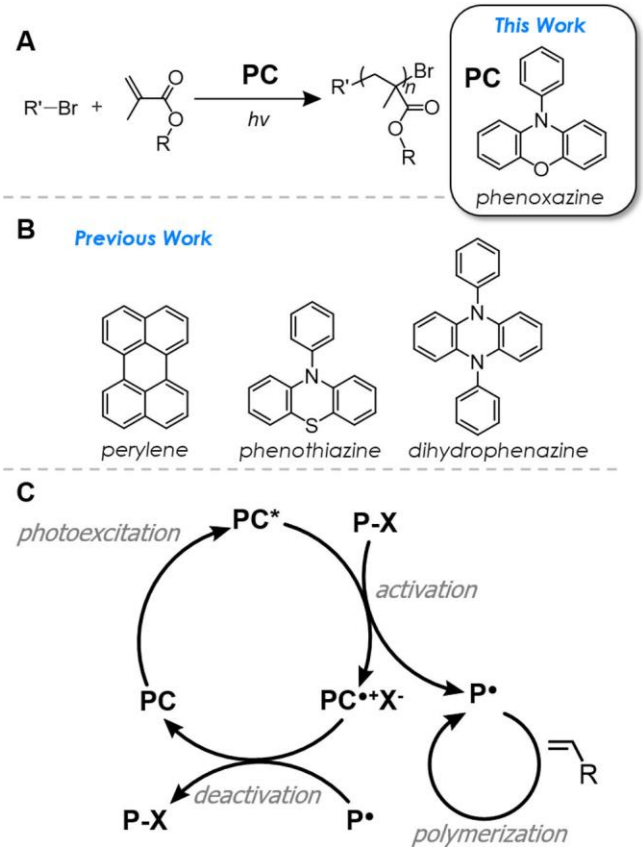

Figure 2.1. *(A) O-ATRP mediated by organic PCs using alkyl bromide initiators and aryl phenoxazines studied in this work. (B) Organic PCs examined in previous work. (C) Proposed, general photoredox catalytic cycle of O-ATRP.*

A proposed general photoredox O-ATRP mechanism involves photoexcitation of the PC to an excited state PC (PC^*) which is capable of reducing alkyl bromides via an oxidative quenching pathway to generate the active radical for polymerization propagation, while yielding the radical cation PC ($^2PC^{\bullet+}$) and Br^- ion pair complex, $^2PC^{\bullet+}Br^-$ (Figure 2.1C). Efficient deactivation is central to the production of well-defined polymers. Deactivation requires the $^2PC^{\bullet+}Br^-$ complex to be sufficiently oxidizing relative to the propagating radical to regenerate the alkyl bromide and ground state PC; subsequent photoexcitation of the PC reinitiates the catalytic cycle. Here, we report *N*-aryl phenoxazines as a new class of PCs for O-ATRP which produce well-defined polymers with low dispersities. Through following our maturing catalyst design principles, we report a visible light phenoxazine PC that produces polymers with $Đ$ ranging from 1.13 to 1.31 over a range of polymer MWs while achieving quantitative initiator efficiency (I^*).

To accelerate our progress in developing O-ATRP, we previously used quantum chemical calculations to guide the discovery and design of strongly reducing diaryl dihydrophenazines PCs for O-ATRP.[17] We based our computationally directed strategy on the hypothesis that photoexcitation of the PC delivers, through intersystem crossing (ISC) from the singlet excited state PC ($^1PC^*$), a triplet excited state PC ($^3PC^*$) which is responsible for the alkyl bromide reduction. This hypothesis hinges on the necessity of the photoexcited species to possess a sufficiently long lifetime for photoredox catalysis.

Our continued work in this field has been piqued by the impressively strong excited state reduction potentials ($E^{0*} = E^0(^2PC^{\bullet+}/PC^*)$) of N,N-diaryl dihydrophenazines and *N*-aryl phenothiazines (∼−2 V vs SCE), which are even more reducing than commonly used metal PCs, such as fac-$Ir(ppy)_3$ (−1.73 V vs SCE).[18] These strong E^{0*}s and the success of the diaryl dihydrophenazines in O-ATRP further drew our attention toward *N*-aryl phenoxazines as a

potential class of organic PCs for O-ATRP. We hypothesized that phenoxazines possessed characteristic traits that would distinguish them as organic PCs and make them successful catalysts for O-ATRP. Interestingly, these N, S, and O containing heterocycles are found in biologically relevant molecules[19] and organic electronic applications.[20]

Results and Discussion

DFT calculations predict that *N*-aryl phenoxazines possess similarly strong E^{0*}s (∼ −2 V vs SCE) in their lowest lying triplet excited state as dihydrophenazines and phenothiazines, which was corroborated experimentally.[21] Although dihydro- phenazines are stronger excited state reductants, the radical cations of phenoxazines and phenothiazines [$E^0(^2PC^{\bullet+}/PC^*)$ = ∼0.5 V vs SCE] are more oxidizing than those of dihydro- phenazines [$E^0(^2PC^{\bullet+}/PC^*)$ = ∼0.0 V vs SCE]; all three classes of PCs possess an oxidation potential capable of deactivating the propagating radical (e.g., ∼−0.8 V vs SCE for methyl methacrylate), as required for a successful O-ATRP. Lastly, reports on the photophysical properties of phenoxazines suggested their promise as PCs; the phosphorescence quantum yield of 10-phenylphenoxazine (**1**) at 77 K was reported to be 94% with a lifetime as long as 2.3s.[22] These properties highlight the efficient ISC to the triplet manifold and slow non- radiative decay attributed to small Franck−Condon vibrational overlap factors between $^3PC^*$ and the ground state.

Our analysis of exchanging the sulfur in phenothiazines with the oxygen in phenoxazines identified several distinct phenomena that alter the physical properties of these molecules and which we propose manifest in improvements in PC performance for O-ATRP, qualitatively assessed through analysis of the polymer product. The significant distinction between these two systems is the conformation of their heterocyclic rings. The smaller van der Waals radius of oxygen (1.52 Å) relative to sulfur (1.80 Å) permits the ground state phenoxazine (e.g., PC 1) to access a

planar geometry similarly to dihydrophenazines (nitrogen, 1.55, Å). In contrast, phenothiazine adopts a bent boat conformation in its ground state, observable in crystal structures[23] and predicted by our computations (Figure 2.2). However, upon oxidation to the radical cation state $^{2}PC^{\bullet+}$, all three PCs adopt a planar conformation.

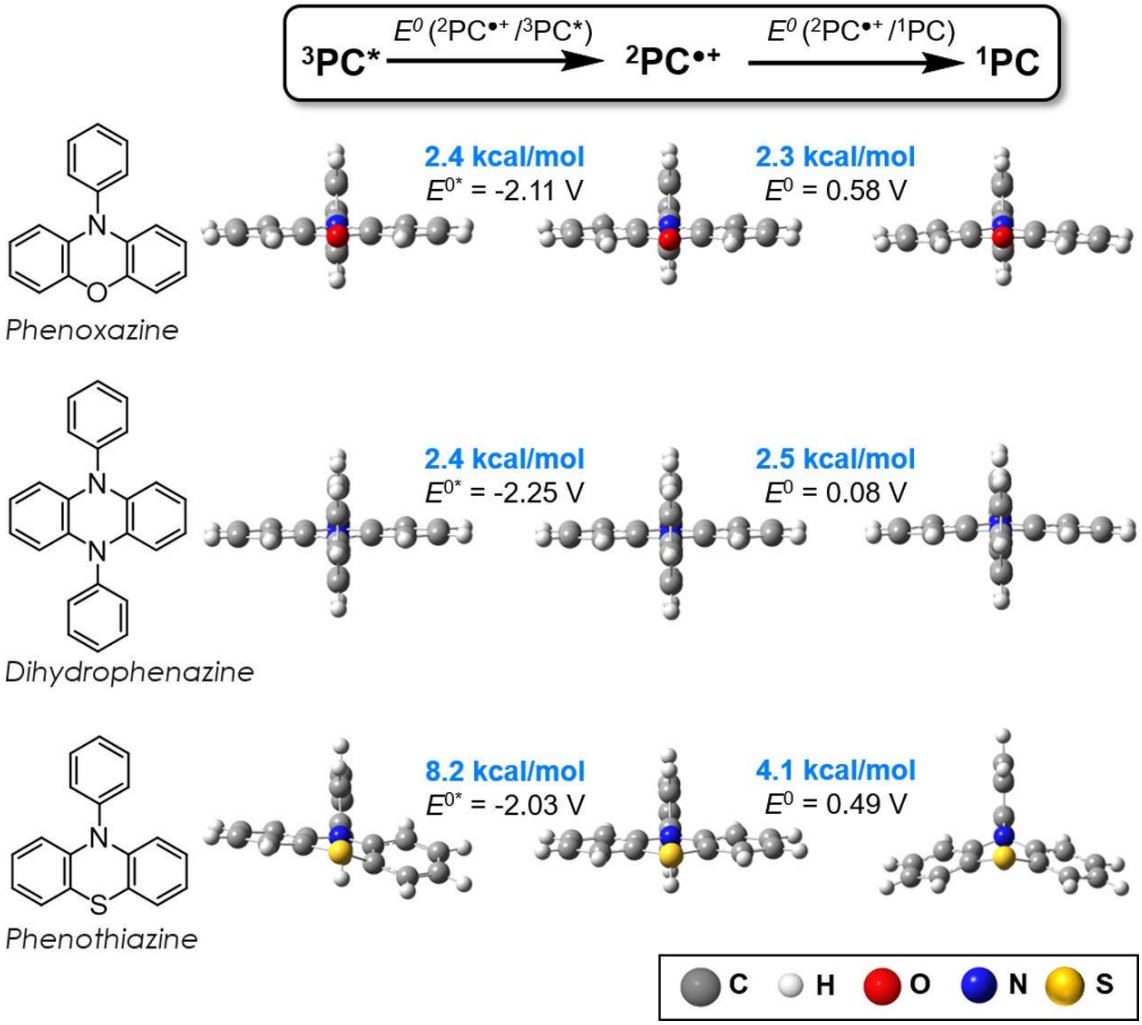

Figure 2.2. *Geometric reorganization energies and reduction potentials (vs SCE) for 10-phenylphenoxazine, diphenyl dihydrophenazine, and 10-phenylphenothiazine (bottom) transitioning from the $^{3}PC^{*}$ to $^{2}PC^{\bullet+}$ to ^{1}PC species involved in the proposed mechanism for photoredox O-ATRP. Reduction potentials were computed here with the improved 6-311+G** basis set compared to 6-31+G** used in the previous report.*[17]

The consequences of phenothiazine adopting bent con- formations in the ground and triplet states, but a planar geometry in the radical cation state, introduce larger structural reorganizations during electron transfer (ET) as compared to the consistently planar phenoxazines and

dihydrophenazines. We calculated a structural reorganization penalty associated with oxidation of the bent 10-phenylphenothiazine triplet state to the planar radical cation of 8.2 kcal/mol. In contrast, the triplet and radical cation states of **1** are both planar, analogous to diaryl dihydrophenazines, which results in a lower reorganization energy of only 2.4 kcal/mol. As phenoxazine, dihydrophenazine, and phenothiazine derivatives, possess similar E^{0*}s (−2.11, −2.25, and −2.03 V, respectively), we expect a kinetically faster activation (reduction of the alkyl bromide) in O-ATRP by phenoxazines and dihydrophenazines because of their lower reorganization energies for ET.

Polymerization deactivation involves reduction of the planar phenylphenothiazine radical cation to regenerate the bent ground state. We calculate a reorganization energy for this ET of 4.1 kcal/mol. For **1** or diphenyl dihydrophenazine, the same reduction process requires lower reorganization energies of 2.3 or 2.5 kcal/mol, respectively consistent with the conservation of the planarity of the cation radical and ground states. Given the similar ground state oxidation potentials for the phenoxazine and phenothiazine (0.58 and 0.49 V), the radical cation of **1** is likely kinetically faster in deactivation, which imparts better control in O-ATRP (*vide infra*). How this concept pertains to the less oxidizing dihydrophenazine $^{2}PC^{\bullet+}$ requires further investigation, although previous results demonstrated that dihydrophenazines are efficient PCs for O-ATRP.[17]

Toward the goal of designing phenoxazines as PCs for O-ATRP we applied the concepts conceived from our previous study of diaryl dihydrophenazines, which revealed that PCs with spatially separated singly occupied molecular orbitals (SOMOs) in their $^{3}PC^{*}$ state yielded PCs with superior performance in O-ATRP in regards to achieving the highest I^{*} and producing polymers with the lowest $Đ$. As such, we investigated strongly reducing *N*-aryl phenoxazines with spatially separated SOMOs (with the lower lying SOMO localized on the phenoxazine core and

the higher lying SOMO localized on the aryl substituent) and localized SOMOs (with both SOMOs localized on the phenoxazine core), to evaluate their performance as O-ATRP PCs and determine if this concept extends to phenoxazines (Figure 2.3).

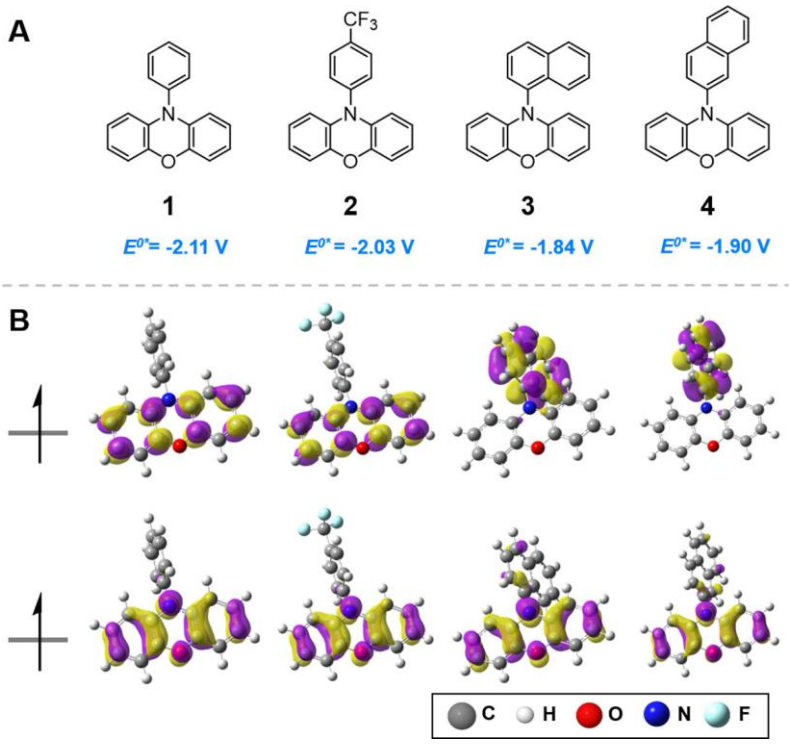

Figure 2.3. *(A) N-Aryl phenoxazines studied in this work along with computed triplet state reduction potentials. (B) Computed triplet state SOMOs of phenoxazine derivatives.*

In the cases of diphenyl dihydrophenazine and **1**, we calculate that neither exhibits spatially separated SOMOs. In contrast, incorporation of electron withdrawing trifluoromethyl functionalization on the para position of the *N*-phenyl substituents of the dihydrophenazine yielded spatially separated SOMOs whereas this substitution on phenoxazine (**2**) results in both SOMOs localized on the phenoxazine core. However, for both dihydrophenazines and phenoxazines, *N*-aryl functionalization(s) with 1- or 2-naphthalene yielded molecules with spatially separated SOMOs and thus predicted intramolecular charge transfer from the heterocyclic ring to the naphthalene substituent upon photoexcitation and subsequent intersystem crossing to the triplet state.

All four phenoxazine derivatives were synthesized through C−N cross-couplings from commercially available reagents and employed in the polymerization of MMA.[21] A screen of common ATRP alkyl bromide initiators revealed that diethyl 2-bromo-2-methylmalonate (DBMM) served as the superior initiator to produce polymers with the lowest $Đ$ while achieving the highest I^* (Table 2.1). To evaluate the PCs, polymerizations using DBMM as the initiator were conducted in dimethylacetamide and irradiated with a 365 nm UV nail curing lamp (54 W) (Table 2.1). In accord with diaryl dihydrophenazines, *N*-aryl phenoxazines possessing localized SOMOs (PCs **1** and **2**) did not perform as well as the PCs with separated SOMOs (PCs **3** and **4**). Specifically, **1** and **2** produced poly(methyl methacrylate) (PMMA) with a relatively high $Đ$ of 1.48 and 1.45, respectively (runs 1 and 2). Polymerization results with PCs 3 and 4 were superior, and produced PMMA with lower dispersities ($Đ$ = 1.22 and 1.11, respectively) while achieving high I^*s of 92.6 and 77.3%, respectively (runs 3 and 4).

Further, molecular weight control could be obtained using either PC through modulation of the monomer (runs 5 to 9 for PC **3**; runs 13-17 for PC **4**) or initiator (runs 10-12 for PC **3**; runs 18-20 for PC **4**) ratios (Table 2.2). Overall, PC **3** produced PMMA through higher I^* (∼80−100%) while PC **4** produced PMMA with lower $Đ$ (as low as 1.07). This 1-naphthalene versus 2-naphthalene substitution effect influencing high I^* or low $Đ$, respectively was also observed with diaryl dihydrophenazines.

Table 2.1. *Results of the O-ATRP of MMA Using PCs 1 through 4*[a].

Run No.	PC	Conv. (%)	M_w (kDa)	M_n (kDa)	Dispersity ($Đ$)	I^* (%)
1	**1**	95.6	10.6	7.2	1.48	137
2	**2**	55.3	9.5	6.5	1.45	85.5
3	**3**	78.8	10.8	8.8	1.22	92.6
4	**4**	80.2	11.9	10.8	1.11	77.3

[a]*[MMA]:[DBMM]:[PC] = [1000]:[10]:[1]; 9.35 μmol PC, 1.00 mL dimethylacetamide, and irradiated with a 54 W 365 nm light source for 8 h*

Our analysis of the polymerization of MMA by **3** and **4** showed that both PCs imparted control over the polymerization that is becoming expected from O-ATRP. Specifically, a linear growth in polymer molecular weight as well as a low dispersity during the course of polymerization was attained (Figure 2.4A and B). Additionally, temporal control was demonstrated using a pulsed irradiation sequence (Figure 2.4C−F). Monomer conversion was only observed during irradiation, which resulted in a linear increase in number-average MW (M_n) while producing PMMA with low $Đ$.

Table 2.2. *Results of the O-ATRP of MMA Using PCs 3 and 4.*[a]

Run No.	PC	[MMA]:[DBMM]:[PC]	Conv. (%)	M_w (kDa)	M_n (kDa)	Dispersity ($Đ$)	I^* (%)
5	**3**	[500]:[10]:[1]	80.8	5.8	4.9	1.16	86.1
6	**3**	[1000]:[10]:[1]	78.8	10.8	8.8	1.22	92.6
7	**3**	[1500]:[10]:[1]	72.2	11.4	9.5	1.19	116
8	**3**	[2000]:[10]:[1]	76.5	18.4	14.6	1.26	107
9	**3**	[2500]:[10]:[1]	78.4	25.9	19.8	1.31	101
10	**3**	[1000]:[5]:[1]	74.6	26.4	19.1	1.38	79.6
11	**3**	[1000]:[15]:[1]	74.5	8.3	6.9	1.20	75.7
12	**3**	[1000]:[20]:[1]	80.7	5.5	4.6	1.19	92.9
13	**4**	[500]:[10]:[1]	85.1	5.9	5.4	1.09	84.1
14	**4**	[1000]:[10]:[1]	80.2	11.9	10.7	1.11	77.3
15	**4**	[1500]:[10]:[1]	68.9	12.2	9.8	1.25	109
16	**4**	[2000]:[10]:[1]	58.2	14.7	112.5	1.17	95.2
17	**4**	[2500]:[10]:[1]	65.9	21.2	17.3	1.23	96.6
18	**4**	[1000]:[5]:[1]	70.5	22.3	16.8	1.35	85.3
19	**4**	[1000]:[15]:[1]	70.9	9.3	8.3	1.12	60.6
20	**4**	[1000]:[20]:[1]	76.1	6.8	6.1	1.07	64.0

[a]*See the experimental section for details.*

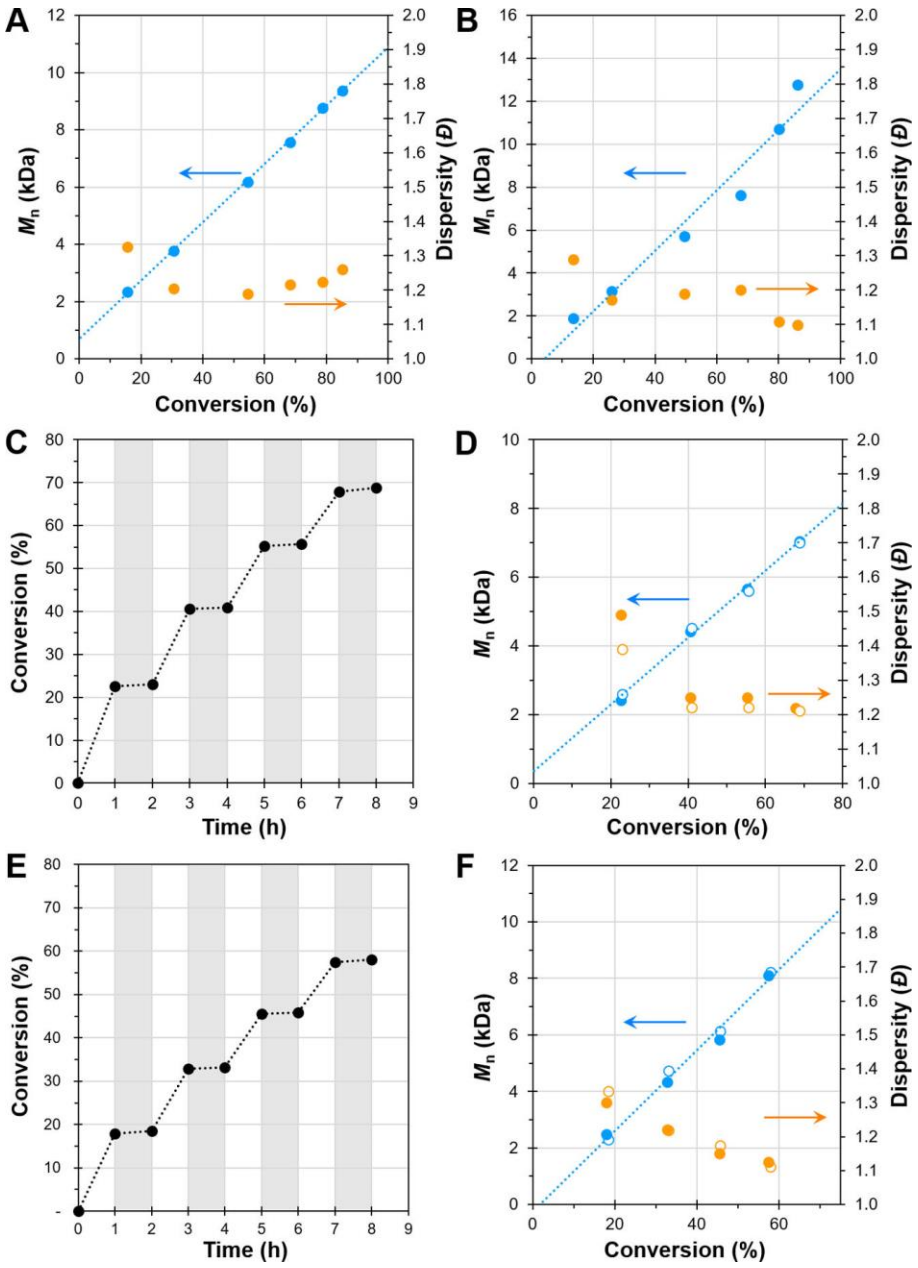

Figure 2.4. *Plots of molecular weight (M_n, blue) and dispersity (Đ, orange) as a function of monomer conversion for the polymerization of MMA catalyzed by* ***3*** *(A) and* ***4*** *(B). Plots of conversion vs time using 3 (C) or 4 (E) (irradiation in white and dark periods in gray) and plots of molecular weight (M_n, blue) and dispersity (Đ, orange) as a function of MMA conversion using a pulsed-irradiation sequence and PC* ***3*** *(D) or* ***4*** *(F) (filled markers are data directly after irradiation while open markers are data directly after the dark period) Conditions for all plots: [MMA]:[DBMM]: [PC] = [1000]:[10]:[1]; 9.35 μmol PC, 1.00 mL dimethylacetamide, and irradiated with UV-light.*

Both PCs also efficiently polymerized other methacrylates, including benzyl methacrylate (BnMA), isobutyl methacrylate (BMA), and isododecyl methacrylate (IDMA) (Table 2.5). As such, **3** was used to perform chain extension polymerizations from an isolated PMMA (M_w = 9.9 kDa, $Đ$ = 1.12) macro- initiator because the ATRP mechanism inherently reinstalls the bromine chain end group onto the growing polymer chain (Figure 2.5). Chain extensions from this PMMA macroinitiator with MMA, DMA, BnMA, and BMA were successful, both confirming high bromine chain end group fidelity and allowing the synthesis of block polymers.

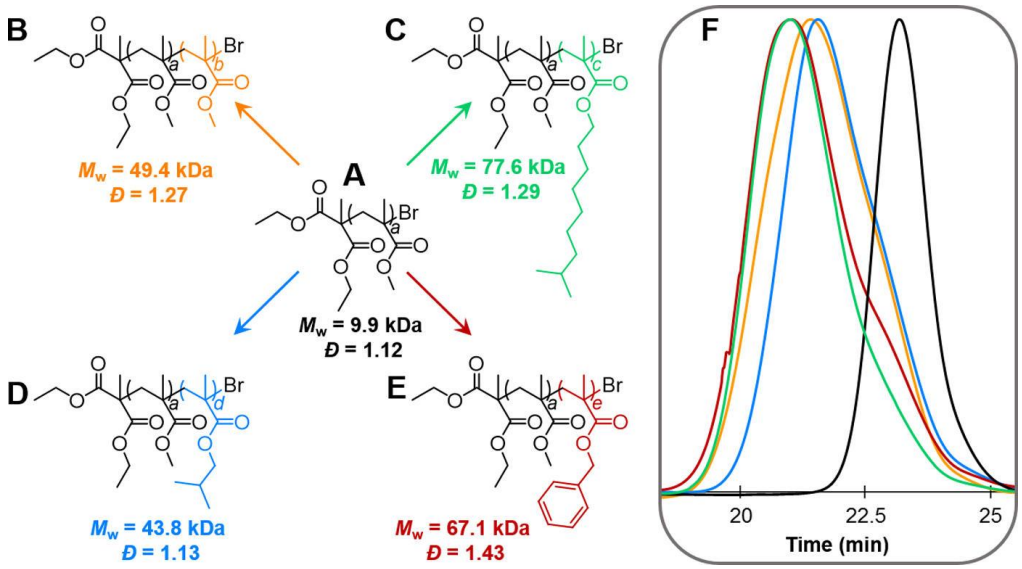

Figure 2.5. *Chain extension polymerizations from a PMMA macroinitiator (A) with MMA (B), IDMA (C), BMA (D), and BnMA (E). Gel permeation chromatography traces of the polymers depicted by the chemical structures with corresponding color schemes (F).*

To further establish these naphthalene phenoxazines as efficient PCs, we next directly compared **3** and 1-naphthalene- 10-phenothiazine as PCs for O-ATRP under our polymerization conditions (Figure 2.16). Both catalysts exhibited nearly identical rates of polymerization, achieving 85.1% and 88.4% monomer conversion after 10 h for **3** and the phenothiazine,

respectively. Additionally, both PCs achieved high I^*s of 93.5% and 95.6%, respectively. However, a significant difference in polymerization performance was observed when comparing the $Đ$ of the resulting PMMA. When using **3**, PMMA was produced with $Đ$ = 1.26, while the phenothiazine produced PMMA with comparatively higher $Đ$ = 1.66, consistent with previous reports[16a,b] using this PC.

As inferred above, the higher $Đ$ of the PMMA produced by the phenothiazine is attributed to the larger reorganization energies of the phenothiazines. Incorporation of O versus S in the core of phenoxazines versus the core of phenothiazines imparts distinct quantitative differences in the electronic and geometric structures of these molecules that affect their performance as PCs for O-ATRP. As such, the planarity of phenoxazines throughout the photoexcitation and ET processes causes them to perform more closely to diaryl dihydrophenazines as PCs for O-ATRP. We hypothesize that the differences between these PCs specifically manifest in each of their abilities to balance the rates of activation and deactivation which results in the differences observed in the $Đ$ of the resulting PMMA produced by each PC.

An additional consideration when comparing phenoxazines, dihydrophenazines, and phenothiazines is that the planar core of phenoxazines and dihydrophenazines promotes intra-molecular charge transfer to charge separated SOMOs while the bent phenothiazine core limits electronic coupling between the heterocyclic ring and the *N*-aryl substituent and consequently the ability to form an intramolecular charge transfer complex.[24] The planar phenoxazine core versus the bent phenothiazine core can be visualized in the X-ray crystal structures of the PCs (Figure 2.6). The electrostatic potential (ESP) mapped electron density of the $^3PC^*$ state of these compounds reveal that electron density is transferred to the naphthalene substituent (red region) in

phenoxazine upon photoexcitation and ISC from ^{1}PC, even more so with dihydrophenazines, while electron density remains localized on the phenothiazine core (Figure 2.7).

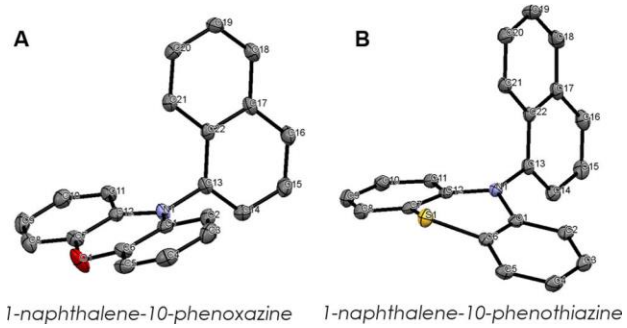

Figure 2.6. *X-ray crystal structures of 1-naphthalene substituted planar phenoxazine (A) and bent phenothiazine (B).*

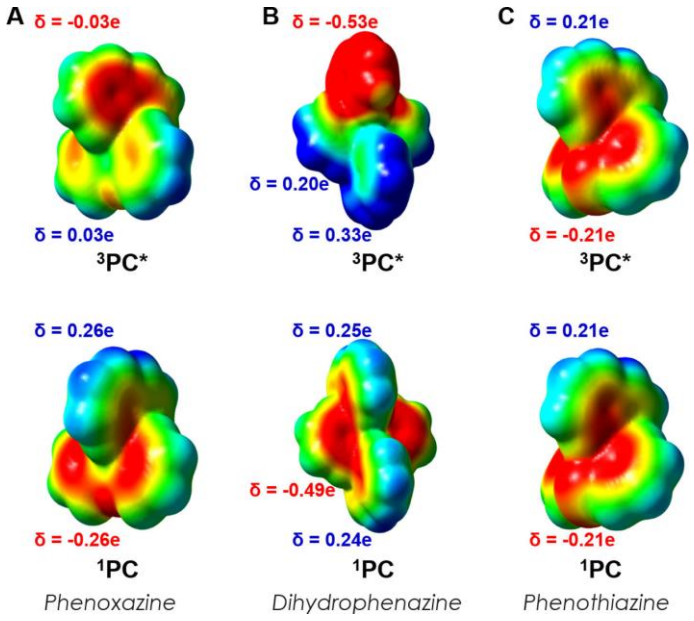

Figure 2.7. *ESP mapped electron density of ^{1}PC and ^{3}PC* of 1-naphthalene substituted phenoxazine (A), dihydrophenazine (B), and phenothiazine (C).*

We further envisaged that a visible light absorbing phenoxazine derivative would provide an even more efficient polymerization catalyst, as irradiation of the reaction with high energy UV-

light can initiate non-desirable reaction pathways, which may increase the $Đ$ of the produced polymer and lower I^*.[25] To realize a visible light absorbing PC we explored a core substituted phenoxazine derivative. Computations predicted that PC **5**, possessing 4-biphenyl core substitutions, would be an excellent target PC with $^3PC^*$ possessing a strong reduction potential and spatially separated SOMOs, while ^1PC would exhibit an absorbance profile in the visible spectrum. The visible light absorbing PC **5** was synthesized in high yield from PC **3** through selective bromination at the 3- and 7-positions on the phenoxazine core using *N*-bromosuccinimide followed by Suzuki cross-coupling.[21] A similar synthetic strategy was recently reported to synthesize thiophene core substituted phenothiazines for use as visible light absorbing catalysts for cationic polymerization.[26] The absorbance profile of PC **5** was not only red-shifted ($\Delta\lambda_{max}$ = 65 nm versus noncore substituted PC **3**) into the visible spectrum (λ_{max} = 388 nm), but also exhibited an extremely enhanced molar extinction coefficient (ε = 26635 $M^{-1}cm^{-1}$ at λ_{max} = 388 nm), making it significantly more efficient at absorbing visible light than the noncore substituted 1-napthalene functionalized phenoxazine, dihydro- phenazine, or phenothiazine (Figure 2.8).

The polymerization performance of PC **5** confirmed our predictions that it would be an excellent PC for O-ATRP, demonstrating superior control over the polymerization than the UV-absorbing phenoxazines or even previously reported dihydrophenazines. The polymerization of MMA using PC **5** irradiated by white LEDs was efficient and showcased characteristics of a controlled polymerization with a linear increase in polymer M_n and a low polymer $Đ$ during the course of polymerization (Figure 2.8C). Furthermore, the molecular weight of the polymer could be tailored through manipulation of either the monomer or initiator loading, while keeping the polymerization otherwise constant, to produce polymers with $Đ$ of 1.13−1.31 while achieving quantitative I^* (Table 2.3).

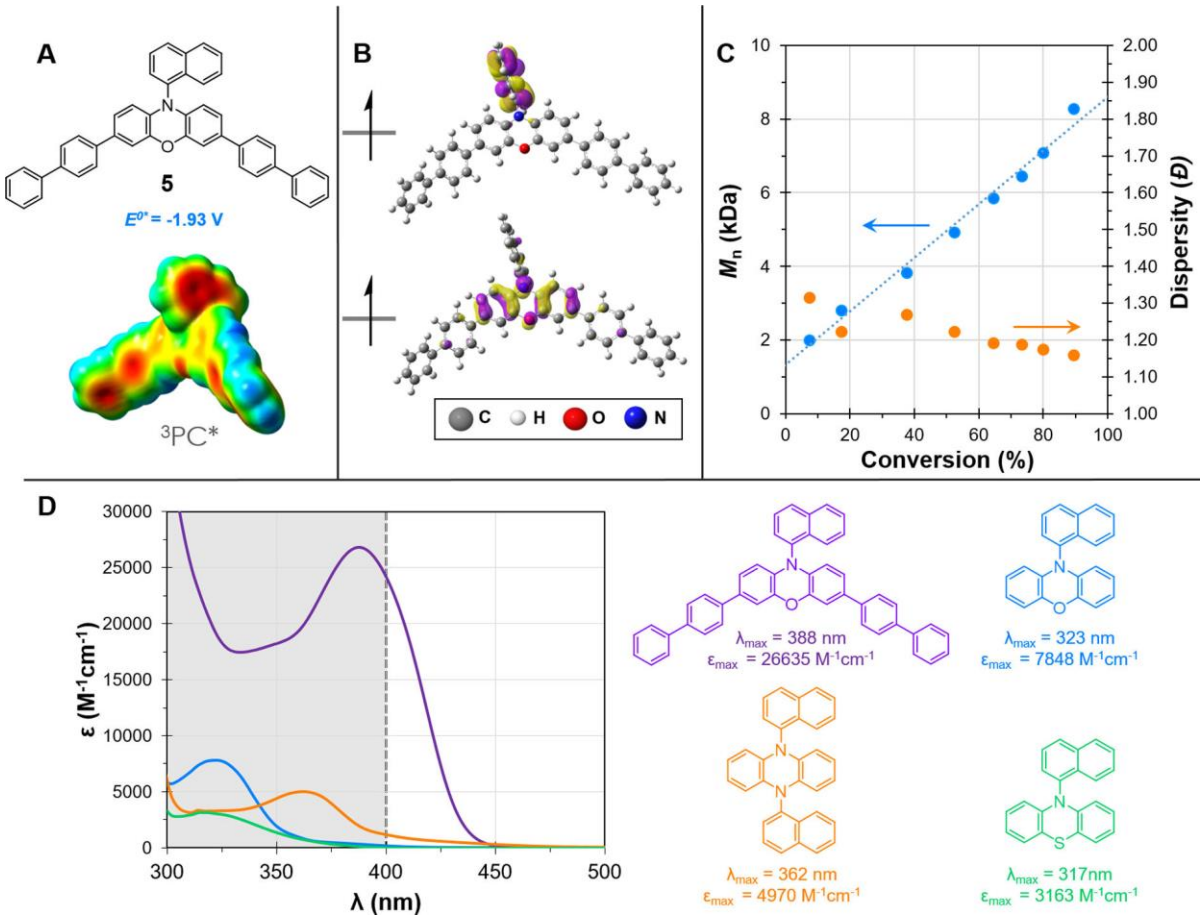

Figure 2.8. *Properties of PC* ***5****. (A) Structure, computed triplet excited state reduction potential, and ESP mapped electron density of* $^3PC^*$ *5. (B) Computed triplet state SOMOs of PC 5. (C) Plot of* M_n *and Đ as a function of monomer conversion for the polymerization of MMA by PC 5; [MMA]:[DBMM]:[5] = [1000]:[10]:[1]; 9.35 μmol PC, 1.00 mL dimethylacetamide, and irradiated with white LEDs. (D) UV−vis spectrum of PC 5 and 1-naphthalene functionalized phenoxazine, dihydrophenazine, and phenothiazine, with color coded structures, and extinction coefficients at their respective* λ_{max} *with the visible absorbance spectrum highlighted in white.*

Table 2.3. *Results of the O-ATRP of MMA Using PC 5*[a]

Run No.	PC	[MMA]:[DBMM]:[PC]	Conv. (%)	M_w (kDa)	M_n (kDa)	Dispersity (Đ)	I^* (%)
21	**5**	[500]:[10]:[1]	67.2	4.07	3.64	1.13	99.4
22	**5**	[1500]:[10]:[1]	75.2	13.7	11.8	1.16	98.0
23	**5**	[2000]:[10]:[1]	90.9	22.9	17.5	1.31	105
24	**5**	[2500]:[10]:[1]	87.5	27.5	21.3	1.29	104
25	**5**	[1000]:[5]:[1]	89.9	23.0	18.1	1.27	101
26	**5**	[1000]:[15]:[1]	73.8	6.17	5.31	1.16	97.5
27	**5**	[1000]:[20]:[1]	72.1	4.52	3.76	1.20	103

[a]*See the Supporting Information for experimental details.*

Conclusion

N-Aryl phenoxazines have proven to be efficient PCs for O- ATRP that produce polymers with controlled molecular weights and low dispersity. Through the culmination of computational and experimental results, we report a visible light absorbing phenoxazine photoredox catalyst that produces polymers with controlled molecular weights and low dispersities, achieving quantitative initiator efficiencies that out- compete previously reported organic PCs for O-ATRP. The continued establishment of design principles for PCs capable of mediating O-ATRP will further expand the scope and impact of this polymerization methodology, which we foresee will translate to an additional means for selective small molecule transformations. Our future work will investigate the intricacies of the charge transfer state that is responsible for efficient photoredox catalysis, which we hypothesize provides extended excited state lifetimes and minimizes undesirable back electron transfer.

Experimental

1. Materials and Methods

Phenoxazine was purchased from Beantown Chemical. 4-biphenyl boronic acid was purchased from TCI America. Glacial acetic acid was purchased from VWR. All other reagents were purchased from Sigma-Aldrich. Chemicals used in polymerizations, including isobutyl methacrylate (BMA), benzyl methacrylate (BnMA), isodecyl methacrylate (IDMA), methyl methacrylate (MMA), diethyl 2-bromo-2-methyl malonate (DBMM), dimethylacetamide (DMA) were purified by vacuum distillation followed by three freeze-pump-thaw cycles and stored under nitrogen atmosphere. Dioxane was purified using an mBraun MB-SPS-800 solvent purification system and kept under nitrogen atmosphere. Dicyclohexylphosphino-2,6-diisopropoxybiphenyl

(RuPhos) and chloro-(2-dicyclohexylphosphino-2,6-diisopropoxy-1,1-biphenyl) [2-(2-aminoethyl)phenyl] palladium(II) - methyl-t-butyl ether adduct (RuPhos precatalyst) were stored under nitrogen atmosphere and used as received. Aryl halides used in the catalyst synthesis were degassed and stored under nitrogen. A Vogue Professional Powerful & Double Wide 54 watt UV lamp Light Nail Dryer was used as the UV light source. One sixteen inch strip of double-density white LEDs, purchased from Creative Lighting Solutions (item no. CL-FRS1210-5M-12V-WH), was wrapped inside a 400 mL beaker and used as a visible light source.

Nuclear magnetic resonance spectra were recorded on a Varian 300 MHz NMR Spectrometer for polymerization conversions and using a Varian 400 MHz or Varian 500 MHz NMR Spectrometer for all other characterizations. All ^{1}H NMR experiments are reported in δ units, parts per million (ppm), and were measured relative to the signals for residual chloroform (7.26 ppm) or benzene (7.15 ppm) in the deuterated solvent. All ^{13}C NMR spectra are reported in ppm relative to $CDCl_3$ (77.23 ppm) or C_6D_6 (128.62 ppm). Analysis of polymer molecular weights was performed via gel permeation chromatography (GPC) coupled with multi-angle light scattering (MALS), using an Agilent HPLC fitted with one guard column, three PLgel 5 μm MIXED-C gel permeation columns, a Wyatt Technology TrEX differential refractometer, and a Wyatt Technology miniDAWN TREOS light scattering detector, using THF as the eluent at a flow rate of 1.0 mL/min. Ultraviolet-visible spectroscopy was performed on an Cary 5000 spectrophotometer using DMA as the solvent. Emission spectroscopy was performed on a SLM 8000C spectrofluorimeter using DMA as the solvent. Cyclic voltammetry was performed with a CH Instruments electrochemical analyzer with a $Ag/AgNO_3$ (0.01 M in MeCN) reference electrode using DMA as the solvent for the working electrode. Samples were sparged with argon for 5 minutes prior to both emission and electrochemical measurements.

2. Procedures

Synthesis of N-aryl phenoxazine catalysts:

10-Phenylphenoxazine (1) A 50 mL storage flask was charged with a stir bar, flame dried under vacuum and back filled with nitrogen three times. The flask was then charged with phenoxazine (183 mg, 1.0 mmol, 1.00 eq.), NaO^tBu (192.2 mg, 2.0 mmol, 2.00 eq.), and RuPhos (12 mg, 0.03 mmol, 0.03 eq.). The flask was taken into a nitrogen filled glovebox where RuPhos Precat (21mg, 0.03 mmol, 0.03 eq.), 1 mL dry dioxane and bromobenzene (0.11 mL, 2.0 mmol 2.00 eq.) were added. The flask was placed in an oil bath at 130º C while stirring for 48 hours. The flask was then cooled to room temperature, diluted with CH_2Cl_2, and the solution was washed with water three times, brine once, dried over $MgSO_4$ and purified by recrystallization from CH_2Cl_2 layered with hexanes at - 25º C to give 60 mg of yellow crystals, 23% yield. NMR matched that reported previously.[27]

4-Trifluoromethylphenyl -10-phenoxazine (2) A 100 mL storage flask was charged with a stir bar, flame dried under vacuum and back filled with nitrogen three times. The flask was then charged with phenoxazine (800 mg, 4.37 mmol, 1.00 eq.), NaO^tBu (840 mg, 8.74 mmol, 2.00 eq.), and RuPhos (52.4 mg, 0.13 mmol, 0.03 eq.). The flask was placed into a nitrogen filled glovebox where RuPhos Precat (91.77 mg, 0.13 mmol, 0.03 eq.), and 4 mL dry dioxane and 4-bromobenzotrifluoride (1.22 mL, 8.74 mmol, 2.00 eq.) were added. The flask was placed in an oil bath at 130º C while stirring for 48 hours. The flask was then cooled to room temperature, diluted with CH_2Cl_2, and the solution was washed with water three times, brine once, dried over $MgSO_4$ and purified by recrystallization from CH_2Cl_2 layered with hexanes on top at - 25º C to yield 987 mg of yellow crystals, 69% yield. Final purification was conducted via sublimation at 100 mTorr

at 175º C. ^{1}H NMR ($CDCl_3$, 500 MHz) δ 7.87 (d, J = 8.20 Hz, 2H), 7.51 (d, J = 8.15 Hz, 2H), 6.73 (dd, J = 7.85, 1.75 Hz, 2H), 6.68 (m, 2H), 6.62 (td, J = 7.85, 1.75 Hz, 2H), 5.90 (d, J = 8.20 Hz , 2H). ^{13}C NMR ($CDCl_3$, 400MHz) δ 144.10, 142.73, 133.89, 131.76, 130.97, 130.64, 128.44, 123.52, 122.09, 115.93, 113.39. ^{19}F NMR ($CDCl_3$, 300MHz) δ 62.55. HRMS (ESI): calculated for M+ $C_{19}H_{12}F_3NO$, 327.0871; observed 327.0869.

1-Naphthalene-10-phenoxazine (3) A stir bar was placed into a 100 mL storage flask, flame dried under vacuum and then back filled with nitrogen three times. The flask was then charged with phenoxazine (1.00 g, 5.46 mmol, 1.00 eq.), NaO^tBu (1.054 g, 10.92 mmol, 2.00 eq.), and RuPhos (65.6 mg, 0.16 mmol, 0.03 eq.). The flask was taken into a nitrogen filled glovebox where RuPhos Precat (114.75 mg, 0.16 mmol, 0.03 eq.), 6 mL dry dioxane and 1-bromonaphthalene (1.53 mL, 10.92 mmol, 2.00 eq.) were added. The flask was placed in an oil bath at 130º C while stirring for 48 hours. The flask was then cooled to room temperature, diluted with CH_2Cl_2, and the solution was washed with water three times, brine once, dried over $MgSO_4$ and purified by recrystallization from CH_2Cl_2 layered with hexanes on top at -25º C to yield 790 mg of yellow crystals, 47% yield. Final purification was conducted via sublimation at 100 mTorr at 190º C. ^{1}H NMR ($CDCl_3$, 500 MHz) δ 8.08 (d, J = 8.35 Hz, 1H), 7.99 (dd, J = 8.20, 3.95 Hz, 2H), 7.66 (t, J = 7.25 Hz, 1H), 7.56 (m, 2H), 7.48 (m, 1H), 6.74 (dd, J = 7.90, 1.45 Hz, 2H), 6.63 (t, J = 7.85 Hz, 2H), 6.49 (td, J = 7.85, 1.45 Hz, 2H), 5.71 (dd, J = 7.90, 1.45 Hz, 2H). ^{13}C NMR ($CDCl_3$, 400MHz) δ 144.09, 135.77, 135.24, 134.48, 131.56, 129.35, 129.14, 128.95, 127.50, 127.07, 127.04, 123.57, 123.53, 121.47, 115.58, 113.57. HRMS (ESI): calculated for M+ $C_{22}H_{15}NO$, 309.1154; observed 309.1152.

2-Naphthalene-10-phenoxazine (4) A 100 mL storage flask was charged with a stir bar, flame dried under vacuum then back filled with nitrogen three times. The flask was then charged with phenoxazine (1.00 g, 5.46 mmol, 1.00 eq.), NaO^tBu (1.054 g, 10.92 mmol, 2.00 eq.), and RuPhos (65.6 mg, 0.16 mmol, 0.03 eq.). The flask was taken into a nitrogen filled glovebox where RuPhos Precat (114.75 mg, 0.16 mmol, 0.03 eq.), 6mL dry dioxane and 2-bromonaphthalene (2.26 mg, 10.92 mmol, 2.00 eq.) were added. The flask was placed in an oil bath at 130º C while stirring for 48 hours. The flask was then cooled to room temperature, diluted with CH_2Cl_2, and the solution was washed with water three times, brine, dried over $MgSO_4$ and purified by recrystallization from CH_2Cl_2 at -25º C to yield 890 mg of light yellow, flakey crystals, 53% yield. Final purification was conducted via sublimation at 100 mTorr at 195º C. ^{1}H NMR ($CDCl_3$, 400 MHz) δ 8.08 (d, J = 8.60 Hz, 1H), 7.95 (d, J = 7.00 Hz, 1H), 7.88 (m, 2H), 7.57 (m, 2H), 7.42 (dd, J = 8.64, 2.04 Hz, 1H), 6.73 (dd, J = 7.84, 1.56 Hz, 2H), 6.66 (t, J = 7.52 ,2H), 6.57 (td, J = 8.12, 1.60 Hz, 2H), 5.99 (d, J = 7.96, 2H). ^{13}C NMR ($CDCl_3$, 400 MHz) δ 144.42, 136.74, 135.06, 134.78, 133.28, 131.55, 130.29, 128.23, 128.15, 127.12, 126.78, 123.49, 121.66, 115.74, 113.78. HRMS (ESI): calculated for M+ $C_{22}H_{15}NO$, 309.1154; observed 309.1151.

1-Naphthalene-10-phenothiazine A stir bar was placed in a 50 mL storage flask, flame dried under vacuum and then back filled with nitrogen three times. The flask was then charged with phenothiazine (0.600 g, 3.01 mmol, 1.00 eq.), NaO^tBu (0.578 g, 6.02 mmol, 2.00 eq.), and RuPhos (42.2 mg, 0.09 mmol, 0.03 eq.). The flask was taken into a nitrogen filled glovebox where RuPhos Precat (73.8 mg, 0.09 mmol, 0.03 eq.), 3 mL dry Dioxane and 1-bromonaphthalene (0.84 mg, 6.02 mmol, 2.00 eq.) were added. The flask was placed in an oil bath at 130º C while stirring for 48 hours. The flask was then cooled to room temperature, diluted with CH_2Cl_2, and the solution was

washed with water three times, brine once, dried over $MgSO_4$ and purified by recrystallization from CH_2Cl_2 layered with hexanes on top at -25º C to yield 253 mg of a yellowish solid, 26% yield. Final purification was conducted via sublimation at 100 mTorr at 155º C. NMR matched that reported previously.[28]

3,7-Dibromo 1-Naphthalene-10-phenoxazine A literature procedure was adapted for this synthesis.[29] 1-Naphthalane-10-phenoxazine (800 mg, 2.58 mmol, 1eq.) was dissolved in 80mL of chloroform. 80mL of glacial acetic acid was then added to the stirring mixture. Aluminum foil was thoroughly wrapped around to cover the reaction vial, blocking out light. In the dark, powdered N-Bromosuccinimide (944 mg, 5.30 mmol, 2.05 eq.) was added in small portions over a 20 minute period. After 2 hours at room temperature the reaction mixture was concentrated under vacuum. The resulting solid was washed three times with water, brine, then dried with $MgSO_4$. A light tan powder (1.0 g, 2.14 mmol, 82.8% yield) was collected. This was used for the Suzuki coupling without further purification. ^{1}H NMR (C_6D_6, 500 MHz) δ 7.82 (d, J = 8.48 Hz, 1H), 7.57 (dd, J = 25.02, 8.3 Hz, 2H), 7.19 (m, 1H), 7.12 (t, J = 8.03 Hz, 2H), 6.88 (dd, J = 7.32, 0.57 Hz, 3H), 6.84 (d, J = 2.19 Hz, 2H), 6.36 (dd, J = 8.54, 2.21 Hz, 2H). ^{13}C NMR ($CDCl_3$, 400MHz) δ144.27, 135.82, 134.22, 133.32, 130.91, 129.88, 129.15, 128.87, 127.83, 127.29, 127.06, 126.62, 123.02, 118.86, 114.74, 113.06.

3,7-Di(4-biphenyl) 1-Naphthalene-10-Phenoxazine (5) A 200mL schlenk flask was flame dried, filled with nitrogen, and equipped with a stir bar and reflux condenser before 3,7-Dibromo 1-Naphthalene-10-phenoxazine (225 mg, 0.48 mmol, 1 eq.), 4-biphenylboronic acid (381.8 mg, 1.9 mmol, 4 eq.) was added, then dissolved in 20 mL of THF. 6 mL of K_2CO_3 (2M) was syringed into

the solution and then heated to 80ºC and stirred for 20 minutes. After which, Palladium tetrakis(triphenylphosphine) (93 mg, 15% mol) in a 20mL solution of THF was added then heated to 100ºC and left to run for 24 hours. Once complete, the reaction was concentrated under vacuum, dissolved in DCM, and washed with water two times, brine, then dried with $MgSO_4$. A bright yellow powder was collected (270 mg, 0.44 mmol, 91.6% yield) after recrystallization in DCM/Methanol. ^{1}H NMR (C_6D_6, 500 MHz) δ 8.18 (d, J = 8.35 Hz, 1H), 7.69 (d, J = 8.09 Hz, 2H), 7.66 (dd, J = 7.21, 2.22 Hz, 2H), 7.51 (d, J = 7.21 Hz, 4H), 7.46 (m, 8H), 7.37 (d, J = 2.0 Hz, 2H), 7.25 (m, 8H), 6.73 (dd, J = 2.03 Hz, 2H), 5.88 (d, J = 8.28 Hz, 2H) . ^{13}C NMR (C_6D_6, 300 MHz) δ 144.49, 140.93, 139.74, 139.02, 135.69, 135.17, 134.49, 133.60, 131.47, 129.06, 128.82, 128.72, 127.52, 127.08, 126.95, 126.86, 126.76, 126.56, 123.38, 122.05, 114.23, 113.98.

Control experiments

Control polymerizations revealed negligible or no polymerization in the absence of any of the components pertinent to the O-ATRP system (light, PC, or initiator) or in the presence of oxygen.

General procedure for O-ATRP of MMA using a UV light source

A 20 mL scintillation vial equipped with a small stirbar was transferred into a nitrogen-atmosphere glove box. To this vial DMA, methyl methacrylate (MMA), photocatalyst from a stock solution in DMA and initiator were added in that order via pipette. The vial was tightly sealed and wrapped in aluminum foil. The vial was transferred out of the glove box, the aluminum foil was removed, then placed under UV irradiation while stirring (Figure 2.9). Timing of the polymerization started once the vial was placed under irradiation. To analyze the progress of the polymerization at a given

time point, aluminum foil was wrapped around the vial, the timer was stopped and the sample was taken back into the glove box where a 0.1 mL aliquot of the reaction was removed via syringe and injected into a vial containing 0.7 mL $CDCl_3$ with 250 ppm butylated hydroxytoluene (BHT) to quench the reaction. The reaction vessel was then transferred back under UV irradiation where the timer was once again started. This aliquot was then analyzed via NMR for conversion. After NMR, the volatiles were removed from the sample, re-dissolved in THF and passed through a syringe filter for analysis by gel permeation chromatography coupled with multi-angle light scattering.

Figure 2.9. *Photograph of the reaction setup for O-ATRP using UV irradiation.*

Monomer scope

The polymerization of different monomers - BMA, BnMA and DMA - were carried out using the general polymerization conditions described above. A ratio of [1000]:[10]:[1], [monomer]:[initiator]:[catalyst] was used with 9.35 mmol of monomer used in each trial. An equal volume of DMA to monomer was used. After the polymerization was allowed to run for 8 hours an aliquot was taken for analysis of monomer conversion by ^{1}H NMR, after which, methanol was immediately added to the reaction mixture to precipitate out the polymer. The resulting solid

polymer was filtered then dried and used for analysis by gel permeation chromatography coupled with multi-angle light scattering. The results from these polymerizations are given in Table 2.5.

General procedure for chain extension of poly methyl methacrylate with various monomers by photocatalyzed O-ATRP

Synthesis of PMMA Macroinitiator

Catalyst 3 (23.2 mg, .0748 mmol, 8 eq.) was dissolved in 8.00 mL DMA and stirred with MMA (8.00 mL, 74.8 mmol, 1000 eq.), and DBMM (143 µL, 0.748 mmol, 10 eq.) in a 20 mL scintillation vial in a nitrogen-filled glove box. The reaction mixture was then wrapped in aluminum foil, removed from the glove box and placed into the aforementioned UV apparatus. The reaction ran for 4 hours before the reaction media was poured into 800 mL of stirring room temperature methanol. The resulting polymer was stirred for an hour before being dissolved in a minimal amount of dichloromethane. The polymer was dissolved with dichloromethane and re-precipitated into stirring methanol a total of three times to remove unreacted monomer, initiator or catalyst (M_n = 8.83 kDa, M_w = 9.85 kDa, $Đ$ = 1.12).

Synthesis of Block Copolymers from isolated macroinitiator

Block copolymers were synthesized using a ratio of [1500]:[10]:[1], [monomer]:[initiator]:[catalyst] using 0.100 g of macroinitiator in each trial, and catalyst 3. Each reaction was set up using the same method as the general polymerization procedure described above. The polymerizations were all run for 10 hours before the reaction media was poured into 100 mL of stirring, room temperature methanol. The resulting polymers were collected via vacuum filtration and dried under vacuum. The results from these polymerizations are given in Table 2.6.

General procedure for O-ATRP of MMA using a visible light source

A 20 mL scintillation vial equipped with a small stirbar was transferred into a nitrogen-atmosphere glove box. To this vial DMA, methyl methacrylate (MMA), photocatalyst from a stock solution in DMA and initiator were added in that order via pipette. Timing of the polymerization started once the vial was placed into an LED-lined beaker (Figure 2.10). To analyze the progress of the polymerization at a given time point, a 0.1 mL aliquot of the reaction was removed via syringe and injected into a vial containing 0.7 mL $CDCl_3$ with 250 ppm butylated hydroxytoluene (BHT) to quench the reaction. This aliquot was then analyzed via NMR for conversion. After NMR, the volatiles were removed from the sample, re-dissolved in THF and passed through a syringe filter for analysis by gel permeation chromatography coupled with multi-angle light scattering.

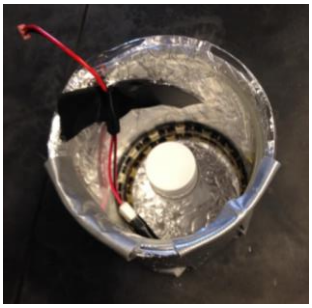

Figure 2.10. *Photograph of the reaction setup for O-ATRP using visible light LED beakers.*

3. Characterization of Catalysts' Photoredox Properties

UV-vis absorption spectroscopy

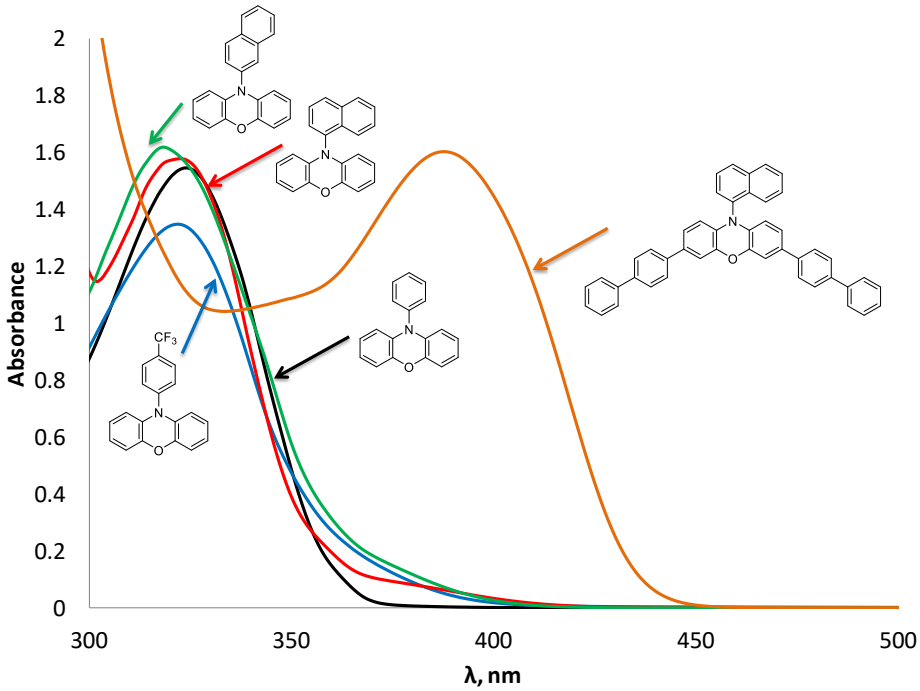

Figure 2.11. *UV-vis absorption spectra of the phenoxazine photocatalysts. PC 1-4 were taken at 0.20 mM and PC 5 was taken at 0.06mM. Solvent = DMA. Path length = 1cm.*

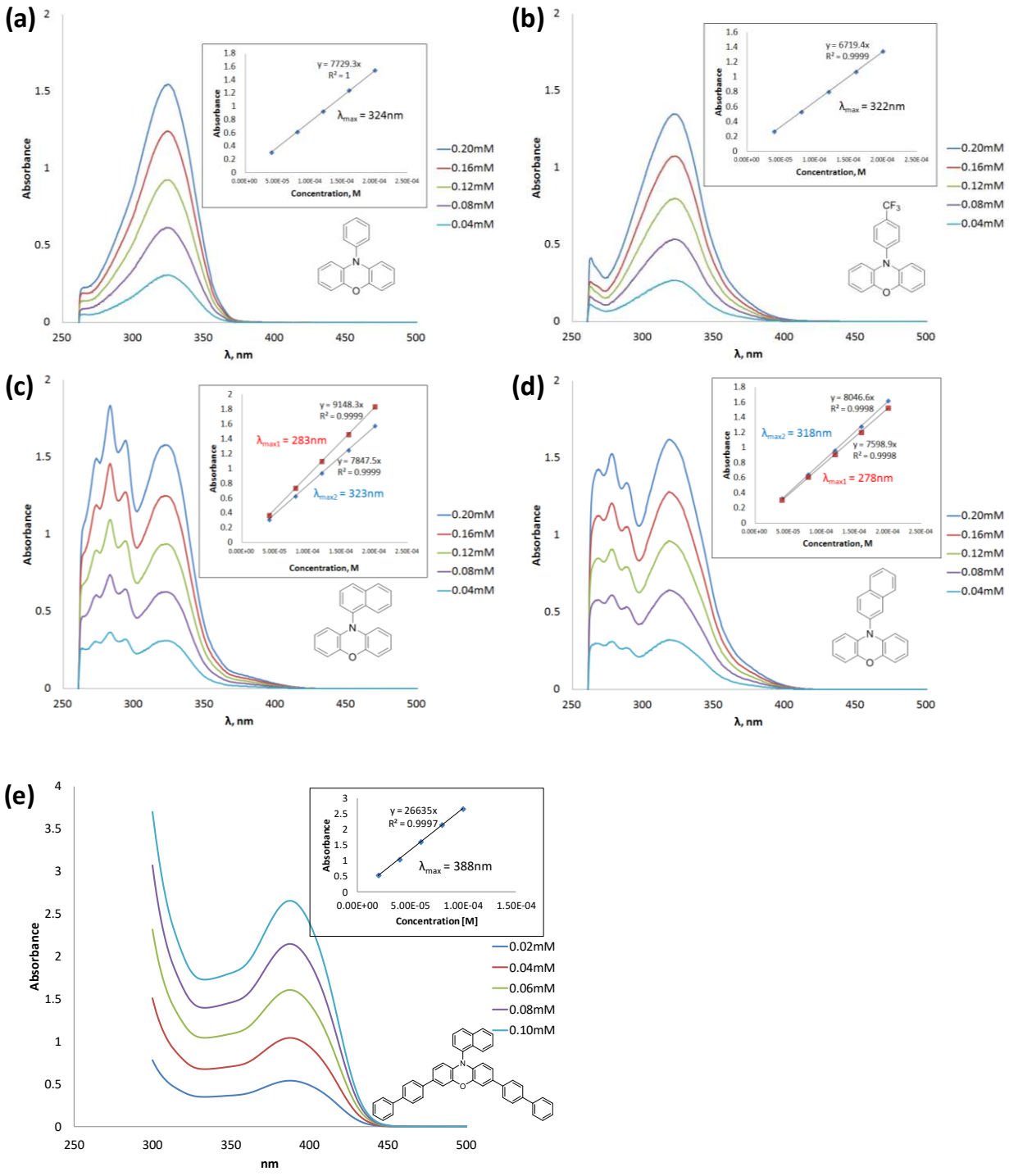

Figure 2.12. *UV-vis absorption of the phenoxazine catalysts taken at different concentrations in DMA. Path length = 1cm.*

Fluorescence spectroscopy

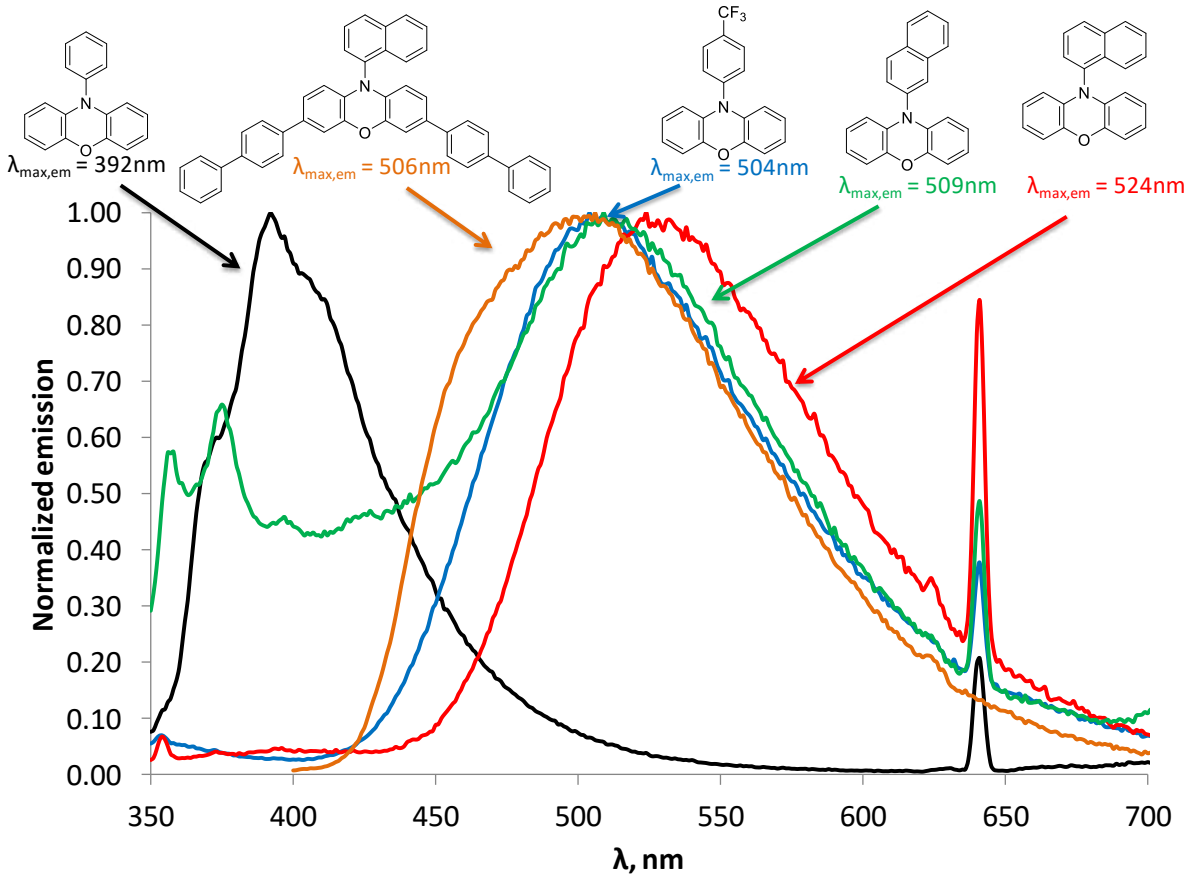

Figure 2.13. *Plot of the normalized emission spectra of the phenoxazine photocatalysts in DMA. PC 1-4 were irradiated with 320 nm light while PC 5 was irradiated with 380nm light.*

Cyclic voltammetry

Work performed by co-author Chern-Hooi Lim

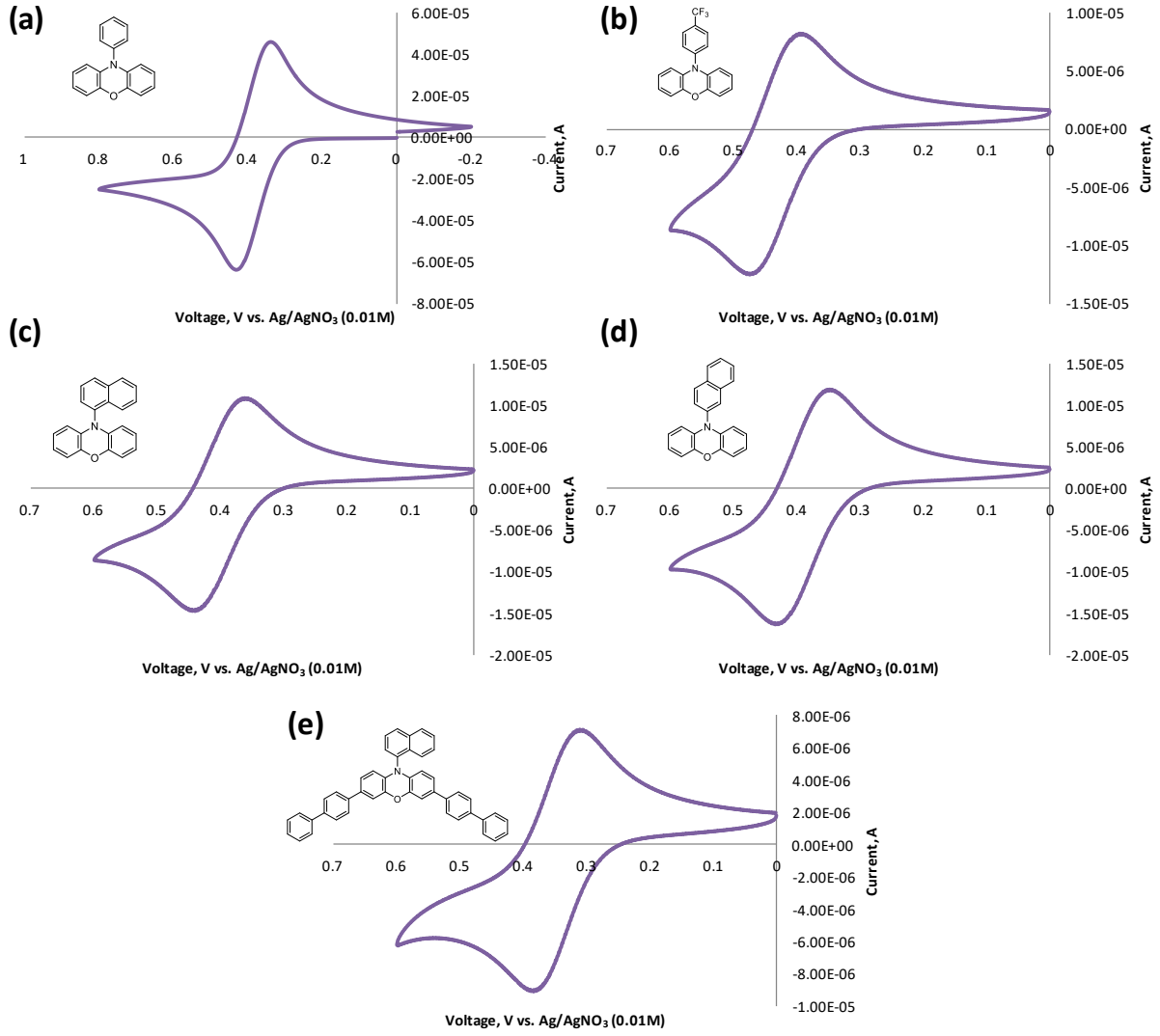

Figure 2.14. *Cyclic voltammograms of the phenoxazine photocatalysts performed in a 3-compartment electrochemical cell. Reference electrode: Ag/AgNO₃ (0.01M) in MeCN; electrolyte: 0.1 M NBu₄PF₆; scan rate: 0.10 V/s. DMA is used as the solvent in the working electrode compartment for (b)-(e) while MeCN is used as the solvent in (a). Platinum is used as both the working and counter electrodes.*

Experimental and theoretical determination of excited state reduction potentials

Work performed by co-author Chern-Hooi Lim

Table 2.4. *Calculation of excited state reduction potentials of photocatalysts 1-5.*

PC	abs λ_{max} (nm)[a]	$\varepsilon_{\lambda max}$ ($M^{-1}cm^{-1}$)[b]	em λ_{max} (nm)[c]	$E_{(em\ \lambda max)}$ (V vs. SCE)[d]	$E_{(triplet),\ theo}$ (V vs. SCE)[e]
1	324	7729	392	3.16	2.69
2	322	6719	504	2.46	2.63
3	323	7848	524	2.37	2.39
4	318	8047	509	2.44	2.45
5	388	26635	506	2.45	2.41

PC	$E_{1/2}$ ($PC^{\bullet+}$/PC) (V vs. SCE)[f]	E^0 ($PC^{\bullet+}$/PC), theo (V vs. SCE)[e]	E^{0*}($PC^{\bullet+}$/PC^*) (V vs. SCE)	E^{0*}($PC^{\bullet+}$/$^3PC^*$), theo (V vs. SCE)[e]
1	0.68	0.58	-2.48[g]	-2.11
2	0.73	0.59	-1.73	-2.03
3	0.70	0.55	-1.67	-1.84
4	0.69	0.55	-1.75	-1.90
5	0.65	0.48	-1.80	-1.93

[a]Maximum absorption wavelength; PC 3 and 4 exhibit another λ_{max} at higher energy wavelengths of 283 nm and 278 nm, respectively. [b]Molar absorptivity at the reported λ_{max}. [c]Maximum emission wavelength when irradiated with 320 nm light (PC 1-4) and 380 nm light (PC 5). [d]Energy of emitted photons. [e]Theoretical predictions from DFT calculations at uM06/6-311+Gdp/CPCM-H_2O//uM06/6-31+Gdp/CPCM-H_2O level of theory. [f]Obtained from cyclic voltammetry. [g]The E^{0*} of PC 1 is significantly more negative than PC 2-5 and deviates from the predicted trend. In the DFT calculations, the triplet excited state was explicitly assumed while the observed emission is likely fluorescence from the relaxed singlet excited state.

4. Computational Details

Work performed by co-author Chern-Hooi Lim

Standard reduction potentials (E^0) were calculated following previously reported procedures.[30,31,32,33] A value of -100.5 kcal/mol was assumed for the reduction free energy of the standard hydrogen electrode (SHE) as described in Ref. 26. Thus, $E^0 = (-100.5 - \Delta G_{red})/23.06$ (V

vs. SHE); for E^0 ($PC^{\bullet+}/{}^3PC^*$), ΔG_{red} = $G({}^3PC^*)$ - $G(PC^{\bullet+})$ while for E^0 ($PC^{\bullet+}$/PC), ΔG_{red} = G(PC) - $G(PC^{\bullet+})$. The Gibbs free energies of ${}^3PC^*$, $PC^{\bullet+}$, and PC (for PC 1-4) were calculated at the unrestricted M06/6-311+G** level of theory in CPCM-H_2O solvent (single point energy) using geometries optimized at unrestricted M06/6-31+G** level of theory in CPCM-H_2O solvent. The triple zeta basis set (6-311+G**) generally improves the E^0 ($PC^{\bullet+}$/PC) by ~0.1V relative to 6-31+G**, while the triplet energy is invariant for these two basis sets. To reference to the Saturated Calomel Electrode (SCE), E^0 (vs. SHE) is converted to E^0 (vs. SCE) using E^0 (vs. SCE) = E^0 (vs. SHE) - 0.24 V. Triplet energies (in eV) of PCs were obtained by [$G({}^3PC^*)$ - G(PC), in kcal/mol]/23.06. Population analysis was performed using electrostatic potential-derived charges with the CHELPG method[34] performed at the unrestricted M06/6-31G** level of theory in CPCM-H_2O solvent.

Geometry optimization of PC 5 (3,7-Di(4-biphenyl) 1-Naphthalene- 10-Phenoxazine) was performed at the unrestricted M06/Lanl2dz level of theory in CPCM-H_2O solvent; the smaller Lanl2dz basis sets was employed for computational efficiency due to its extensive structure. Singlet point calculation at the converged M06/Lanl2dz geometry was then performed at the unrestricted M06/6-311+G** level of theory in CPCM-H_2O solvent.

5. Additional Polymerization Data

Table 2.5. *Polymerization Results of O-ATRP of Methacrylates.*[a]

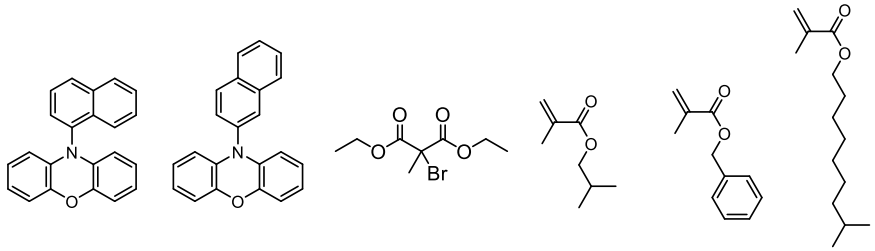

[a]*Polymerizations of vinyl monomers were performed at [1000]:[10]:[1] using DBMM as the initiator and the same volume of solvent as that of the monomer added.*

Table 2.6. *Polymerization Results of O-ATRP PMMA chain extensions.*[a]

PC	Monomer A	Monomer B	Time (h)	M_n (kDa)	M_n (kDa)	$Đ$ (M_w / M_n)
3	MMA	MMA	10	38.8	49.4	1.27
3	MMA	BMA	10	38.8	43.8	1.13
3	MMA	IDMA	10	59.8	77.6	1.29
3	MMA	BnMA	10	46.8	67.1	1.43

PC	Monomer	Time (h)	Conv (%)	M_n (kDa)	M_w (kDa)	$Đ$ (M_w/ M_n)	I^* (%)
3	BMA	8	62.0	13.5	16.4	1.22	67.4
3	BnMA	8	46.1	8.2	11.6	1.41	102
3	DMA	8	87.5	20.9	28.3	1.35	42.9
4	BMA	8	62	15.2	17.3	1.14	59.7
4	BnMA	8	77.1	12.5	16.0	1.28	110
4	IDMA	8	83.2	21.7	28.4	1.31	39.6

[a]*Polymerization chain extensions were performed at [1500]:[10]:[1] using a PMMA macroinitiator and the same volume of solvent as that of the monomer added.*

Table 2.7. *Polymerization Results of O-ATRP initiator screen for PC 1-4.*[a]

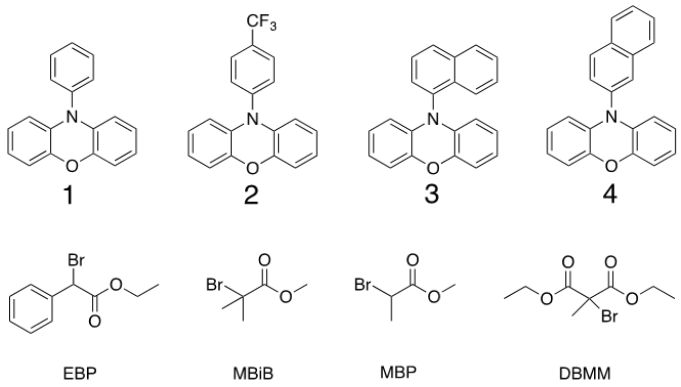

PC	Initiator	Time (h)	Conv. (%)	M_n (kDa)	M_w (kDa)	$Đ$ (M_w/ M_n)	I^* (%)
1	EBP	8	92.2	8.01	14.3	1.79	119
1	DBMM	8	95.6	7.16	10.6	1.48	137
2	EBP	8	61.2	15.4	20.7	1.34	41.2
2	DBMM	8	55.3	6.54	9.48	1.45	85.5
3	EBP	8	66.4	9.29	12.6	1.36	74.2
3	MBiB	8	76.5	9.58	11.8	1.23	81.8
3	MBP	8	70.7	10.9	14.1	1.29	66.4
3	DBMM	8	78.8	8.79	10.8	1.22	92.6
4	EBP	8	59.0	11.3	13.6	1.21	54.7
4	MBiB	8	69.2	11.3	15.0	1.34	63.3
4	MBP	8	31.7	5.80	6.87	1.19	57.6
4	DBMM	8	80.2	10.7	11.9	1.11	77.3

[a]*Polymerizations were performed at [1000]:[10]:[1] for [MMA]:[Initiator]:[PC] using the same volume of DMA as that of the monomer added.*

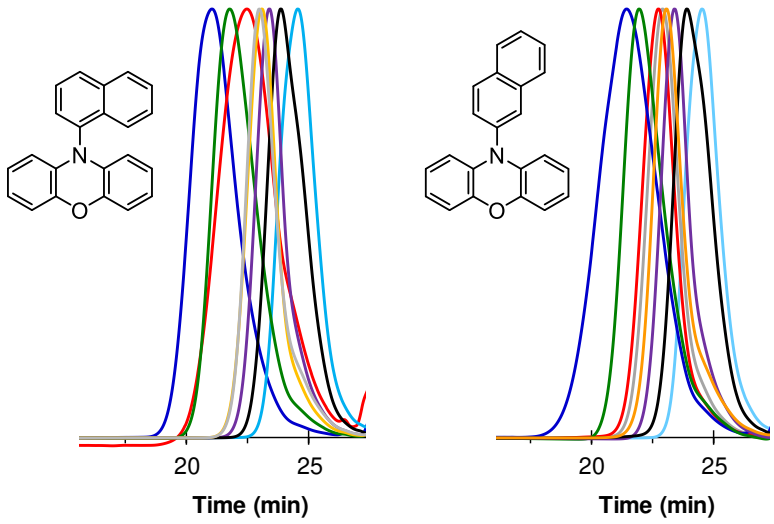

Figure 2.15. *Gel permeation traces of PMMA produced using 3 (left) and 4 (right) reported in Table 2.2. Color scheme corresponds to: (left plot) run 5 (light blue), run 6 (gray), run 7 (orange), run 8 (red), run 9 (green), run 10 (blue), run 11 (purple), rune 12 (black); (right plot) run 13 (light blue), run 14 (orange), runt 15 (gray), run 16 (red), run 17 (green), run 18 (blue), run 19 (purple), run 20 (black).*

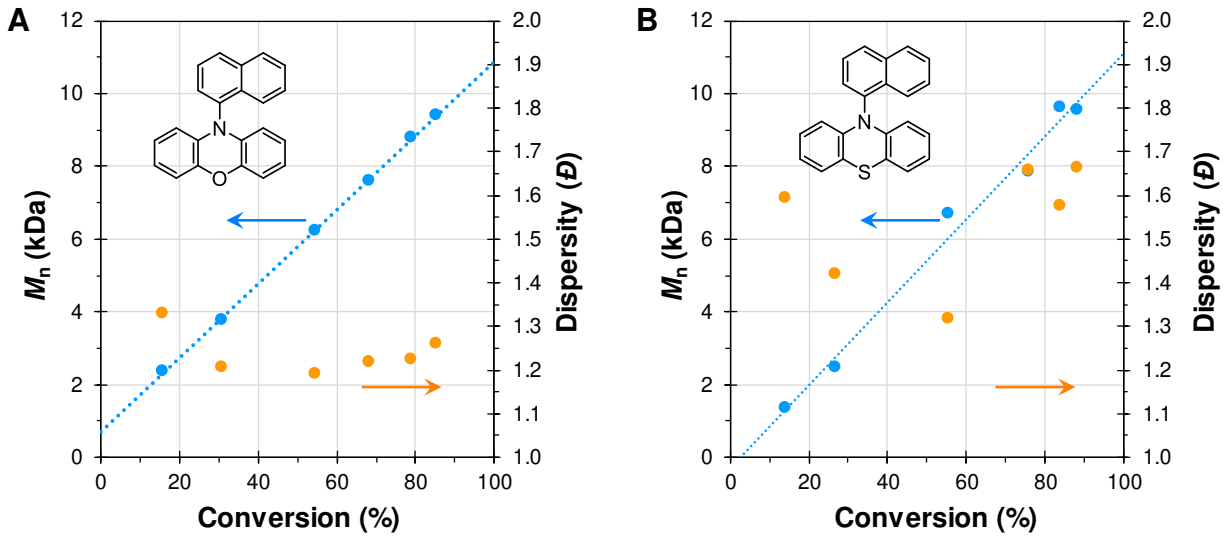

Figure 2.16. *Plots of number average molecular weight (blue) and dispersity (orange) as a function of monomer conversion in the polymerization of methyl methacrylate catalyzed by 1-napthylene-10-phenoxazine (A) and 1-napthylene-10-phenothiazine (B). Conditions: [MMA]:[DBMM]:[PC] = [1000]:[10]:[1]; 9.35 µmoles PC, 1.00 mL dimethylacetamide, and irradiated with 365 nm light.*

REFERENCES

(1) (a) Matyjaszewski, K.; Tsarevsky, N. V. *J. Am. Chem. Soc.* **2014**, *136*, 6513−6533. (b) Matyjaszewski, K.; Tsarevsky, N. V. *Nat. Chem.* **2009**, *1*, 276−288. (c) Kamigaito, M.; Ando, T.; Sawamoto, M. *Chem. Rev.* **2001**, *101*, 3689−3745.

(2) (a) Boyer, C.; Corrigan, N. A.; Jung, K.; Nguyen, D.; Nguyen, T.- K.; Adnan, N. N. M.; Oliver, S.; Shanmugam, S.; Yeow, *J. Chem. Rev.* **2016**, *116*, 1803−1949. (b) Ouchi, M.; Terashima; Sawamoto, M. *Chem. Rev.* **2009**, *109*, 4963−5050. (c) Rosen, B. M.; Percec, V. *Chem. Rev.* **2009**, *109*, 5069−5119.

(3) (a) Tsarevsky, N. V.; Matyjaszewski, K. *Chem. Rev.* **2007**, *107*, 2270−2299. (b) Ding, M.; Jiang, X.; Zhang, L.; Cheng, Z.; Zhu, X. *Macromol. Rapid Commun.* **2015**, *36*, 1702−1721. (c) Matyjaszewski, K.; Jakubowski, W.; Min, K.; Tang, W.; Huang, J.; Braunecker, W. A.; Tsarevsky, N. V. *Proc. Natl. Acad. Sci. U. S. A.* **2006**, *103*, 15309−15314.

(4) (a) Shanmugam, S.; Boyer, C. *J. Am. Chem. Soc.* **2015**, *137*, 9988−9999. (b) Xu, J.; Shanmugam, S.; Boyer, C. *ACS Macro Lett.* **2015**, *4*, 926−932. (c) Xu, J.; Shanmugam, S.; Duong, H. T.; Boyer, C. *Polym. Chem.* **2015**, *6*, 5615−5624. (d) Chen, M.; MacLeod, M. J.; Johnson, J. A. *ACS Macro Lett.* **2015**, *4*, 566−569. (e) Ohtsuki, A.; Lei, L.; Tanishima, M.; Goto, A.; Kaji, H. *J. Am. Chem. Soc.* **2015**, *137*, 5610−5617. (f) Goto, A.; Zushi, H.; Hirai, N.; Wakada, T.; Tsujii, Y.; Fukuda, T. *J. Am. Chem. Soc.* **2007**, *129*, 13347−13354.

(5) (a) Roth, G. H.; Romero, N. A.; Nicewicz, D. A. *Synlett* **2016**, *27*, 714−723. (b) Isse, A. A.; Lin, C. Y.; Coote, M. L.; Gennaro, A. *J. Phys. Chem. B* **2011**, *115*, 678−684.

(6) (a) Corrigan, N.; Shanmugam, S.; Xu, J.; Boyer, C. *Chem. Soc. Rev.* **2016**, *45*, 6165−6212. (b) Schultz, D. M.; Yoon, T. P. *Science* **2014**, *343*, 1239176. (c) Prier, C. K.; Rankic, D. A.; MacMillan, D. W. C. *Chem. Rev.* **2013**, *113*, 5322−5363. (d) Narayanam, J. M. R.; Stephenson,

C. R. *J. Chem. Soc. Rev.* **2011**, *40*, 102−113. (e) Yoon, T. P.; Ischay, M. A.; Du, *J. Nat. Chem.* **2010**, *2*, 527−532. (f) Juris, A.; Balzani, V.; Barigelletti, F.; Campagna, S.; Belser, P.; Von Zelewsky, A. *Coord. Chem. Rev.* **1988**, *84*, 85−277.

(7) (a) Wallentin, C.-J.; Nguyen, J. D.; Finkbeiner, P.; Stephenson, C. R. J. *J. Am. Chem. Soc.* **2012**, *134*, 8875−8884. (b) Furst, L.; Matsuura, B. S.; Narayanam, J. M. R.; Tucker, J. W.; Stephenson, C. R. *J. Org. Lett.* **2010**, *12*, 3104−3107.

(8) (a) Liu, X.; Zhang, L.; Cheng, Z.; Zhu, X. *Polym. Chem.* **2016**, *7*, 689−700. (b) Zhang, G.; Song, I. Y.; Ahn, K. H.; Park, T.; Choi, W. *Macromolecules* **2011**, *44*, 7594−7599.

(9) Nguyen, J. D.; Tucker, J. W.; Konieczynska, M. D.; Stephenson, C. R. J. *J. Am. Chem. Soc.* **2011**, *133*, 4160−4163.

(10) (a) Knorn, M.; Rawner, T.; Czerwieniec, R.; Reiser, O. *ACS Catal.* **2015**, *5*, 5186−5193. (b) Paria, S.; Reiser, O. *ChemCatChem* **2014**, *6*, 2477−2483. (c) Pirtsch, M.; Paria, S.; Matsuno, T.; Isobe, H.; Reiser, O. *Chem. - Eur. J.* **2012**, *18*, 7336−7340.

(11) (a) Yang,Q.; Dumur,F.; Morlet-Savary,F.; Poly,J.; Laleveé, J. *Macromolecules* **2015**, *48*, 1972−1980. (b) Treat, N. J.; Fors, B. P.; Kramer, J. W.; Christianson, M.; Chiu, C.-Y.; Read de Alaniz, J. R.; Hawker, C. J. *ACS Macro Lett.* **2014**, *6*, 580−584. (c) Fors, B. P.; Hawker, C. J. *Angew. Chem., Int. Ed.* **2012**, *51*, 8850−8853.

(12) (a) Chen, M.; Zhong, M.; Johnson, J. A. *Chem. Rev.* **2016**, DOI: 10.1021/acs.chemrev.5b00671. (b) Pan, X.; Tasdelen, M. A.; Laun, J.; Junkers, T.; Yagci, Y.; Matyjaszewski, K. *Prog. Polym. Sci.* **2016**, DOI: 10.1016/j.progpolymsci.2016.06.005. (c) Dadashi-Silab, S.; Doran, S.; Yagci, Y. *Chem. Rev.* **2016**, DOI: 10.1021/ acs.chemrev.5b00586. (d) Zivic, N.; Bouzrati-Zerelli, M.; Kermagoret, A.; Dumur, F.; Fouassier, J.-P.; Gigmes, D.; Laleveé, J. *ChemCatChem* **2016**, *8*, 1617−1631.

(13) (a) Joshi-Pangu, A.; Leśvesque, F.; Roth, H.G.; Oliver, S.F.; Campeau, L.-C.; Nicewicz, D.; DiRocco, D. A. *J. Org. Chem.* **2016**, DOI: 10.1021/acs.joc.6b01240. (b) Nicewicz, D. A.; Nguyen, T. M. *ACS Catal.* **2014**, *4*, 355−360. (c) Ravelli, D.; Fagnoni, M.; Albini, A. *Chem. Soc. Rev.* **2013**, *42*, 97−113. (d) Ravelli, D.; Fagnoni, M. *ChemCatChem* **2012**, *4*, 169−171. (e) Fagnoni, M.; Dondi, D.; Ravelli, D.; Albini, A. *Chem. Rev.* **2007**, *107*, 2725−2756.

(14) Romero, N. A.; Nicewicz, D. A. *Chem. Rev.* **2016**, DOI: 10.1021/acs.chemrev.6b00057.

(15) Miyake, G. M.; Theriot, J. C. *Macromolecules* **2014**, *47*, 8255− 8261.

(16) (a) Yan, J.; Pan, X.; Schmitt, M.; Wang, Z.; Bockstaller, M. R.; Matyjaszewski, K. *ACS Macro Lett.* **2016**, *5*, 661−665. (b) Discekici, E. H.; Pester, C. W.; Treat, N. J.; Lawrence, J.; Mattson, K. M.; Narupai, B.; Toumayan, E. P.; Luo, Y.; McGrath, A. J.; Clark, P. G.; Read de Alaniz, J.; Hawker, C. J. *ACS Macro Lett.* **2016**, *5*, 258−262. (c) Pan, X.; Fang, C.; Fantin, M.; Malhotra, N.; So, W. Y.; Peteanu, L. A.; Isse, A. A.; Gennaro, A.; Liu, P.; Matyjaszewski, K. *J. Am. Chem. Soc.* **2016**, *138*, 2411−2425. (d) Pan, X.; Lamson, M.; Yan, J.; Matyjaszewski, K. *ACS Macro Lett.* **2015**, *4*, 192−196. (e) Treat, N. J.; Sprafke, H.; Kramer, J. W.; Clark, P. G.; Barton, B. E.; Read de Alaniz, J.; Fors, B. P.; Hawker, C. J. *J. Am. Chem. Soc.* **2014**, *136*, 16096−16101.

(17) Theriot, J. C.; Lim, C.-H.; Yang, H.; Ryan, M. D.; Musgrave, C. B.; Miyake, G. M. *Science* **2016**, *352*, 1082−1086.

(18) Prier, C. K.; Rankic, D. A.; MacMillan, D. W. C. *Chem. Rev.* **2013**, *113*, 5322−5363.

(19) (a) Laursen, J. B.; Nielsen, J. *Chem. Rev.* **2004**, *104*, 1663−1686. (b) Palmer, B. D.; Rewcastle, G. W.; Atwell, G. J.; Baguley, B. C.; Denny, W. A. *J. Med. Chem.* **1988**, *31*, 707−712.

(20) (a) Tanaka, H.; Shizu, K.; Miyazaki, H.; Adachi, C. *Chem. Commun.* **2012**, *48*, 11392−111394. (b) Park, Y.; Kim, B.; Lee, C.; Hyun, A.; Jang, S.; Lee, J.-H.; Gal, Y.-S.; Kim, T.

H.; Kim, K.-S.; Park, J. *J. Phys. Chem. C* **2011**, *115*, 4843−4850. (c) Okamoto, T.; Terada, E.; Kozaki, M.; Uchida, M.; Kikukawa, S.; Okada, K. *Org. Lett.* **2003**, *5*, 373−376.

(21) See the *Experimental* section.

(22) Huber, J. R.; Mantulin, W. W. *J. Am. Chem. Soc.* **1972**, *94*, 3755−3760.

(23) (a) Liu, N.; Wang, B.; Chen, W.; Liu, C.; Wang, X.; Hu, Y. *RSC Adv.* **2014**, *4*, 51133. (b) Klein, J. C. L.; Conrad, M., III; Morris, S. A. *Acta Crystallogr., Sect. C: Cryst. Struct. Commun.* **1985**, *C41*, 1202− 1204.

(24) (a) Malińska,M.;Nowacki,J.;Kapturkiewicz,A.;Wozńiak,K. *RSC Adv.* **2012**, *2*, 4318−4328. (b) Borowicz, P.; Herbich, J.; Kapturkiewicz, A.; Anulewicz-Ostrowska, R.; Nowacki, J.; Grampp, G. *Phys. Chem. Chem. Phys.* **2000**, *2*, 4275−4280. (c) Borowicz, P.; Herbich, J.; Kapturkiewicz, A.; Opallo, M.; Nowacki, *J. Chem. Phys.* **1999**, *249*, 49−62.

(25) (a) Frick, E.; Anastasaki, A.; Haddleton, D. M.; Barner-Kowollik, C. *J. Am. Chem. Soc.* **2015**, *137*, 6889−6896. (b) Ribelli, G. G.; Konkolewicz, D.; Bernhard, S.; Matyjaszewski, K. *J. Am. Chem. Soc.* **2014**, *136*, 13303−13312.

(26) Chao, P.; Gu, R.; Ma, X.; Wang, T.; Zhao, Y. *Polym. Chem.* **2016**, DOI: 10.1039/C6PY01095D.

(27) Liu, N.; Wang, B.; Chen, W.; Liu, C.; Wang, X.; Hu, Y. *RSC Adv.* **2014,** *4*, 51133−51139.

(28) Pan, X.; Lamson, M.; Yan, J.; Matyjaszewski, K. *ACS Macro Letters.* **2015,** *2,* 192−196.

(29) Zhu, Y.; Kulkarni, A. P.; Wu, P.-T.; Jenekhe, S. A. *Chem. Mater.* **2008**, *20*, 4200−4211.

(30) He, H.; Zapol, P.; Curtiss, L. A. *The Journal of Physical Chemistry C* **2010**, *114*, 21474–21481.

(31) Tossell, J. A. *Computational and Theoretical Chemistry* **2011**, *977*, 123–127.

(32) Winget, P.; Cramer, C. J.; Truhlar, D. G. *Theoretical Chemistry Accounts: Theory, Computation, and Modeling (Theoretica Chimica Acta)* **2004**, *112*, 217–227.

(33) Zhao, Y.; Truhlar, D. *Theoretical Chemistry Accounts* **2008**, *120*, 215–241.

(34) Spackman, M. A. *J. Comput. Chem.* **1996**, *17*, 49–56.

CHAPTER 3 – STRUCTURE-PROPERTY RELATIONSHIPS FOR TAILORING PHENOXAZINES AS REDUCING PHOTOREDOX CATALYSTS

Overview

Through the study of structure−property relationships using a combination of experimental and computational analyses, a number of phenoxazine derivatives have been developed as visible light absorbing, organic photoredox catalysts (PCs) with excited state reduction potentials rivaling those of highly reducing transition metal PCs. Time-dependent density functional theory (TD-DFT) computational modeling of the photoexcitation of *N*-aryl and core modified phenoxazines guided the design of PCs with absorption profiles in the visible regime. In accordance with our previous work with *N*,*N*-diaryl dihydrophenazines, characterization of noncore modified *N*-aryl phenoxazines in the excited state demonstrated that the nature of the *N*-aryl substituent dictates the ability of the PC to access a charge transfer excited state. However, our current analysis of core modified phenoxazines revealed that these molecules can access a different type of CT excited state which we posit involves a core substituent as the electron acceptor. Modification of the core of phenoxazine derivatives with electron-donating and electron-withdrawing substituents was used to alter triplet energies, excited state reduction potentials, and oxidation potentials of the phenoxazine derivatives. The catalytic activity of these molecules was explored using organocatalyzed atom transfer radical polymerization (O-ATRP) for the synthesis of poly(methyl methacrylate) (PMMA) using white light irradiation. All of the derivatives were determined to be suitable PCs for O-ATRP as indicated by a linear growth of polymer molecular weight as a function of monomer conversion and the ability to synthesize PMMA with moderate to low dispersity (dispersity less than or equal to 1.5) and initiator efficiencies typically greater than 70%

at high conversions. However, only PCs that exhibit strong absorption of visible light and strong triplet excited state reduction potentials maintain control over the polymerization during the entire course of the reaction. The structure−property relationships established here will enable the application of these organic PCs for O-ATRP and other photoredox-catalyzed small molecule and polymer syntheses.

Introduction

Increased interest in photoredox catalysis for small molecule and macromolecular synthesis during the past decade has led to the development of new catalytic transformations using mild conditions.[1] Critical to these advancements has been the use of ruthenium complexes, which were first demonstrated as photoredox catalysts (PCs) several decades ago,[2] and iridium complexes, both of which are capable of absorbing visible light to initiate electron or energy transfer reactions from their reactive photoexcited states. The impressive performance of these catalysts arises from their redox stability and photophysical properties including visible light absorption and formation of excited states that can engage in both reductive and oxidative electron transfers.[1,3] Despite the success of ruthenium and iridium-containing PCs, the use of these transition metal complexes in catalysis has some limitations. For example, the use of ruthenium and iridium-containing PCs in polymer synthesis can limit the application scope for the materials synthesized since these complexes can be challenging to remove from the polymer matrix leading to contamination of the final polymer product. Polymeric materials contaminated with transition metals may not be suitable for biomedical or electronic applications, which limits the broad use of these synthetic methods. As such, the development of organic PCs is desirable.[4] While organic PCs that are strong excited state reductants have recently been reported,[5] it is imperative to establish the structure−property relationships and molecular design principles that govern the

photophysical and catalytic capabilities of these organic molecules to develop new PCs, expand their use in photoredox catalysis, and enable the development of new transformations.

Our work in the field of photoredox catalysis originated with our interest in organocatalyzed atom transfer radical polymerization (O-ATRP), a method to synthesize well-defined polymers using organic PCs activated by UV or visible light. The O-ATRP method originated with the application of UV-light-absorbing N-phenyl phenothiazine,[5b] or visible light absorbing perylene[5e] as organic PCs for the polymerization of vinyl monomers. *N*-phenyl phenothiazine is proposed to access a highly reducing excited state and operate via an oxidative quenching pathway analogous to previously used iridium-catalyzed ATRP systems.[6] Perylene was the first example of a visible light-absorbing PC for O-ATRP, but it is less efficient compared to these other PC families.[5e] We have also investigated *N*,*N*-diaryl dihydrophenazines[5f] and *N*-aryl phenoxazines[5g] as PCs for O-ATRP. *N*,*N*-Diaryl dihydrophenazines absorb visible light to access highly reducing excited states with computationally predicted triplet excited state reduction potentials ($E^{0*}_{T1,calc}[^2PC^{\bullet+}/^3PC^*]$) that can exceed −2.0 V versus SCE. Furthermore, it has been shown that *N*,*N*-diaryl dihydrophenazines bearing electron poor or highly conjugated *N*-aryl substituents access charge transfer (CT) excited states, a property that is proposed to engender superior performance compared to related systems that do not access such states.[7] The CT excited states of these molecules are analogous to the metal-to-ligand charge transfer (MLCT) excited states of transition metal complexes. Similar to how transition metal complexes transfer electron density from an electron-rich metal center to an electron-deficient ligand to access MLCT states, *N*,*N*-diaryl dihydrophenazines transfer electron density from the electron-rich tricyclic phenazine core to one or both *N*-aryl "ligand(s)" to access intramolecular CT excited states if the *N*-aryl substituents are sufficient electron acceptors (exhibit a low-lying π^*). Following this work, we

explored structurally similar *N*-aryl phenoxazines, which typically absorb UVA light to access excited states with similar reduction potentials to those of *N*,*N*-diaryl dihydrophenazines ($E^{0*}_{T1,calc}$ ~ −1.8 to −2.0 V vs SCE). Computational modeling of *N*-aryl phenoxazines predicted that derivatives bearing *N*-naphthyl substituents possess spatially separated singularly occupied molecular orbitals (SOMOs) in the triplet excited state, a feature that is characteristic of CT species.[7] These *N*-naphthyl phenoxazine derivatives were found to be effective PCs for O-ATRP.

Despite the excellent performance of *N*-naphthyl phenoxazine PCs in O-ATRP, we aimed to design visible light-absorbing derivatives because UV light can initiate undesirable side reactions in ATRP.[8] We reasoned that visible light-absorbing phenoxazines could be realized through extending the conjugation on the phenoxazine core via installation of biphenyl core substituents.[5g] For organic light-emitting diodes (OLEDs), core modified phenoxazines were reported for use as donor−acceptor molecules.[9] Guided by this precedence for synthetic modification of the phenoxazine core, we synthesized visible light absorbing PC 1 via installation of biphenyl groups at the 3- and 7-positions of the phenoxazine core of 2 (Figure 3.1A). Indeed, PC 1 absorbs visible light and catalyzes the O-ATRP of methacrylate monomers to synthesize polymers of target MWs with improved control compared to the noncore modified parent compound (2). In addition, PC 1 exhibits robust catalytic performance for O-ATRP carried out in flow reactors[10] and in varied reaction irradiation conditions.[11] More recently, we demonstrated that PC 1 was also effective in catalyzing small molecule transformations such as atom transfer radical additions, substitution trifluoromethylations, and dual photoredox/nickel-catalyzed C−N and C−S cross-coupling reactions that were previously exclusive to transition metal complexes.[12] Given that the phenoxazine core structure can be synthetically modified and that 1 exhibits excellent catalytic

performance for numerous transformations, we envisioned a versatile scaffold for the development of superior organic PCs using core modified *N*-aryl phenoxazines.

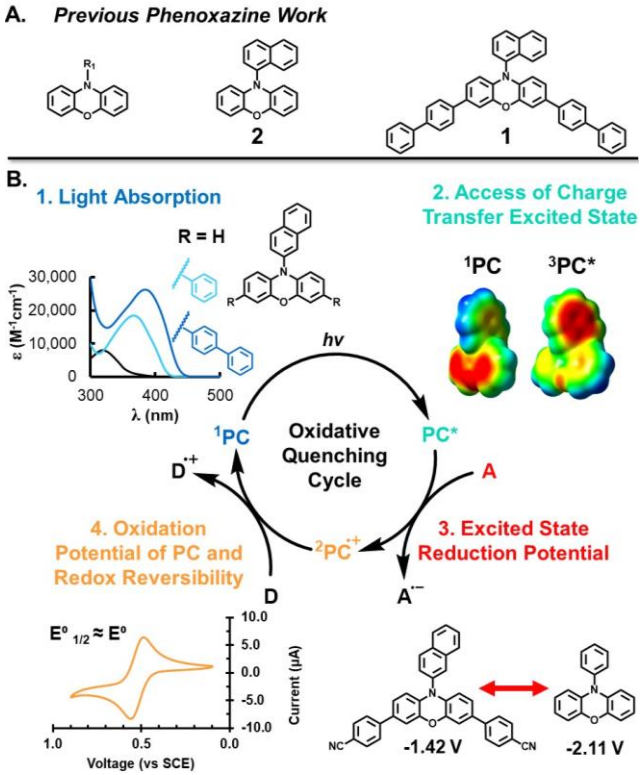

Figure 3.1. *(A) Our previous work with phenoxazine PCs focused on non-core modified PCs and core modified PC* ***1****. (B) Proposed general photoredox cycle that proceeds via an oxidative quenching pathway.* ^{1}PC*: ground state PC;* PC^{*}*: excited state PC, which can be either in the singlet (*$^{1}PC^{*}$*) or triplet (*$^{3}PC^{*}$*) excited state;* $^{2}PC^{\bullet+}$*: radical cation of the photoredox catalyst.*

While our previous work with PC 1 demonstrated the ability to alter the absorption properties of *N*-aryl phenoxazines, broadening the reaction scope and increasing the selectivity of reactions catalyzed by these molecules may require further alteration of their redox properties. In photoredox catalysis employing ruthenium and iridium PCs, alteration of the redox properties of these catalysts has been achieved by changing the electronics of the ligand set.[1,13] Analogous to transition metal PCs, we hypothesized that alteration of the electronics of the phenoxazine scaffold via modification of the *N*-aryl and core substituent(s) would enable the redox properties of the parent catalyst to be tuned. In this work, we investigate this hypothesis as well as characterize the

absorption properties and ability of core modified phenoxazines to access CT excited states. We experimentally and computationally characterize the properties of four previously reported phenoxazines (PCs 1-3 and 6) and 15 new *N*-aryl core modified phenoxazines (PCs 4, 5, and 7-19) to identify structure−property relationships for tailoring organic PC properties (Figure 3.2). In addition, these new phenoxazine derivatives are employed as PCs for photoredox-catalyzed polymer synthesis via O-ATRP to demonstrate their catalytic activity and to understand how differences in PC properties manifest in differences in catalytic performance in OATRP. To the best of our knowledge, this is the first report that characterizes the structure−property relationships of phenoxazine derivatives in the context of photoredox catalysis, and we envision that the design principles established herein will encourage the discovery of photoredox-catalyzed transformations using these PCs.

Results and Discussion

Desirable PC features can be identified with guidance from the photophysical and redox processes involved in a photoredoxcatalyzed oxidative quenching cycle (Figure 3.1B). PCs that absorb visible light are preferred over ultraviolet (UV) light absorbers as UV light can cause undesirable side reactions. Moreover, PCs that possess high molar extinction coefficients (ε) absorb light more efficiently which may increase the population of the reactive excited state catalyst. In general, upon light absorption, the PC is promoted to a singlet excited state (S_n, $n \geq 1$), whereupon, in accordance with Kasha's rule, it quickly relaxes via internal conversion (IC) to S_1. From S_1, triplet states (T_n, $n \geq 1$) can be accessed via intersystem crossing (ISC). Similar to the singlet manifold, higher-energy triplets (T_n) relax via IC to the lowest-energy T_1. Electron transfer processes pertinent to photoredox catalysis can occur from either the S_1 or T_1 state; however, the

longer-lived T_1 state is typically invoked to be responsible for photoredox catalysis when its initiation requires bimolecular collision events.

The ability to access an excited state with CT character in which electron density has been shifted from a donor moiety to an acceptor moiety in the molecule has been identified in both transition metal and organic PCs (Figure 3.1B). Polypyridyl ruthenium and iridium complexes are known to access metal to ligand charge transfer (MLCT) T_1 excited states, where energy wasting charge recombination is slowed, leading to improved catalytic efficiency.[2,14] Analogous to the MLCT states of transition metal complexes, several of the organic molecules that our group[7] and others[15] have investigated are capable of accessing CT excited states. Regardless of whether the PC exhibits CT character in the excited state, it can transfer an electron to a substrate acting as an electron acceptor (A) and enable further reaction. The ability of the photoexcited catalyst (PC^*) to transfer an electron is partially dictated thermodynamically by the excited state reduction potential (E^{0*}). Following the oxidative electron transfer reaction, the catalytic cycle is completed when the oxidized PC (radical cation [$^2PC^{\bullet+}$]) is reduced back to the ground state (^1PC) by an electron donor (D).

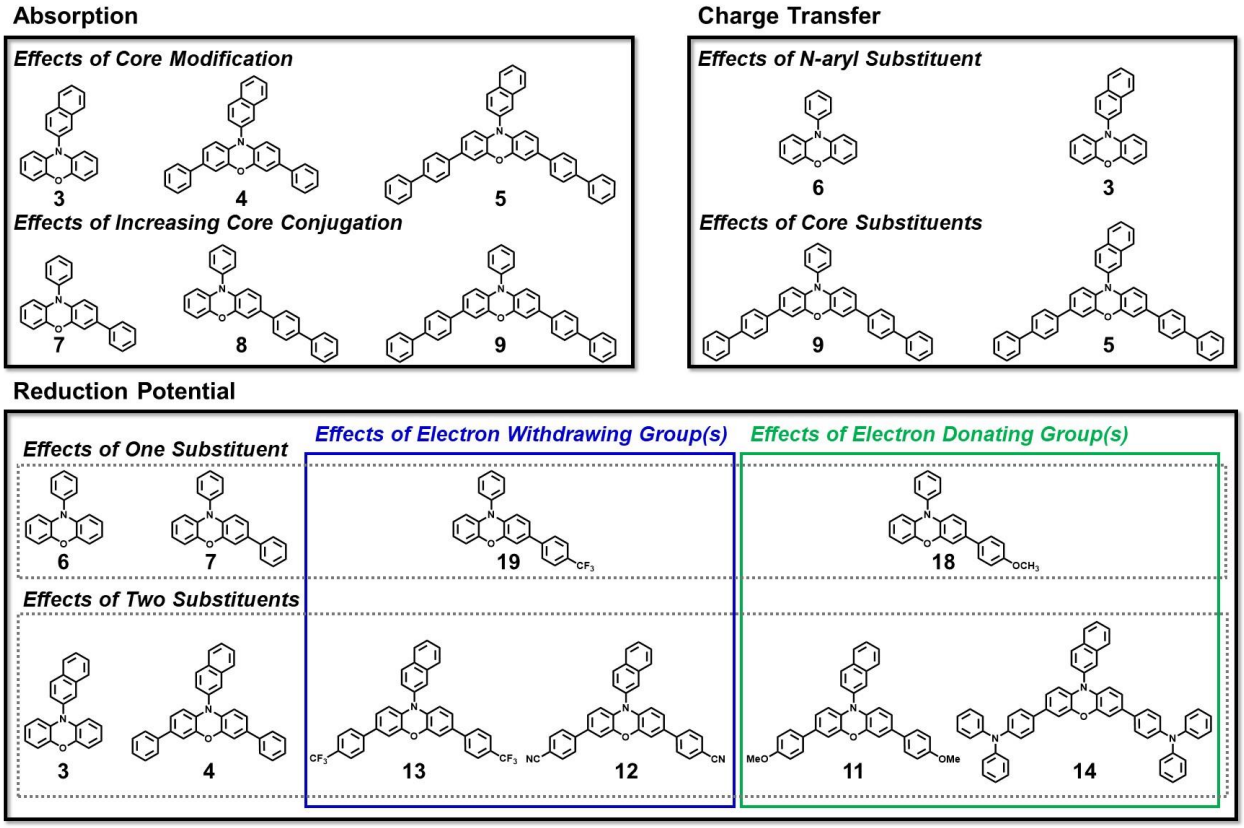

Figure 3.2. *Schematic representation of the subsets of catalysts compared in this work to identify structure-property relationships. The absorption profiles of several phenoxazines were investigated to determine the effects that core modification has on photon absorption in these molecules in order to design visible light-absorbing derivatives (top left). The ability of non-core modified and core modified phenoxazines to access CT excited states was evaluated computationally and spectroscopically (top right). Alteration of the reduction potentials of N-aryl phenoxazines via mono- and di-core substitutions was explored; key comparisons within this group included investigating the effects of electron withdrawing groups (highlighted in blue) and electron donating groups (highlighted in green).*

The four major steps of the catalytic cycle (Figure 3.1B): (1) light absorption, (2) access of a CT excited state, (3) excited state reduction potential, and (4) oxidation potential and redox reversibility were used as criteria to investigate how structural modification of organic excited state reductants impact PC properties. The fundamental questions guiding investigation of these catalyst properties were as follows: (I) How does core modification affect photoexcitation events in *N*-aryl phenoxazines and how does extending the conjugation of the phenoxazine core affect the absorption profiles of these molecules? (II) How does core modification affect the ability of *N*-

aryl phenoxazines to access CT excited states? (III) How does alteration of the electronics of the core substituents affect the excited and ground state redox properties and redox reversibility of core modified phenoxazines? To answer these questions, we designed and investigated three series of phenoxazine derivatives (Figure 3.2). Comparison of PCs within each of these series was used to test our hypotheses corresponding to each of the aforementioned questions.

Light Absorption. In our initial design of PC 1, we hypothesized that installation of aryl core substituents would stabilize the π^* orbitals involved in photon absorption, allowing for photoexcitation using lower-energy visible light (Figure 3.1A). This hypothesis was corroborated by observing that installation of biphenyl substituents onto the core of PC 2 red shifts the maximum wavelength of absorption ($\lambda_{max,abs}$) from 323 to 388 nm (PC 1) with an absorption profile that tails into the visible regime. Very recently, a similar approach was applied to develop visible light absorbing phenothiazine-based PCs.[16] Given that PCs that absorb visible light rather than UV light are more desirable for minimization of side reactions,[1b,8] we were driven to better understand how these structural modifications fundamentally affect photon absorption. Herein, we disclose studies on how systematic core modification alters the energies of the π^* orbitals of phenoxazine PCs, which in turn affects the wavelength of light absorbed and energies of the S_1 and T_1 states (Figure 3.2). Furthermore, the energies of these states dictate the reducing power of the PC in each respective state. Time-dependent density functional theory (TD-DFT) calculations at the CAM-B3LYP/6-31+g(d,p) level of theory were employed to understand the orbitals involved in the $\lambda_{max,abs}$ of photoexcitation for phenoxazine derivatives with increasing aryl conjugation on the core, namely noncoremodified PC 3, phenyl core-modified PC 4, and biphenyl core- modified PC 5 (Figure 3.3). We note that 2-naphthalene is used as the *N*-aryl substituent for the PCs investigated in this work, rather than the 1-naphthalene substitution used previously, in order to expand our

overall understanding of these types of systems, and the noncore-substituted derivative (3) was shown to synthesize polymers with low dispersity (*Đ*) via O-ATRP.[5g]

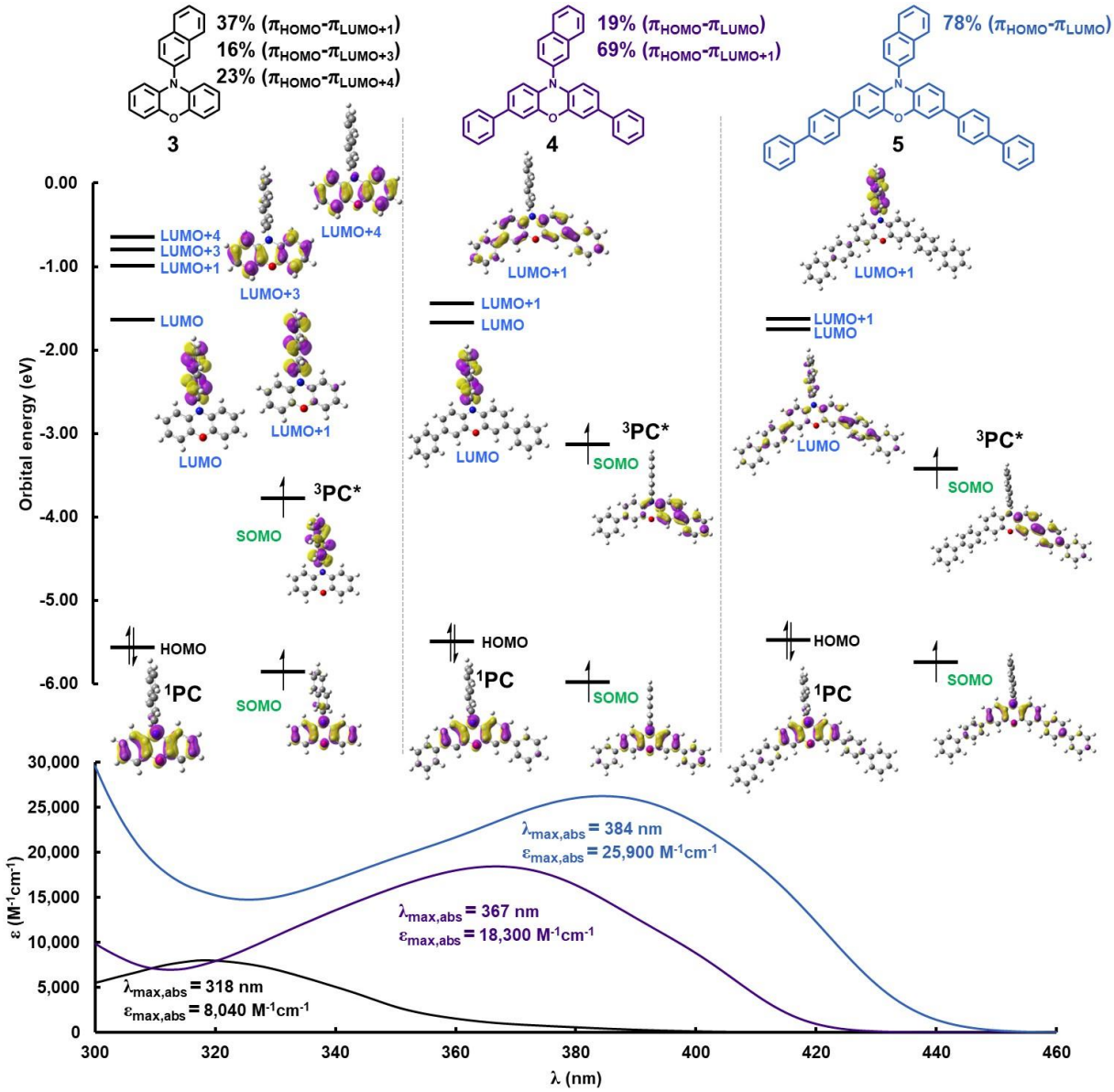

Figure 3.3. *(Top) Time-dependent density functional theory calculations of orbitals involved in photoexcitation of PCs* ***3***, ***4***, *and* ***5*** *at their corresponding* $\lambda_{max,\ abs}$. *Computationally predicted percentage contribution of corresponding orbitals involved in photoexcitation at the* $\lambda_{max,\ abs}$ *are also presented. The zero point on the orbital axis is defined as the electron in a vacuum. (Bottom) UV-vis spectra of each PC acquired in N,N-dimethyl acetamide (DMAc) with the observed* $\lambda_{max,\ abs}$ *and* $\varepsilon_{max,\ abs}$ *shown.*

As can be seen with PCs 3, 4, and 5, regardless of aryl core substituents, the highest occupied molecular orbital (HOMO) is localized on the phenoxazine core with lowest-energy excitation involving these π_{HOMO} electrons (Figure 3.3). Further, these aryl core substituents do not appreciably perturb the energy of the π_{HOMO}, as demonstrated by the similar calculated energies of −5.57 eV, −5.49 eV, and −5.46 eV for PCs 3, 4, and 5, respectively. However, aryl core substituents do significantly change the energies and nature of the low-lying π_{LUMO} orbitals. For PC 3, which lacks core substituents, the energies of unoccupied π orbitals involved in photoexcitation are −0.99 eV (π_{LUMO+1}), −0.79 eV (π_{LUMO+3}), and −0.63 eV (π_{LUMO+4}). PC 3 was experimentally determined to absorb primarily UVA light ($\lambda_{max,abs}$ = 318 nm, Figure 3.3), which is computationally predicted to be the result of excitation from π_{HOMO} into the aforementioned high-lying orbitals, namely π_{LUMO+1}, π_{LUMO+3}, and π_{LUMO+4}, with respective contributions of 37%, 16%, and 23%. In PC 4, core substitution with phenyl groups introduces a new lower-lying π_{LUMO+1} orbital (−1.43 eV) with character inclusive of the phenoxazine core's π^* with extended conjugation into the phenyl substituents. Excitation from π_{HOMO} into this low-lying π_{LUMO+1} (69% contribution) is corroborated by the observed red shift of $\lambda_{max,abs}$ to 367 nm. A similar trend is observed for PC 5, but with a notably larger effect, where biphenyl substituents exert greater stabilization on the phenoxazine core's π^* to yield an even lower-lying π_{LUMO} (−1.74 eV). Thus, the observed $\lambda_{max,abs}$ is red-shifted even further to 384 nm (contributed by 78% π_{HOMO}–π_{LUMO} transition). These analyses and observations highlight the importance of aryl core substituents for the design of visible light-absorbing PCs.

In addition to red-shifting the $\lambda_{max,\ abs}$, core modification also increases the ε_{max} of PC 3 from 8,040 $M^{-1}cm^{-1}$ to 18,300 $M^{-1}cm^{-1}$ (PC 4) and 25,900 $M^{-1}cm^{-1}$ (PC 5), improving the efficiency of photoexcitation (Figure 3.3, bottom). This observation motivated us to determine

trends in how structural modifications affect the efficiency of photon absorption in phenoxazine PCs. As a simple phenoxazine scaffold, phenyl-10- phenoxazine (PC 6) was decorated with a single phenyl (7) or biphenyl (8) core substituent. Systematically increasing the aryl conjugation on the core position increases the ε_{max} value from 6,580 $M^{-1}cm^{-1}$ in PC 7, to 10,300 $M^{-1}cm^{-1}$ in PC 8 (Figure 3.4A). A further increase of ε_{max} was achieved with installation of a second biphenyl core substituent (PC 9) which more than doubles the ε_{max} of PC 8 (ε_{max} = 24,000 $M^{-1}cm^{-1}$ for 9). These data are supported by higher values in the computationally predicted oscillator strength (f) for these PCs (see Table 3.4 in the *Experimental* section).

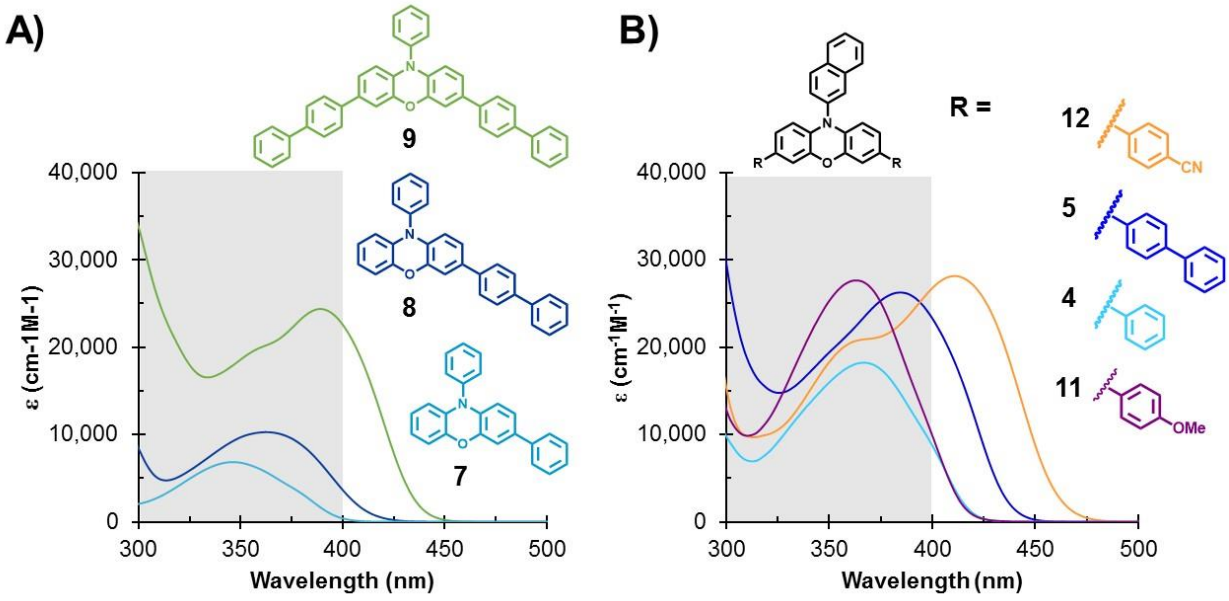

Figure 3.4. *(A) UV-vis absorption spectra acquired in DMAc for N-phenyl phenoxazines. (B) UV-vis absorption spectra for N-2-naphthyl phenoxazines with electron withdrawing, neutral, and donating core substituents. The light grey area indicates the UV regime of the electromagnetic spectrum.*

Previously, we showed that *N*-2-naphthyl phenoxazine (3) exhibits superior catalytic performance in O-ATRP (as indicated by producing polymeric material with lower $Đ$, higher I^* and with a more linear growth of polymer molecular weight as a function of conversion) compared to *N*-phenyl phenoxazine (6), which we proposed is due to the ability of noncore-modified *N*-

naphthyl phenoxazines to access CT excited states.[5g] The better performance of PC 3, motivated investigation of the effects of core modification on the absorption profiles of *N*-2-naphthyl phenoxazines (Figure 3.4B). Core modification with electron-donating 4-methoxyphenyl groups (PC 11) leads to a 4 nm blue-shift relative to PC 4, while core modification with aryl electron-withdrawing substituents has the opposite effect, and the $\lambda_{max,abs}$ of PCs 12 (R= 4-cyanophenyl) and 13 (R= 4-trifluoromethylphenyl) are red-shifted 44 and 21 nm, respectively (Figure 3.4B and see Figures 3.73–75 in the *Experimental* section). In fact, the cyano-containing PC 12 exhibits the most red-shifted absorption spectrum of the phenoxazines investigated, being the only PC with a $\lambda_{max,abs}$ in the visible regime ($\lambda_{max,abs}$ = 411 nm, ε = 22,300 $M^{-1}cm^{-1}$). Exceptions to these trends are observed in the absorption profiles of PCs 14, 15, and 16 (Figures 3.76, 3.71, and 3.72, respectively, and Table 3.5 of the *Experimental* section). PC 14, which possesses electron-donating diphenyl amino core substituents, does not exhibit a blue shift in absorption compared to PC 4. Installation of more highly conjugated phenanthracenyl (15) and pyrenyl (16) core substituents does not lead to a red shift of the $\lambda_{max,abs}$ compared to PC 4. In these cases, in-depth evaluation of the destabilizing or stabilizing effects of aryl core-substituents on π_{core} (HOMO) and π^*_{core} (LUMOs) have to be considered to determine the net effect on $\lambda_{max,abs}$. Ultimately, the design of core-modified phenoxazines enabled 12 visible light absorbing *N*-aryl phenoxazine PCs to be realized with red-shifted $\lambda_{max,abs}$s compared to non-core-modified derivatives, with one derivative exhibiting a $\lambda_{max,abs}$ = 411 nm (PC 12). In addition, these derivatives exhibit ε_{max}s typically greater than 10,000 $M^{-1}cm^{-1}$, with one derivative exhibiting a ε_{max} of 37,700 $M^{-1}cm^{-1}$ (PC 14).

Access of Charge Transfer Excited State. Previously, we observed that *N*,*N*-diaryl dihydrophenazine PCs, which are structurally similar to *N*-aryl phenoxazines, are capable of accessing CT excited states.[7] In the lowest excited state of these compounds, CT occurs from the

electron-rich dihydrophenazine core (electron donor) to the *N*-aryl substituents (electron acceptor), given that the substituents possess a low-lying π^* orbital (e.g., 2-naphthyl). We empirically observed that *N*,*N*-diaryl dihydrophenazine PCs that exhibit CT character perform better in O-ATRP, which we posit is due, in part, to minimization of unproductive back electron transfer.[7] In our previous work with *N*-aryl phenoxazines, we observed a similar trend. Specifically, PCs with *N*-naphthyl substituents (PCs 1, 2, and 3) are computationally predicted to possess spatially separated SOMOs in the triplet excited state (for the SOMOs of PC 3 see Figure 3.3), and these PCs (1, 2, and 3) perform better in O-ATRP compared to those that do not exhibit this feature (PC 6).[5g] However, experimental characterization of the nature of CT in phenoxazine PCs was only recently investigated using PC 1.[12] In the current work, CT character in core and noncore modified *N*-phenyl and *N*-2-naphthyl phenoxazines is explored.

To investigate the nature of the excited states of *N*-aryl phenoxazines, the properties of $^3PC^*$, $^1PC^*$, and ^1PC for 3 and 6 were explored. Electrostatic potential (ESP)-mapped electron density diagrams were used to predict the distribution of electron density for PCs 3 and 6 in their ground and triplet excited states (Figure 3.5A). In PC 6, similar electron density distributions (depicted in red) are observed in both ^1PC and $^3PC^*$, which indicates a lack of CT character. We reason that the *N*-phenyl substituent in PC 6 does not possess a π^* that is low enough in energy to accept an electron from the phenoxazine core in the excited state, thus preventing CT. On the contrary, PC 3, which possesses a lower-lying 2- naphthyl π^* orbital, exhibits a shift in electron density for ^1PC versus the $^3PC^*$, suggesting that the T_1 state has CT character with transfer of electron density to the 2-naphthyl substituent and depletion on the phenoxazine core.

For these same molecules, fluorescence studies enable exploration of CT character (Figure 3.5B). The observed emission in PCs 3 and 6 is likely from the S_1 state since the emission is not

quenched by the presence of oxygen, a known triplet quencher. On one hand, PC 6 exhibits a small Stokes shift, Δλ (difference between its $\lambda_{max,abs}$ [324 nm] and $\lambda_{max,em}$ [392 nm]), in DMAc [Δλ = 68 nm (0.66 eV)] with a sharp and featured emission peak. In contrast, PC 3 exhibits a larger Stokes shift in DMAc [Δλ = 191 nm (1.46 eV)] and a broad and featureless emission profile, a hallmark of a CT emission.[7,15] These data suggest that the S_1 state of PC 3, possessing significant CT character, is qualitatively different from that of PC 6.

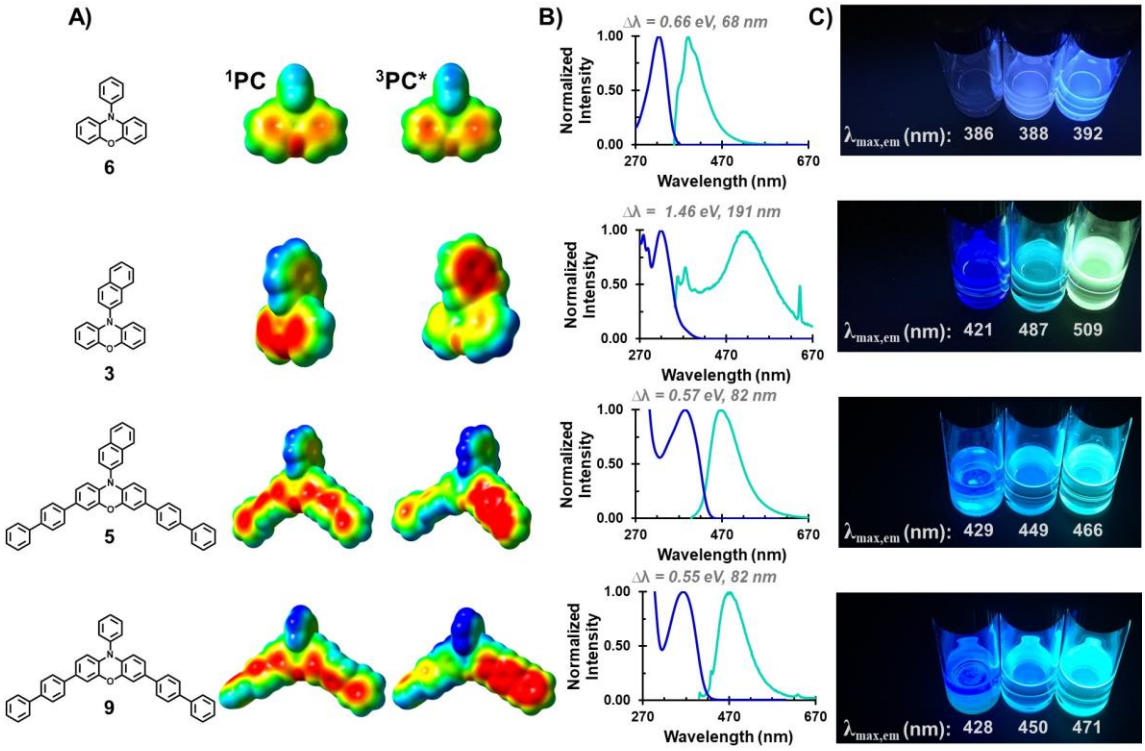

Figure 3.5. *(A) Electrostatic potential (ESP)-mapped electron density of phenoxazine PCs **3**, **5**, **6**, and **9** are shown for the singlet ground state (left) and triplet excited state (right). (B) Overlays of the absorption profiles acquired in DMAc (dark blue) and emission profiles acquired in DMAc (turquoise) with the experimentally determined Stoke Shifts (Δλ) are shown for each PC. (C) Photographs of the PCs dissolved in solvents with increasing polarity, as indicated by their increasing Reichardt parameter ($E_T(30)$ in kcal/mol). From left to right: 1-hexene ($E_T(30)$ = 32.4 kcal/mol), THF ($E_T(30)$ = 37.4 kcal/mol), , and DMAc ($E_T(30)$ = 42.9 kcal/mol). The maximum wavelength of emission ($\lambda_{max,em}$) of PCs **3**, **5**, **6**, and **9** acquired in each of these solvents is shown below the corresponding scintillation vial in the photograph. For the full emission spectra of PCs **3**, **5**, **6**, and **9** in these solvents, please see Figures S89-S92 in the supporting information.*

Further support for the assignment of CT character in the excited state is the observance of fluorescence solvatochromism with changing solvent polarity.[17] The intramolecular transfer of electron density in CT molecules typically creates a larger molecular dipole in the excited state (compared to the ground state), which is more stabilized in polar solvents, leading to lower energy emission. To qualitatively and quantitatively determine the presence or absence of solvatochromic behavior in PCs 6 and 3, the emission of these PCs was studied in three solvents (1-hexene, tetrahydrofuran [THF], and DMAc) of varying polarity, as indicated by their different Reichardt polarity parameters, ET(30), expressed in kcal per mole [$E_T(30)$ = 32.4, 37.4, 42.9, respectively, Figure 3.5C].[17] While PC 3 clearly exhibits solvatochromic behavior, as indicated by a change in the color of its emission in different solvents, PC 6 qualitatively appears to emit the same color. Moreover, the wavelength of emission for PC 6 was measured in these three solvents and found to shift by no more than 6 nm or 0.05 eV (Figure 3.98, *Experimental*). In contrast, the $\lambda_{max,em}$ for PC 3 red shifts 66 nm (0.40 eV) going from 1-hexene to THF and another 22 nm (0.11 eV) going from THF to DMAc (Figure 3.99, *Experimental*). The emission profiles, Stokes shifts, and solvatochromic behavior of PCs 6 and 3 are analogous to that of *N*,*N*-diphenyl and *N*,*N*-dinaphthyl dihydrophenazines, respectively, suggesting that noncore modified *N*-aryl phenoxazines must also be designed with an *N*-aryl substituent possessing a low-lying π^* to yield PCs with accessible CT states.

After gaining an understanding of the nature of CT in 3 and 6, we were motivated to determine if core modification affects the ability of *N*-aryl phenoxazines to access CT excited states (Figure 3.5). To do this, we performed a similar analysis of PCs 5 and 9, which are core modified derivatives of PCs 3 and 6, respectively. We initially hypothesized that the excited states of these core-modified derivatives would mimic that of the parent molecules such that PC 5

accesses an excited state with CT character and exhibits similar emission to PC 3 while PC 9 exhibits no CT character. However, in comparing PC 5 in the ground state and T_1 state, the ESP diagrams show that electron density has moved from the phenoxazine core in the ground state to one of the biphenyl core substituents in the triplet excited state. This observation is qualitatively different from PC 3, in which CT is predicted to be toward the *N*-naphthyl substituent in the triplet excited state. PC 5 exhibits bathochromic emission behavior similar to PC 3 but to a lesser extent. For PC 5, its $\lambda_{max,em}$ red shifts from 1-hexene [$E_T(30)$ = 32.4 kcal/mol] to THF [$E_T(30)$ = 37.4 kcal/mol] by 20 nm and exhibits another 17 nm red shift in DMAc [ET(30) = 42.9 kcal/mol, Figure 3.100, *Experimental*]. In addition, PC 5 exhibits a smaller $\Delta\lambda$ (82 nm, 0.57 eV in DMAc) than PC 3, suggesting a smaller energy difference between the initially excited S_n state and the relaxed S_1 state. In concert, these findings refute our original hypothesis by indicating that PC 5 can access a CT excited state that is qualitatively distinct from PC 3. This conclusion is corroborated by the emission data of PC 9. To our surprise, the $\lambda_{max,em}$, $\Delta\lambda$, and solvatochromic behavior of PC 9 is similar to that of PC 5, indicating that it can access a CT excited state despite bearing an *N*-phenyl group rather than an *N*-naphthyl group (Figure 3.5 and Figure 3.101 of the *Experimental* section). These observations support the notion that photon emission in PCs 5 and 9 is CT in nature but is tied to the phenoxazine core and its biphenyl substituents.

Excited State Reduction Potential. An inherent challenge in the design of visible light absorbing PCs lies in lowering the energy of photoexcitation without sacrificing excited state reducing power. Ideally, one would like to lower the energy of the S_n state for visible excitation while maintaining similar energies for the S_1 or T_1 state required for excited state redox chemistry with similar reactivity. This principle was applied to design visible light absorbing phenoxazine PCs that are still strongly reducing in their excited states. For example, noncore-modified PC 3

absorbs in the UV regime but core-modified PC 5 absorbs in the visible regime, indicating that photoexcitation is to higher energy Sn states for PC 3 compared to PC 5. Since the T_1 state is typically assigned as the reactive species in photoredox-catalyzed transformations requiring bimolecular collisions, the triplet excited state reduction potentials of these PCs ($E^{0*}_{T1,calc}$) were computationally calculated (Figure 3.6). The $E^{0*}_{T1,\,calc}$ was determined to be −1.90 V versus SCE[5g] for UV-light absorbing PC 3 and somewhat lower (−1.70 V vs SCE) for visible light absorbing PC 5 (Figure 3.6). Even though the $E^{0*}_{T1,\,calc}$ is lower for PC 5, this value is still on par with some of the most reducing transition metal PCs such as fac-Ir(ppy)$_3$, which exhibits a triplet excited state reduction potential of −1.73 V versus SCE.[1b] This example demonstrates that the strong reducing power of *N*-aryl phenoxazines in the excited state can still be maintained after core modification is used to lower the energy of light required for photoexcitation.

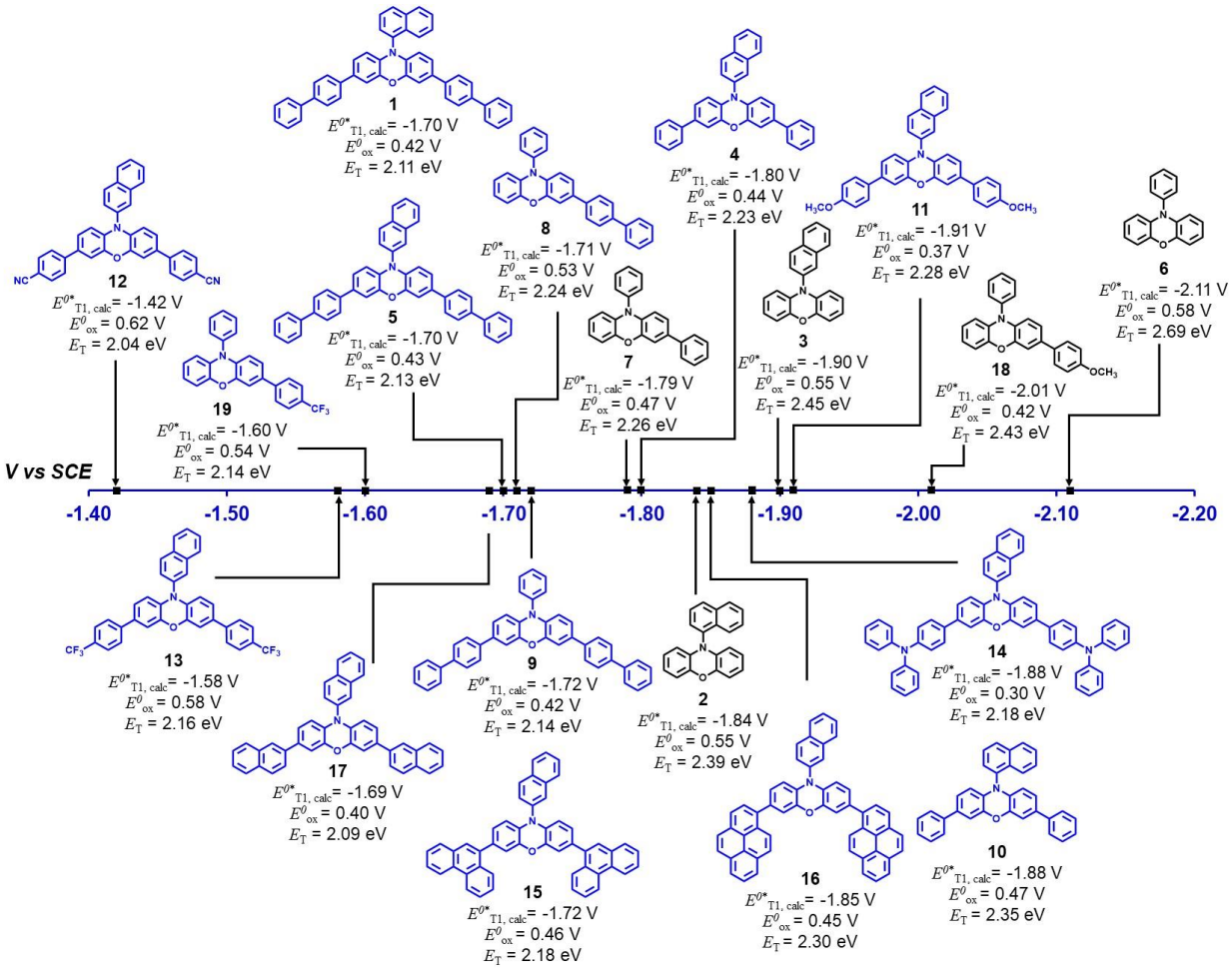

Figure 3.6. *Structures, calculated triplet excited state reduction potentials ($E^{0*}_{T1,calc}[PC^{\bullet+}/^3PC^*]$), calculated oxidation potential of $^2PC^{\bullet+}$ ($E^0_{ox}=E^0[^2PC^{\bullet+}/^1PC]$), and calculated triplet energies (E_T) of phenoxazines investigated in this study. Catalysts colored in grey are UVA-light absorbing and catalysts colored in blue are visible light-absorbing.*

In addition to designing visible light absorbing PCs that are strong excited state reductants, we sought to design PCs with a range of excited state reduction potentials. The triplet excited state reduction potential (E^{0*}_{T1}) is defined as E^{0*}-[$^2PC^{\bullet+}/^3PC^*$] = $E^0[^2PC^{\bullet+}/^1PC]$ − ET, where ET is the triplet energy (the difference in energy between T_1 excited state and S_0 ground state) and E^0_{ox} = $E^0[^2PC^{\bullet+}/^1PC]$ is the potential to oxidize ^1PC to $^2PC^{\bullet+}$. Thus, for catalysts with similar triplet energies, those that are easier to oxidize will be more strongly reducing in the excited state. We envisioned that the excited state reduction potentials (E^{0*}s) of *N*-aryl core modified phenoxazines

could be tuned through alteration of the electronics of the core substituents which would in turn alter the values of E^0_{ox}, the singlet energy (ES), or ET and lead to alteration of the singlet and triplet E^{0*}s.

To investigate the range of E^{0*}s that can be achieved with the phenoxazine PC scaffold, core-modified PCs bearing electron-donating and electron-withdrawing groups (4, 5, and 7−19) were synthesized and their triplet excited state reduction potentials ($E^{0*}_{T1,\ calc}$) were calculated using computationally determined values for ET and E^0_{ox} (Figure 3.6). It is important to note that aryl core substituents were chosen for the design of these derivatives in pursuit of making them visible light absorbers (*vide supra*). Core modification of PCs 6 and 3 with aryl substituents (4, 5, 7−9, and 11−19) lowers the computationally calculated ETs compared to the parent compounds but with ETs still exceeding 2.0 eV in all cases (Figure 3.6). Core modification of PCs 6 and 3 with electronwithdrawing trifluoromethyl (13, 19) or cyano (12) substituents, or highly conjugated (15, 16) substituents, yields PCs with lower ETs that are also more difficult to oxidize. Consequently, these PCs exhibit more positive values of $E^{0*}_{T1,\ calc}$ rendering them less reactive PCs in the excited state. We reason that derivatives bearing electron-withdrawing groups exhibit these redox properties because electron-withdrawing core substituents shift electron density away from the phenoxazine core making them more challenging to oxidize to the $^2PC^{\bullet+}$. Conversely, installation of electron-donating methoxy (11, 18) or diphenyl amino (14) core substituents leads to PCs with higher ETs and are easier to oxidize (exhibit lower E^0_{ox} values), making them stronger excited state reductants (as indicated by their more negative E^{0*}s).

In addition to computationally calculating the triplet excited state reduction potentials, we experimentally determined the singlet excited state reduction potentials ($E^{0*}_{S1,\ exp}[^2PC^{\bullet+}/^1PC^*]$) using a combination of fluorescence spectroscopy and electrochemistry (Table 3.1). This analysis

is particularly useful for PCs capable of accessing CT excited states in which the donor and acceptor likely exhibit minimal electronic coupling as the S_1 and T_1 states in these systems are nearly degenerate, such that the singlet E^{0*}_{S1} approximates the triplet E^{0*}_{T1}.[7,18] The singlet energies determined from fluorescence emission (which correspond to emission from the S_1 state and are denoted as $E_{S1,exp}$ in Table 3.1) were found to be smaller than the computationally calculated T_1 energies in two cases (for PC 10 and PC 16). We note that the differences in these cases are 0.02 and 0.10 eV, which is within the expected error of ±0.2 eV for DFT calculations. We also note that while S_1 and T_1 energies are close to degenerate for species that exhibit extensive charge transfer, the S_1 and T_1 energy splitting gets increasing larger as the extent of CT decreases.

The experimentally determined singlet excited state reduction potential ($E^{0*}_{S1,\,exp}$) values were found to follow the same trends as the computationally calculated triplet reduction potentials ($E^{0*}_{T1,\,calc}$). Namely, PCs bearing electron-donating core substituents were more strongly reducing in the singlet excited state and typically more easily oxidized in the ground state while the opposite trends were observed for PCs bearing electron-withdrawing core substituents. We note that the $E_{1/2}$ ($^2PC^{\bullet+}/^1PC$) values determined computationally (E^0_{ox}) are systematically ~0.2 eV less positive than the values determined experimentally, which demonstrates the utility of these computational calculations as a predictive tool for this application. From the computational and experimental data, we demonstrate that core-modified derivatives exhibit a wide range of excited state reduction potentials with experimentally determined $E^{0*}_{S1,exp}$ values spanning from −1.54 V to −2.25 V versus SCE and computationally predicted $E^{0*}_{T1,calc}$ values spanning from −1.42 V to −2.01 V versus SCE. Notably, $E^{0*}_{S1,exp}$ values of PCs 11 and 14 were experimentally determined to be −1.81 V and −1.83 V versus SCE, respectively, with $E^{0*}_{T1,calc}$ values of −1.91 V and −1.88 V vs SCE, respectively, making them some of the strongest visible light absorbing organic excited state

reductants reported to date. For example, these PCs are on par with highly reducing organic PCs such as UV-absorbing phenyl phenothiazine ($E^{0*}_{S1,exp}$ = −2.10 V vs SCE)[4c] and visible light-absorbing *N*,*N*-diaryl dihydrophenazines ($E^{0*}_{T1,calc}$ ~ −2.2 V vs SCE).[5f]

Table 3.1. *Redox Properties of Core Modified Phenoxazines.*

PC	em λ_{max} (nm) [a]	$E_{S1,exp}$ (eV) [b]	$E_{T1,calc}$ (eV) [c]	$E_{1/2}$ ($^2PC^{\bullet+}/^1PC$) (V vs. SCE) [d]	E^0_{ox} ($^2PC^{\bullet+}/^1PC$) (V vs. SCE) [c]	$E^{0*}_{S1,exp}$ ($^2PC^{\bullet+}/^1PC^*$) (V vs. SCE) [e]	$E^{0*}_{T1,calc}$ ($^2PC^{\bullet+}/^3PC^*$) (V vs. SCE) [c]
N-phenyl PCs							
7	427	2.90	2.26	0.65	0.47	-2.25	-1.79
8	472	2.63	2.24	0.64	0.53	-1.99	-1.71
9	471	2.63	2.14	0.62	0.42	-2.01	-1.72
18	412	3.01	2.43	0.60	0.42	-2.41	-2.01
19	476	2.60	2.14	0.69	0.54	-1.91	-1.60
N-(1-naphthyl) PCs							
1 [f]	506	2.45	2.11	0.65	0.42	-1.80	-1.70
10	532	2.33	2.35	0.64	0.47	-1.69	-1.88
N-(2-naphthyl) PCs							
4	514	2.41	2.23	0.64	0.44	-1.77	-1.80
5	466	2.66	2.13	0.63	0.43	-2.03	-1.70
11	532	2.33	2.28	0.52	0.37	-1.81	-1.91
12	508	2.44	2.04	0.69	0.62	-1.75	-1.42
13	467	2.65	2.16	0.72	0.58	-1.93	-1.58
14 [g]	522	2.37	2.18	0.54	0.30	-1.83	-1.88
15 [g]	489	2.53	2.18	0.67	0.46	-1.86	-1.72
16 [g]	564	2.20	2.30	0.66	0.45	-1.54	-1.85
17	466	2.66	2.09	0.63	0.40	-2.03	-1.69

[a]Emission wavelength measured using fluorescence spectroscopy in DMAc. See supporting information for more details. [b]Singlet energies were calculated using the maximum wavelength of emission. [c]DFT calculations performed at the uM06/6-311+G(d,p)//uM06/6-31+G(d,p) level of theory with CPCM-described solvation in aqueous solvent. [d]All measurements were performed in a 3-compartment electrochemical cell with an $Ag/AgNO_3$ reference electrode in MeCN (0.01 M) and 0.1 M NBu_4PF_6 electrolyte solution. DMAc was used to solvate the PCs and in the working electrode compartment while platinum was used as both the working and counter electrodes. E (V vs. SCE) = E (V vs $Ag/AgNO_3$ [0.01 M]) + 0.298 V. [e]Singlet excited state reduction potentials were calculated using the singlet energies (estimated from the maximum wavelength of emission) and the $E_{1/2}$. [f]Values for the properties of PC 1 were taken from reference 5g. [g]Due to the extensive

molecular structure, frequency calculations of these compounds were computed at the uM06/6-31G(d,p)/CPCM-H_2O level of theory.

Oxidation Potential of PC and Redox Reversibility. After the photoexcited catalyst reduces a substrate in an oxidative quenching catalytic cycle, the PC is oxidized to a radical cation, $^2PC^{\bullet+}$. To complete the catalytic cycle, the $^2PC^{\bullet+}$ must be reduced to regenerate ^1PC. Therefore, the efficiency of the catalytic cycle is reliant to a large degree on the ability of the $^2PC^{\bullet+}$ to engage in rapid and reversible electron transfer reactions. Previously, it was shown that PC 1 exhibits a reversible cyclic voltammogram in DMAc for the $^2PC^{\bullet+}/^1PC$ redox couple and that electron transfer reactions involving this PC and the electrode are diffusion-limited.[12] To evaluate electron transfer reactions involving the phenoxazine derivatives explored in this work, CV was performed to analyze their oxidation potentials (Table 3.1) and redox reversibility (Figure 3.7) and Figures 3.52−3.66). The oxidation potential of each PC was approximated from its half wave potential, where $E^0_{ox}[^2PC^{\bullet+}/^1PC] \approx E_{1/2}[^2PC^{\bullet+}/^1PC]$.[19] In particular, we sought to determine whether installation of electron-donating, electron-withdrawing, or highly conjugated core substituents on phenoxazine PCs affects the reversibility of electron transfer processes. Additionally, the cyclic voltammograms of the PCs were acquired at different scan rates to gain insight into the kinetics of electron transfer processes involving these PCs.

PCs with electron-donating core substituents transfer electron density to the oxidized phenoxazine core and thus stabilize formation of the $^2PC^{\bullet+}$, such that they are more easily oxidized ($E_{1/2}$= ~ 0.50 to 0.60 V vs SCE for PCs 11 and 14) compared to those bearing electronically neutral core substituents or no core substituents ($E_{1/2}$ = ~0.60 to 0.69 V vs SCE for PCs 4, 5, 7−10, and 15−18). These PCs are observed to exhibit reversible cyclic voltammograms when acquired in DMAc (Figures 3.52−3.57 and Figures 3.60−3.65). A representative example is the cyclic voltammogram of PC 11, in which the difference between the anodic and cathodic peak potentials

(ΔE_p) is 75 mV (compared to the theoretical value of 59 mV for a reversible system) and the ratio of peak anodic current (i_{pa}) to peak cathodic current (i_{pc}) is 1.07 (compared to a theoretical value of 1 for a reversible system) when acquired with a scan rate of 0.05 V/s (Figure 3.7A, blue trace). The reversibility of this redox couple is maintained at different scan rates (0.02 V/s to 0.10 V/s) across which the ΔE_p (65−78 mV) and i_{pa}/i_{pc} values are also consistent (1.06−1.07).

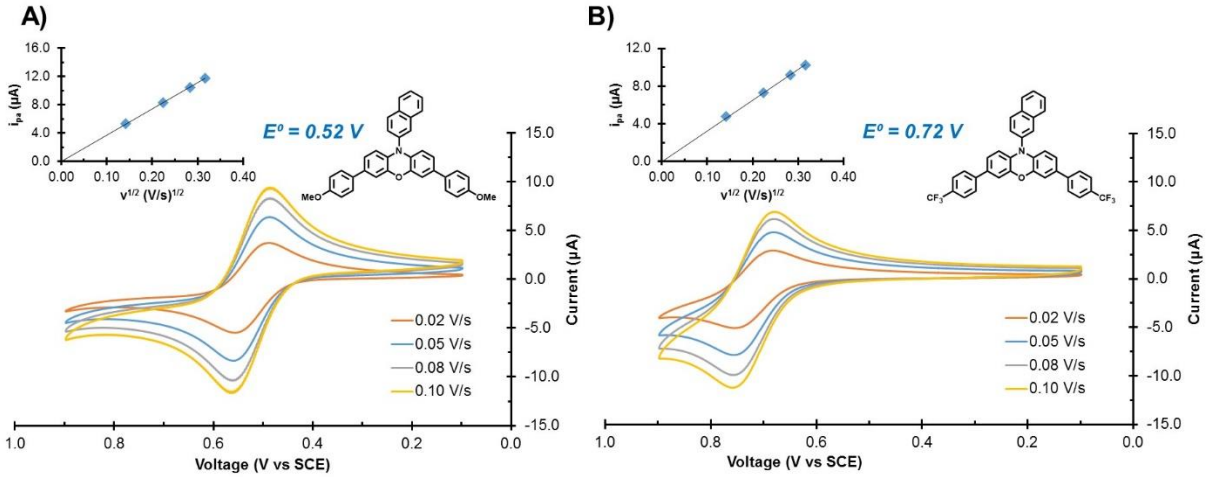

Figure 3.7. *Cyclic voltammograms (CVs) of PCs* ***11*** *(A) and* ***13*** *(B) acquired at different scan rates 0.02 V/s, 0.05 V/s, 0.08 V/s and 0.10 V/s.*

Although $^2PC^{\bullet+}$'s with electron-withdrawing core substituents (PCs 12, 13, and 19) are more destabilized ($E_{1/2}$ > 0.69), reversible CVs are still observed for these species (Figures 3.58, 3.59, and 3.66). For example, the most oxidizing $^2PC^{\bullet+}$ (the radical cation of PC 13) exhibits a reversible CV with a ΔE_p of 78 mV in DMAc (Figure 3.7B). The i_{pa}/i_{pc} could not be accurately determined for this catalyst in DMAc due to the proximity of its oxidation potential to that of the solvent window. Therefore, CV with PC 13 was also conducted in THF for which the i_{pa}/i_{pc} is 1.10 at the same scan rate of 0.05 V/s (Figure 3.66). To evaluate whether electron transfer reactions between the PC and the electrode are faster than the rate of diffusion of the PC, the cyclic voltammograms were acquired at different scan rates ranging from 0.02 V/s to 0.10 V/s. A linear relationship between the i_{pa} and the square root of the scan rate ($v^{1/2}$) is observed for both PCs 11

and 13 (Figure 3.7, insets). This observation indicates that the electron transfer process involving these PCs and the electrode is fast and diffusion-limited. Overall, these studies demonstrate that regardless of the nature of the substituents installed onto the phenoxazine core, all of the derivatives explored herein engage in reversible and diffusion-limited electron transfer reactions with an electrode.

Application of Core Modified Phenoxazines as PCs in O-ATRP. After establishing structure−property relationships for the phenoxazines presented in this work, we aimed to better understand how differences in the phenoxazines' properties manifest in differences in catalytic performance in O-ATRP. We first compared the performance of noncore modified phenoxazines 3 and 6 (Figure 3.6) and then extended this comparison to core-modified derivatives of these molecules. Next, we compared the performance of all the *N*-2-naphthyl core modified phenoxazines (4, 5, and 11−17, Figure 3.6) in OATRP. Through this study, we provide insight for the development of improved O-ATRP catalysts (*vide infra*).

While these PCs are likely capable of catalyzing a range of transformations, we originally designed them for application in O-ATRP. A suitable PC for O-ATRP must be both strongly reducing in the excited state and sufficiently stable and oxidizing as $^{2}PC^{\bullet+}$ in order to synthesize well-defined polymers (Figure 3.8).[20] Specifically, O-ATRP initiators and the alkyl bromide polymer chain-end group possess reduction potentials from ∼ −0.6 V to −0.8 V vs SCE, requiring a strong excited state reductant for the reaction to occur without addition of sacrificial electron donors.[21] Additionally, the $^{2}PC^{\bullet+}$ must be sufficiently stable and more oxidizing than the propagating radical of the polymer chain end, for which E^{0} ∼ −0.8 V vs SCE, to deactivate the propagating chain.[5f] Since these catalysts likely operate via an outer-sphere electron transfer (O-SET) pathway (more specifically that of dissociative electron transfer),[5g] Marcus theory predicts

that the redox properties of these PCs (and those of the electron donor or acceptor) will directly relate to the rates of activation and deactivation in OATRP (Figure 3.8). Importantly, the synthesis of well-defined polymers via any controlled radical polymerization requires a low concentration of radical species in solution, and in ATRP this is maintained by a fast rate of deactivation relative to the rates of activation and propagation.[22] If an O-ATRP PC possesses the required redox properties for efficient reversible deactivation then the polymerization is expected to proceed with linear reaction kinetics that are first-order with respect to monomer consumption and a linear growth of polymer molecular weight (MW) as a function of monomer conversion. As such, polymers of target MWs (quantified by initiator efficiency, $I^* = M_{n(theo)}/M_{n(actual)}$, where M_n is the number-average MW) and low dispersity ($Đ = M_w/M_n$, where M_w is the weight-average MW) can be synthesized.[22] Advances in controlled radical polymerization methodologies such as ATRP over the last few decades have enabled the synthesis of polymers with near quantitative I^*'s with moderate ($Đ < 1.3$) to low ($Đ < 1.1$) dispersity.[23] Guided by these standards, the success of these phenoxazines to efficiently catalyze O-ATRP was evaluated. In particular, it was determined whether O-ATRP employing these PCs demonstrates linear growth of polymer MW as a function of conversion and produces polymeric material with $Đ < 1.3$ and high I^* (for an ideal O-ATRP $I^* = 100\%$).

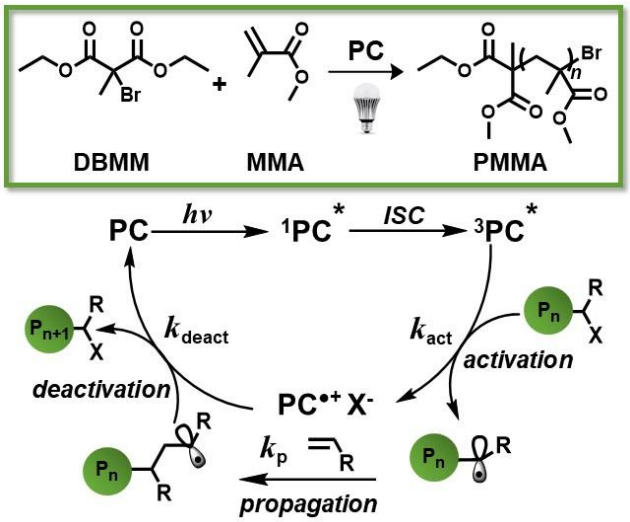

Figure 3.8. *Reaction scheme for the polymerization of MMA (top) and proposed mechanism of O-ATRP using alkyl halide initiators (bottom) are shown. In the proposed mechanism of O-ATRP, initiation occurs once the excited state organic PC reduces the alkyl halide bond of the initiator or halide-capped polymer chain-end (Figure 3.8). This reaction generates a carbon centered radical on the initiator or polymer chain end that can propagate via reaction with monomers. Meanwhile, the same reduction event also yields a bromide anion, which we propose associates with the oxidized* $^2PC^{\bullet+}$ *to form the* $^2PC^{\bullet+}Br^-$ *ion pair. We hypothesize this ion pair is responsible for deactivating the polymer chain by reinstalling the halide end group and regenerating the ground state* ^1PC*, which can re-enter the catalytic cycle.*

Previously, we observed that the O-ATRP of methyl methacrylate (MMA) catalyzed by *N*-phenyl phenoxazine (6) using UV-light yields polymers of less predictable MW (I^* = 137%) and relatively high $Đ$ ($Đ$ = 1.48) compared to *N*-2- naphthyl phenoxazine 3 (I^* = 77%, $Đ$ = 1.11). The comparatively better performance of PC 3 in O-ATRP is further exemplified by the linear growth of polymer MW with respect to monomer conversion with close agreement to the theoretical growth of MW for a well-controlled polymerization (Figure 3.9A).[15] In contrast, O-ATRP catalyzed by 6 exhibits less linear growth of polymer MW throughout the polymerization with more appreciable deviation from theoretical MW values (Figure 3.9B). Notably, the O-ATRP catalyzed by 6 suffers from poor control at low monomer conversions (at 24% conversion I^* = 41%). In addition, the $Đ$ of the PMMA synthesized using PC 6 is higher and more erratic throughout the polymerization. The superior performance of PC 3 compared to PC 6 in O-ATRP

demonstrates the importance of the *N*-aryl substituent in designing noncore-modified *N*-aryl phenoxazine PCs. Due to the similar absorption and redox properties of PCs 3 and 6, we posit that the significant difference in their catalytic performance is a result of differences in the nature of these molecules in the excited state. Namely, the *N*-naphthyl-substituted PC (3) exhibits a polar, CT excited state while the *N*-phenyl substituted PC (6) exhibits a less polar, locally excited state (*vide supra*). Future photophysical investigation will be aimed at understanding the connection between the ability of these molecules to access CT excited states and their catalytic performance in O-ATRP.

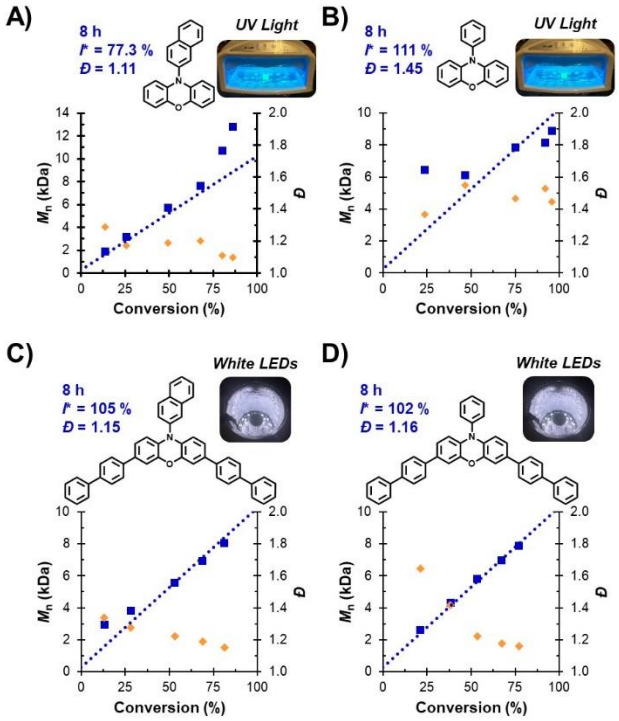

Figure 3.9. *Plots of growth of the experimentally measured number average molecular weight (M_n) as a function of monomer conversion (blue squares) with theoretical values (blue dotted line). The dispersity of each corresponding sample is shown as a function of monomer conversion (orange diamonds). Data for the aliquots of each polymerization taken after eight hours are shown above each plot. All polymerizations (A-D) were run with [1000]:[10]:[1] of [MMA]:[DBMM]:[PC] in an equal volume of DMAc as that of MMA. Polymerizations catalyzed by PC* ***3*** *(A) and PC* ***6*** *(B) were performed in a UV-nail apparatus while polymerizations catalyzed by PC* ***5*** *(C) and PC* ***9*** *(D) were run in the presence of white-light LEDs. The polymerization data*

*acquired for PC **3** were acquired from reference 5g. Additional experimental details are provided in the experimental section.*

After furthering our understanding of the performance of noncore-modified phenoxazines 3 and 6 in O-ATRP, we compared biphenyl core-modified derivatives of these molecules (5 and 9). Characterization of the absorption properties, nature of the excited state, and redox properties of these molecules revealed that the nature of the core substituents, rather than the *N*-aryl substituent, more greatly dictates the properties of these PCs. In particular, 5 and 9 exhibit similar absorption profiles (λ_{max} = 389 and 389 nm, respectively, and ε = 25900 and 24,000 $M^{-1}cm^{-1}$, respectively), and in contrast to their parent molecules, both absorb in the visible regime. Investigation of the nature of 5 and 9 in the excited state revealed that they both access similar CT excited states which likely involve one of their biphenyl core substituents. This property again stands in contrast to the noncore modified molecules for which 3 (the parent molecule of 5) exhibits CT involving the *N*-naphthyl substituent and 6 (the parent compound of 9) does not exhibit CT character in the excited state. Furthermore, these core-modified derivatives exhibit redox properties that are very similar to each other but distinct from that of 3 and 6 (Table 3.1).

Given the similar overall properties of PCs 5 and 9, we hypothesized that they would exhibit similar performance in OATRP, as quantified by the parameters described above. To test this hypothesis, the O-ATRP of MMA was performed employing 5 and 9 as catalysts in the presence of white light LEDs (Figure 3.9, panels C and D, for emission of white light LEDs see Figure 3.50). O-ATRP with both PCs demonstrates linear growth of polymer MW with respect to monomer conversion with close agreement to theoretical MW values throughout the entire polymerization. As a result, 5 and 9 are able to synthesize PMMA with nearly quantitative I^* at high monomer conversions, a marked improvement over the performance of PCs 3 and 6. In addition, O-ATRP catalyzed by these core-modified derivatives exhibits a lowering of $Đ$

throughout the polymerization, with $Đ$ values rivaling that of PC 3 at high conversions. In summary, the performance of 5 and 9 remains similar to each other through the entire polymerization and is distinct from the performance of their parent molecules. Together, these studies highlight the importance of determining which structural motifs lead to improved catalytic properties and performance within each subset of noncore-modified and core-modified *N*-aryl phenoxazines.

To further investigate our overarching hypothesis that catalyst structure dictates catalyst properties (specifically their absorption and redox properties) which in turn affects catalyst performance, the *N*-2-naphthyl core-modified phenoxazines (4, 5, and 11−17) were used as catalysts for O-ATRP. Specifically, these phenoxazines were employed for the O-ATRP of MMA using the alkyl bromide initiator diethyl 2-bromo-2-methylmalonate (DBMM) and white light LEDs (see scheme in Figure 3.8). These O-ATRP conditions were previously found to be the optimal batch reactor conditions for *N*-aryl phenoxazine PCs.[5g] Analysis of the polymerization results at reasonably high conversions revealed that all of the PCs investigated were able to synthesize PMMA with typically moderate to low $Đ$ and $I^* \geq 77\%$ (Table 3.2). These data demonstrate that the phenoxazines explored are all competent PCs for O-ATRP. However, closer analysis of the evolution of these parameters throughout the entire polymerization reveals more stark discrepancies in the catalytic performance of these molecules.

Table 3.2. *O-ATRP results from employing visible light-absorbing core modified phenoxazines for the polymerization of methyl methacrylate (MMA).*[a]

PC	Conv. (%)	$M_{n(theo)}$ (kDa)	M_n (kDa)	M_w (kDa)	$Đ$[b]	I^*[c] (%)
3[c]	80	8.26	10.7	11.9	1.11	77
4	69	7.16	8.38	12.1	1.45	85
5	81	8.36	8.02	9.24	1.15	105
11	80	8.26	8.07	10.9	1.36	102
12	85	8.76	8.11	10.6	1.30	108
13	87	8.96	9.08	11.7	1.29	99
14	76	7.86	8.66	10.3	1.19	91
15	75	7.76	9.11	13.7	1.50	85
16	67	6.96	7.25	8.75	1.21	96
17	82	8.46	8.98	10.4	1.17	94

[a]*All polymerizations were conducted using the initiator diethyl 2-bromo-2-methylmalonate (DBMM) in a ratio of 1000:10:1 of MMA:DBMM:PC with DMAc as a solvent. See the supporting information for more experimental details. All Calculated by* M_w/M_n. [b]*Calculated by* $M_{n(theoretical)}/M_{n(GPC)}$. [c]*Data obtained from reference 5g. Omission of initiator, light, or PC results in no monomer conversion or a small degree of uncontrolled polymerization (Table 3.3).*

Analysis of the high conversion data points shown in Table 3.2 demonstrates that most of the PCs synthesize polymeric material with moderate to low $Đ$ ($Đ$ < 1.3) except for PCs 4 ($Đ$ = 1.45), 11 ($Đ$ = 1.36), and 15 ($Đ$ = 1.50). To determine whether the latter three cases of high $Đ$ represented outliers of these polymerization data sets, we analyzed the $Đ$ of the PMMA synthesized by these three PCs at different conversions throughout the polymerization (Figures 3.110, 3.117 and 3.113, respectively of the *Experimental* section). Indeed, for these PCs polymer $Đ$ is greater than 1.4 at all conversions, indicating poor control over the polymerization. For the other PCs, half of them (5, 14, and 17) synthesize PMMA with $Đ$ that never exceeds 1.4 throughout the polymerization (Figures 3.111, 3.118, and 3.111, respectively of the *Experimental* section) while the other half (12, 13, and 16) exhibit relatively high $Đ$ ($Đ$ > 1.4) at low conversions (conversion <40%, Figures 3.116, 3.115, and 3.114, respectively of the *Experimental* section).

We posit that efficient photon absorption is key for successful catalytic performance in O-ATRP since this characteristic partially dictates the population of the catalyst in the excited state

present early in the reaction. Sufficient population of PC^* at early reactions times is likely necessary for fast and uniform initiation and rapid buildup of the deactivating species ($^2PC^{\bullet+}$), which is necessary to control the polymerization.[11] As such, we attribute the inability of PCs 4, 11, and 15 to synthesize polymers with moderate to low $Đ$ to their poor absorption of light emitted by the white light LEDs used for the reactions. In particular, 4, 11, and 15 exhibit the most blue-shifted absorption profiles (λ_{maxs} = 367, 363, and 355, respectively) of the PCs investigated. While we recognize that the performance of a PC is dictated by a combination of its photophysical and electrochemical properties, these PCs clearly exhibit poorer control of polymer $Đ$ despite their different redox properties (Table 3.1).

Further analysis of the catalytic performance of phenoxazines with stronger visible light absorption (5, 12−14, and 16−17) reveals another trend. At high monomer conversions, these PCs synthesize PMMA with moderate to low $Đ$ ($Đ$ ranges from 1.30 to 1.15) and nearly quantitative I^* (I^* ranges from 94% to 108%), indicating good control over the polymerization. However, comparison of the growth of polymer molecular weight as a function of conversion for these O-ATRP reactions allows us to further sort them into two distinct categories based on their performance and properties. Specifically, PCs 5, 14, and 17 exhibit very linear growth of polymer molecular weight as a function of conversion, with trendlines that agree well with the trendline for the theoretical growth of polymer molecular weight (Figures 3.111, 3.118, and 3.112, respectively of the *Experimental* section). On the other hand, PMMA synthesized by PCs 12, 13, and 16 approaches ideal molecular weights only at high conversions. This phenomenon can clearly be seen by the convergence of the trendline for experimentally determined growth of polymer molecular weight as a function of conversion with that of the theoretical trendline for the polymerizations using these PCs (Figures 3.116, 3.115, and 3.114, respectively of the

Experimental section). Again, we suggest that these distinct differences in catalytic performance are a manifestation of the properties of the PCs. PCs 5, 14, and 17 exhibit stronger excited state reduction potentials ($E^{0*}_{T1,\ calc}$ = −1.70, −1.88, and −1.69 V, respectively) than PCs 12 and 13 ($E^{0*}_{T1,\ calc}$ = −1.42 V and −1.58 V, respectively) which bear electron-withdrawing core substituents. Thus, we posit that the redox properties of PCs 5, 14, and 17 are in a more ideal range for the polymerization of MMA. Given that the PCs with strong excited state reduction potentials and strong visible light absorption performed the best overall of the PCs investigated, our data suggests that PCs that exhibit these properties execute O-ATRP more efficiently for methacrylate monomers.

The case of PC 16 is interesting since this PC absorbs strongly in the visible regime compared to derivatives 4, 11, and 15 and is predicted to exhibit a relatively strong triplet excited state reduction potential ($E^{0*}_{T1,\ calc}$ = −1.85 V) but suffers from poor control early in the polymerization, similar to PCs 12 and 13. While the performance of this PC appears to be an anomaly, the singlet excited state reduction potential for this PC was experimentally determined to be −1.54 V, which is evidence that the PC must be less reducing in the triplet excited state (i.e., have a more positive potential than −1.54 V). As such, the triplet excited state reduction potential of PC 16 is likely to be on par with those of PCs 12 and 13. However, the effects of the properties of this PC on its performance in O-ATRP warrant further future investigation since the performance of these PCs arises from a multitude of factors.

Conclusion

Investigation of the properties of a new family of core-modified phenoxazines revealed several design principles that we foresee will enable the use of these organic PCs in a range of

photoredox-catalyzed transformations. For the phenoxazine PC properties explored in this work, the core substituents played a greater role than the *N*-aryl substituent in dictating the catalysts' properties. This observation was further supported by the similar performance in O-ATRP of catalysts with the same core substituents but different *N*-aryl substituents (Figure 3.9, PC 5 vs PC 9). To design *N*-aryl phenoxazine catalysts that absorb in the visible regime, this study suggests that two aryl core substituents should be installed (Figure 3.4A, PC 8 vs PC 9), and to maximize visible light absorption, the substituents of choice are biphenyl groups or aryl electron-withdrawing groups (Figure 3.4B).

For the design of phenoxazine catalysts that can access CT excited states, more highly conjugated groups such as *N*-naphthyl substituents are required for noncore modified phenoxazines, as no CT character is observed for *N*-phenyl phenoxazine. However, the presence of core substituents can be used to alter the nature of these molecules in the excited state. In particular, we found that even *N*-phenyl phenoxazines can access CT excited states if suitable core substituents are installed (Figure 3.5, e.g. PC 6 vs PC 9). These differences in the excited states of core-modified phenoxazines compared to their parent *N*-aryl phenoxazines warrants future photophysical investigation, as the nature of these molecules in the excited state may greatly affect their catalytic performance.

To design phenoxazine catalysts with different reduction potentials that retain redox reversibility, aryl electron-donating or electron-withdrawing groups can be installed (Figure 3.6). In particular, installation of 4-methoxy phenyl core substituents (PC 11) yielded the most highly reducing catalyst, and installation of 4-cyano phenyl substituents (PC 12) yielded the least strongly reducing catalyst of the dicore-modified PCs investigated. Notably, we established that through functionalization at the phenoxazine core, a wide range of excited state reduction potentials can be

achieved (e.g., $E^{0*}_{T1,calc}$ values spanning from −1.42 V to −2.01 V vs SCE.). Thus, with this degree of tunability, we envision that core-modified phenoxazine PCs are promising in existing applications[5g,10–12] and enable new synthetic methodologies with improved selectivity to be developed.

Lastly, the application of these molecules as PCs for the OATRP of methyl methacrylate revealed their competency as catalysts for this transformation, with most derivatives synthesizing polymeric material with dispersity typically less than 1.3 and initiator efficiencies ≥95% at high conversions. However, despite their good performance at high conversions, only three of the PCs explored (5, 14, and 17) maintain good control throughout the entire polymerization. We posit that the superior performance of these three PCs compared to the other derivatives investigated is due to their strong absorption of visible light and strong excited state reduction potentials. Ongoing work is aimed at improving our understanding of the capabilities and limitations of these PCs for O-ATRP.

Experimental

1. Materials and Methods

Purchased Chemicals and Experimental Equipment

Buchwald Coupling: Phenoxazine was purchased from Beantown Chemical. Bromobenzene, 2-bromonaphthylene and 1-bromonaphthylene were purchased from VWR. Bis(dibenzylideneacetone) palladium(0) and the 1 M solution of tri-*tert*-butylphosphine in toluene were purchased from Sigma Aldrich. Dicyclohexylphosphino-2,6-diisopropoxybiphenyl (RuPhos) and chloro-(2-dicyclohexylphosphino-2,6-diisopropoxy-1,1-biphenyl) [2-(2-aminoethyl)phenyl] palladium(II) - methyl-t-butyl ether adduct (RuPhos precatalyst) were purchased from Sigma

Aldrich. Sodium tert-butoxide was purchased from Sigma Aldrich. Dioxane and toluene were purified using an mBraun MB-SPS-800 solvent purification system and kept under nitrogen atmosphere.

Bromination: *N*-Bromosuccinimide was purchased from VWR. Acetic acid was purchased from Sigma Aldrich.

Suzuki Coupling: Tetrakis(triphenyl phosphine) palladium (0) was purchased from Sigma Aldrich. Potasssium carbonate was purchased from VWR. The boronic acids were purchased from the following vendors:

Phenylboronic acid: Sigma Aldrich

4-biphenylboronic acid: TCI America

2-naphthylboronic acid: Sigma Aldrich

9-phenanthracenylboronic acid: Sigma Aldrich

pyrene-1-boronic acid: Alfa Aesar

4-(trifluoromethyl)phenylboronic acid: Sigma Aldrich

4-cyanobenzeneboronic acid: Alfa Aesar

4-methoxyphenylboronic acid: Sigma Aldrich

4-(diphenylamino)phenylboronic acid: TCI America

Polymerizations: Methyl methacrylate (MMA), *N*,*N*-dimethyl acetamide (DMAc) and diethyl 2-bromo-2-methyl malonate (DBMM) were purchased from Sigma Aldrich. One sixteen-inch strip of double-density white LEDs, purchased from Creative Lighting Solutions (item no. CL-FRS1210-5M-12V-WH), was wrapped inside a 400 mL beaker and used as a visible light source. A Vogue Professional Powerful & Double Wide 54 watt UV lamp Light Nail Dryer was used as the UV light source

Chemical Preparation and Storage

Methyl methacrylate (MMA) was dried with calcium hydride, distilled, and degassed via three freeze-pump thaw cycles before being put into a nitrogen-filled glovebox freezer for storage. RuPhos, RuPhos precatalyst, and tetrakis(triphenyl phosphine) palladium (0) were stored in a nitrogen-filled glovebox before use. Dioxane, toluene, and THF were purified using an mBraun MB-SPS-800 solvent purification system and stored under nitrogen.

Instruments for Compound Characterization

Nuclear magnetic resonance spectra were recorded on a Varian 300 MHz NMR Spectrometer to analyze polymerization conversion and a Varian 400 MHz or Varian 500 MHz NMR Spectrometer for all other characterizations. All ^{1}H NMR experiments are reported in δ units, parts per million (ppm), and were measured relative to the signals for residual chloroform (7.26 ppm) or benzene (7.15 ppm) in the deuterated solvent. All ^{13}C NMR spectra are reported in ppm relative to $CDCl_3$ (77.23 ppm) or C_6D_6 (128.62 ppm). Analysis of polymer molecular weights were performed via gel permeation chromatography (GPC) coupled with multi-angle light scattering (MALS), using an Agilent HPLC fitted with one guard column, three PLgel 5 μm MIXED-C gel permeation columns, a Wyatt Technology TrEX differential refractometer, and a Wyatt Technology miniDAWN TREOS light scattering detector, using THF as the eluent at a flow rate of 1.0 mL/min and a dn/dc value of 0.084. Ultraviolet-visible spectroscopy was performed on an Cary 5000 spectrophotometer using DMAc as the solvent. Emission spectroscopy was performed on a SLM 8000C spectrofluorimeter using DMAc, THF or 1-hexene as the solvent. Cyclic voltammetry was performed with a CH Instruments electrochemical analyzer with a $Ag/AgNO_3$ (0.01 M in MeCN) reference electrode using DMAc as the solvent for the working electrode.

Samples were sparged with argon for 5 minutes prior to both emission and electrochemical measurements.

2. Procedures

General Synthetic Scheme for 1-Naphthyl- and 2-Naphthyl-10-Phenoxazines

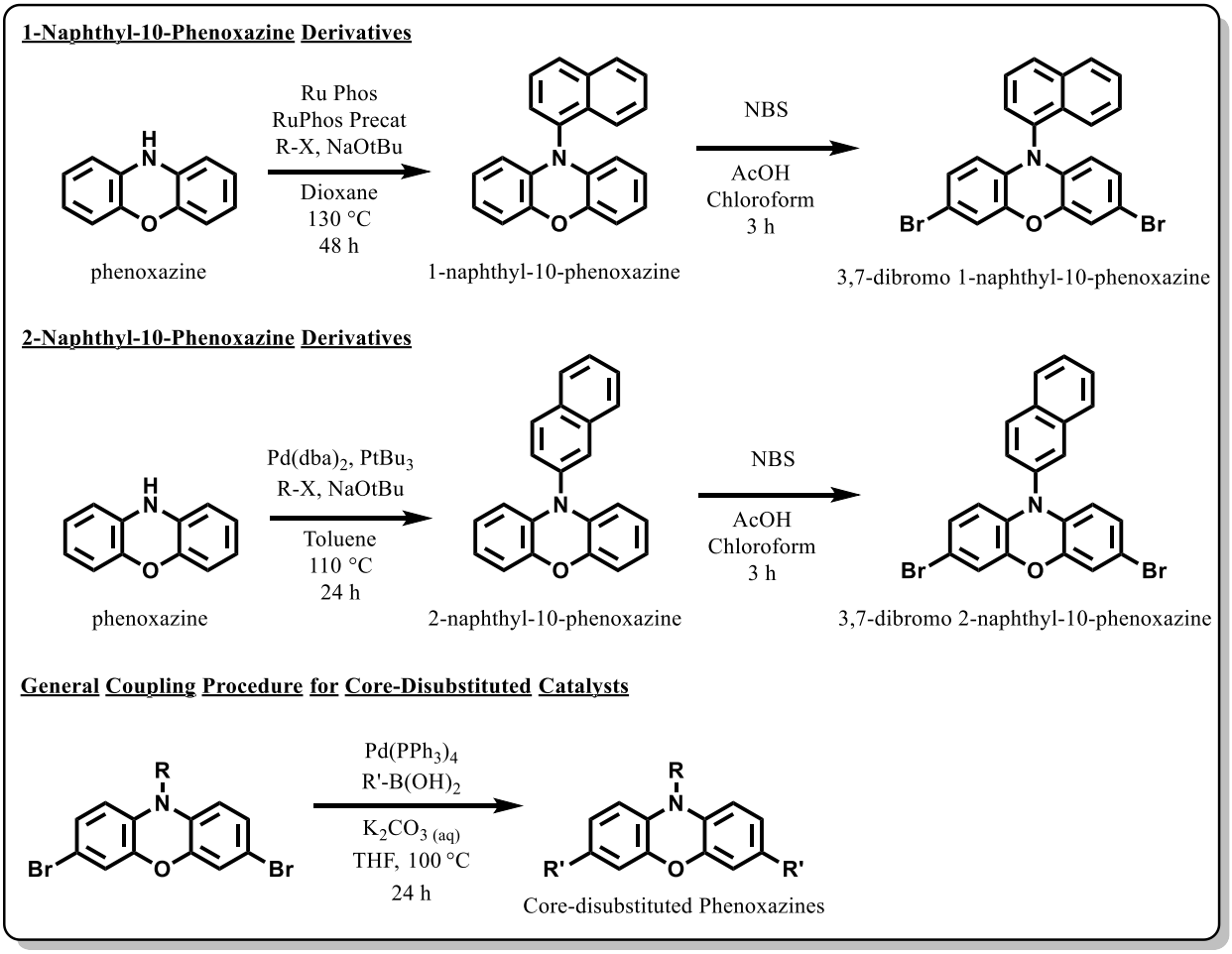

Figure 3.10. *The general synthetic scheme for 1-naphthyl and 2-naphthyl-10-phenoxazines.*

Synthesis of PCs 1-5 & 10-17

Syntheses of PC **1**, PC **3** and 3,7-dibromo 1-naphthyl-10-phenoxazine were performed using previously reported procedures. [5g]

Synthesis of 2-Naphthyl-10-Phenoxazine (4)

Phenoxazine (1.00 g, 5.46 mmol, 1.00 equiv.), 2-bromonaphthalene, (1.70 g, 8.19 mmol, 1.50 equiv.), and sodium tert-butaoxide (1.57 g, 16.4 mmol, 3.00 equiv.) were combined in a 250 mL flame-dried storage tube and cycled under nitrogen and vacuum three times before being brought into a nitrogen-filled glovebox where bis(dibenzylideneacetone)palladum(0) (0.031g, 0.0546 mmol, 0.0100 equiv.) 0.164 mL of a 1.00 M solution of tri-tertbutyl phosphine in toluene, and 50.0 mL of toluene were added. The flask was sealed, removed from the glovebox, and heated to 110 °C for 24 hours before it was allowed to cool to room temperature. The toluene was removed under reduced pressure and the reaction mixture was dissolved in DCM before being washed twice with de-ionized water and once with brine. The organic layer was collected, dried over magnesium sulfate, and concentrated under vacuum. The resulting solid was recrystallized from DCM/MeOH at -25 °C to afford the product in 69% yield. NMR characterization matched that previously reported.[1]

Synthesis of 3,7-Dibromo 2-Naphthyl-10-Phenoxazine

2-Naphthyl-10-phenoxazine (0.600 g, 1.94 mmol, 1.00 equiv.) was dissolved in 60.0 mL of acetic acid and 60.0 mL of chloroform before NBS (0.708 g, 3.98 mmol, 2.05 equiv.) was added portion-wise over twenty minutes. The reaction was allowed to run for three hours at room temperature before de-ionized water and saturated sodium bicarbonate solution were added and allowed to stir for fifteen minutes. Organic solvent was removed under reduced pressure before the reaction mixture was diluted with DCM. The organic layer was washed twice with de-ionized water, washed once with brine, dried over magnesium sulfate, and concentrated under vacuum. The resulting solid was recrystallized from DCM/hexanes at -25 °C to afford the product in 83% yield (1.61 mmol, 0.752 g). ^{1}H NMR ($CDCl_3$, 400 MHz) δ 8.09 (d, J = 8.6 Hz, 1H), 7.94 (d, J =

7.8 Hz, 1H), 7.88 (d, *J* = 7.7 Hz, 1H), 7.82 (s, 1H), 7.59 (pd, *J* = 6.9, 1.5 Hz, 2H), 7.34 (dd, *J* = 8.7, 2.1 Hz, 1H), 6.84 (d, *J* = 2.2 Hz, 2H), 6.67 (dd, *J* = 8.6, 2.2 Hz, 2H), 5.80 (d, *J* = 8.6 Hz, 2H). ^{13}C NMR (75 MHz, $CDCl_3$) δ 144.15, 135.23, 134.64, 133.24, 133.07, 131.80, 129.77, 128.00, 127.97, 127.26, 126.86, 126.28, 118.61, 114.60, 112.94. HRMS (ESI): calculated for M+ $C_{22}H_{13}Br_2NO$, 466.9345; observed 466.9349.

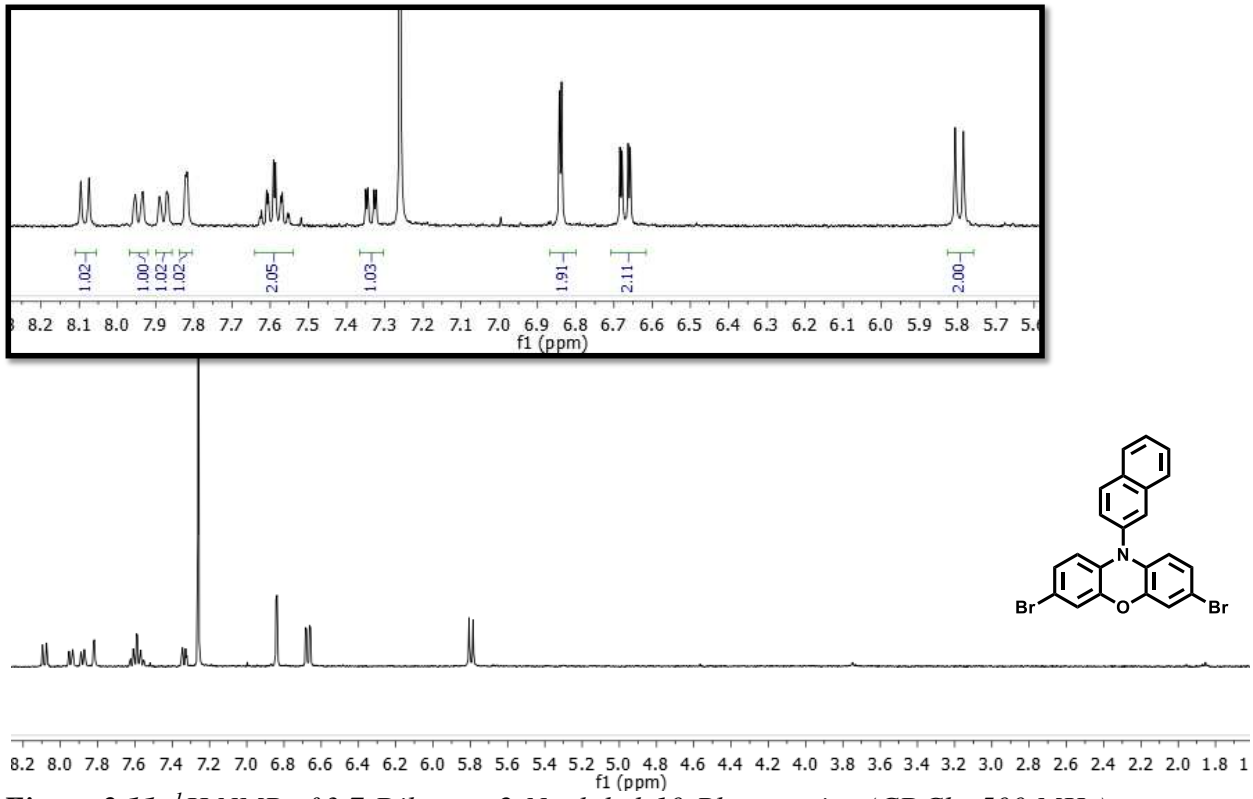

Figure 3.11. *^{1}H NMR of 3,7-Dibromo 2-Naphthyl-10-Phenoxazine ($CDCl_3$, 500 MHz).*

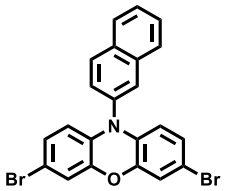

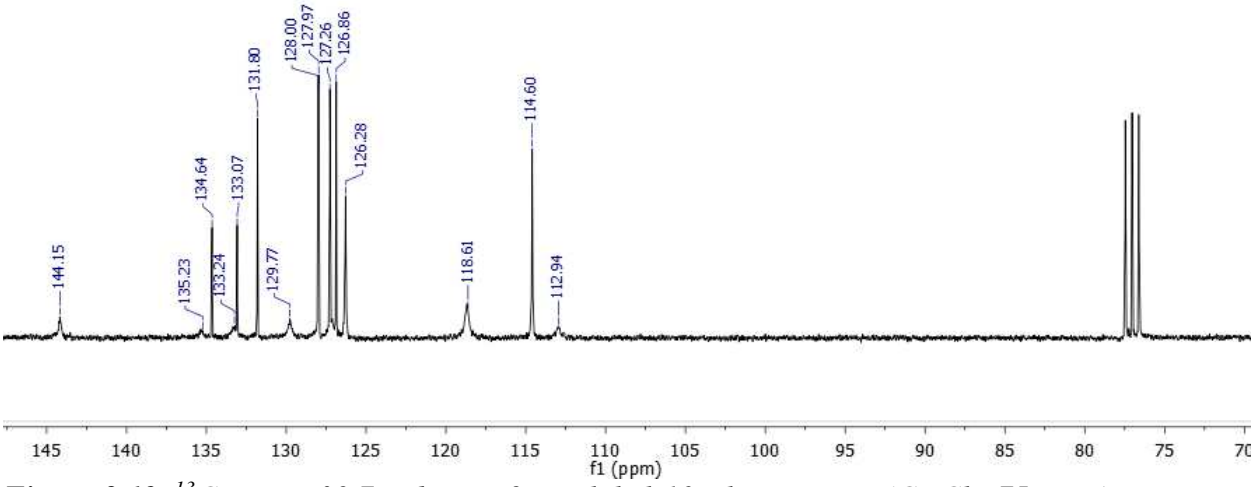

Figure 3.12. *^{13}C NMR of 3,7-Dibromo 2-Naphthyl-10-Phenoxazine ($CDCl_3$, 75 MHz).*

Synthesis of 3,7-Di(4-phenyl) 1-Naphthalene-10-Phenoxazine (11)

3,7-dibromo 1-naphthyl-10-phenoxazine (0.200 g, 0.646 mmol, 1.00 equiv.), phenyl boronic acid (0.315 g, 2.59 mmol, 4.00 equiv.) were added to a storage tube and cycled under vacuum and nitrogen three times before 7.00 mL of dried and degassed THF and 6.00 mL of a sparged 2.00 M K_2CO_3 aqueous solution were added. In a nitrogen-filled glovebox, palladiumtetrakis(triphenyl phosphine) (0.030 g, 0.0258 mmol, 0.0400 equiv.) was added to a separate Schlenk flask and brought out of the glovebox before being dissolved in 7.00 mL of THF, which was subsequently added to the reaction mixture. The reaction was performed for 24 hours at 100 °C before it was allowed to cool to room temperature and exposed to oxygen. Volatiles were removed under reduced pressure and the mixture was re-dissolved in DCM before being

washed twice with de-ionized water and once with brine. The organic layer was dried over magnesium sulfate and volatiles were removed under reduced pressure. The product was dissolved in 60:40 DCM/ hexanes, filtered through a silica plug, and volatiles were removed under reduced pressure. The product was obtained from recrystallization using DCM/MeOH at -25 °C to give the product as a yellow solid in 55% yield. ^{1}H NMR (C_6D_6, 500 MHz) δ 8.12 (d, *J* = 8.4 Hz, 1H), 7.65 (dd, *J* = 15.3, 8.1 Hz, 2H), 7.44 – 7.35 (m, 5H), 7.27 (d, *J* = 2.0 Hz, 2H), 7.25 – 7.18 (m, 5H), 7.15 – 7.12 (m, 2H), 7.11 – 7.04 (m, 3H), 6.66 (dd, *J* = 8.3, 2.1 Hz, 2H), 5.81 (d, *J* = 8.3 Hz, 2H). ^{13}C NMR (C_6D_6, 75 MHz) δ144.41, 140.19, 135.65, 135.20, 134.96, 133.53, 131.47, 128.98, 128.80, 128.68, 128.66, 126.80, 126.73, 126.69, 126.20, 126.15, 123.37, 122.06, 114.34, 113.89. HRMS (ESI): calculated for M+ $C_{34}H_{23}NO$, 461.1780; observed 461.1782.

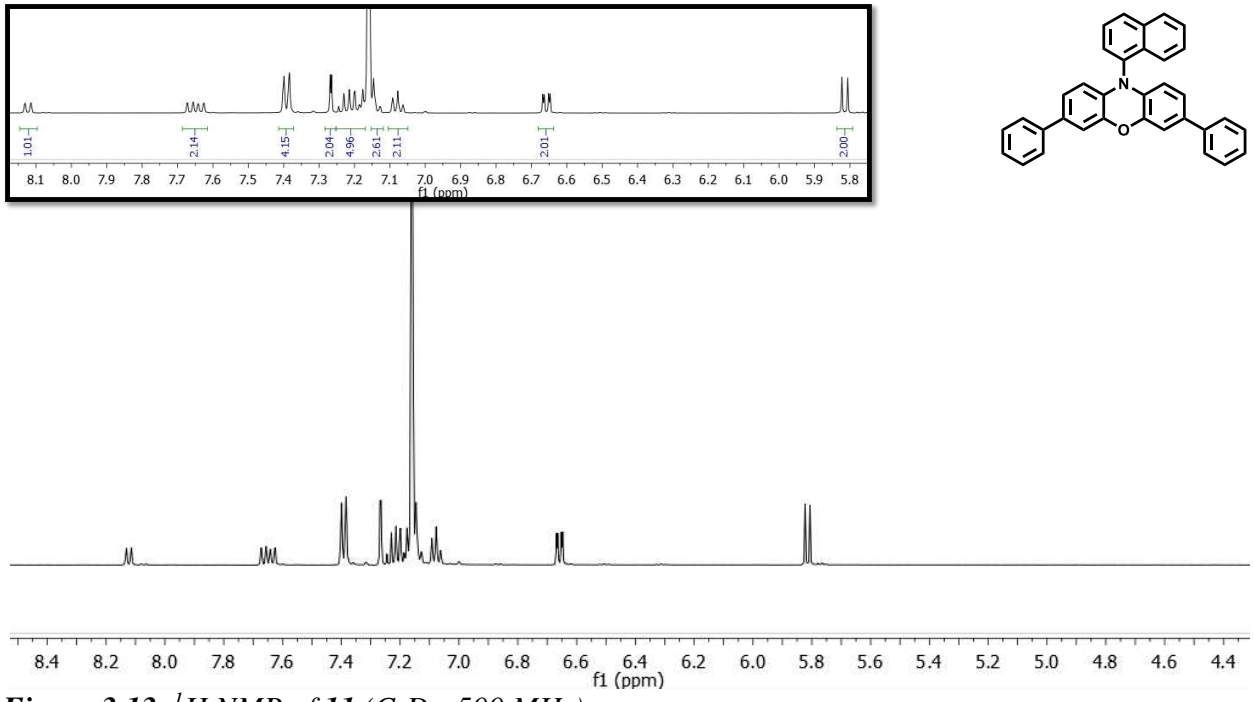

Figure 3.13. *^{1}H NMR of **11** (C_6D_6, 500 MHz).*

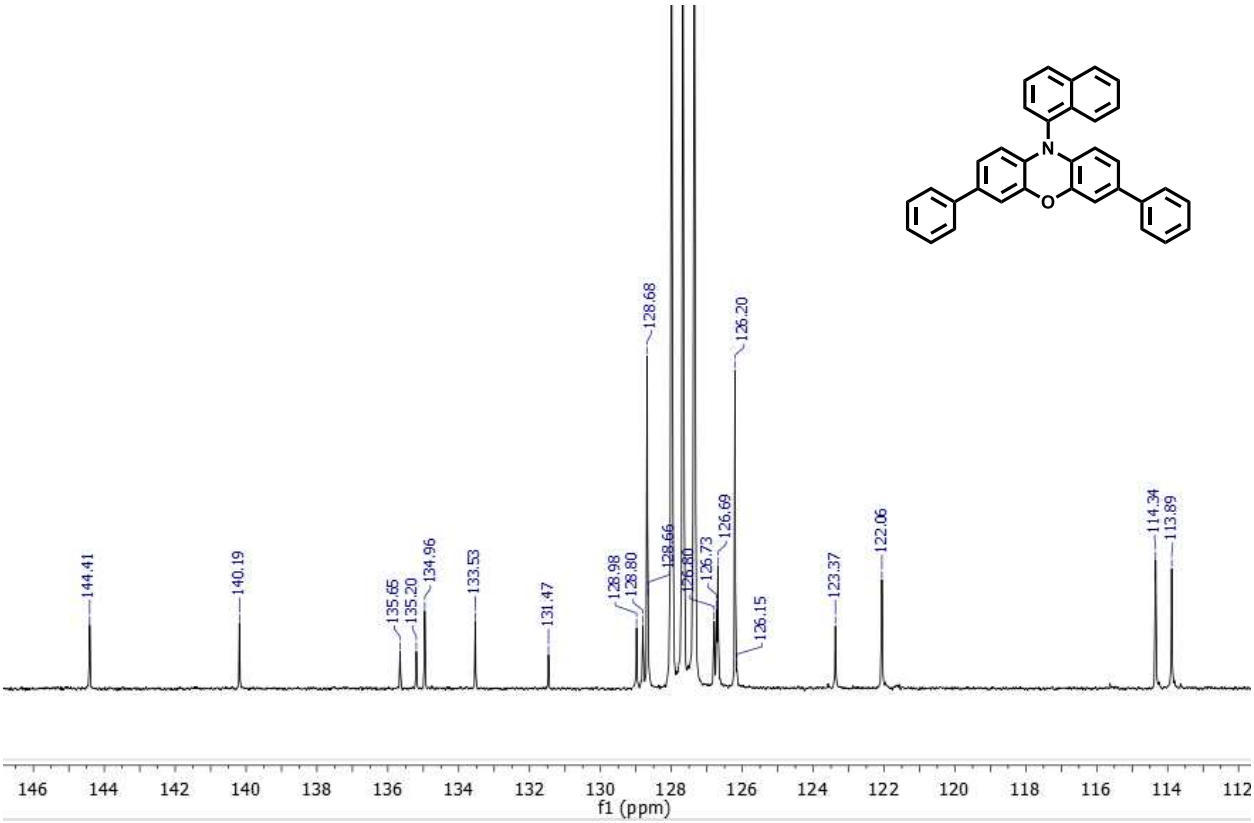

Figure 3.14. *^{13}C NMR of **11** (C_6D_6, 75 MHz).*

Synthesis of 3,7-Di(4-phenyl) 2-Naphthalene-10-Phenoxazine (5)

3,7-Dibromo 2-Naphthalene-10-phenoxazine (0.250 g, 0.535 mmol, 1.0 equiv.) and phenyl boronic acid (0.261 g, 2.14 mmol, 4.00 equiv.) were added to a 250 mL storage tube flask and cycled between vacuum and nitrogen three times before 20.0 mL of dried and degassed THF was added. Once all reagents were dissolved, 7.00 mL of a 2.00 M aqueous solution of K_2CO_3, which had been sparged with nitrogen, was added and the biphasic system was heated to 80 °C. In a separate Schlenk flask, palladiumtetrakis(triphenyl phosphine) (0.148 g, 0.128 mmol, 0.150 equiv.) was dissolved in 20.0 mL of THF under inert atmosphere. The solution of $Pd(PPh_3)_4$ was then added to the reaction mixture and the reaction was heated at 100 °C for 24 h, before it was exposed to oxygen and allowed to cool to room temperature. The reaction mixture was concentrated under reduced pressure, diluted with DCM/Hexanes, and passed through a short plug

of silica gel. The solution was then moved to a separatory funnel, washed with de-ionized water three times and brine one time. The solution was dried over magnesium sulfate, concentrated under vacuum, and recrystallized using DCM/methanol at -25 °C. The product was collected via vacuum filtration as a yellow solid (0.108 g, 0.234 mmol, 44.0% yield) ^{1}H NMR ($CDCl_3$, 400 MHz) δ 7.93 (d, *J* = 1.11 Hz, 2H), 7.63 (m, 12H), 7.42 (d, *J* = 2.03 Hz, 2H), 7.28 (m, 7H), 6.94 (dd, *J* = 8.32, 2.08 Hz, 2H), 6.10 (d, *J* = 8.31 Hz, 2H). ^{13}C NMR ($CDCl_3$, 400 MHz) δ 144.68, 137.60, 136.23, 134.98, 134.90, 134.13, 133.78, 133.12, 132.79, 131.41, 129.98, 128.57, 128.25, 127.89, 127.65, 126.88, 126.52, 126.16, 125.62, 124.97, 124.82, 122.36, 114.73, 114.10. HRMS (ESI): calculated for M+ $C_{34}H_{23}NO$, 461.1786; observed 461.1786.

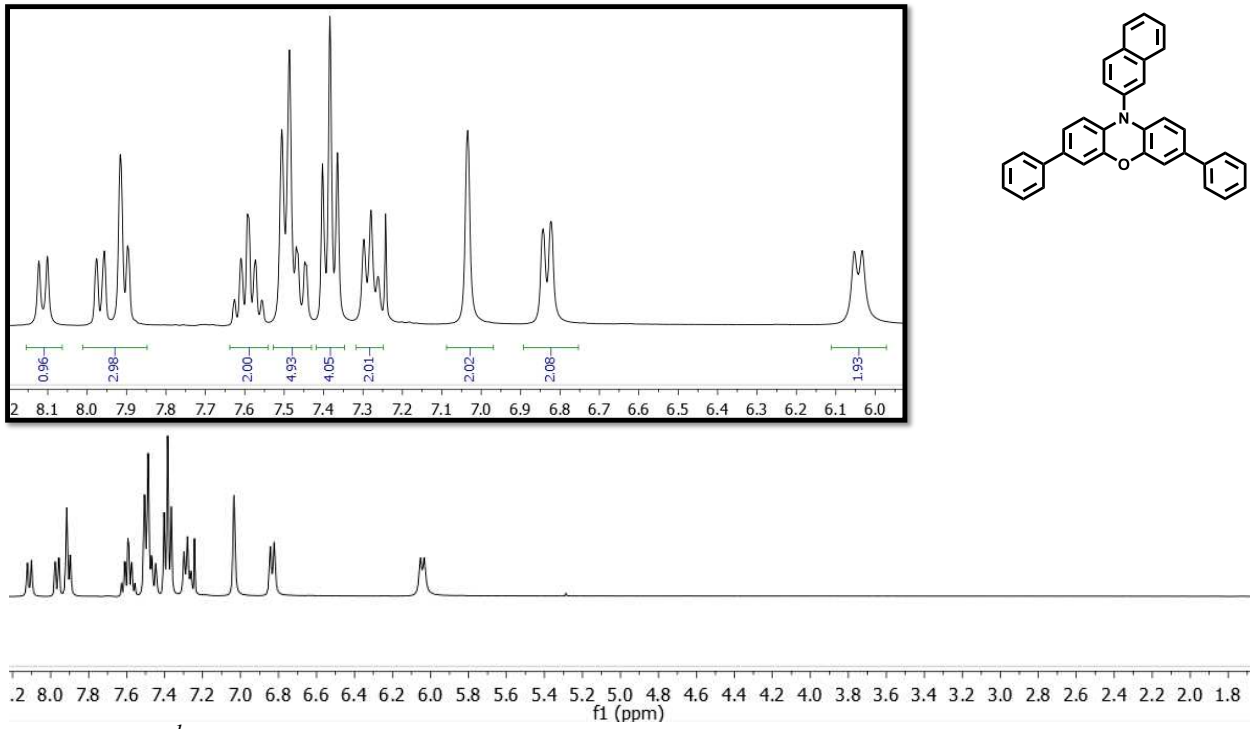

Figure 3.15. *^{1}H NMR of **5** ($CDCl_3$, 400 MHz).*

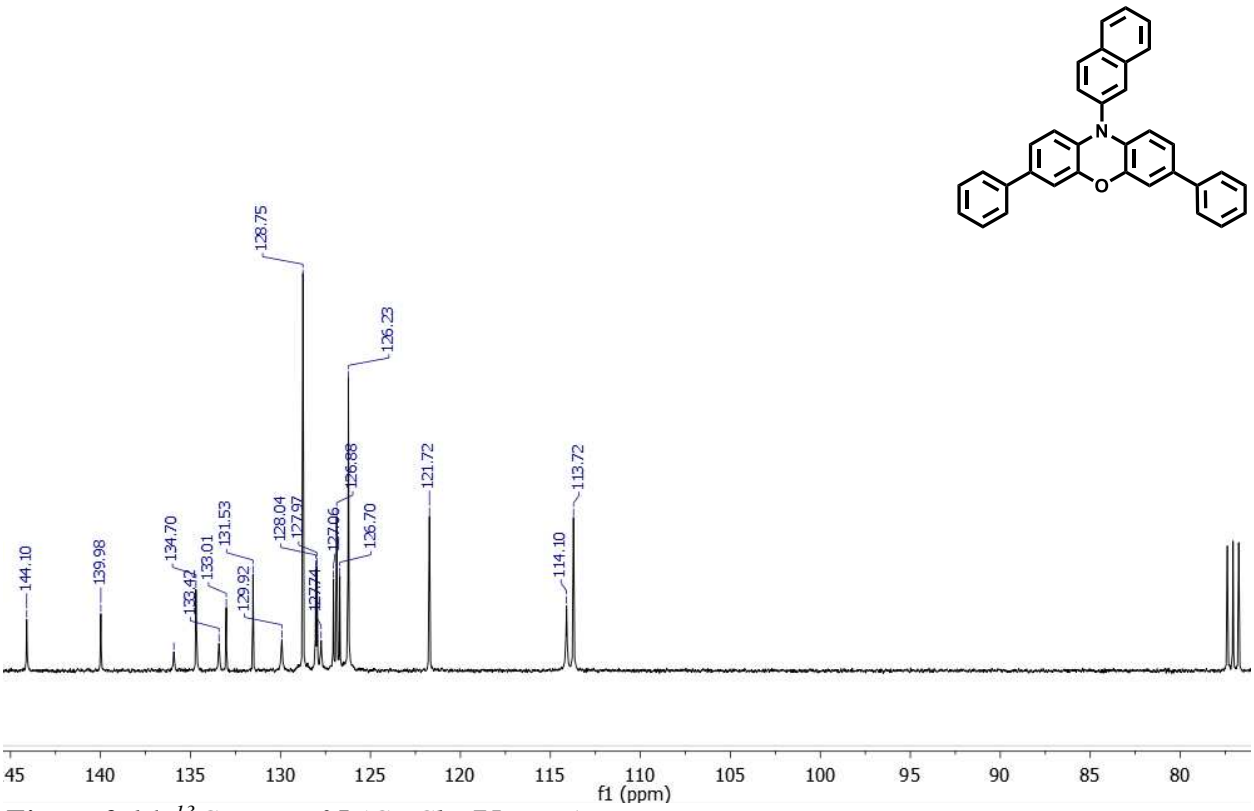

Figure 3.16. *^{13}C NMR of **5** ($CDCl_3$, 75 MHz).*

Synthesis of 3,7-Di(4-biphenyl) 2-Naphthalene-10-Phenoxazine (6)

3,7-Dibromo 2-Naphthalene-10-phenoxazine (0.400 g, 0.856 mmol, 1.00 equiv.) and 4-biphenyl boronic acid (0.678 g, 3.42 mmol, 4.00 equiv.) were added to a 250 mL storage tube flask and cycled between vacuum and nitrogen three times before 37.0 mL of dried and degassed THF was added. Once all reagents were dissolved, 11.0 mL of a 2.00 M aqueous solution of K_2CO_3, which had been sparged with nitrogen, was added and the biphasic system was heated to 80 °C. In a separate Schlenk flask, palladiumtetrakis(triphenyl phosphine) (0.148 g, 0.128 mmol, 0.150 equiv.) was dissolved in 37.0 mL of THF under inert atmosphere. The solution of $Pd(PPh_3)_4$ was then added to the reaction mixture and the temperature was raised to 100 °C for 24 h before it was allowed to cool to room temperature and exposed to oxygen. The reaction mixture was concentrated under reduced pressure, diluted with DCM/Hexanes, and passed through a short plug

of silica gel. The solution was then moved to a separatory funnel, washed with de-ionized water three times and brine one time. The solution was dried over magnesium sulfate, concentrated under vacuum, and recrystallized using DCM/methanol at -25 °C. The product was collected via vacuum filtration as a yellow solid (0.351 g, 0.571 mmol, 66.7% yield).^{1}H NMR (C_6D_6, 500 MHz) δ 7.68 (d, *J* = 8.63 Hz, 1H), 7.64 (d, *J* = 7.93 Hz, 1H), 7.52 (m, 15H), 7.35 (d, *J* = 2.07 Hz, 2H), 7.27 (m, 8H), 6.89 (dd, *J* = 8.31, 2.08 Hz, 2H), 6.07 (d, *J* = 8.31 Hz, 2H). ^{13}C NMR (C_6D_6, 300 MHz) δ 144.58, 14096, 139.81, 139.04, 136.15, 134.83, 134.55, 133.70, 131.33, 129.91, 128.73, 127.56, 127.10, 126.97, 126.81, 126.59, 126.44, 121.85, 114.24, 114.01. HRMS (ESI): calculated for M+ $C_{46}H_{31}NO$, 613.2405; observed 613.2412.

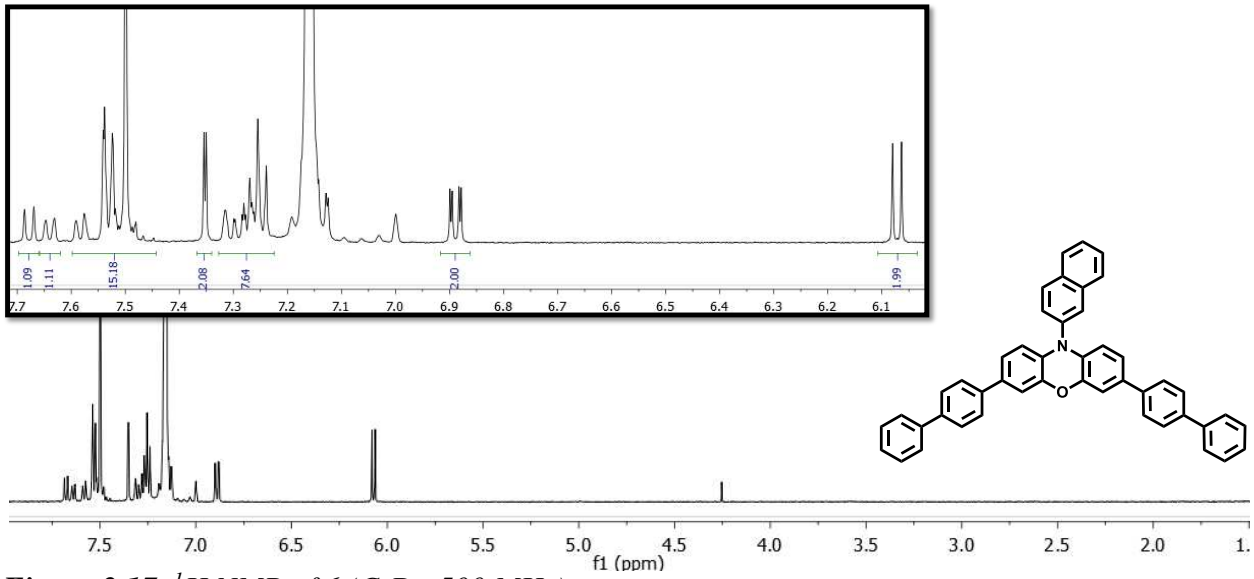

Figure 3.17. *^{1}H NMR of **6** (C_6D_6, 500 MHz).*

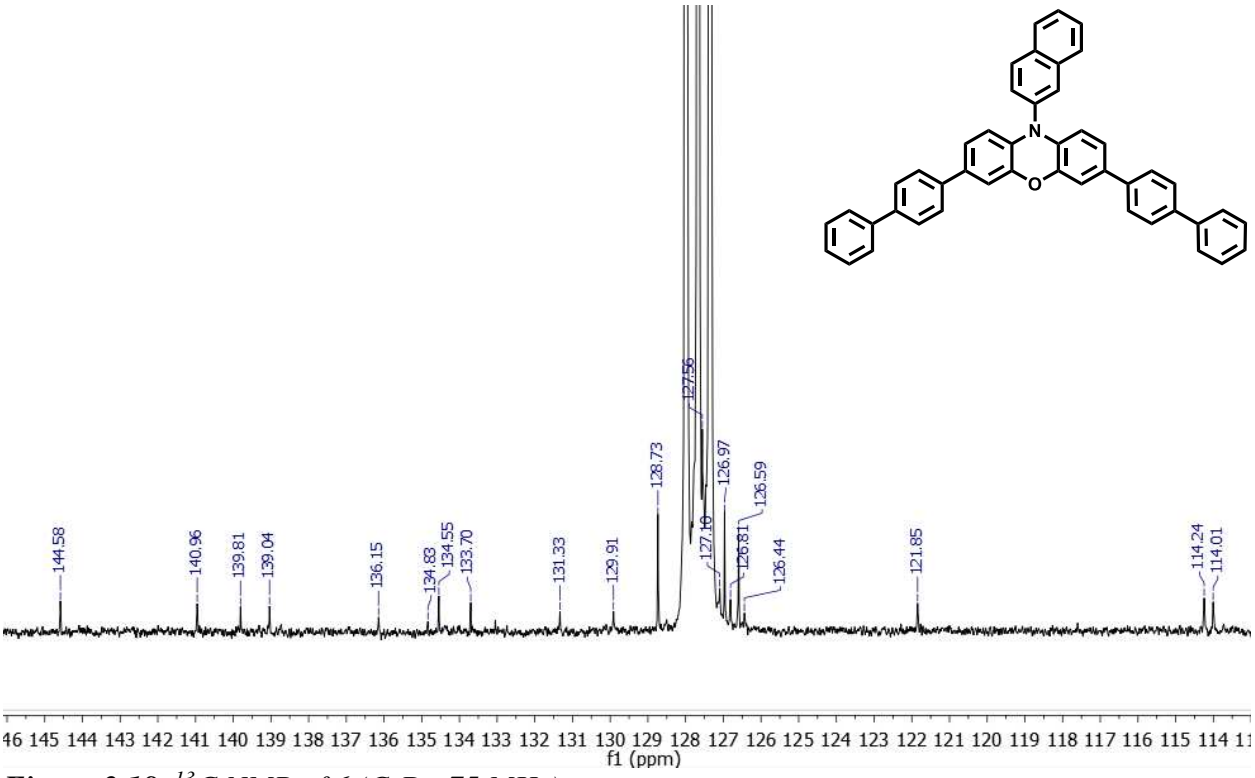

Figure 3.18. *^{13}C NMR of **6** (C_6D_6, 75 MHz).*

Synthesis of 3,7-Di(2-naphthyl) 2-Naphthalene-10-Phenoxazine (18)

3,7-Dibromo 2-Naphthalene-10-phenoxazine (0.400 g, 0.856 mmol, 1.00 equiv.) and 2-naphthalene boronic acid (0.589 g, 3.43 mmol, 4.00 equiv.) were added to a 250 mL storage tube flask and cycled between vacuum and nitrogen three times before 37.0 mL of dried and degassed THF was added. Once all reagents were dissolved, 11.0 mL of a 2.00 M aqueous solution of K_2CO_3, which had been sparged with nitrogen, was added and the biphasic system was heated to 80 °C In a separate Schlenk flask, palladiumtetrakis(triphenyl phosphine) (0.148 g, 0.128 mmol, 0.150 equiv.) was dissolved in 37.0 mL of THF under inert atmosphere. The solution of $Pd(PPh_3)_4$ was then added to the reaction mixture and the reaction was heated at 100 °C for 24 h before it was allowed to cool to room temperature and exposed to oxygen. The reaction mixture was concentrated under reduced pressure, diluted with DCM/Hexanes, and passed through a short plug of silica gel. The solution was then moved to a separatory funnel, washed with de-ionized water

three times and brine one time. The solution was dried over magnesium sulfate, concentrated under vacuum, and recrystallized using DCM/methanol at -25 °C. The product was collected via vacuum filtration as a yellow solid (0.481 g, 0.281 mmol, 32.8% yield).^{1}H NMR (C_6D_6, 500 MHz) δ 7.93 (d, *J* = 1.20 Hz, 2H), 7.63 (m, 12H), 7.42 (d, *J* = 2.06 Hz, 2H), 7.28 (m, 7H), 6.94 (dd, *J* = 8.31, 2.06 Hz, 2H), 6.10 (d, *J* = 8.31 Hz, 2H). ^{13}C NMR (C_6D_6, 300 MHz) δ 149.68, 137.60, 136.23, 134.98, 134.90, 134.13, 133.78, 133.12, 132.79, 131.41, 129.98, 128.57, 128.25, 127.89, 127.65, 126.88, 126.52, 126.16, 125.62, 124.97, 124.82, 122.36, 114.73, 114.10. HRMS (ESI): calculated for M+ $C_{42}H_{27}NO$, 661.2405; observed 661.2413.

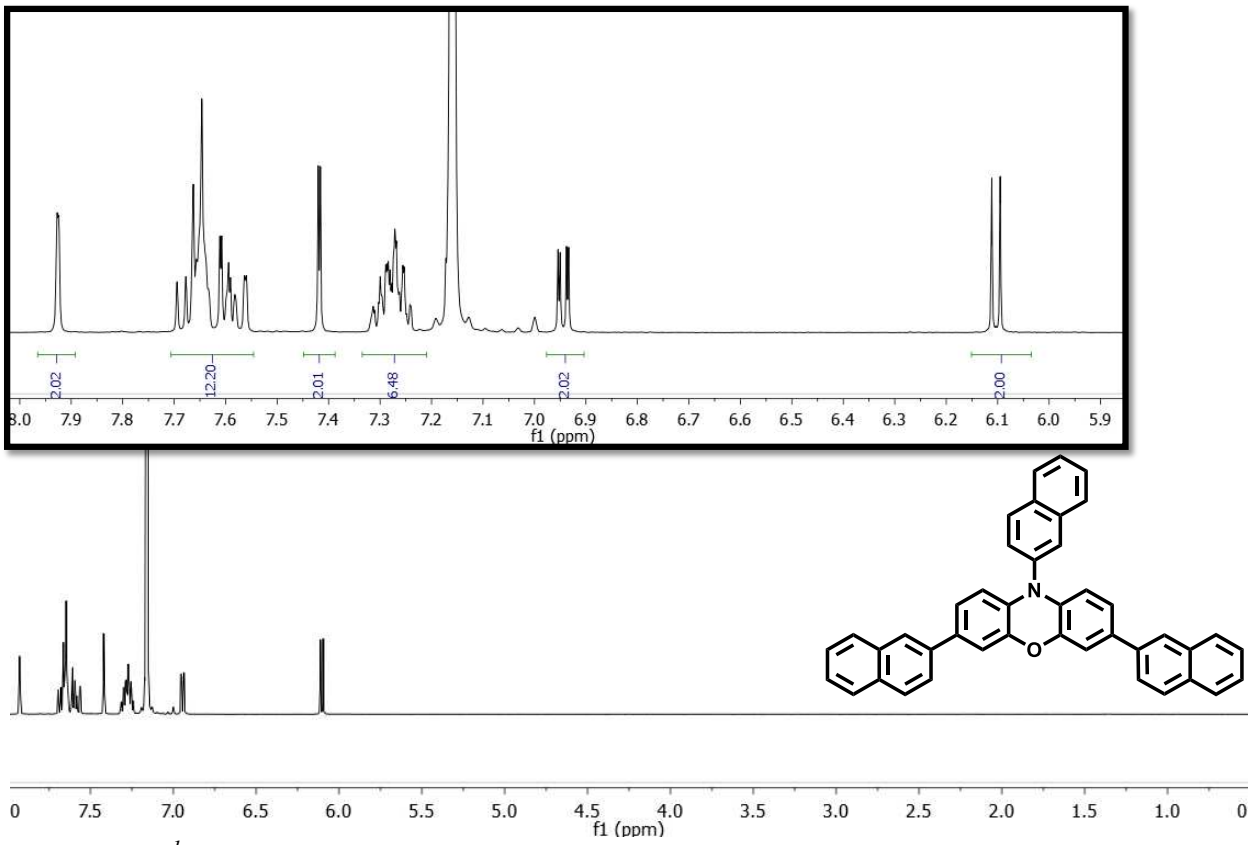

Figure 3.19. *^{1}H NMR of* ***18*** *(C_6D_6, 500 MHz).*

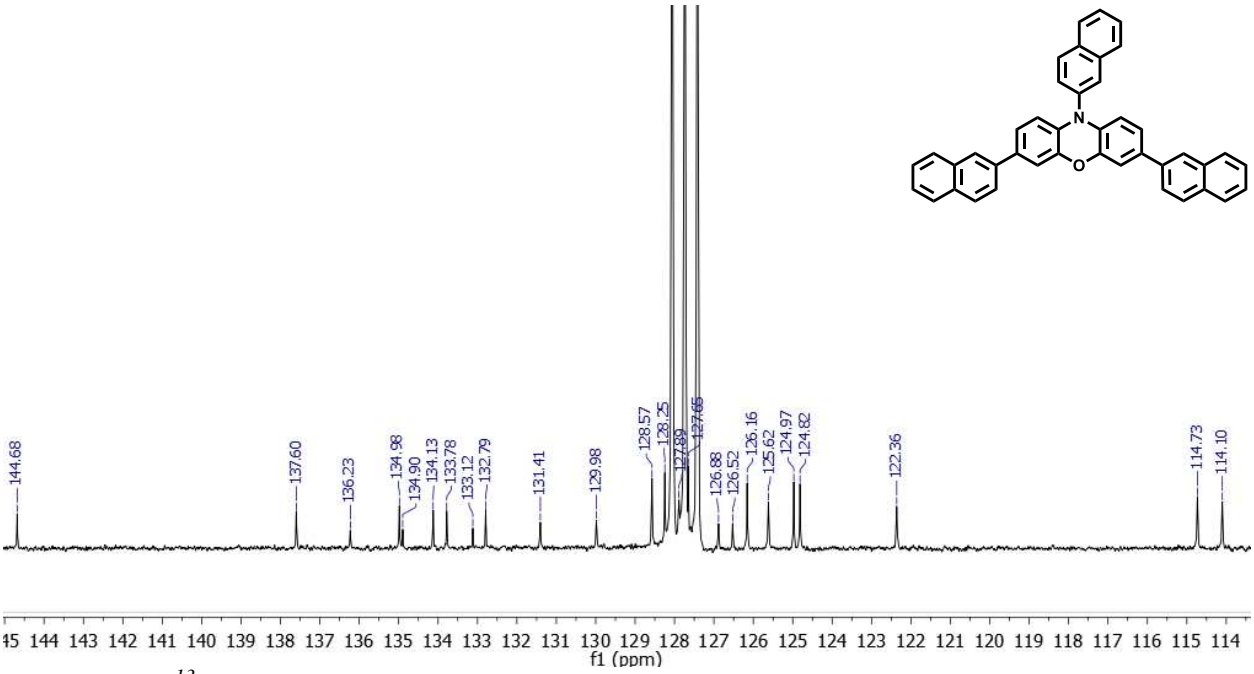

Figure 3.20. *^{13}C NMR of **18** (C_6D_6, 75 MHz).*

Synthesis of 3,7-Di(9-phenanthracenyl) 2-Naphthalene-10-Phenoxazine (16)

3,7-Dibromo 2-Naphthalene-10-phenoxazine (0.350 g, 0.749 mmol, 1.00 equiv.) and 9-phenanthracenyl boronic acid (0.569 g, 3.00 mmol, 4.00 equiv.) were added to a 250 mL storage tube flask and cycled between vacuum and nitrogen three times before 30.0 mL of dried and degassed THF was added. Once all of the reagents were dissolved, 10.0 mL of a 2.00 M aqueous solution of K_2CO_3, which had been sparged with nitrogen, was added and the biphasic system was heated to 80 °C. In a separate Schlenk flask, palladiumtetrakis(triphenyl phosphine) (0.130 g, 0.112 mmol, 0.150 equiv.) was dissolved in 30.0 mL of THF under inert atmosphere. The solution of $Pd(PPh_3)_4$ was then added to the reaction mixture and the reaction was heated at 100 °C for 24 h before it was allowed to cool to room temperature and exposed to oxygen. The reaction mixture was concentrated under reduced pressure, diluted with DCM, and passed through a short plug of silica gel. The solution was then moved to a separatory funnel, washed with de-ionized water three times and brine one time. The solution was dried over magnesium sulfate, concentrated under

vacuum, and recrystallized using DCM/methanol at -25 °C. The product was collected via vacuum filtration as a yellow solid (0.408 g, 0.616 mmol, 82.2% yield).^{1}H NMR (C_6D_6, 500 MHz) δ 8.55 (d, *J* = 8.13 Hz, 2H), 8.49 (d, *J* = 8.03 Hz, 2H), 8.26 (d, *J* = 8.18 Hz, 2H), 7.64 (m, 8H), 7.41 (m, 8H), 7.28 (m, 3H), 7.15 (d, *J* = 1.82 Hz, 2H), 6.79 (dd, *J* = 8.18, 1.86 Hz, 2H), 6.14 (d, *J* = 8.19 Hz, 2H). ^{13}C NMR (C_6D_6, 300 MHz) δ 144.15, 137.99, 136.31, 134.93, 134.59, 133.84, 133.09, 131.88, 131.46, 131.40, 130.98, 130.16, 130.00, 128.67, 127.82, 127.77, 127.27, 126.88, 126.80, 126.62, 126.44, 126.36, 126.34, 126.33, 125.25, 123.02, 122.54, 117.70, 113.52. HRMS (ESI): calculated for M+ $C_{50}H_{31}NO$, 661.2405; observed 661.2413.

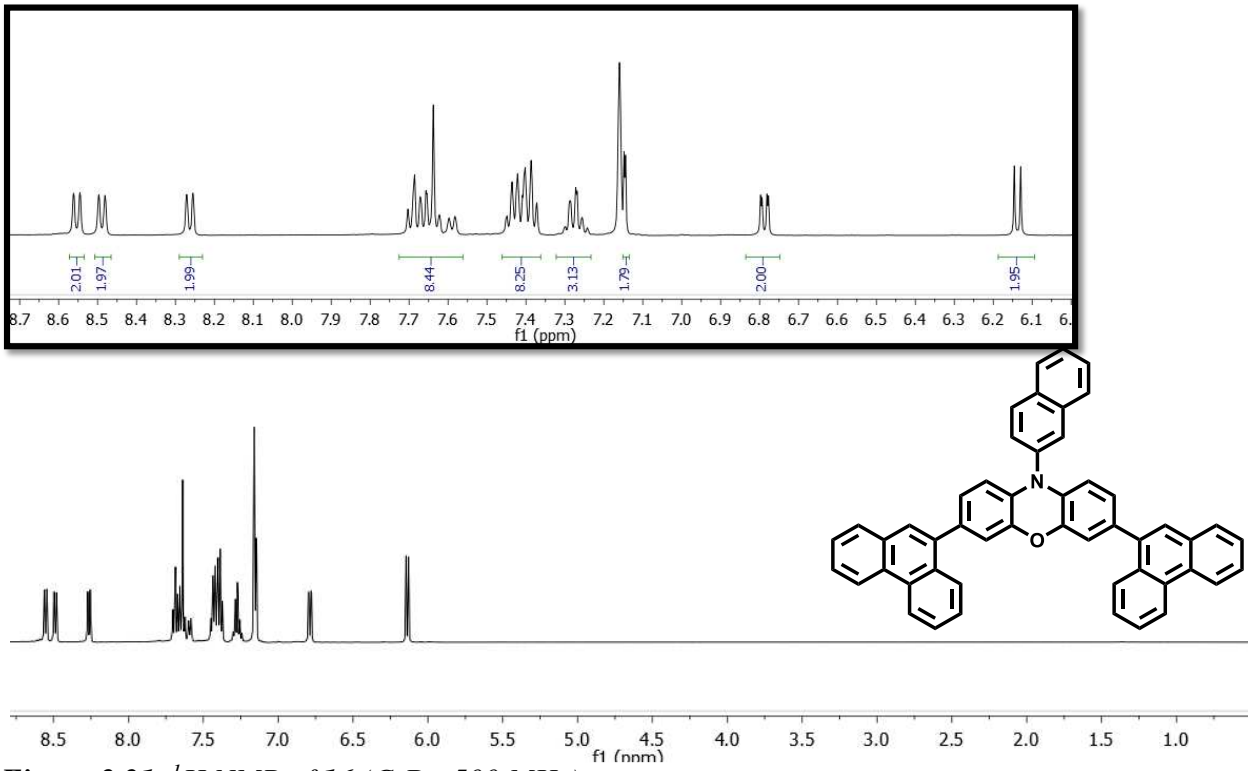

Figure 3.21. *^{1}H NMR of* ***16*** *(C_6D_6, 500 MHz).*

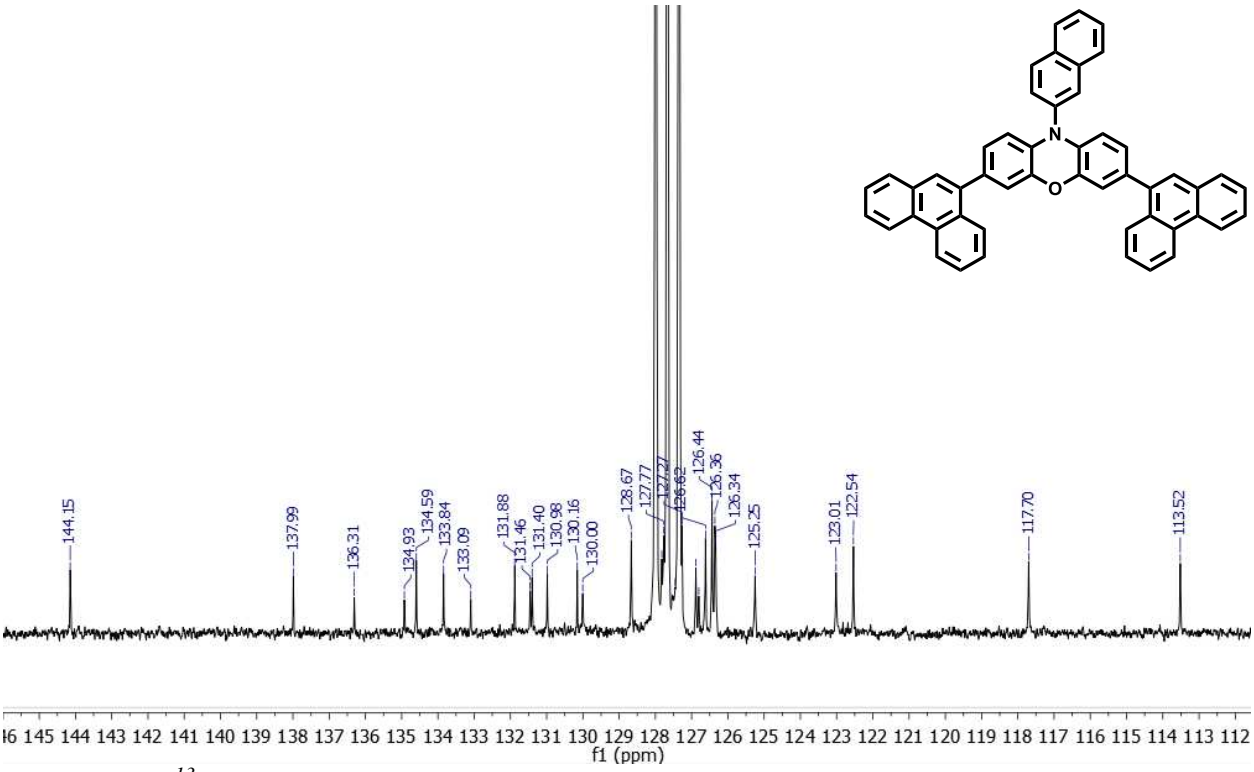

Figure 3.22. *^{13}C NMR of **16** (C_6D_6, 75 MHz).*

Synthesis of 3,7-Di(1-pyrenyl) 2-Naphthalene-10-Phenoxazine (17)

3,7-Dibromo 2-Naphthalene-10-phenoxazine (0.350 g, 0.749 mmol, 1.00 equiv.) and 1-pyrene boronic acid (0.738 g, 3.00 mmol, 4.00 equiv.) were added to a 250 mL storage tube flask and cycled between vacuum and nitrogen three times before 30 mL of dried and degassed THF was added. Once all reagents were dissolved, 10.0 mL of a 2.00 M aqueous solution of K_2CO_3, which had been sparged with nitrogen, was added and the biphasic system was heated to 80 °C. In a separate schlenk flask, palladiumtetrakis(triphenyl phosphine) (0.130 g, 0.112 mmol, 0.150 equiv.) was dissolved in 30.0 mL of THF under inert atmosphere. The solution of $Pd(PPh_3)_4$ was then added to the reaction mixture and the reaction was heated to 100 °C for 24 h before it was allowed to cool to room temperature and exposed to oxygen. The reaction mixture was concentrated under reduced pressure, diluted with DCM/Hexanes, and passed through a short plug of silica gel. The solution was then moved to a separatory funnel, washed with de-ionized water

three times and brine one time. The solution was dried over magnesium sulfate, concentrated under vacuum, and recrystallized using DCM/methanol at -25 °C. The product was collected via vacuum filtration as a yellow solid (0.376 g, 0.530 mmol, 70.8% yield).^{1}H NMR (C_6D_6, 500 MHz) δ 7.86 (d, *J* = 8.34 Hz, 1H), 7.37 (m, 2H), 7.24 (m, 5H), 7.06 (d, *J* = 2.05 Hz, 2H), 6.90 (m, 17H), 6.43 (dd, *J* = 8.30, 2.11 Hz, 2H), 5.57 (d, *J* = 8.32 Hz, 2H). ^{13}C NMR (C_6D_6, 300 MHz) δ 144.30, 136.93, 136.24, 135.05, 134.95, 133.79, 133.12, 131.65, 131.48, 131.23, 130.64, 13.02, 128.85, 128.73, 127.83, 127.79, 127.47, 127.26, 126.85, 126.47, 125.98, 125.85, 125.43, 125.29, 125.28, 125.11, 125.01, 124.84, 124.80, 124.58, 118.09, 113.65. HRMS (ESI): calculated for M+ $C_{54}H_{35}NO$, 709.2405; observed 709.2407.

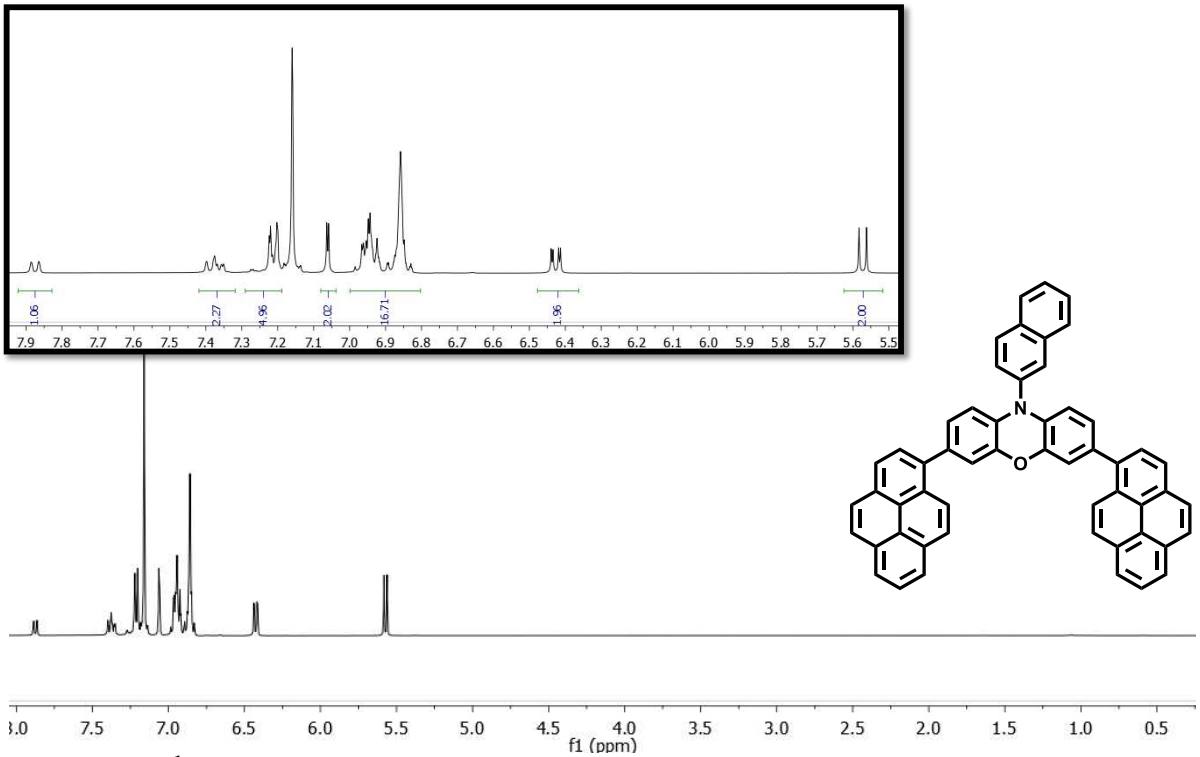

Figure 3.23. *^{1}H NMR of **17** (C_6D_6, 500 MHz).*

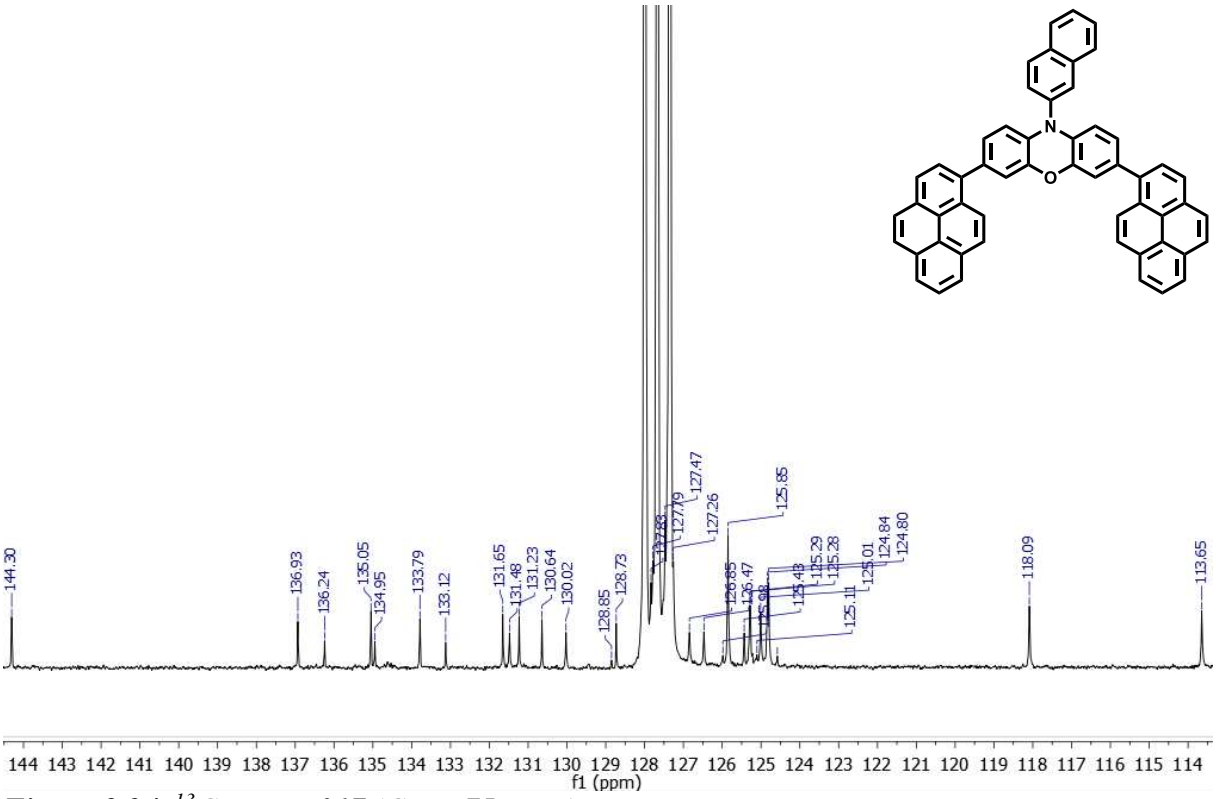

Figure 3.24. *^{13}C NMR of **17** (C_6D_6, 75 MHz).*

Synthesis of 3,7-Di(4-(4-trifluoromethyl)phenyl) 2-Naphthalene-10-Phenoxazine (14)

3,7-Dibromo 2-Naphthalene-10-phenoxazine (0.350 g, 0.749 mmol, 1.00 equiv.) and 4-trifluoromethyl phenyl boronic acid (0.569 g, 3.00 mmol, 4.00 equiv.) were added to a 250 mL storage tube flask and cycled between vacuum and nitrogen three times before 30 mL of dried and degassed THF was added. Once all particulate was dissolved, 10.0 mL of a 2.00 M aqueous solution of K_2CO_3, which had been sparged with nitrogen, was added and the biphasic system was heated to 80 °C. In a separate Schlenk flask, palladiumtetrakis(triphenyl phosphine) (0.130 g, 0.112 mmol, 0.150 equiv.) was dissolved in 30.0 mL of THF under inert atmosphere. The solution of $Pd(PPh_3)_4$ was then added to the reaction mixture and the reaction was heated at 100 °C for 24 h before it was allowed to cool to room temperature and exposed to oxygen. The reaction mixture was concentrated under reduced pressure, diluted with DCM/Hexanes, and passed through a short plug of silica gel. The solution was then moved to a separatory funnel, washed with de-ionized

water three times and brine one time. The solution was dried over magnesium sulfate, concentrated under vacuum, and recrystallized using DCM/methanol at -25 °C. The product was collected via vacuum filtration as a yellow solid (0.247 g, 0.414 mmol, 55.3% yield).^{1}H NMR (C_6D_6, 500 MHz) δ 7.68 (d, *J* = 2.2 Hz, 1H), 7.64 (d, *J* = 7.94 Hz, 1H), 7.58 (d, *J* = 7.98 Hz, 1H), 7.50 (d, *J* = 1.75 Hz, 1H), 7.35 (d, *J* = 7.91 Hz, 4H), 7.28 (m, 3H), 7.19 (s, 3H), 7.12 (d, *J* = 2.07 Hz, 1H), 7.08 (dd, *J* = 8.57, 2.0 Hz, 2H), 6.65 (dd, *J* = 8.32, 2.08, Hz, 2H), 6.00, (d, *J* = 8.35 Hz, 2H). ^{13}C NMR (C_6D_6, 300 MHz) δ 144.43, 143.23, 135.57, 134.78, 134.16, 133.34, 133.10, 131.51, 129.75, 128.86, 128.43, 127.92, 127.84, 127.27, 127.08, 126.68, 126.26, 125.65 (q, *J* = 3.77 Hz), 122.27, 114.33, 114.02. ^{19}F NMR ($CDCl_3$, 300MHz) δ -62.0. HRMS (ESI): calculated for M+ $C_{36}H_{21}NOF_6$, 597.1527; observed 597.1525.

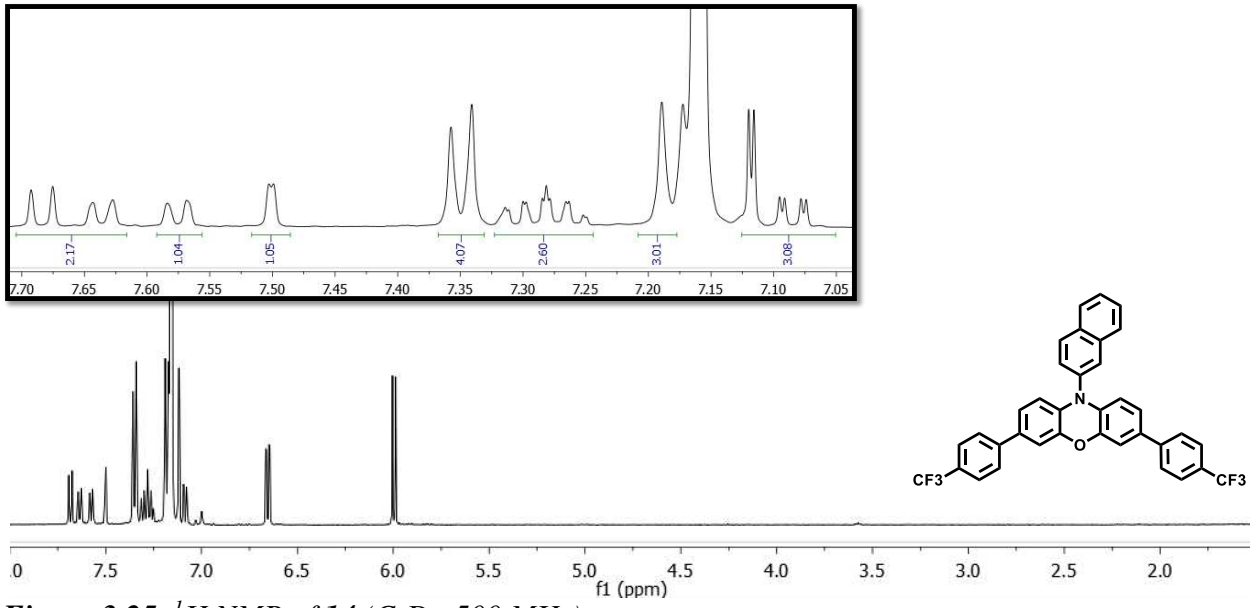

Figure 3.25. *^{1}H NMR of **14** (C_6D_6, 500 MHz).*

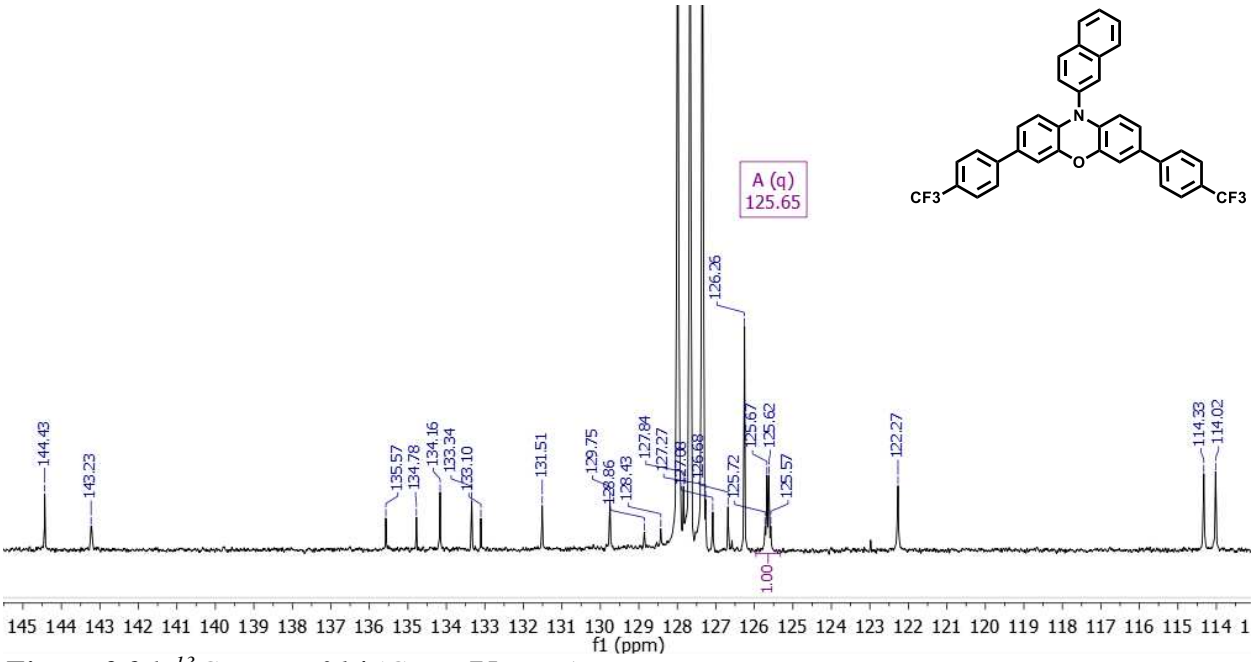

Figure 3.26. *^{13}C NMR of **14** (C_6D_6, 75 MHz).*

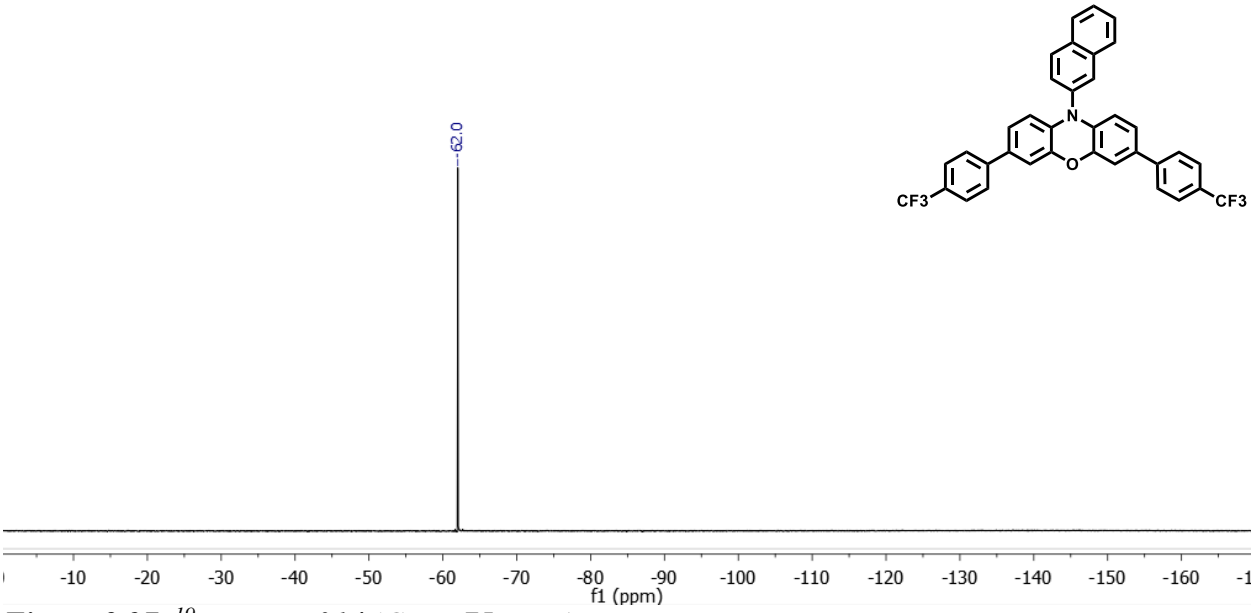

Figure 3.27. *^{19}F NMR of **14** (C_6D_6, 75 MHz).*

Synthesis of 3,7-Di(4-cyanophenyl) 2-Naphthalene-10-Phenoxazine (13)

3,7-Dibromo 2-Naphthalene-10-phenoxazine (0.300 g, 0.642 mmol, 1.00 equiv.) and 4-cyanophenyl boronic acid (0.377 g, 2.57 mmol, 4.00 equiv.) were added to a 250 mL storage tube flask and cycled between vacuum and nitrogen three times before 30.0 mL of dried and degassed THF was added. Once all reagents were dissolved, 10.0 mL of a 2.00 M aqueous solution of K_2CO_3, which had been sparged with nitrogen, was added and the biphasic system was heated to 80°C. In a separate schlenk flask, palladiumtetrakis(triphenyl phosphine) (0.130 g, 0.112 mmol, 0.150 equiv.) was dissolved in 30.0 mL of THF under inert atmosphere. The solution of $Pd(PPh_3)_4$ was then added to the reaction mixture and the reaction was heated at 100 °C for 24 h before it was allowed to cool to room temperature and exposed to oxygen. The reaction mixture was concentrated under reduced pressure, diluted with DCM/Hexanes, and passed through a short plug of silica gel. The solution was then moved to a separatory funnel, washed with de-ionized water three times and brine one time. The solution was dried over magnesium sulfate, concentrated under vacuum, and recrystallized using DCM/methanol at -25 °C. The product was collected via vacuum filtration as a yellow solid (0.251 g, 0.491 mmol, 76.4 % yield). ^{1}H NMR (C_6D_6, 500 MHz) δ 7.67 (d, *J* = 8.64 Hz, 1H), 7.62 (d, *J* = 8.01 Hz, 1H), 7.56 (d, *J* = 8.06 Hz, 1H), 7.45 (d, *J* = 1.58 Hz, 1H), 7.28 (m, 2H), 6.99 (m, 11H), 6.55 (dd, *J* = 8.36, 2.05 Hz, 2H), 5.95 (d, *J* = 8.35 Hz, 2H). ^{13}C NMR (C_6D_6, 400 MHz) δ 144.38, 143.33, 135.28, 134.74, 134.30, 133.11, 132.88, 132.24, 131.58, 129.64, 127.85, 127.18, 127.05, 126.77, 126.15, 122.30, 118.57, 114.17, 114.01, 110.70. HRMS (ESI): calculated for M+ $C_{36}H_{21}N_3O$, 511.1685; observed 511.1682.

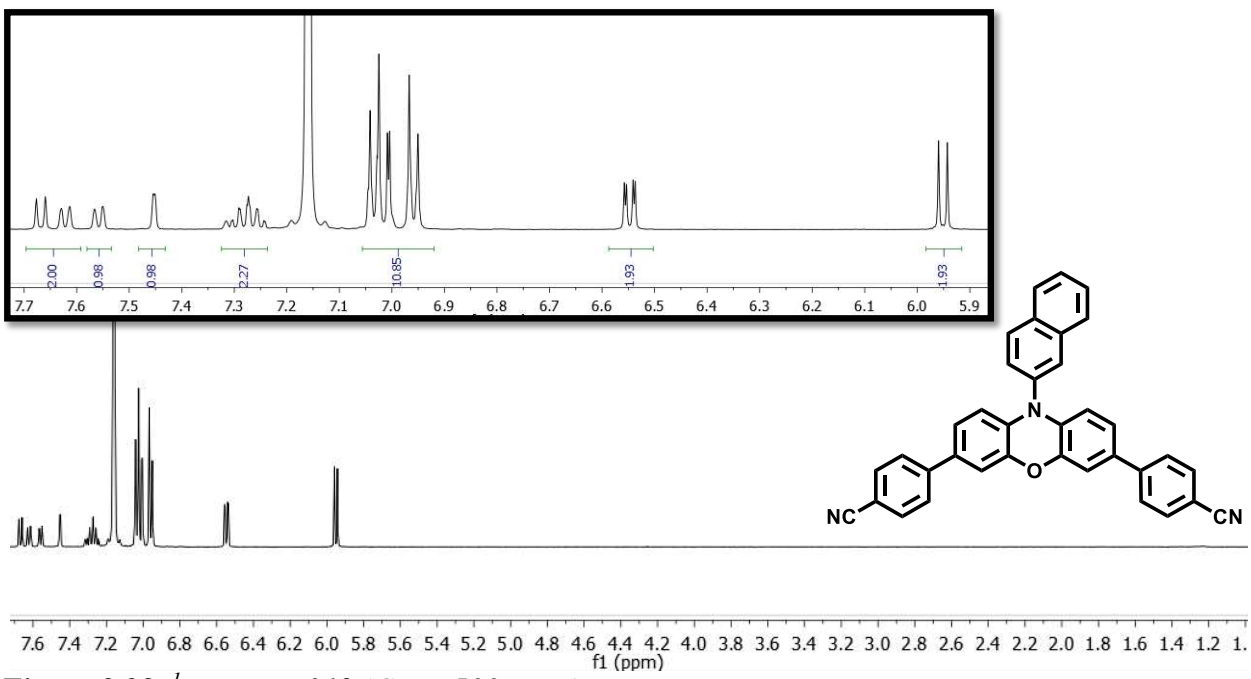

Figure 3.28. *^{1}H NMR of **13** (C_6D_6, 500 MHz).*

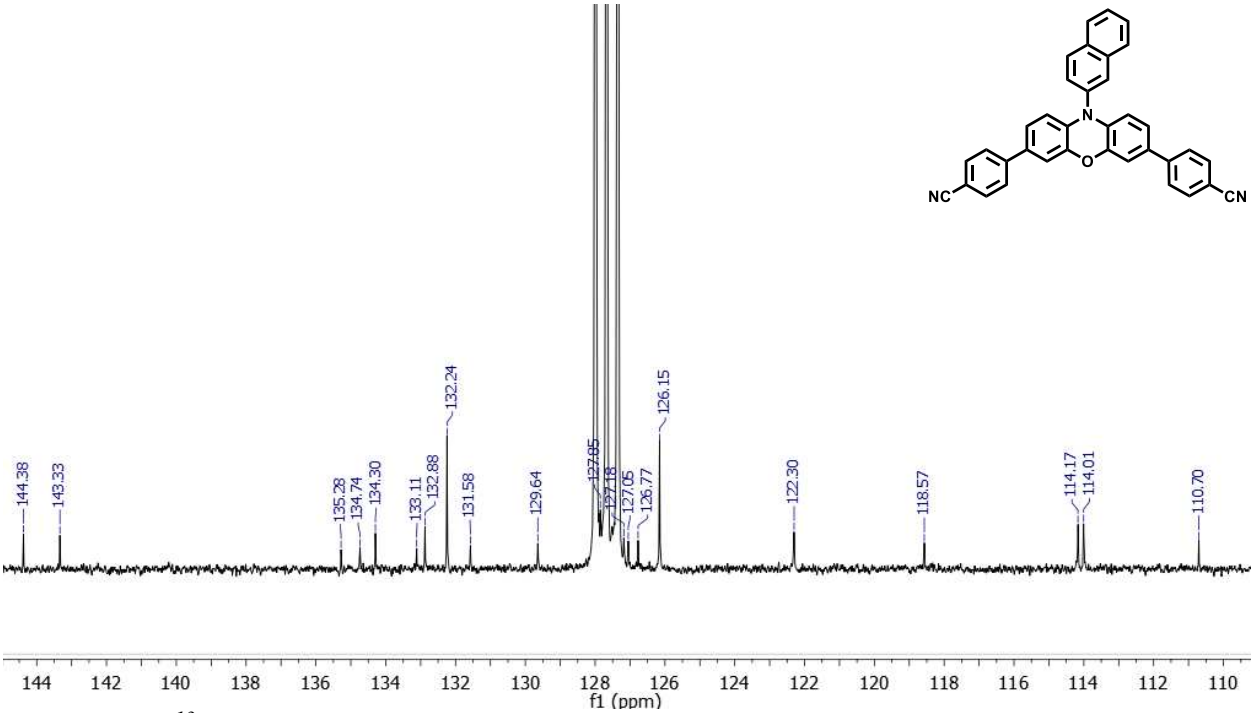

Figure 3.29. *^{13}C NMR of **13** (C_6D_6, 75 MHz).*

Synthesis of 3,7-Di(4-methoxyphenyl) 2-Naphthalene-10-Phenoxazine (12)

3,7-Dibromo 2-Naphthalene-10-phenoxazine (0.250 g, 0.535 mmol, 1.00 equiv.) and 4-methoxyphenyl boronic acid (0.325 g, 2.14 mmol, 4.00 equiv.) were added to a 250 mL storage tube flask and cycled between vacuum and nitrogen three times before 25.0 mL of dried and degassed THF was added. Once all reagents were dissolved, 7.00 mL of a 2.00 M aqueous solution of K_2CO_3, which had been sparged with nitrogen, was added and the biphasic system was heated to 80 °C. In a separate Schlenk flask, palladiumtetrakis(triphenyl phosphine) (0.0928 g, 0.0803 mmol, 0.150 equiv.) was dissolved in 25.0 mL of THF under inert atmosphere. The solution of $Pd(PPh_3)_4$ was then added to the reaction mixture and the reaction was heated at 100 °C for 24 h before it was allowed to cool to room temperature and exposed to oxygen. The reaction mixture was concentrated under reduced pressure, diluted with DCM/Hexanes, and passed through a short plug of silica gel. The solution was then moved to a separatory funnel, washed with de-ionized water three times and brine one time. The solution was dried over magnesium sulfate, concentrated under vacuum, and recrystallized using DCM/methanol at -25 °C. The product was collected via vacuum filtration as a yellow solid (0.0966 g, 0.185 mmol, 34.6% yield). ^{1}H NMR (C_6D_6, 500 MHz) δ 7.57 (m, 4H), 7.36 (d, J = 8.70 Hz, 4H), 7.24 (m, 4H), 7.10 (d, J = 1.64 Hz, 1H), 6.78 (m, 6H), 6.03 (d, J = 8.33 Hz, 2H), 3.30 (s, 6H). ^{13}C NMR ($CDCl_3$, 400 MHz) δ 144.10, 142.73, 133.89, 131.76, 130.97, 130.64, 128.44, 123.52, 122.09, 115.93, 113.39. HRMS (ESI): calculated for M+ $C_{36}H_{27}NO_3$, 521.1991; observed 521.1988.

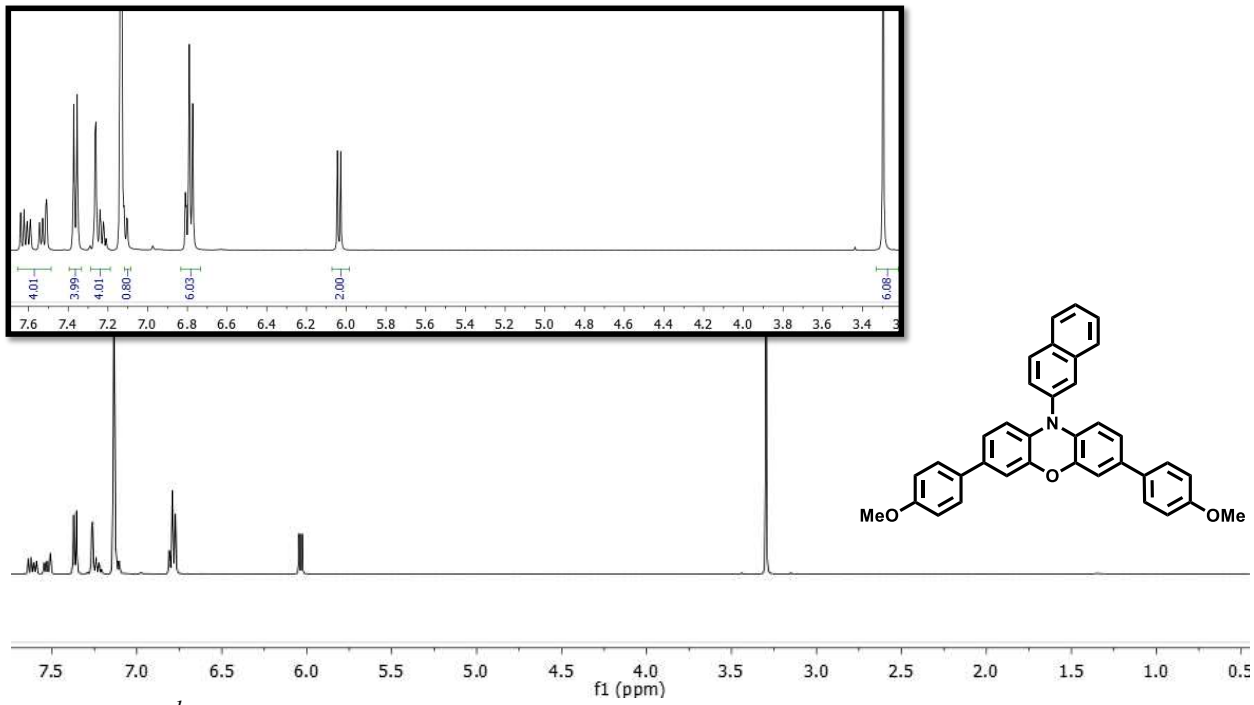

Figure 3.30. *^{1}H NMR of **12** (C_6D_6, 500 MHz).*

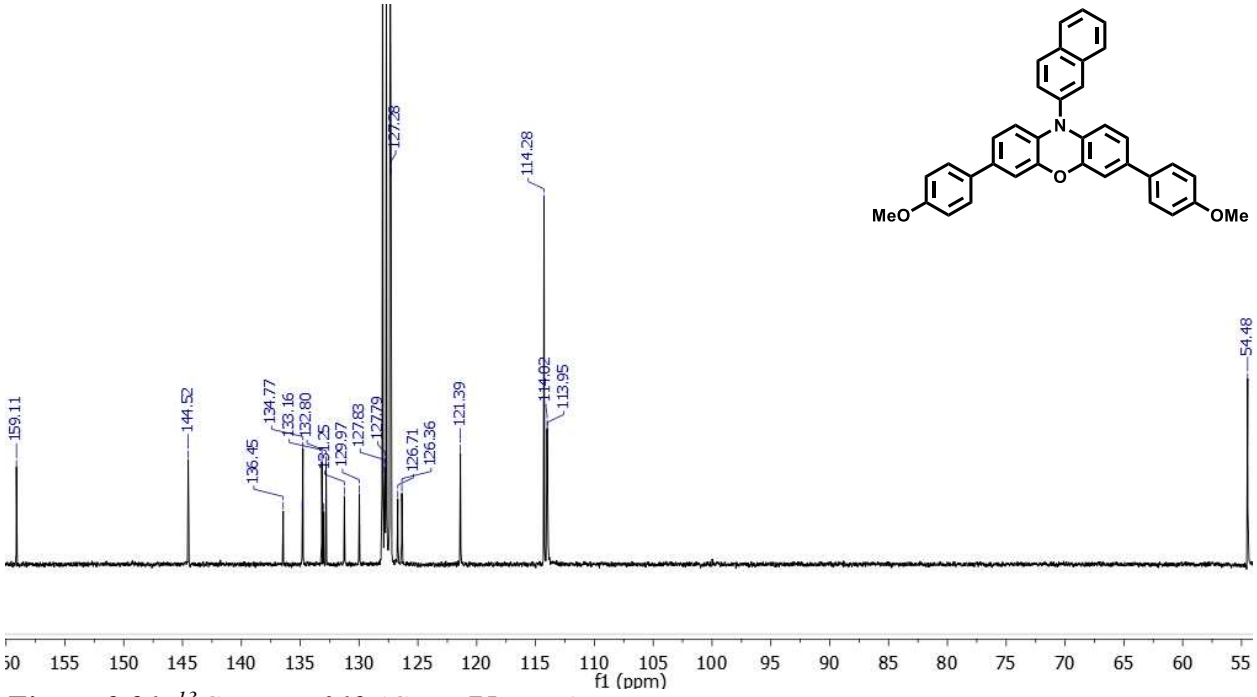

Figure 3.31. *^{13}C NMR of **12** (C_6D_6, 75 MHz).*

Synthesis of 3,7-Di(4-(diphenylamino)phenyl) 2-Naphthalene-10-Phenoxazine (14)

3,7-Dibromo 2-Naphthalene-10-phenoxazine (0.350 g, 0.749 mmol, 1.00 equiv.) and 4-(diphenylamino) phenyl boronic acid (0.867 g, 3.00 mmol, 4.00 equiv.) were added to a 250 mL storage tube flask and cycled between vacuum and nitrogen three times. 30.0 mL of dried and degassed THF was added. Once all reagents were dissolved, 10.0 mL of a 2.00 M aqueous solution of K_2CO_3, which had been sparged with nitrogen, was added and the biphasic system and was heated to 80 °C. In a separate Schlenk flask, palladiumtetrakis(triphenyl phosphine) (0.130 g, 0.112 mmol, 0.150 equiv.) was dissolved in 30.0 mL of THF under inert atmosphere. The solution of $Pd(PPh_3)_4$ was then added to the reaction mixture and the temperature was raised to 100 °C for 24 h before it was allowed to cool to room temperature and exposed to oxygen. The reaction mixture was concentrated under reduced pressure, diluted with DCM/hexanes, and passed through a short plug of silica gel. The solution was then moved to a separatory funnel, washed with de-ionized water three times and brine one time. The solution was dried over magnesium sulfate, concentrated under vacuum, and recrystallized using DCM/methanol at -25 °C. The product was collected as a yellow solid (0.453 mg, 0.569 mmol, 76.3% yield).^{1}H NMR (C_6D_6, 500 MHz) δ 7.60 (m, 2H), 7.53 (d, *J* = 7.90 Hz, 1H), 7.26 (m, 11H), 7.05 (m, 24H), 6.81 (m, 6H), 5.97 (d, *J* = 8.31 Hz, 2H). ^{13}C NMR (C_6D_6, 300 MHz) δ 147.97, 146.92, 144.51, 136.21, 134.81, 134.51, 134.42, 133.30, 133.00, 131.23, 129.91, 129.25, 127.77, 127.00, 126.73, 126.35, 124.50, 124.30, 122.70, 121.36, 113.93, 113.88. HRMS (ESI): calculated for M+ $C_{58}H_{41}N_3O$, 795.3250; observed 795.3256.

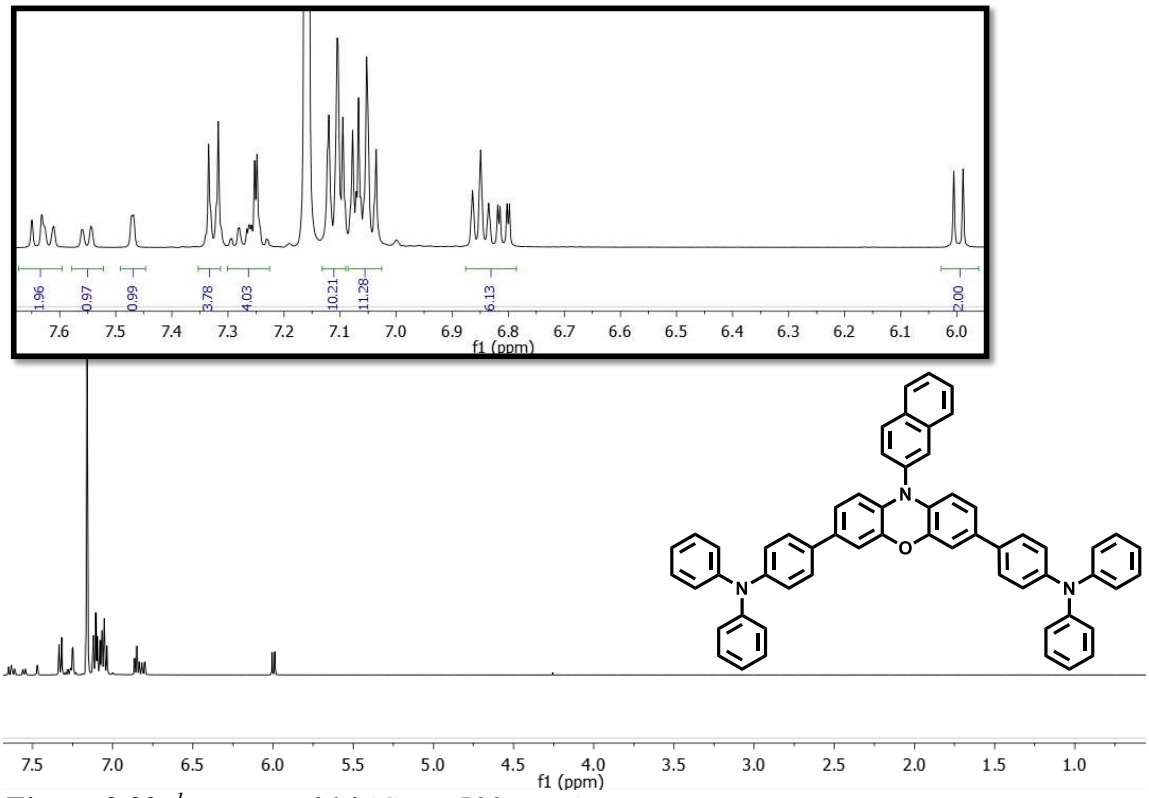

Figure 3.32. *^{1}H NMR of **14** (C_6D_6, 500 MHz).*

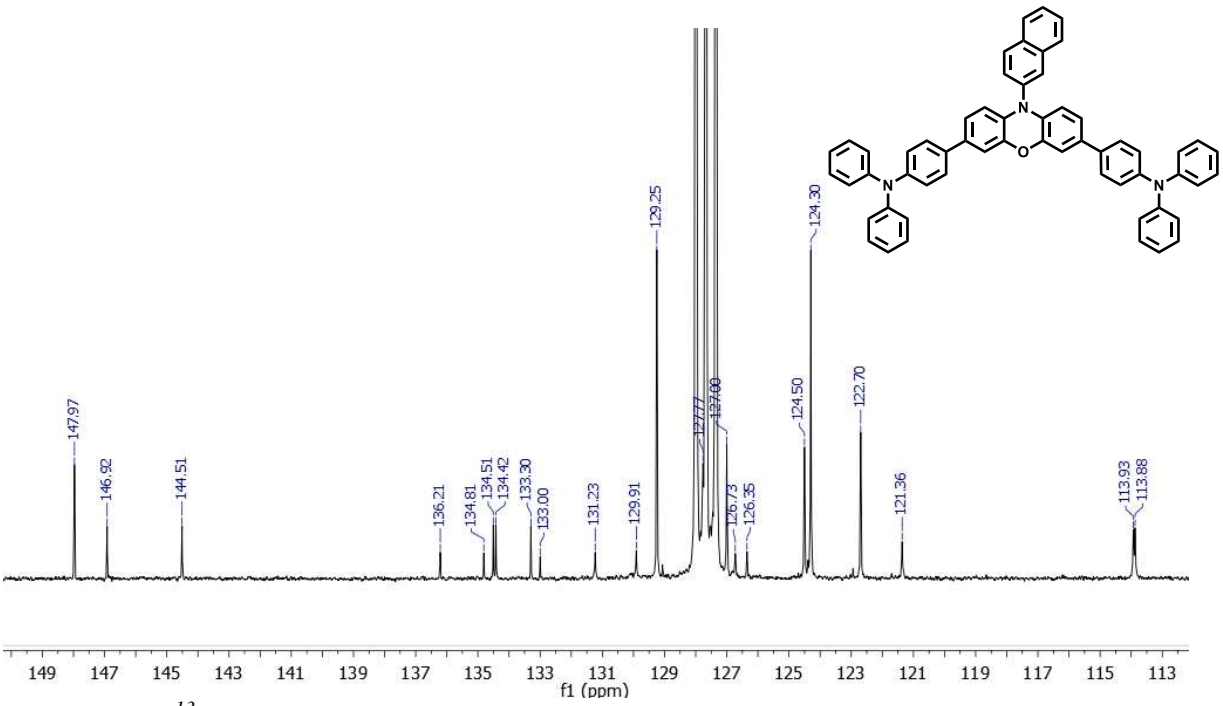

Figure 3.33. *^{13}C NMR of **14** (C_6D_6, 75 MHz).*

Synthesis and Characterization of PCs 6-9 & 18-19

Synthesis of Phenyl-10-Phenoxazine (6)

Phenoxazine (2.00 g, 10.9 mmol, 1.00 equiv.), sodium tert-butoxide (1.57 g, 16.4 mmol, 1.50 equiv.), and 4-bromobenzene (3.45 mL, 32.7 mmol, 3.00 equiv.) were combined in a flame-dried storage flask and the mixture was degassed three times before being brought into a nitrogen-filled glovebox. Then bis(dibenzylideacetone)dipalladium(0) (0.0627 g, 0.109 mmol, 0.0100 equiv.), a solution of tri-tert-butyl phosphine in toluene (0.662 mL, 1.00 M, 0.0300 equiv.), and 80.0 mL of toluene were added. The reaction mixture was removed from the glovebox and brought to 120 °C. After performing the reaction for 48 hours the reaction was allowed to cool to room temperature before the toluene was removed under reduced pressure. The mixture was diluted with DCM then washed once with de-ionized water and twice with brine. The solution was dried over magnesium sulfate, concentrated under vacuum, and recrystallized using DCM/hexanes. The resulting crystals were washed with methanol and hexanes during vacuum filtration and dried under reduced pressure (2.17 g, 76.8% yield). NMR signals matched those previously reported.[1]

Synthesis of 3-Bromo Phenyl-10-Phenoxazine

Phenyl-10-phenoxazine (1.19 g, 4.59 mmol, 1.00 equiv.) was dissolved in 200 mL of THF and the flask was covered in aluminum foil. *N*-bromosuccinimide (0.841 g, 4.72 mmol, 1.03 equiv.) was added portion-wise over thirty minutes. The reaction was performed at room temperature for three hours before the THF was removed under reduced pressure. The reaction was re-dissolved in DCM, washed with de-ionized water once and brine twice before being dried with magnesium sulfate and concentrated under reduced pressure. The crude product was collected as a red oil and purified using column chromatography (silica gel, 15:1 Hexanes/DCM). The

product was collected as a white solid (67.7% yield, R_f = 0.375). ^{1}H NMR ($CDCl_3$, 500 MHz) δ 7.60 (t, *J* = 7.8 Hz, 2H), 7.52 – 7.44 (m, 1H), 7.34 – 7.26 (m, 2H), 6.81 (d, *J* = 2.2 Hz, 1H), 6.72 – 6.56 (m, 4H), 5.92 – 5.86 (m, 1H), 5.74 (d, *J* = 8.5 Hz, 1H). ^{13}C NMR ($CDCl_3$, 75 MHz) δ 144.59, 143.51, 138.55, 133.90, 133.81, 131.19, 130.59, 128.73, 125.84, 123.61, 121.54, 118.46, 115.53, 114.23, 113.38, 112.50. HRMS (ESI): calculated for M+ $C_{18}H_{12}BrNO$, 338.0181; observed 338.0179.

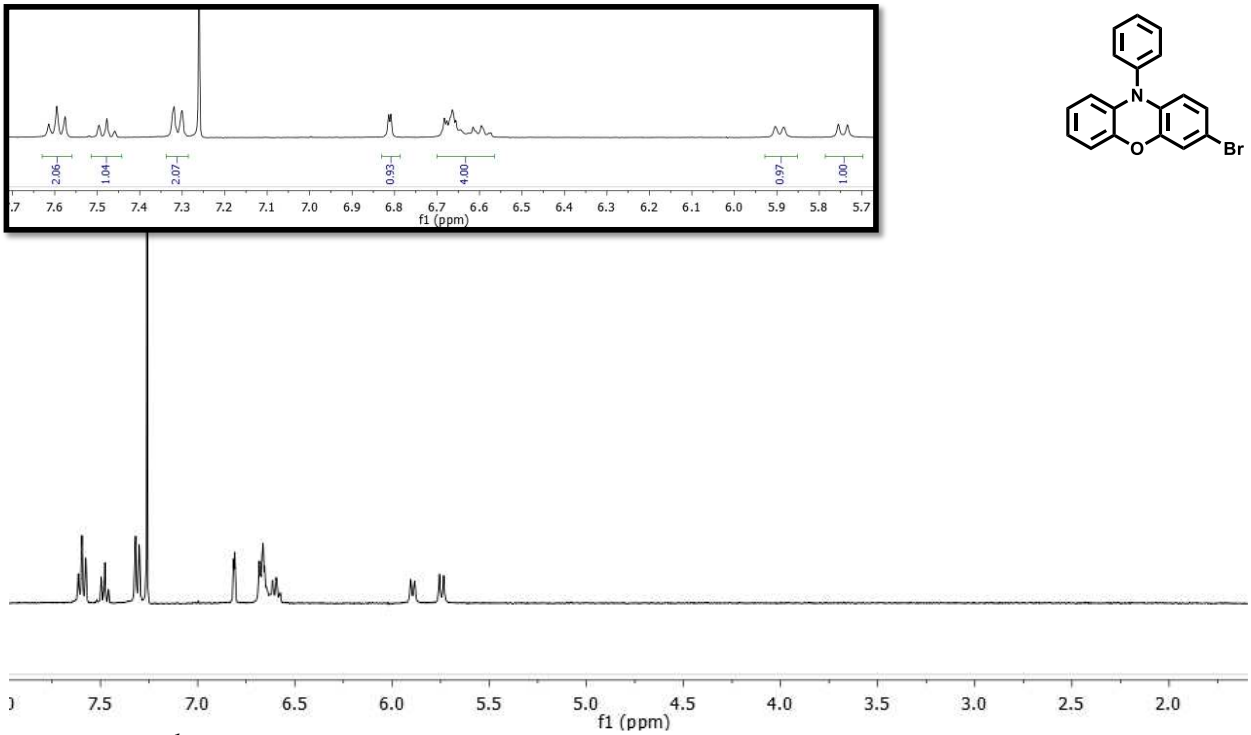

Figure 3.34. *^{1}H NMR of 3-bromo phenyl-10 phenoxazine ($CDCl_3$, 500 MHz).*

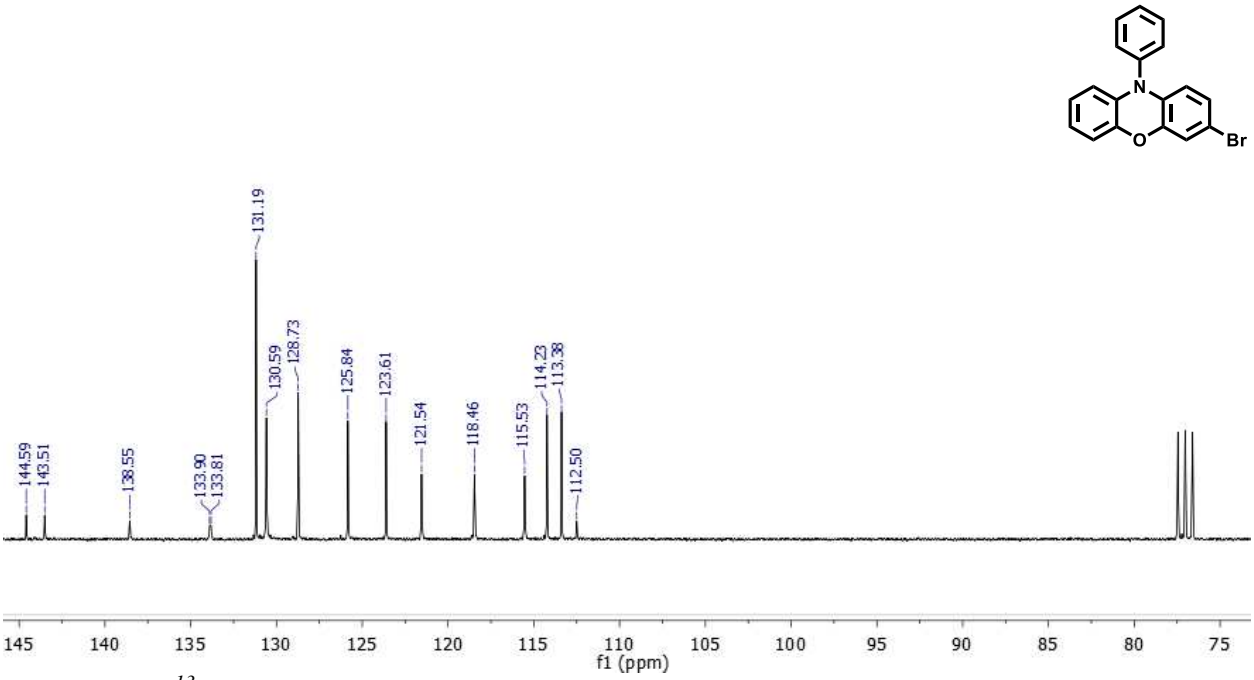

Figure 3.35. *^{13}C NMR of 3-bromo phenyl-10-phenoxazine ($CDCl_3$,75 MHz).*

Synthesis of 3-Phenyl Phenyl-10-Phenoxazine (7)

3-bromo phenyl-10-phenoxazine (0.170 g, 0.502 mmol, 1.00 equiv.) and phenyl boronic acid (0.122 g, 1.00 mmol, 2.00 equiv.) were added to a storage tube and cycled between vacuum and nitrogen three times before 4.00 mL of dried and degassed THF was added. Once all reagents were dissolved, 4.00 mL of a 2.00 M aqueous solution of K_2CO_3, which had been sparged with nitrogen, was added. In a separate Schlenk flask, palladiumtetrakis(triphenyl phosphine) (0.0464 g, 0.0402 mmol, 0.0800 equiv.) was dissolved in 4.00 mL of THF under inert atmosphere. The solution of $Pd(PPh_3)_4$ was then added to the reaction mixture and the reaction was heated at 100 °C for 48 h, before it was exposed to oxygen and allowed to cool to room temperature. The reaction mixture was concentrated under reduced pressure, diluted with DCM/hexanes, and passed through a short plug of silica. The solution was then moved to a separatory funnel, washed with de-ionized water once and brine twice. The solution was dried over magnesium sulfate, concentrated under

vacuum, and recrystallized using DCM/methanol at -25 °C. The product was collected via vacuum filtration as a white solid (0.127 g, 0.378 mmol, 75.2 % yield). ^{1}H NMR (C_6D_6, 400 MHz) δ 7.40 – 7.30 (m, 2H), 7.15 – 7.06 (m, 1H), 7.10 – 6.93 (m, 6H), 6.97 – 6.82 (m, 2H), 6.74 (ddd, *J* = 13.5, 8.1, 1.8 Hz, 2H), 6.43 (dtd, *J* = 31.9, 7.6, 1.5 Hz, 2H), 5.96 – 5.85 (m, 2H). ^{13}C NMR ($CDCl_3$, 75 MHz) δ 144.53, 144.17, 140.19, 139.11, 134.72, 134.35, 133.84, 130.76, 130.64, 128.67, 128.05, 126.64, 126.17, 123.33, 121.69, 121.54, 115.63, 114.24, 113.63, 113.46. HRMS (ESI): calculated for M+ $C_{24}H_{17}NO$ 335.1310; observed 335.1312.

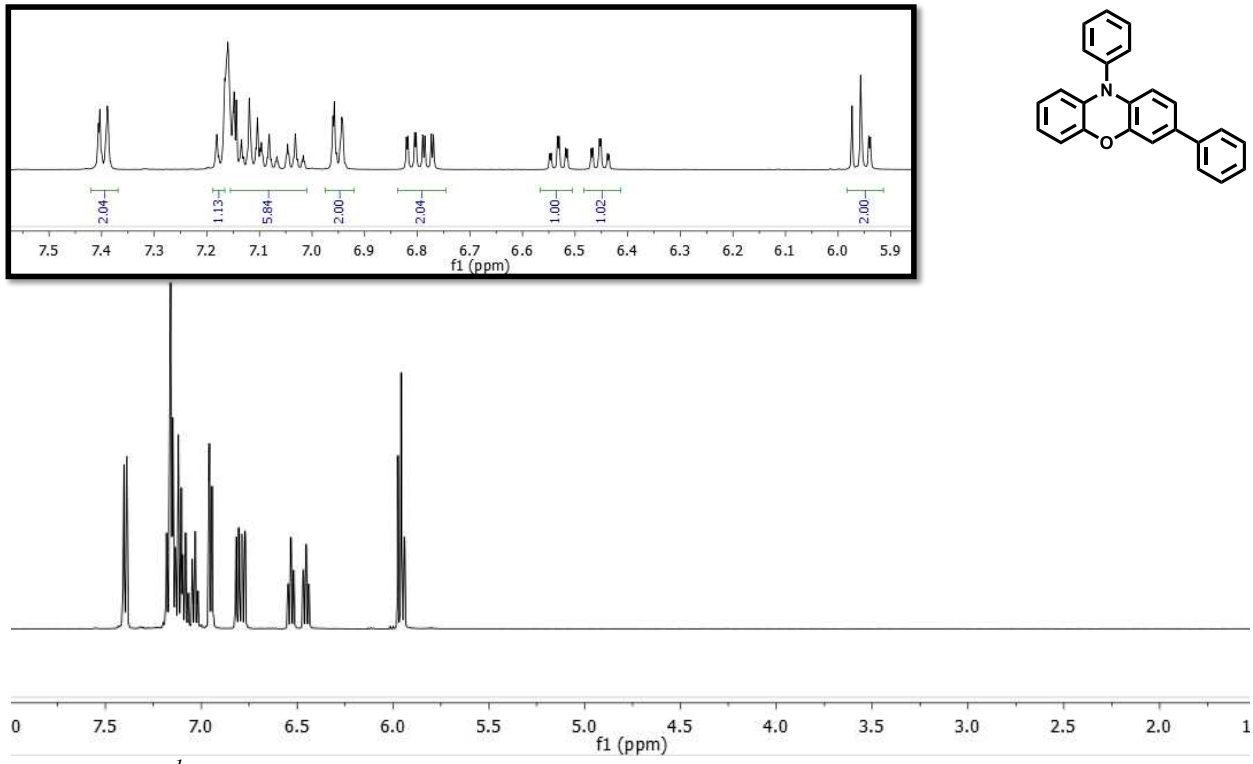

Figure 3.36. *^{1}H NMR of **7** (C_6D_6, 500 MHz).*

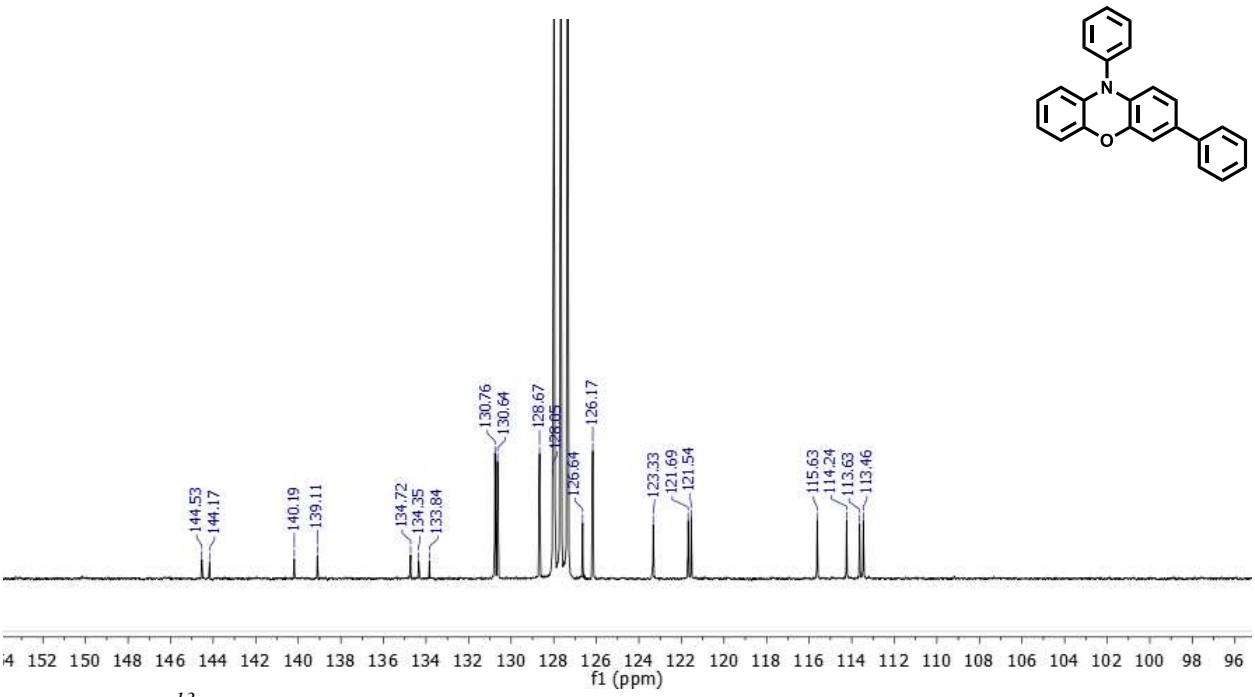

Figure 3.37. *^{13}C NMR of **7** (C_6D_6, 75 MHz).*

Synthesis of 3-(4-biphenyl) Phenyl-10-Phenoxazine (8)

3-bromo phenyl-10-phenoxazine (0.450 g, 0.133 mmol, 1.00 equiv.) and biphenyl boronic acid (0.395 g, 1.99 mmol, 1.50 equiv.) were added to a storage tube and cycled between vacuum and nitrogen three times before 30 mL of dried and degassed THF was added. Once all reagents were dissolved, 11.0 mL of a 2.00 M aqueous solution of K_2CO_3, which had been sparged with nitrogen, was added. In a separate Schlenk flask, palladiumtetrakis(triphenyl phosphine) (0.154 g, 0.133 mmol, 0.100 equiv.) was dissolved in 30.0 mL of THF under inert atmosphere. The solution of $Pd(PPh_3)_4$ was then added to the reaction mixture and the reaction was heated at 100 °C for 24 hours, before it was exposed to oxygen and allowed to cool to room temperature. The reaction mixture was concentrated under reduced pressure, diluted with DCM/hexanes, and passed through a short plug of silica. The solution was then moved to a separatory funnel, washed with de-ionized water once and brine twice. The solution was dried over magnesium sulfate, concentrated under vacuum, and recrystallized using DCM/methanol at -25 °C. The product was collected via vacuum

filtration as a light yellow solid (0.506 g, 1.23 mmol, 92.5% yield). ^{1}H NMR (C_6D_6, 500 MHz) δ 7.54 – 7.49 (m, 2H), 7.46 (d, *J* = 3.2 Hz, 4H), 7.25 (t, *J* = 7.7 Hz, 2H), 7.21 (d, *J* = 2.1 Hz, 1H), 7.13 (d, *J* = 7.9 Hz, 2H), 7.08 – 7.02 (m, 1H), 7.00 – 6.96 (m, 2H), 6.84 (dt, *J* = 8.2, 1.7 Hz, 2H), 6.51 (dtd, *J* = 40.8, 7.6, 1.5 Hz, 2H), 6.01 (d, *J* = 8.3 Hz, 1H), 5.97 (dd, *J* = 7.9, 1.5 Hz, 1H). ^{13}C NMR (C_6D_6, 75 MHz) δ 144.59, 144.19, 140.97, 139.68, 139.10, 139.02, 134.32, 134.18, 133.94, 130.79, 130.64, 128.71, 128.09, 127.48, 127.05, 126.95, 126.50, 123.37, 121.63, 121.60, 115.65, 114.10, 113.68, 113.50. HRMS (ESI): calculated for M+ $C_{30}H_{21}NO$ 411.1623; observed 411.1627.

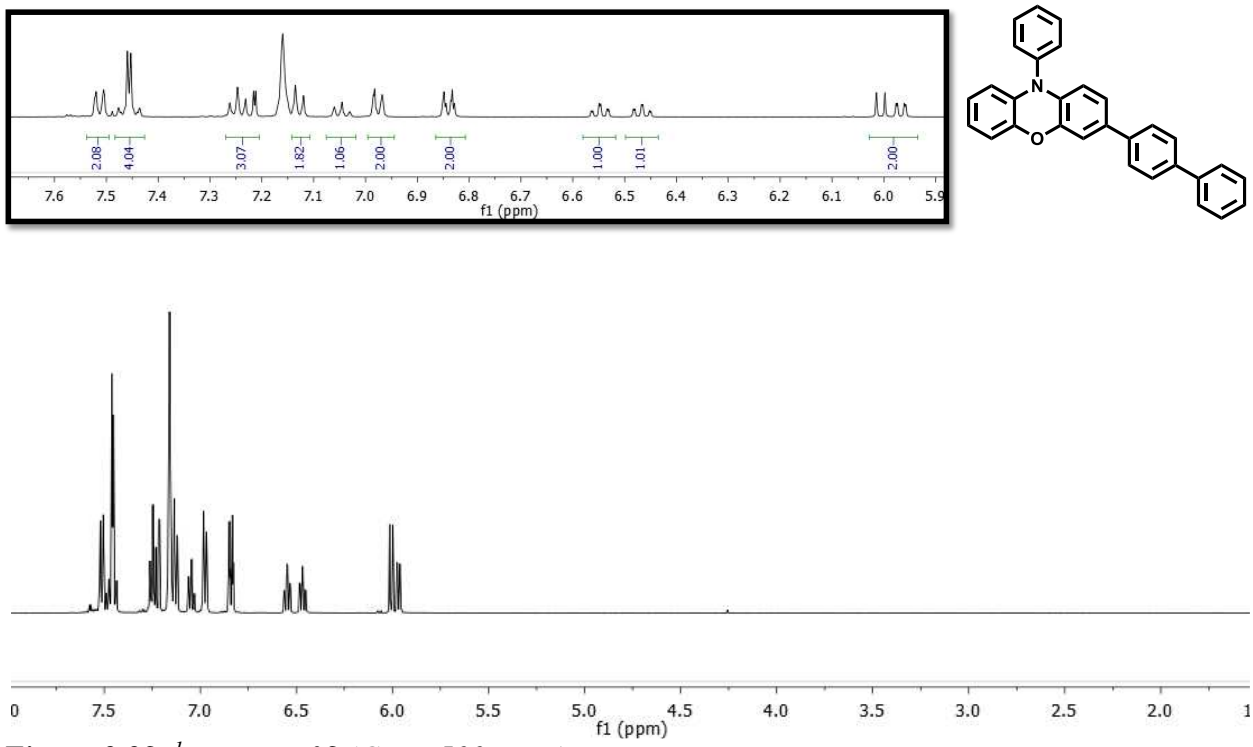

Figure 3.38. *^{1}H NMR of* ***8*** *(C_6D_6, 500 MHz).*

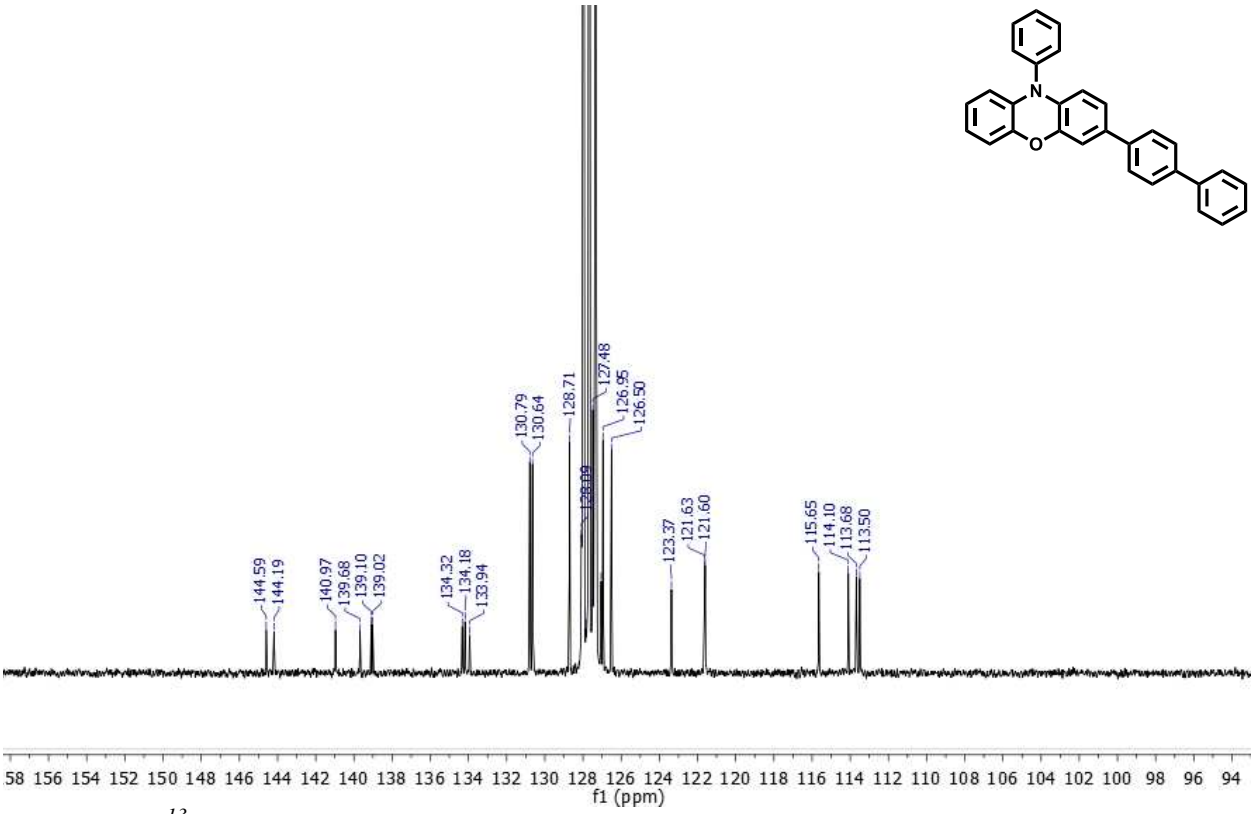

Figure 3.39 *^{13}C NMR of* ***8*** *(C_6D_6, 75 MHz).*

Synthesis of 3-(4-methoxyphenyl) Phenyl-10-Phenoxazine (18)

3-bromo phenyl-10-phenoxazine (0.170 g, 0.502 mmol, 1.00 equiv.) and 4-methoxyphenyl boronic acid (0.153 g, 1.00 mmol, 2.00 equiv.) were added to a storage tube and cycled between vacuum and nitrogen three times before 4.00 mL of dried and degassed THF was added. Once all reagents were dissolved, 4.00 mL of a 2.00 M aqueous solution of K_2CO_3, which had been sparged with nitrogen, was added. In a separate Schlenk flask, palladiumtetrakis(triphenyl phosphine) (0.0464 g, 0.0402 mmol, 0.0800 equiv.) was dissolved in 4.00 mL of THF under inert atmosphere. The solution of $Pd(PPh_3)_4$ was then added to the reaction mixture and the reaction was heated at 100 °C for 48 h, before it was exposed to oxygen and allowed to cool to room temperature. The reaction mixture was concentrated under reduced pressure, diluted with DCM/hexanes, and passed through a short plug of silica. The solution was then moved to a separatory funnel, washed with de-ionized water once and brine twice. The solution was dried over magnesium sulfate,

concentrated under vacuum, and recrystallized using DCM/methanol at -25 °C. The product was collected via vacuum filtration as a white solid (0.140 g, 0.378 mmol, 76.0 % yield). ^{1}H NMR (C_6D_6, 500 MHz) δ 7.37 – 7.31 (m, 2H), 7.13 (td, *J* = 7.4, 6.7, 1.2 Hz, 2H), 7.07 – 7.01 (m, 1H), 7.00 – 6.94 (m, 2H), 6.83 (dd, *J* = 7.8, 1.5 Hz, 1H), 6.80 – 6.76 (m, 3H), 6.54 (td, *J* = 7.6, 1.5 Hz, 1H), 6.46 (td, *J* = 7.7, 1.5 Hz, 1H), 6.00 (d, *J* = 8.3 Hz, 1H), 5.97 (dd, *J* = 7.9, 1.5 Hz, 1H), 3.31 (s, 3H). ^{13}C NMR (C_6D_6, 75 MHz) δ 159.08, 144.53, 144.20, 139.25, 134.61, 134.46, 133.30, 132.77, 130.75, 130.69, 127.22, 123.32, 121.45, 121.24, 115.63, 114.23, 113.92, 113.69, 113.44, 54.46. HRMS (ESI): calculated for M+ $C_{25}H_{19}NO_2$ 365.1416; observed 365.1418.

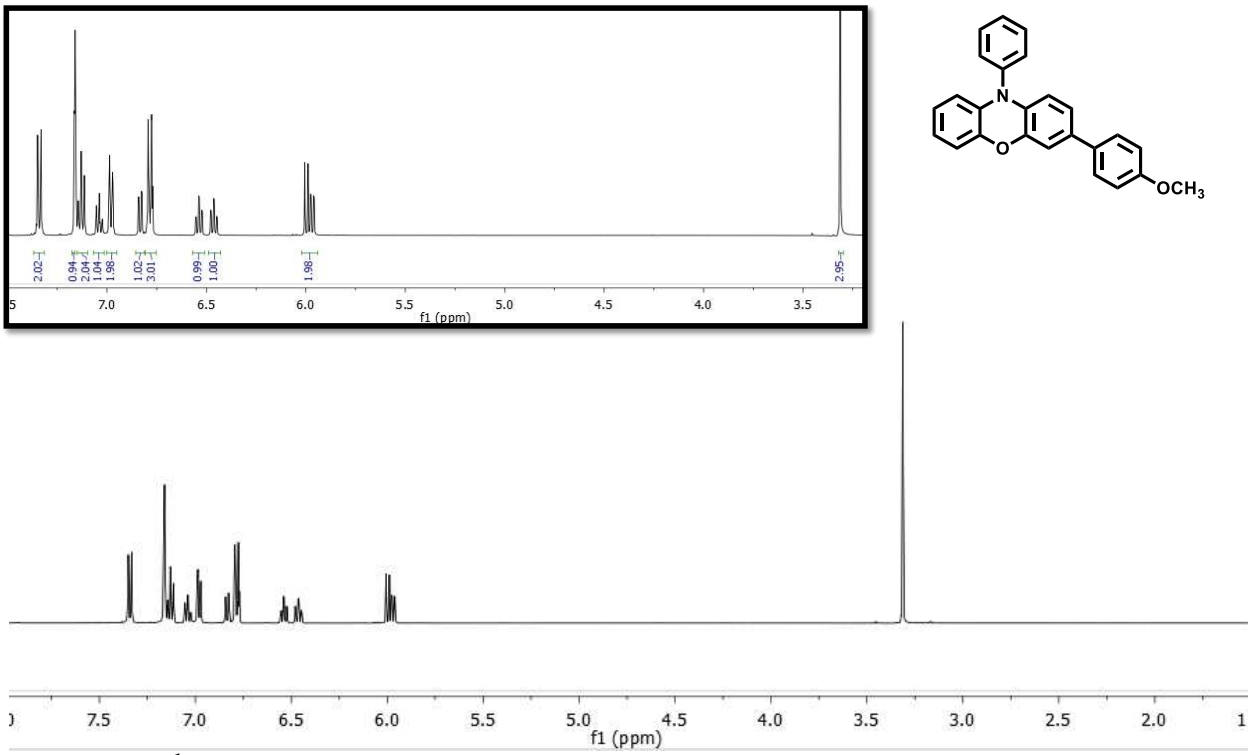

Figure 3.40. *^{1}H NMR of **18** (C_6D_6, 500 MHz).*

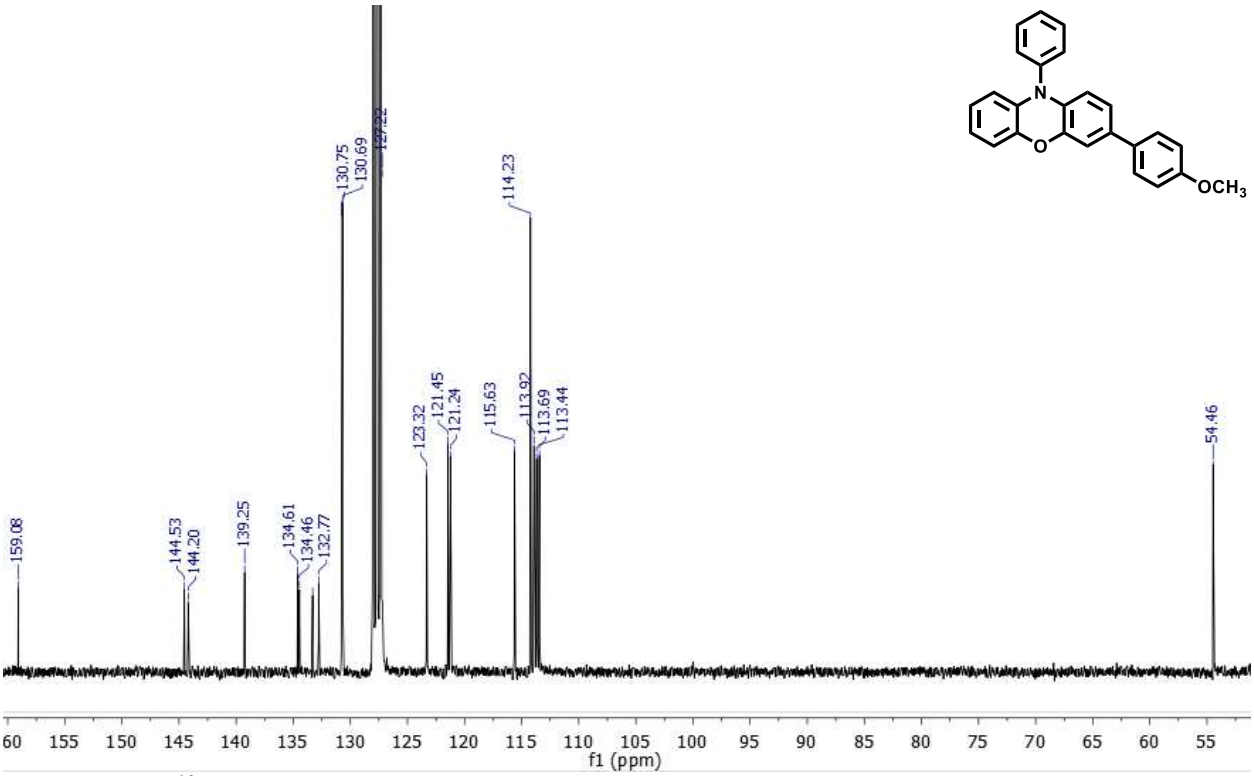

Figure 3.41. *^{13}C NMR of* ***18*** *(C_6D_6, 75 MHz).*

Synthesis of 3-(4-trifluoromethylphenyl) Phenyl-10-Phenoxazine (19)

3-bromo phenyl-10-phenoxazine (0.170 g, 0.502 mmol, 1.00 equiv.) and 4-methoxyphenyl boronic acid (0.191 g, 1.00 mmol, 2.00 equiv.) were added to a storage tube and cycled between vacuum and nitrogen three times before 4.00 mL of dried and degassed THF was added. Once all reagents were dissolved, 4.00 mL of a 2.00 M aqueous solution of K_2CO_3, which had been sparged with nitrogen, was added. In a separate Schlenk flask, palladiumtetrakis(triphenyl phosphine) (0.0464 g, 0.0402 mmol, 0.0800 equiv.) was dissolved in 4.00 mL of THF under inert atmosphere. The solution of $Pd(PPh_3)_4$ was then added to the reaction mixture and the reaction was heated at 100 °C for 48 h, before it was exposed to oxygen and allowed to cool to room temperature. The reaction mixture was concentrated under reduced pressure, diluted with DCM, and passed through a short plug of silica. The solution was then moved to a separatory funnel, washed with de-ionized water once and brine twice. The solution was dried over magnesium sulfate, concentrated under

vacuum, and recrystallized using DCM/methanol at -25 °C. The product was collected via vacuum filtration as a white solid (0.0916 g, 0.378 mmol, 45.0 % yield). ^{1}H NMR (C_6D_6, 500 MHz) δ 7.32 (d, *J* = 8.1 Hz, 2H), 7.13 (dd, *J* = 8.0, 6.2 Hz, 4H), 6.98 (d, *J* = 2.0 Hz, 1H), 6.96 – 6.93 (m, 3H), 6.83 (dt, *J* = 7.8, 1.2 Hz, 1H), 6.61 (dd, *J* = 8.3, 2.0 Hz, 1H), 6.54 (tt, *J* = 7.7, 1.2 Hz, 1H), 6.46 (tt, *J* = 7.8, 1.2 Hz, 1H), 5.97 – 5.91 (m, 2H). ^{13}C NMR (C_6D_6, 75 MHz) δ 144.58, 144.03, 143.36, 138.81, 134.68, 134.04, 132.70, 130.86, 130.51, 128.62, 128.25, 128.20, 126.62, 126.16, 125.54, 123.50, 121.93, 121.84, 115.62, 114.19, 113.60, 113.57.^{19}F NMR (C6D6, 300 MHz) δ 62.01. HRMS (ESI): calculated for M+ $C_{25}H_{16}F_3NO$ 403.1184; observed 403.1184.

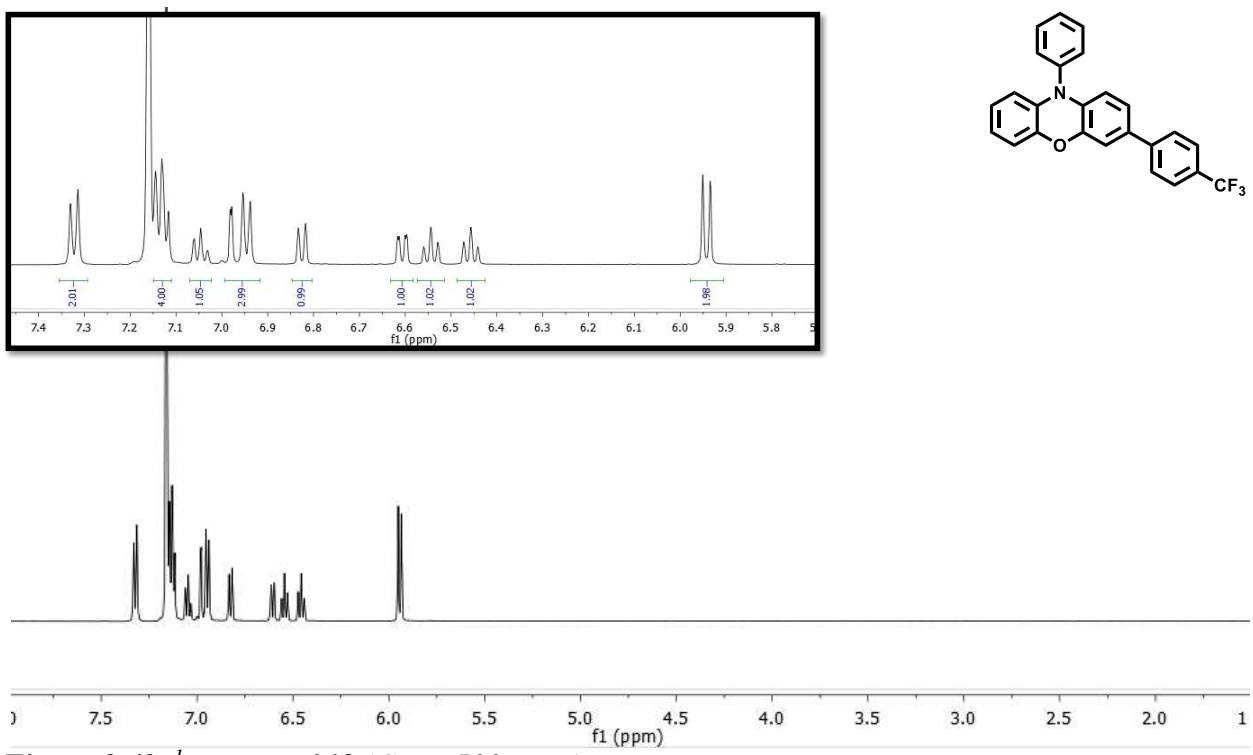

Figure 3.42. *^{1}H NMR of **19** (C_6D_6, 500 MHz).*

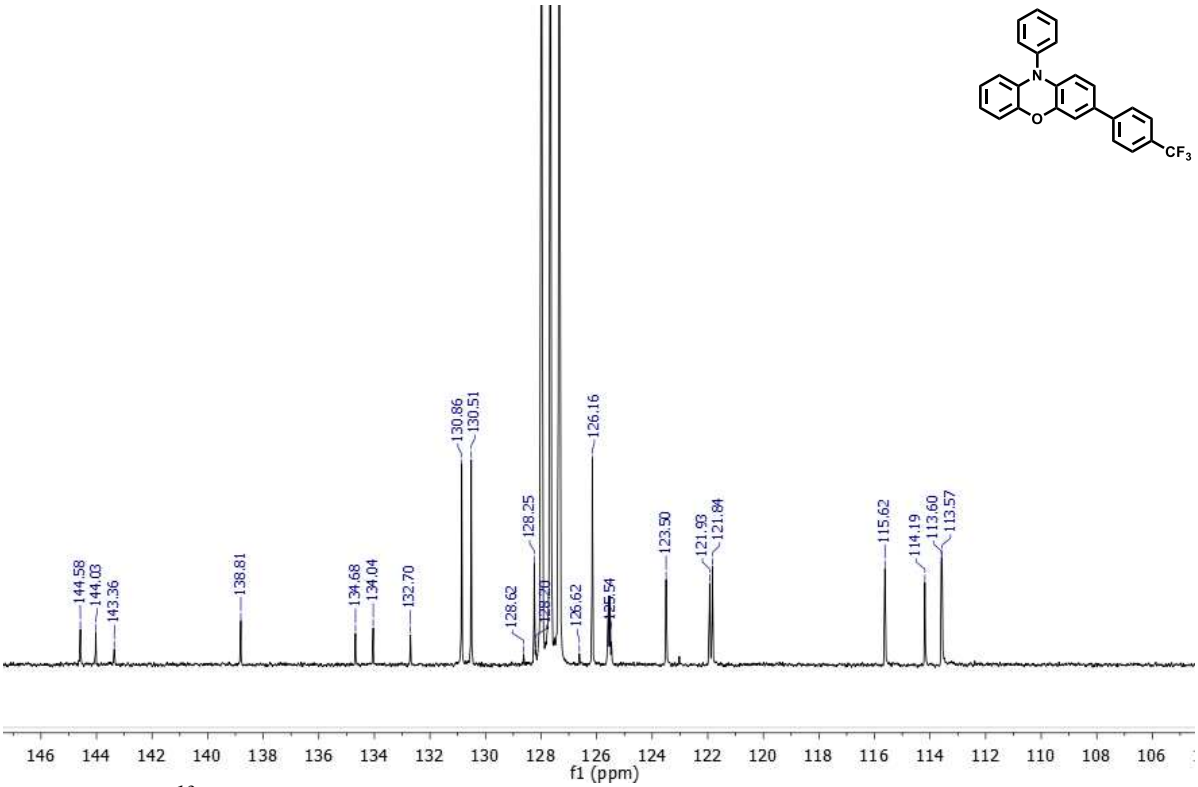

Figure 3.43. *^{13}C NMR of **19** (C_6D_6, 75 MHz).*

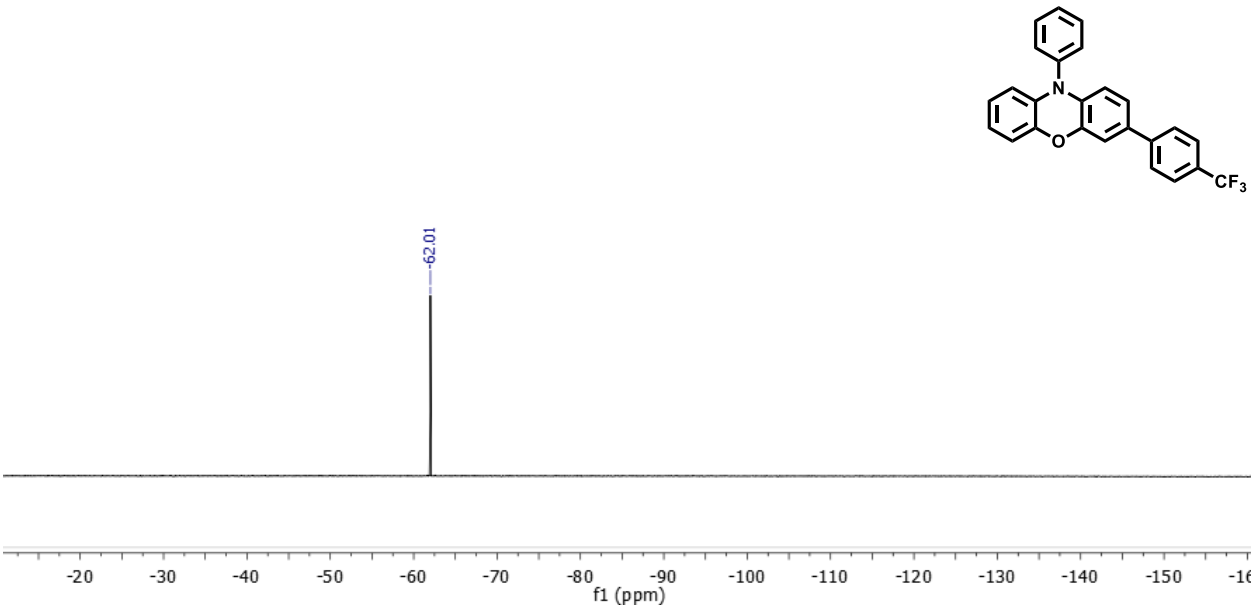

Figure 3.44. *^{19}F NMR of **19** (C_6D_6, 75 MHz).*

Synthesis of 3,7-Dibromo Phenyl-10-Phenoxazine

Phenyl-10-phenoxazine (0.600 g, 2.33 mmol, 1.00 equiv.) was solvated in 60.0 mL of chloroform and 60.0 mL of acetic acid to which NBS (0.851 g, 4.78 mmol, 2.05 equiv.) was added portion-wise over twenty minutes. The reaction was allowed to run for three hours at room temperature before de-ionized water and saturated sodium bicarbonate solution were added and allowed to stir for fifteen minutes. Organic solvent was removed under reduced pressure before the reaction mixture was diluted with DCM. The organic layer was washed twice with de-ionized water, washed once with brine, dried over magnesium sulfate, and concentrated under vacuum. The resulting solid was recrystallized from DCM/hexanes at -25 °C to afford to product in 67.0% yield. ^{1}H NMR ($CDCl_3$, 500 MHz) δ 7.67 – 7.56 (m, 2H), 7.55 – 7.47 (m, 1H), 7.33 – 7.28 (m, 2H), 6.83 (d, *J* = 2.2 Hz, 2H), 6.71 (dd, *J* = 8.6, 2.2 Hz, 2H), 5.76 (d, *J* = 8.6 Hz, 2H). ^{13}C NMR (C_6D_6, 75 MHz) δ 144.10, 138.13, 133.27, 131.33, 130.35, 128.98, 126.25, 118.61, 114.39, 112.82. HRMS (ESI): calculated for M+ $C_{18}H_{11}Br_2NO$, 416.9188; observed 416.9181.

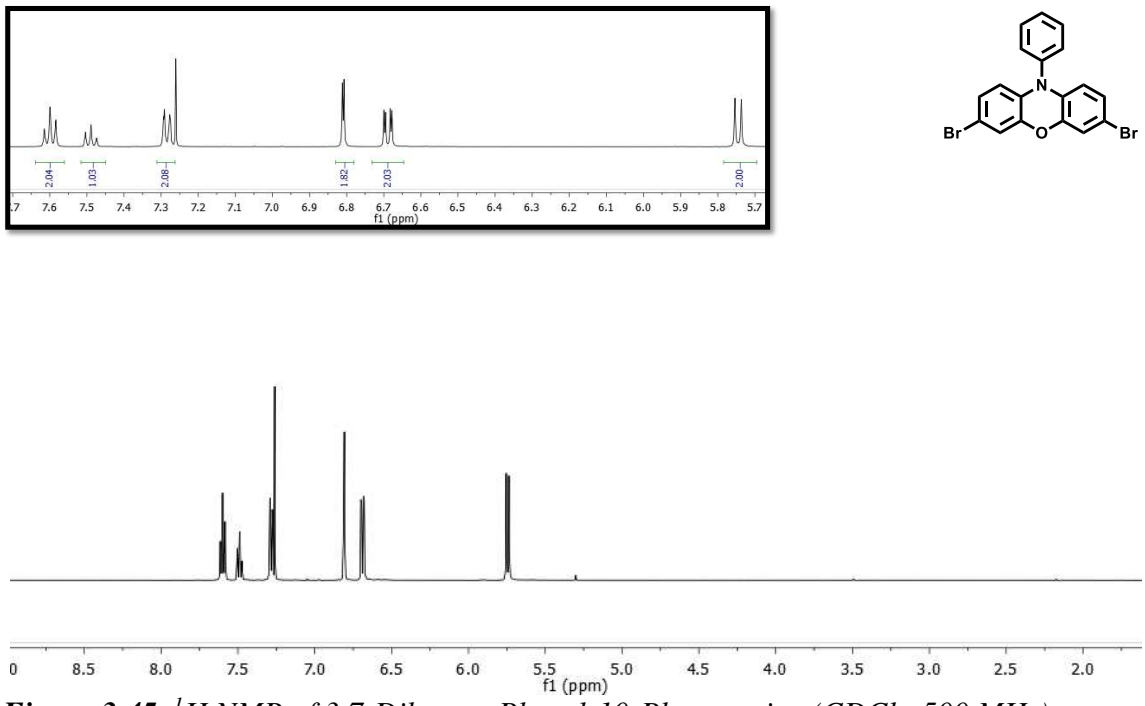

Figure 3.45. *^{1}H NMR of 3,7-Dibromo Phenyl-10-Phenoxazine ($CDCl_3$, 500 MHz).*

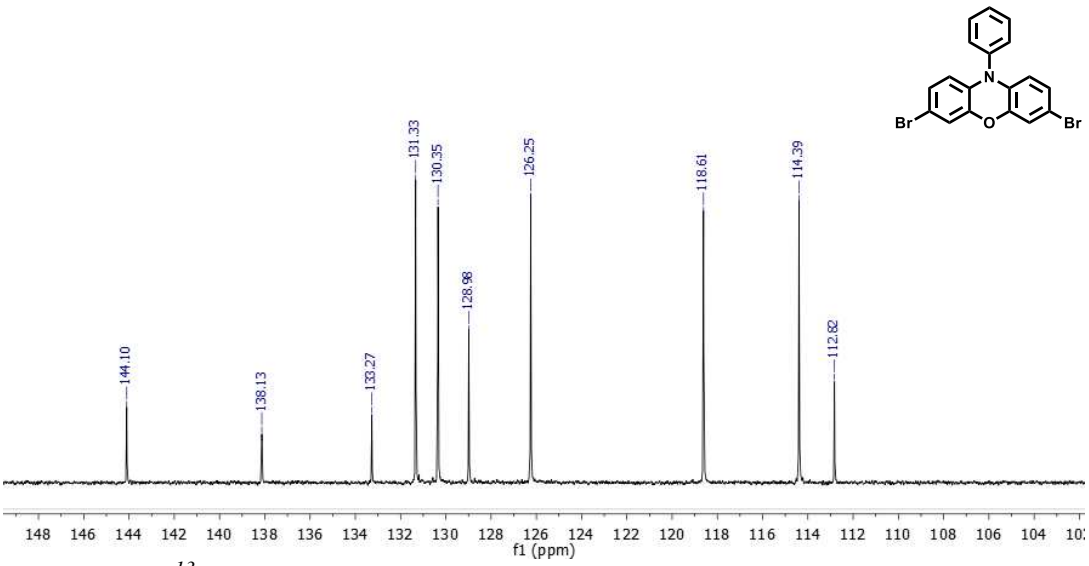

Figure 3.46. *^{13}C NMR of 3,7-Dibromo Phenyl-10-Phenoxazine ($CDCl_3$, 75 MHz).*

Synthesis of 3,7-Di(4-biphenyl) Phenyl-10-Phenoxazine (9)

3,7-dibromo phenyl-10-phenoxazine (0.312 g, 0.749 mmol, 1.00 equiv.) and biphenyl boronic acid (0.519 g, 2.62 mmol, 3.50 equiv.) were cycled under vacuum and nitrogen three times before being dissolved in 4.00 mL of dry and degassed THF. Then 4.00 mL of a sparged 2.00 M K_2CO_3 solution was added to the flask. In a separate Schlenk flask, palladiumtetrakis(triphenyl phosphine) (0.0866 g, 0.0749 mmol, 0.100 equiv.) was dissolved in 4.00 mL of THF under inert atmosphere. The solution of $Pd(PPh_3)_4$ was then added to the reaction flask and it was heated to100 °C for 24 h before it was allowed to cool to room temperature and exposed to oxygen. The reaction mixture was concentrated under reduced pressure, diluted with DCM/Hexanes, and passed through a short plug of silica gel. The solution was then moved to a separatory funnel, washed with de-ionized water three times and brine one time. The solution was dried over magnesium sulfate, concentrated under vacuum, and recrystallized using DCM/methanol at -25 °C. The product was collected as a yellow solid in 83.5% yield. ^1H NMR (C_6D_6, 500 MHz) δ 7.70 – 7.61 (m, 6H), 7.59

(s, 8H), 7.40 (d, *J* = 2.1 Hz, 2H), 7.36 (t, *J* = 7.7 Hz, 4H), 7.31 – 7.27 (m, 2H), 7.21 – 7.14 (m, 3H), 6.98 (dd, *J* = 8.3, 2.1 Hz, 2H), 6.17 (d, *J* = 8.3 Hz, 2H). ^{13}C NMR (75 MHz, C_6D6) δ 144.54, 140.96, 139.79, 139.02, 134.45, 133.66, 130.86, 130.58, 128.73, 127.54, 127.09, 126.96, 126.57, 121.76, 114.22, 113.80. HRMS (ESI): calculated for M+ $C_{42}H_{29}NO$, 563.2249; observed 563.2238.

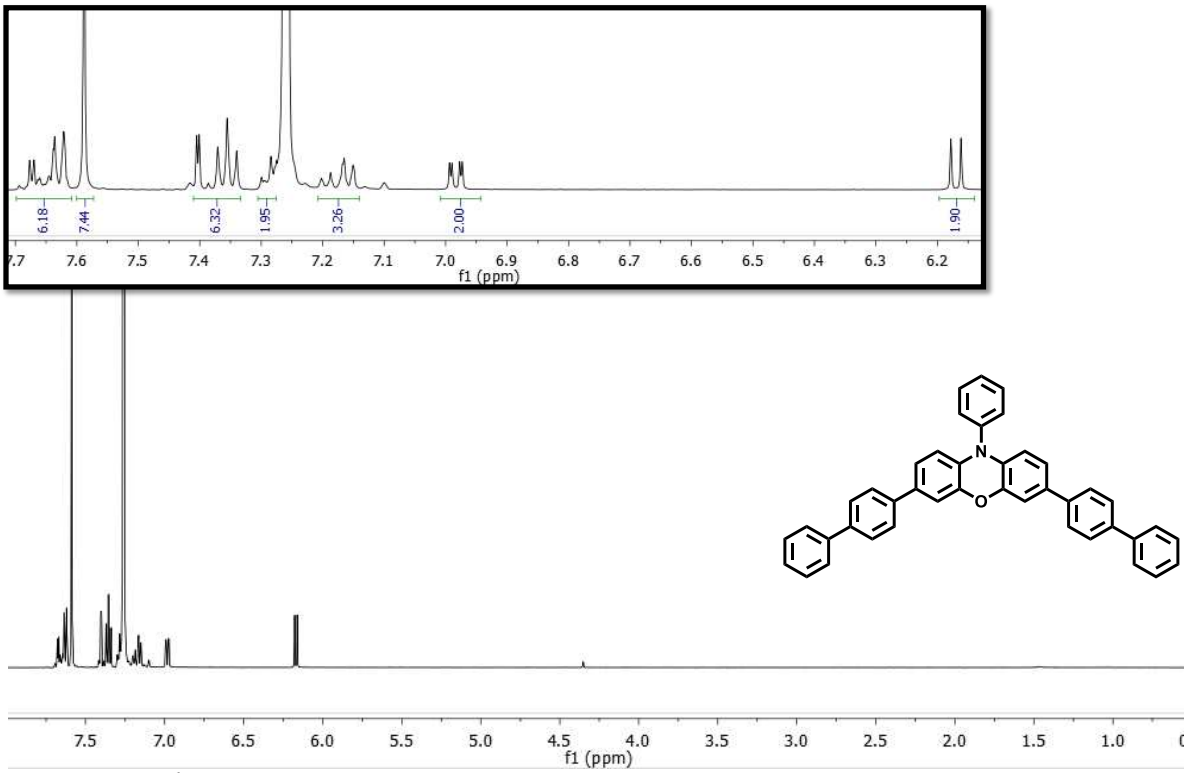

Figure 3.47. *^{1}H NMR of **9** (C_6D_6, 500 MHz).*

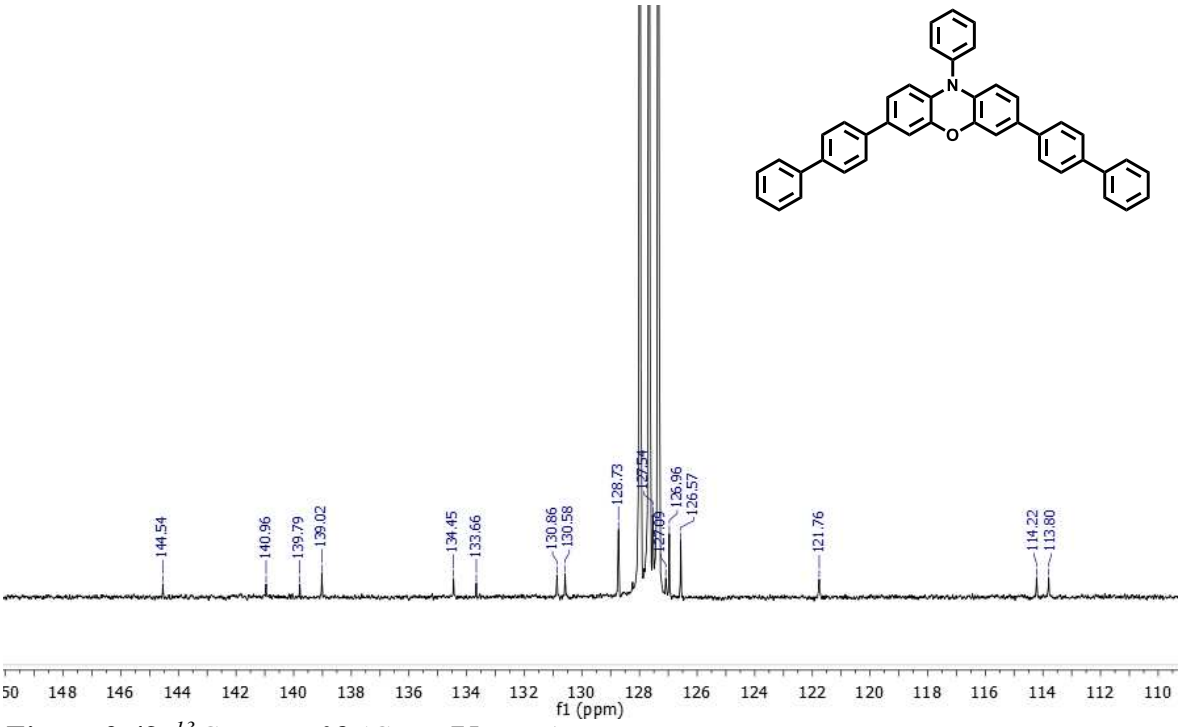

Figure 3.48. *^{13}C NMR of **9** (C_6D_6, 75 MHz).*

3. Control Experiments

Table 3.3. *Control experiments omitting photocatalyst, initiator, or light are shown.*

[MMA]:[DBMM]:[PC]	PC	Time (h)	Light Source	Conv. (%)	M_n (kDa)	M_w (kDa)	$Đ$
1000:10:1	**16**	7	none	9.1	353.6	701.9	1.99
1000:10:1	**14**	7	none	2.9	644.7	1095	1.70
1000:10:1	**5**	7	none	0.0	N/A	N/A	N/A
1000:0:1	**16**	7	White LED	11.5	222.3	381.4	1.72
1000:0:1	**14**	7	White LED	2.9	27.4	49.3	1.80
1000:0:1	**5**	7	White LED	25.9	136.5	243.3	1.78
1000:10:1	**8**	7	none	2.0	888	1,426	1.61
1000:0:1	**8**	7	White LED	31.5	193.1	310.3	1.61
1000:10:0	No PC	7	White LEDs	14.5	231.0	404.2	1.75

4. General Method for Polymer Synthesis

Method using White LEDs: Phenoxazine photoredox catalysts were weighed into a 20 mL scintillation vial equipped with a stir bar and brought into a nitrogen-filled glovebox. Monomer and solvent were added, and the solution was stirred for one minute. Initiator was added, and the reaction vessel was covered while an LED beaker was set up on a magnetic stirring plate. The reaction vessel was placed in the center of the LED beaker and the initial time for the start of the polymerization was noted. All polymerizations were performed at a ratio of 1000:10:1 of monomer: initiator: catalyst with 9.35 $\times 10^{-6}$ moles of catalyst and a 1:1 ratio of solvent: monomer by volume unless otherwise noted.

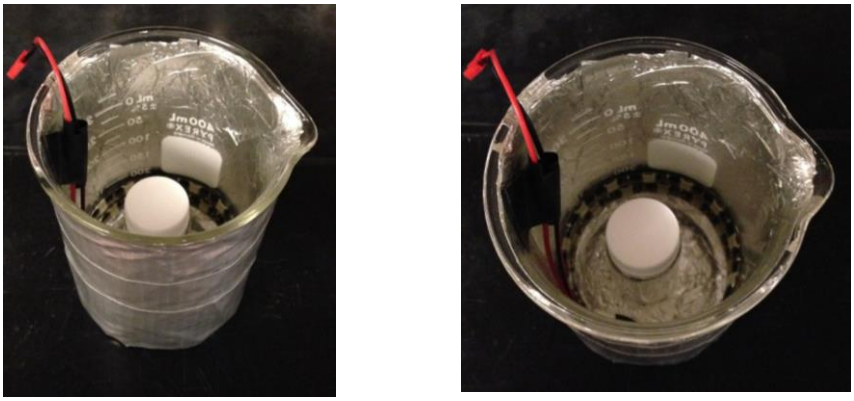

Figure 3.49. *Photograph of the LED beaker setup used for polymerization reactions from the side (left) and top (right) viewpoints.*

Method using UV-Nail Apparatus: Polymerizations performed using the UV nail curing apparatus were carried out according to a previously published procedure.[5g]

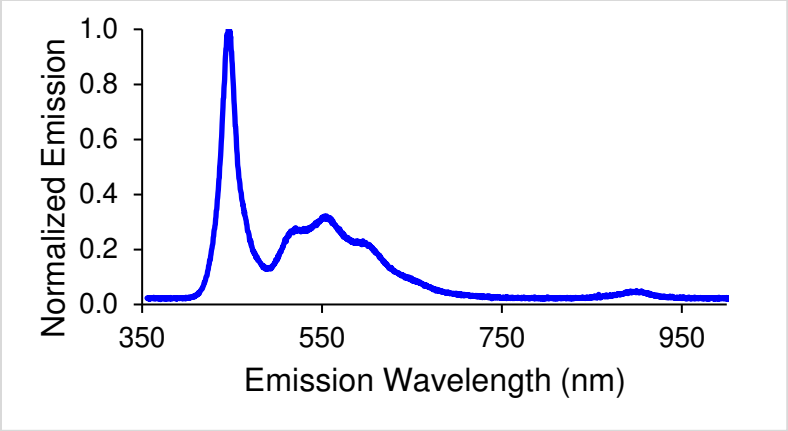

Figure 3.50. *Emission spectra of the white light LED beakers used for O-ATRP.*

5. General Method for Analysis of Kinetics and Molecular Weight Growth

To evaluate the kinetics and growth of molecular weight versus conversion for each polymerization, an aliquot of 0.1 mL of reaction mixture was taken and injected into a solution of chloroform containing the radical inhibitor, butylated hydroxyl toluene (BHT), at the exact time after the start of the polymerization (when the reaction mixture was exposed to light) as indicated. The aliquot was analyzed by ^{1}H NMR spectroscopy to determine the percent conversion at that time. After NMR analysis, the sample was dried under reduced pressure, re-dissolved in tetrahydrofuran, and analyzed by GPC.

6. Characterization of Catalyst Properties

Cyclic Voltammetry

General Procedure

Cyclic voltammograms of the photoredox catalysts were performed in a 3-compartment electrochemical cell with Ag/ $AgNO_3$ (0.01 M) in MeCN as the reference electrode, NBu_4PF_6 in DMAc (0.100 M) as the electrolyte solution, and platinum for the working and counter electrodes.

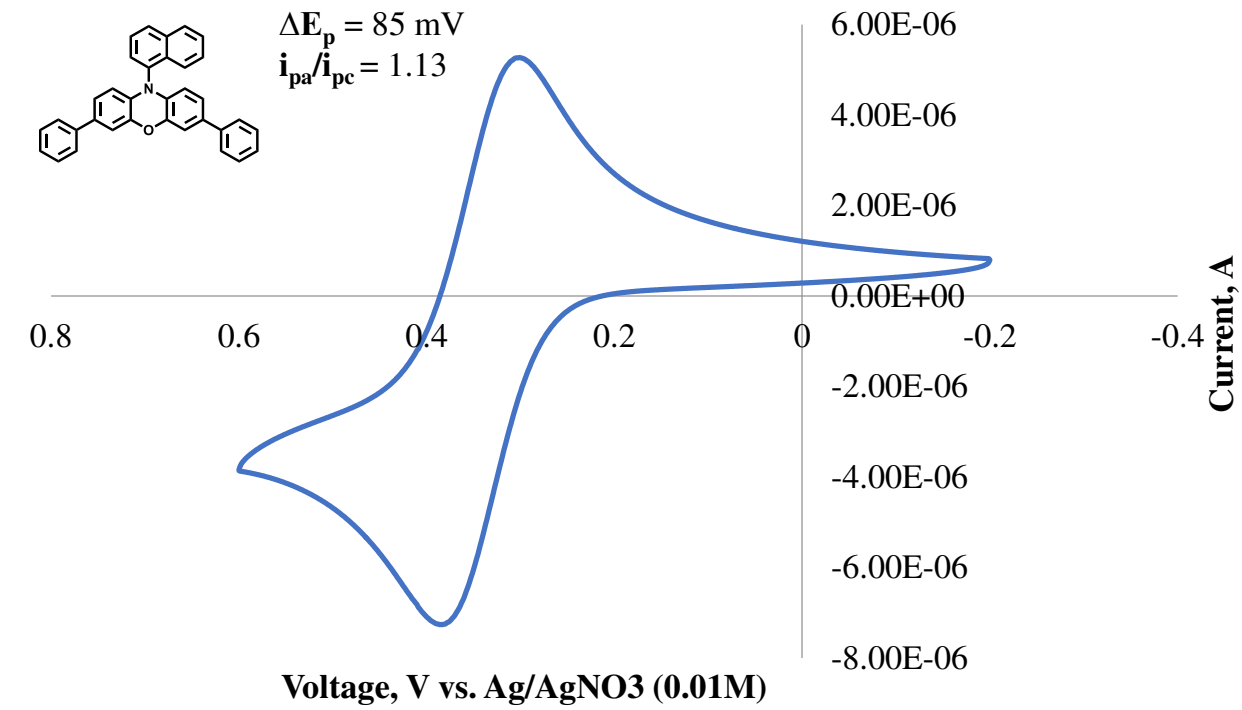

Figure 3.51. *Cyclic voltammogram* ***10*** *of acquired with a scan rate of 0.05 V/s.*

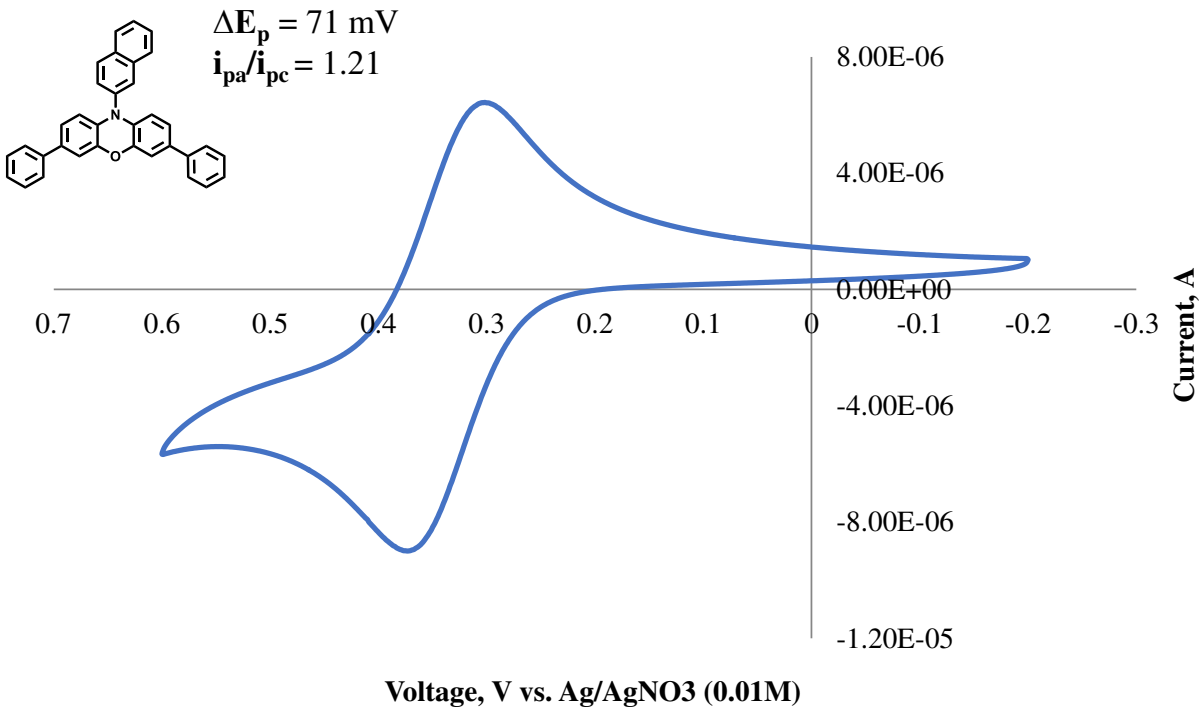

Figure 3.52. *Cyclic voltammogram* ***4*** *of acquired with a scan rate of 0.05 V/s.*

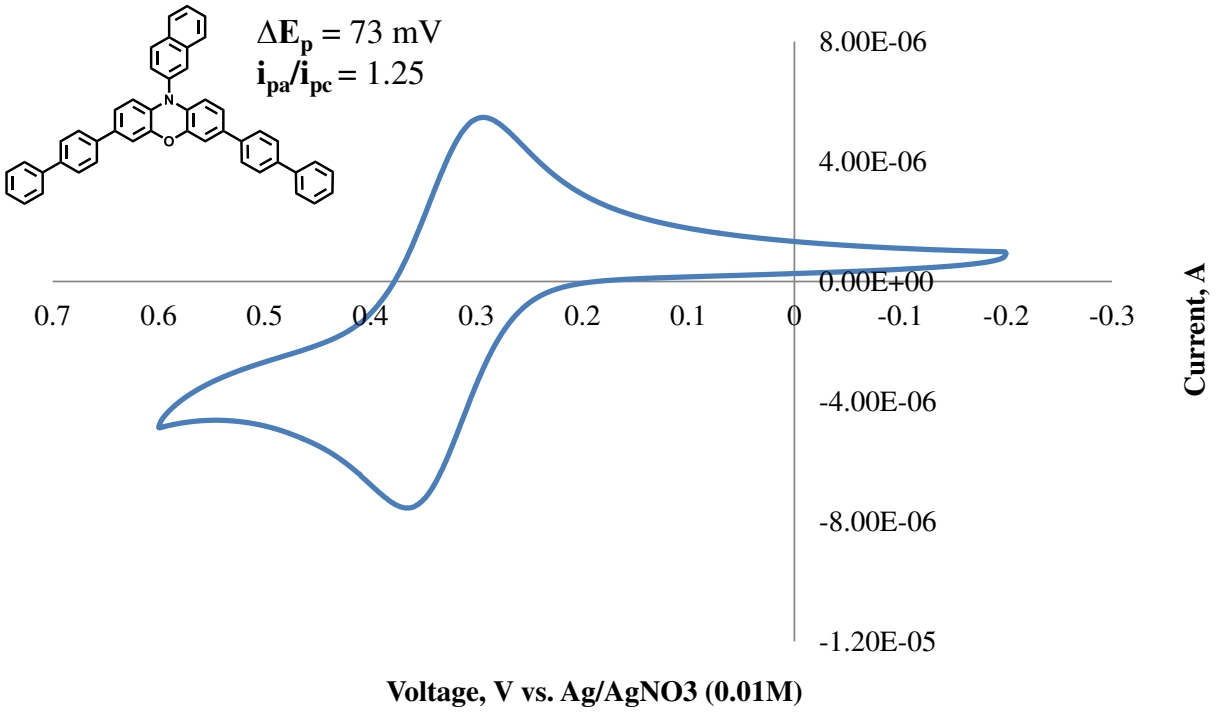

Figure 3.53. *Cyclic voltammogram* ***5*** *of acquired with a scan rate of 0.05 V/s.*

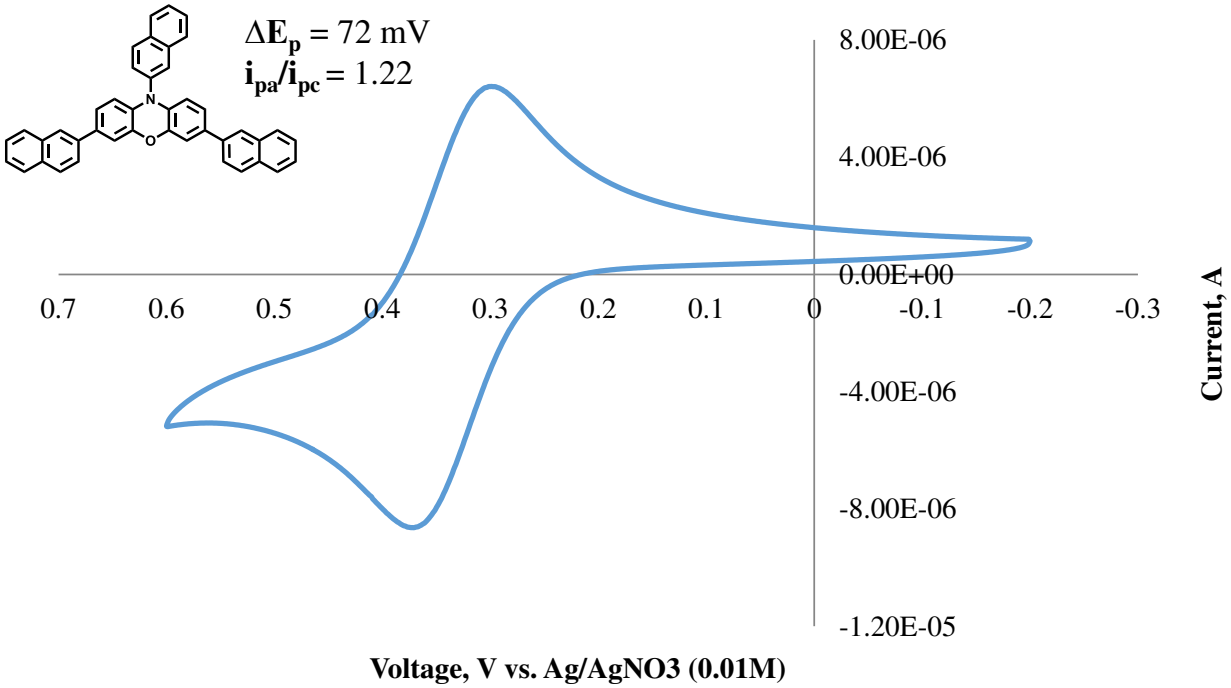

Figure 3.54. *Cyclic voltammogram* ***17*** *of acquired with a scan rate of 0.05 V/s.*

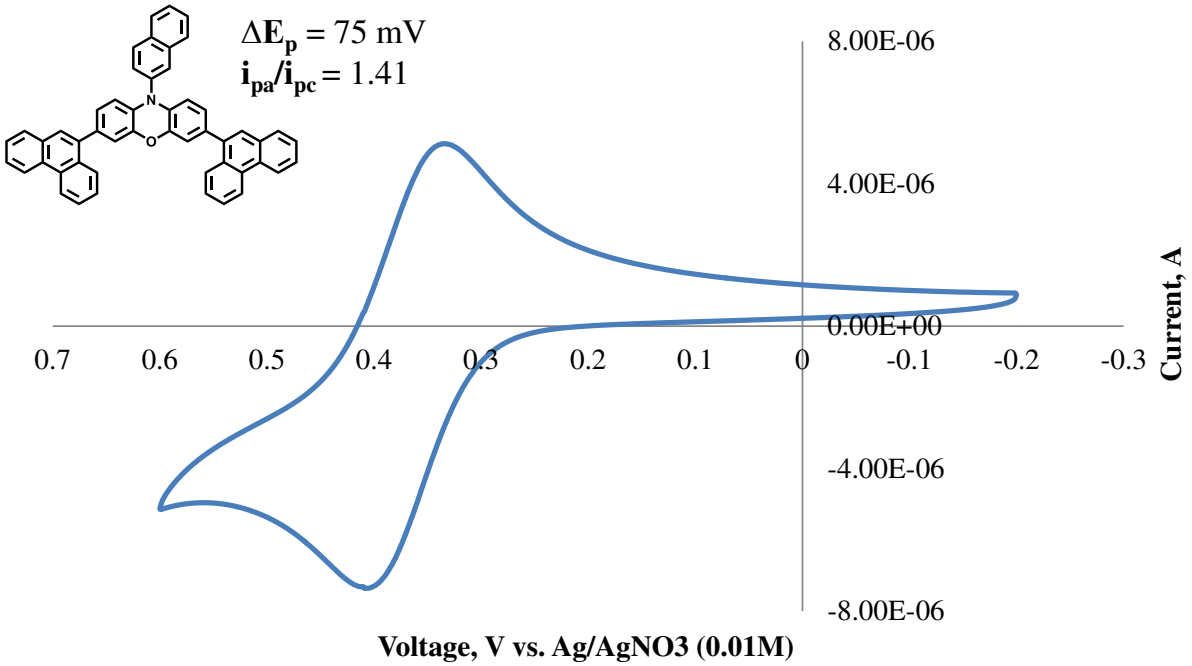

Figure 3.55. *Cyclic voltammogram* ***15*** *of acquired with a scan rate of 0.05 V/s.*

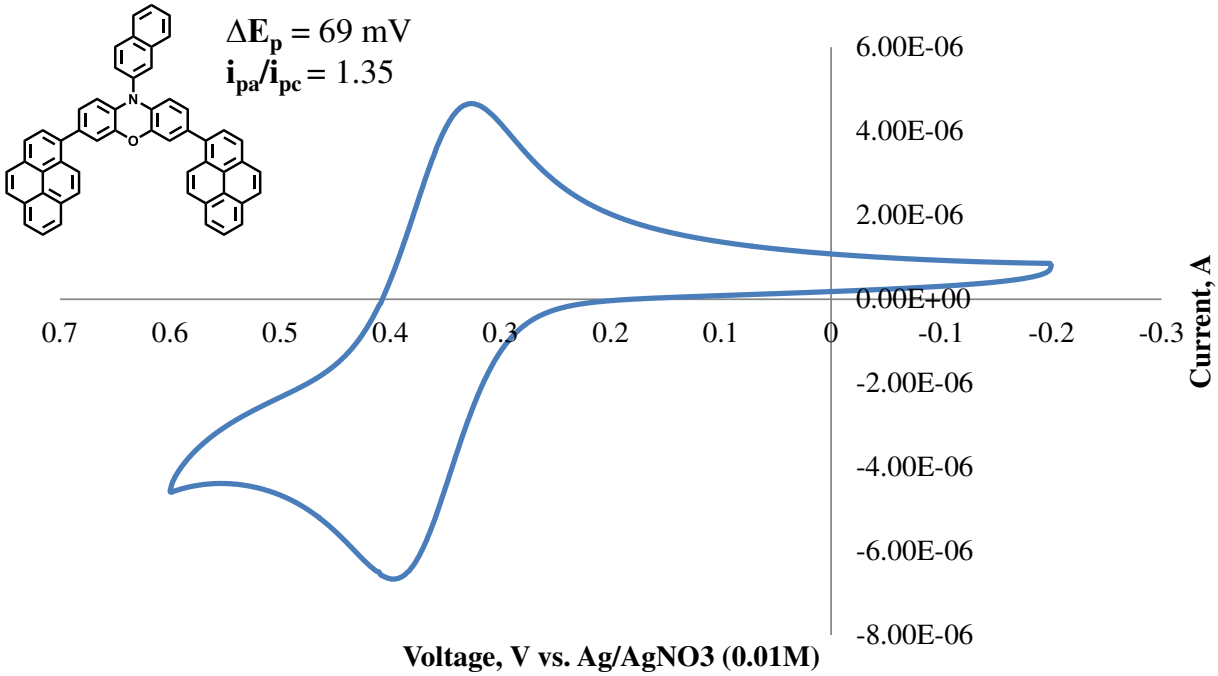

Figure 3.56. *Cyclic voltammogram* ***16*** *of acquired with a scan rate of 0.05 V/s.*

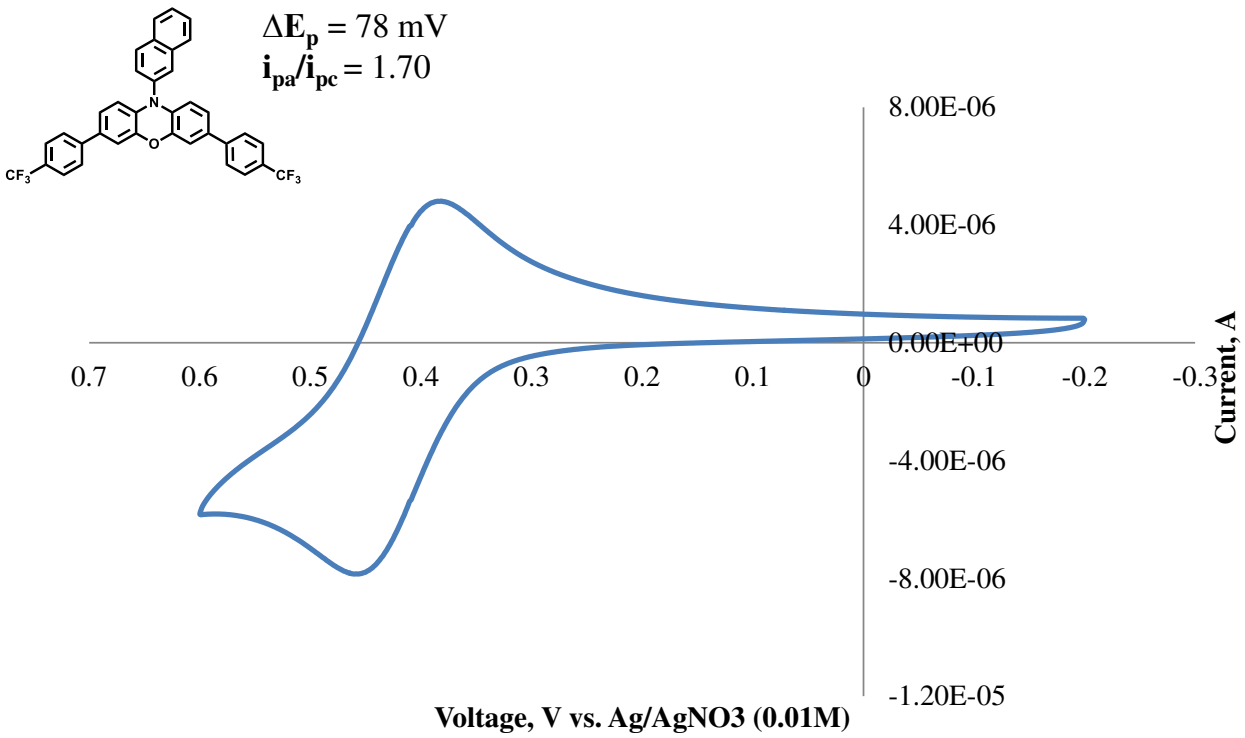

Figure 3.57. *Cyclic voltammogram* ***13*** *of acquired with a scan rate of 0.05 V/s.*

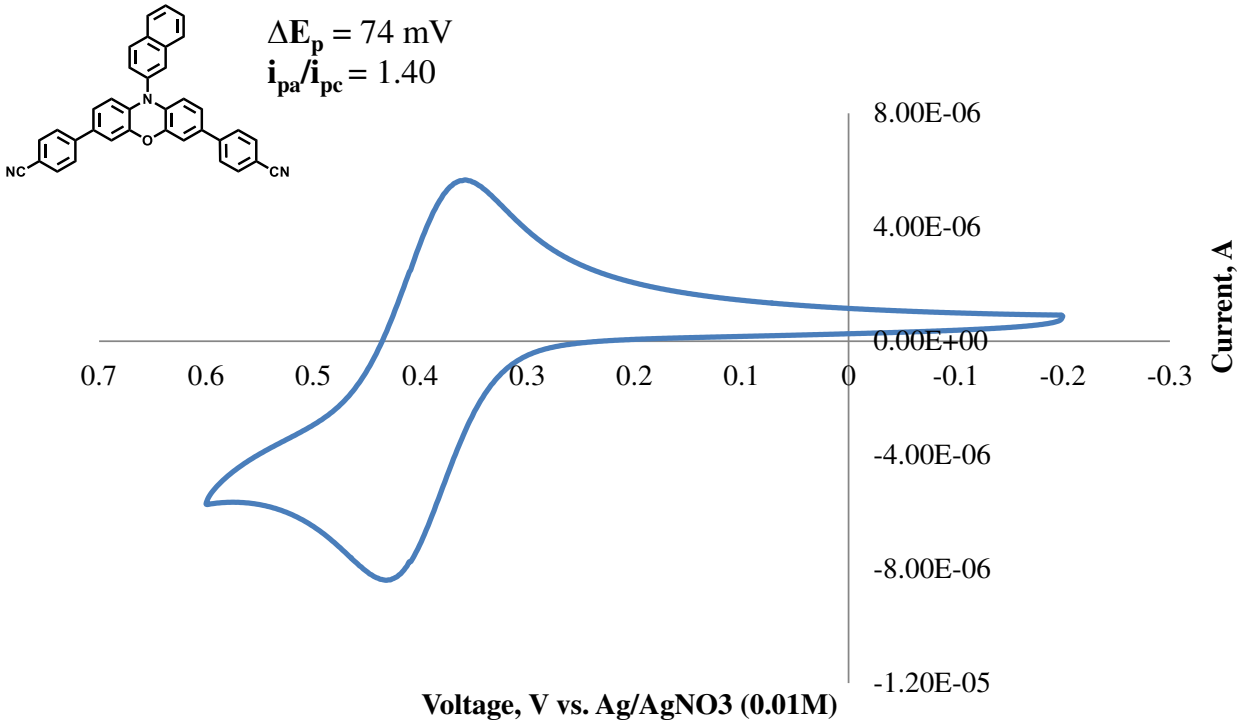

Figure 3.58. *Cyclic voltammogram* ***12*** *of acquired with a scan rate of 0.05 V/s.*

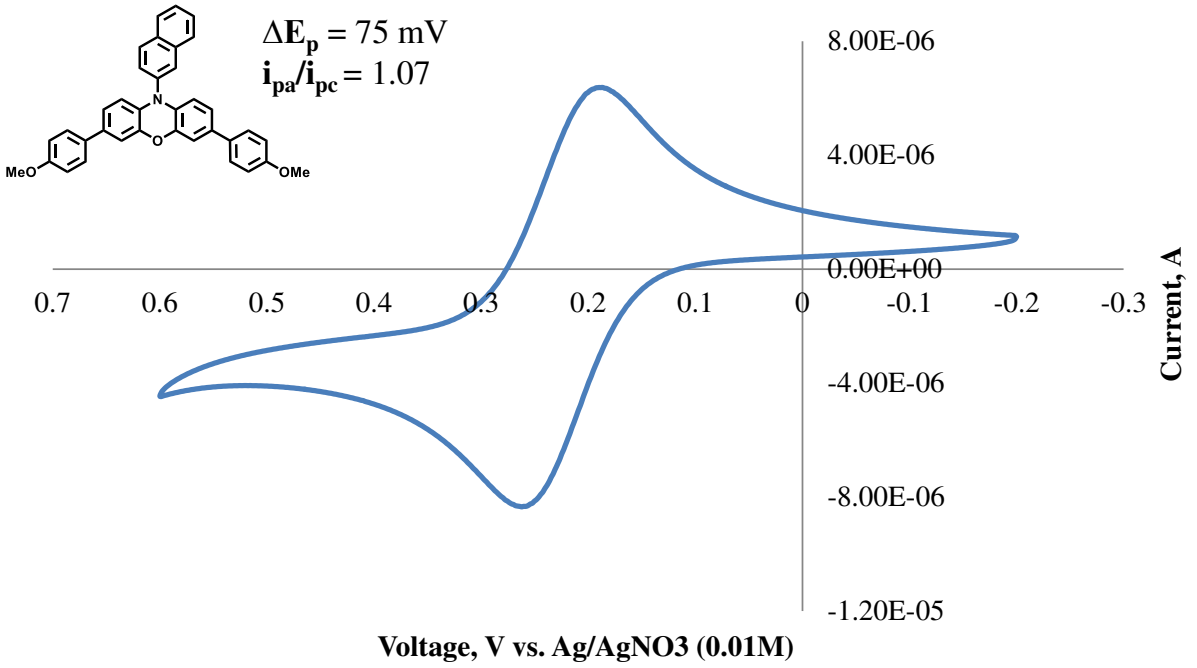

Figure 3.59. *Cyclic voltammogram* ***11*** *of acquired with a scan rate of 0.05 V/s.*

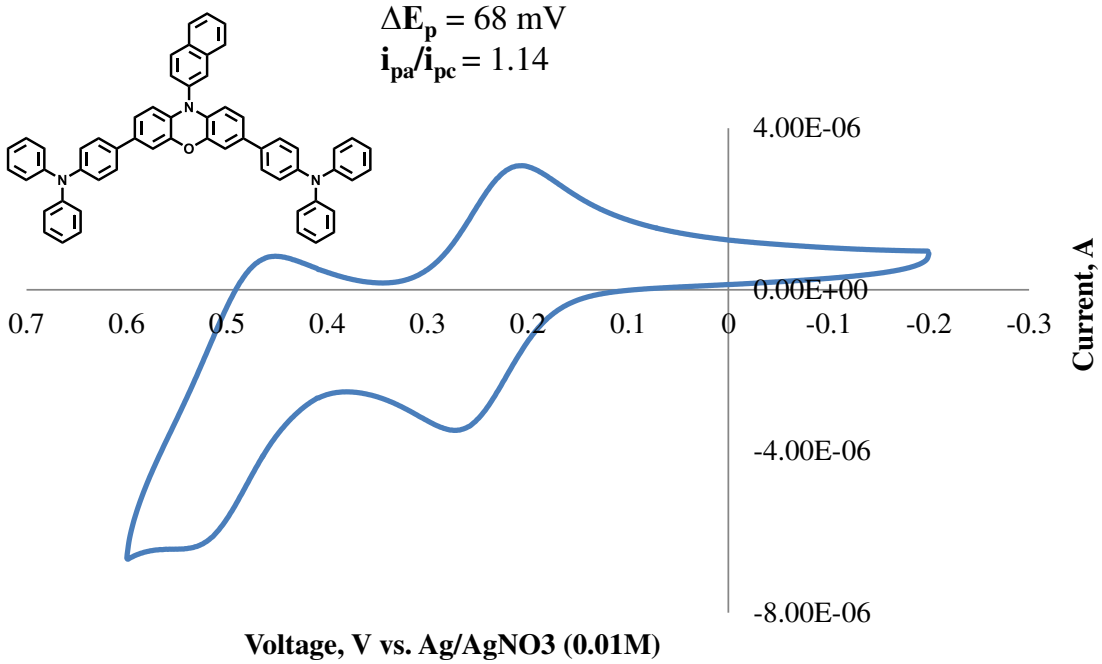

Figure 3.60. *Cyclic voltammogram* ***14*** *of acquired with a scan rate of 0.05 V/s.*

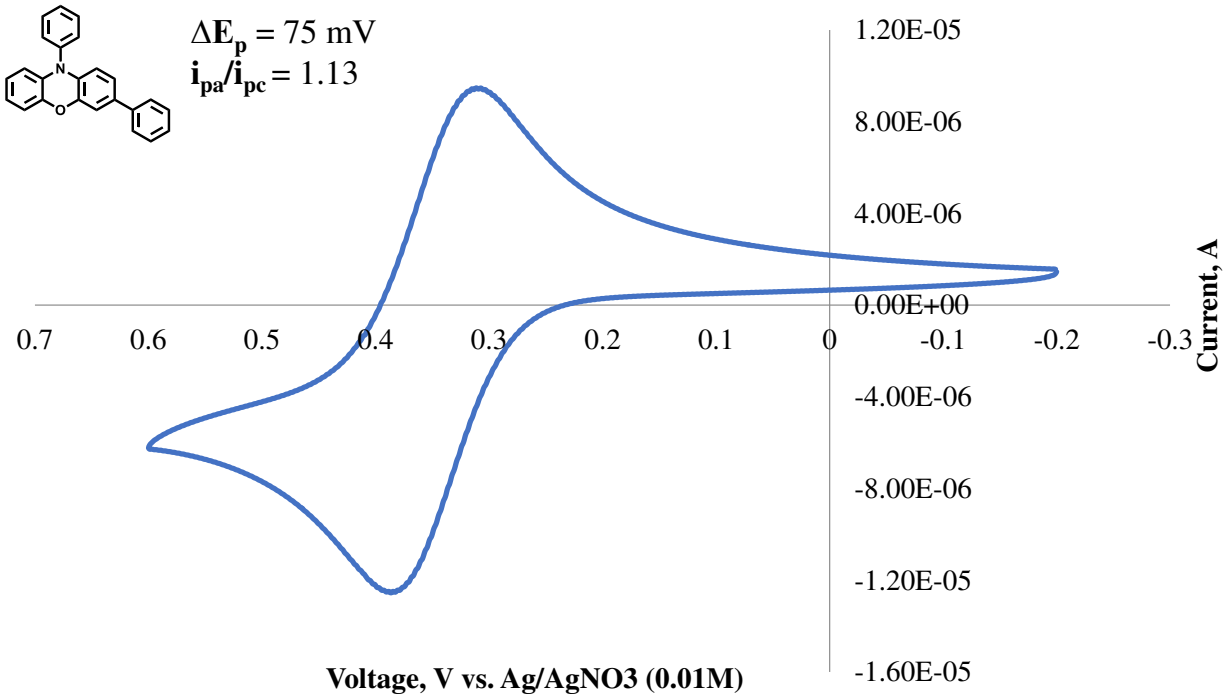

Figure 3.61. *Cyclic voltammogram* ***7*** *of acquired with a scan rate of 0.05 V/s.*

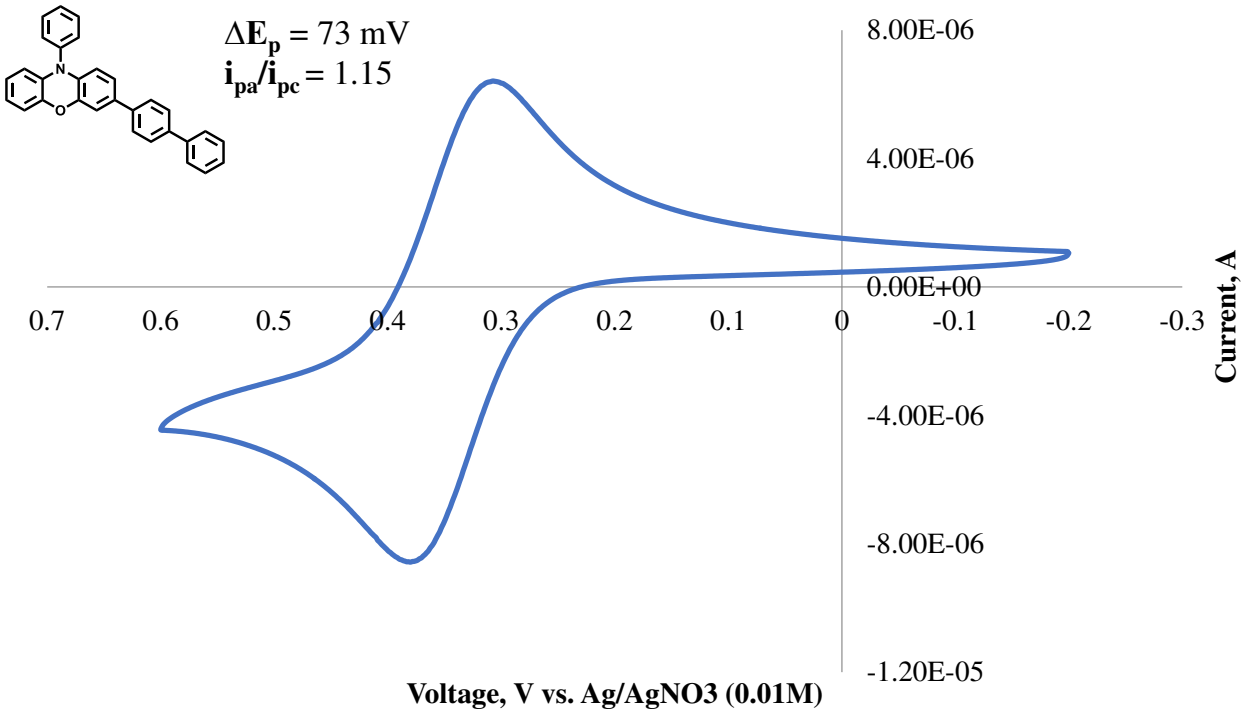

Figure 3.62. *Cyclic voltammogram* ***8*** *of acquired with a scan rate of 0.05 V/s.*

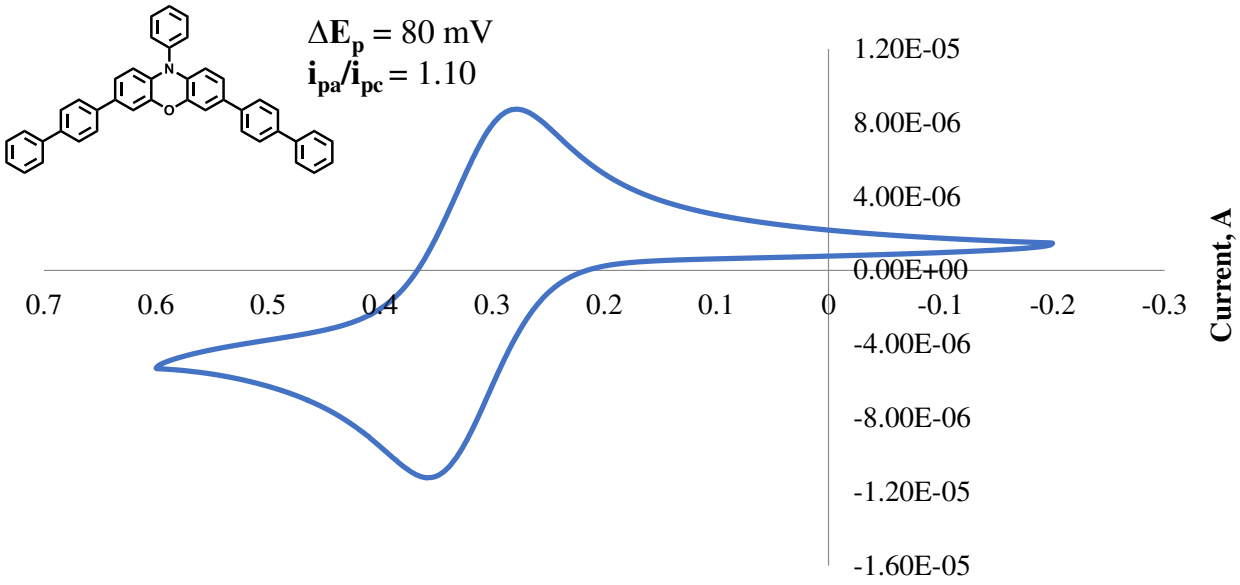

Figure 3.63. *Cyclic voltammogram* ***9*** *of acquired with a scan rate of 0.05 V/s.*

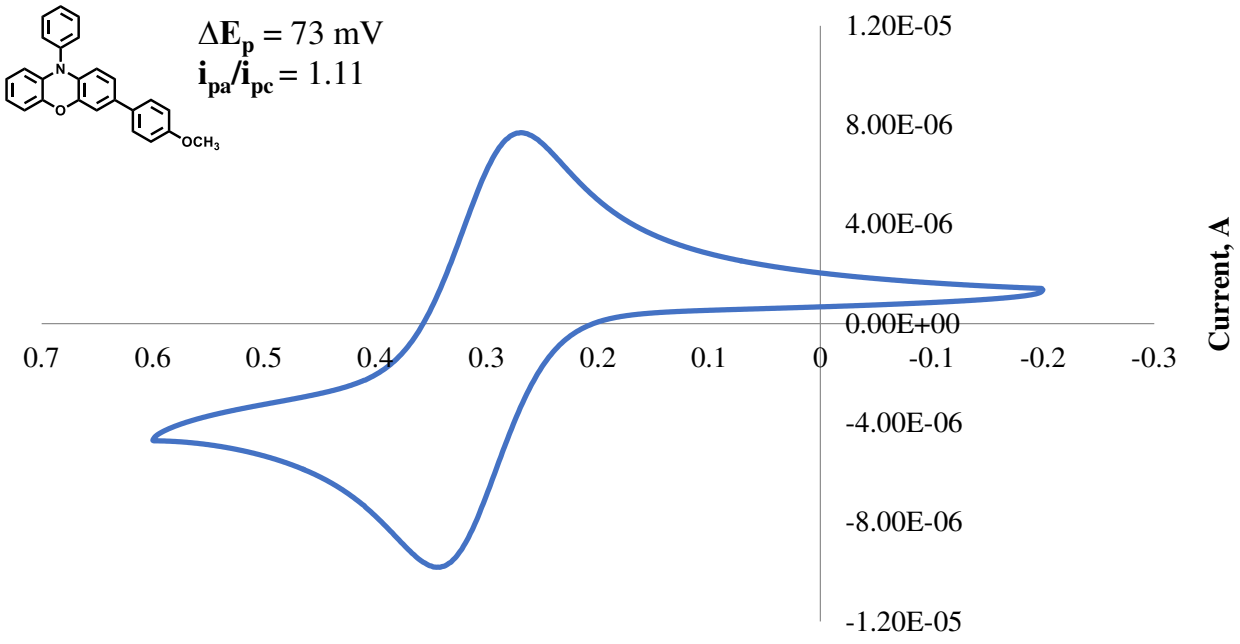

Figure 3.64. *Cyclic voltammogram* ***18*** *of acquired with a scan rate of 0.05 V/s.*

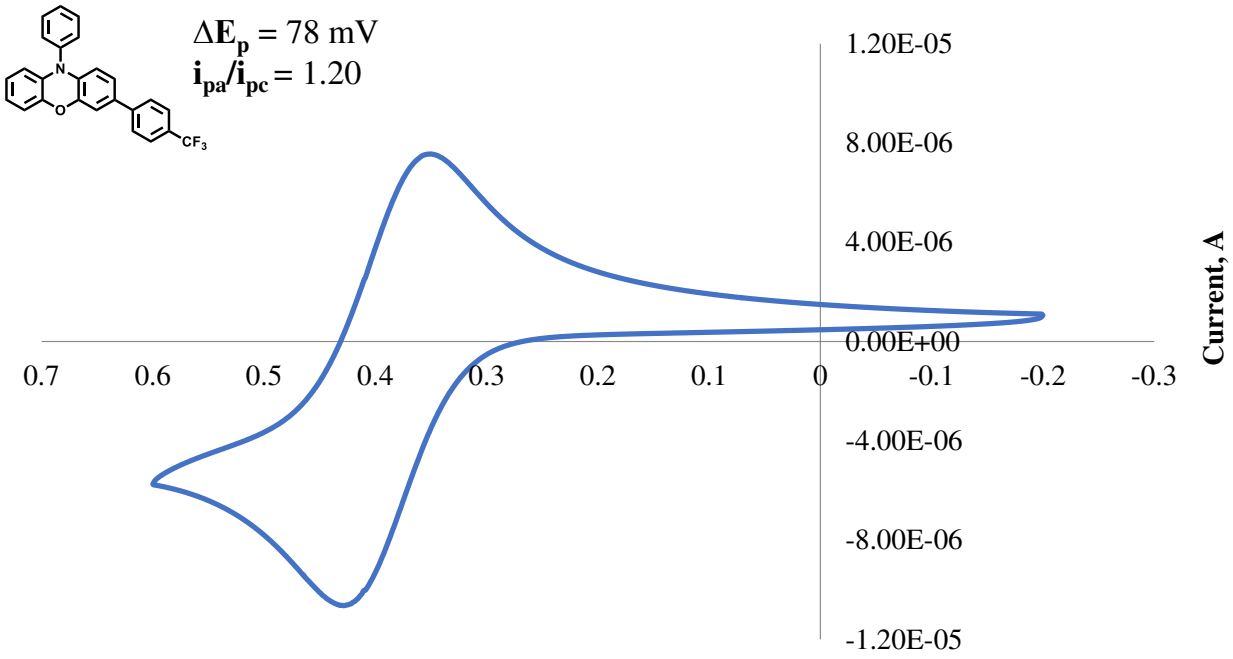

Figure 3.65. *Cyclic voltammogram* ***19*** *of acquired with a scan rate of 0.05 V/s.*

Procedure for Figure S57: Cyclic voltammogram of PC **13** was performed in a 3-compartment electrochemical cell with Ag/ $AgNO_3$ (0.01 M) in MeCN as the reference electrode, NBu_4PF_6 in THF (0.100 M) as the electrolyte solution, and platinum for the working and counter electrodes.

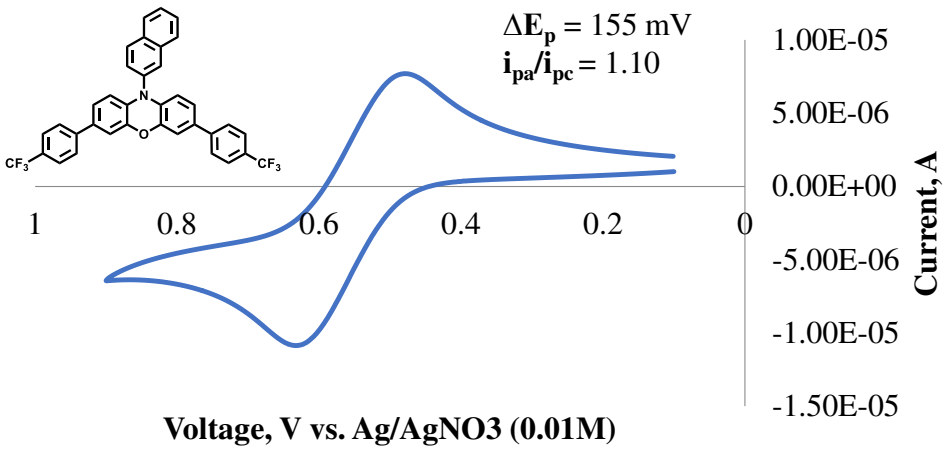

Figure 3.66. *Cyclic voltammogram* ***13*** *of acquired with a scan rate of 0.05 V/s in THF.*

UV-visible Spectroscopy

Table 3.4. *Computationally predicted oscillator strength (f) values.*[a]

PC	Computationally predicted $\lambda_{max,abs}$ (nm)	Computationally predicted oscillator strength
7	328	0.283
8	340	0.533
9	357	0.813

[a]*Predicted at the TD-DFT CAM-B3LYP/6-31+G(d,p)/CPCM-DMA level of theory at the indicated wavelengths.*

Table 5. *Experimentally determined absorption data*

PC	abs λ_{max} (nm)	$\varepsilon_{\lambda max, abs}$ ($M^{-1}cm^{-1}$)
7	346	6,850
8	362	10,250
9	389	24,000
18	345	9,860
19	369	10,810
1	388	26,600
10	371	15,000
4	367	18,300
5	384	25,900
11	363	22,000
12	411	22,300
13	388	21,100
14	382	37,700
15	355	19,110
16	379	20,600
17	384	25,300

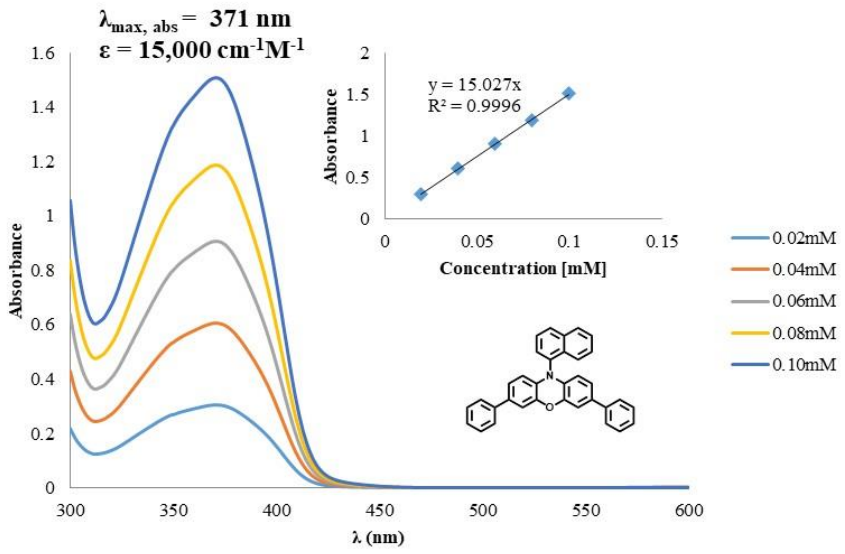

Figure 3.67. *UV-vis spectrum of* ***10*** *at different concentrations in DMAc with a path length of 1 cm. Graph in the upper right hand corner demonstrates adherence to the Beer-Lambert law at the maximum wavelength of absorption.*

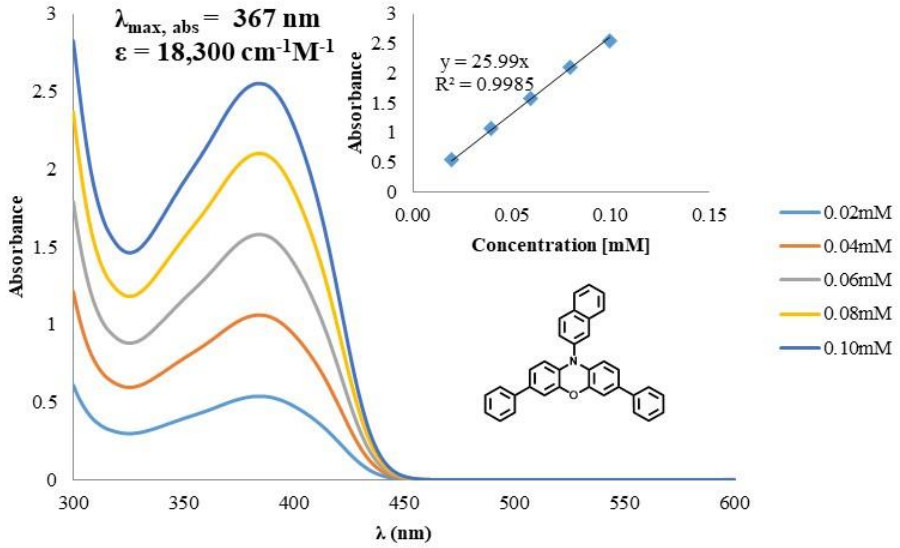

Figure 3.68. *UV-vis spectrum of* ***4*** *at different concentrations in DMAc with a path length of 1 cm. Graph in the upper right hand corner demonstrates adherence to the Beer-Lambert law at the maximum wavelength of absorption.*

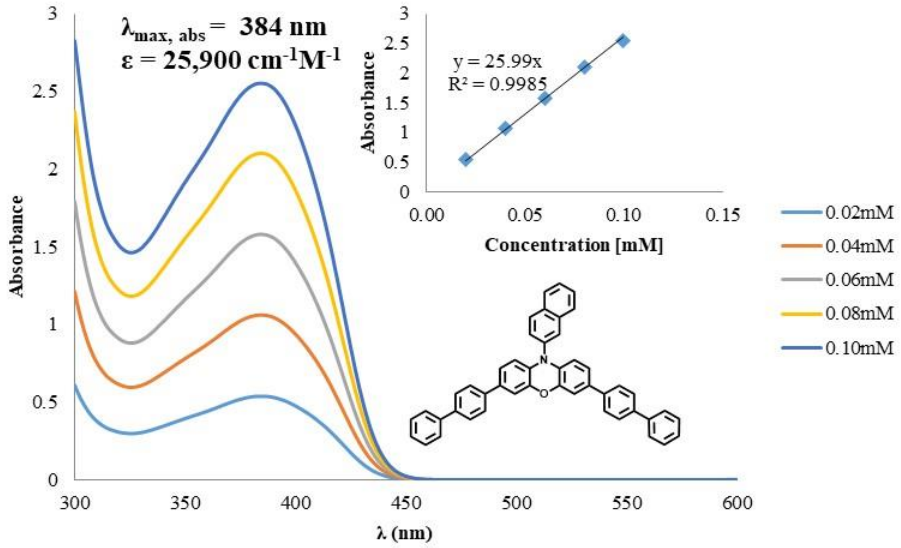

Figure 3.69. *UV-vis spectrum of* ***5*** *at different concentrations in DMAc with a path length of 1 cm. Graph in the upper right hand corner demonstrates adherence to the Beer-Lambert law at the maximum wavelength of absorption.*

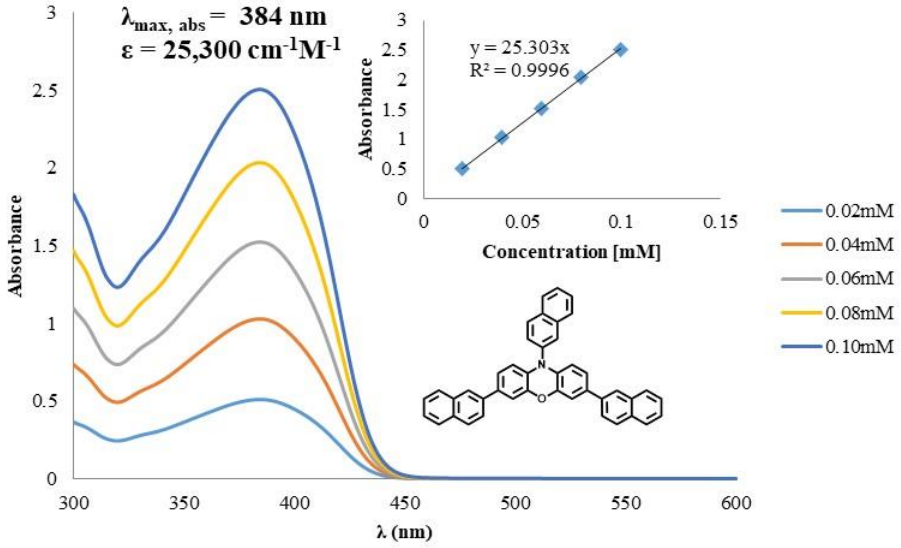

Figure 3.70. *UV-vis spectrum of* ***17*** *at different concentrations in DMAc with a path length of 1 cm. Graph in the upper right hand corner demonstrates adherence to the Beer-Lambert law at the maximum wavelength of absorption.*

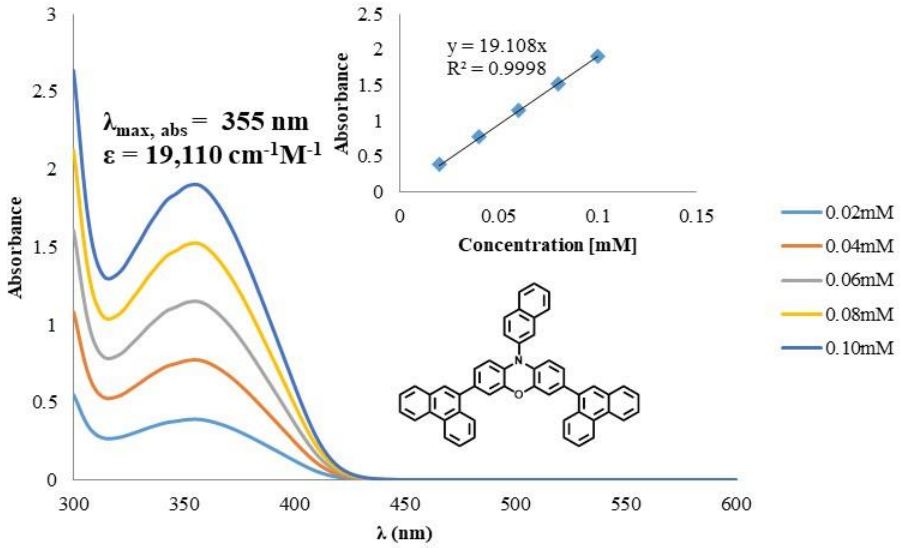

Figure 3.71. *UV-vis spectrum of* ***15*** *at different concentrations in DMAc with a path length of 1 cm. Graph in the upper right hand corner demonstrates adherence to the Beer-Lambert law at the maximum wavelength of absorption.*

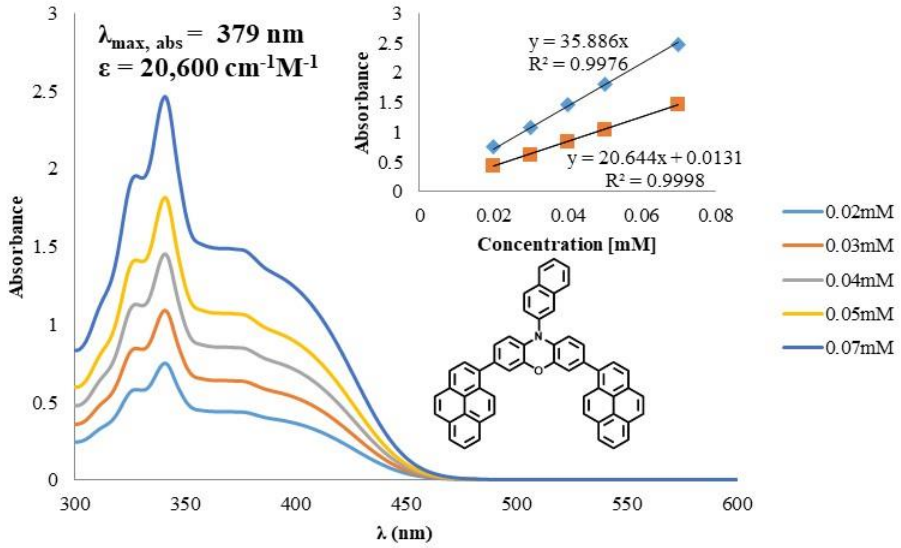

Figure 3.72. *UV-vis spectrum of* ***16*** *at different concentrations in DMAc with a path length of 1 cm. Graph in the upper right hand corner demonstrates adherence to the Beer-Lambert law at the maximum wavelength of absorption.*

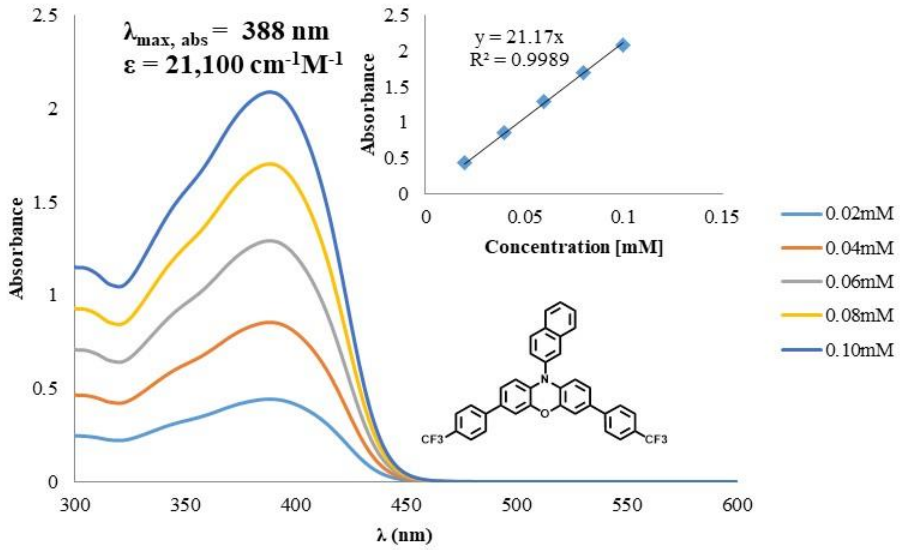

Figure 3.73. *UV-vis spectrum of* ***13*** *at different concentrations in DMAc with a path length of 1 cm. Graph in the upper right hand corner demonstrates adherence to the Beer-Lambert law at the maximum wavelength of absorption.*

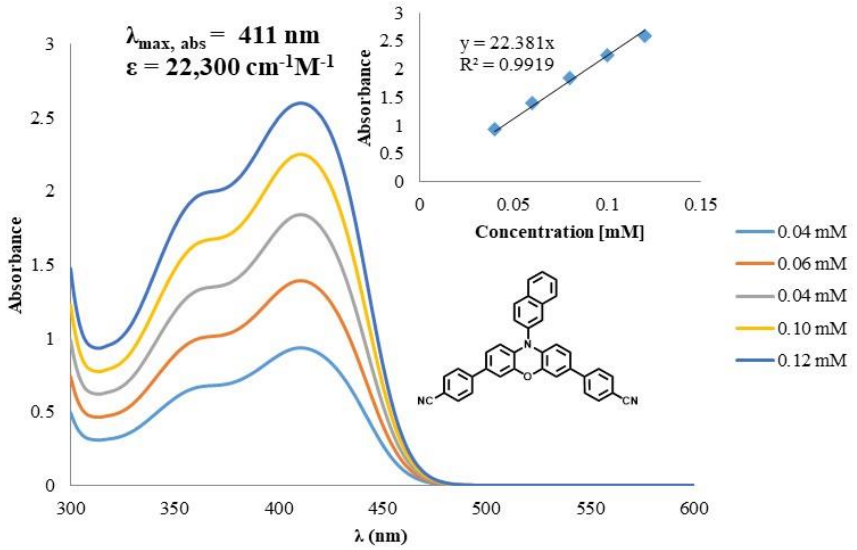

Figure 3.74. *UV-vis spectrum of* ***12*** *at different concentrations in DMAc with a path length of 1 cm. Graph in the upper right hand corner demonstrates adherence to the Beer-Lambert law at the maximum wavelength of absorption.*

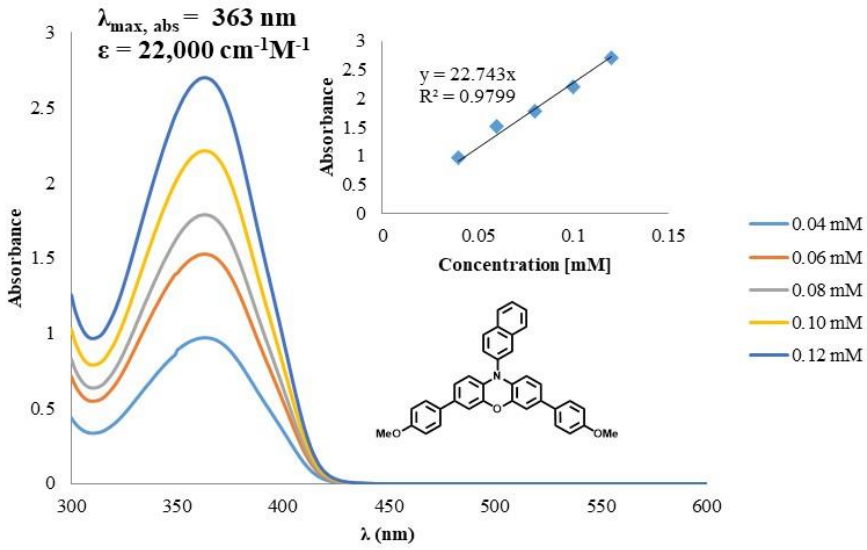

Figure 3.75. *UV-vis spectrum of* ***11*** *at different concentrations in DMAc with a path length of 1 cm. Graph in the upper right hand corner demonstrates adherence to the Beer-Lambert law at the maximum wavelength of absorption.*

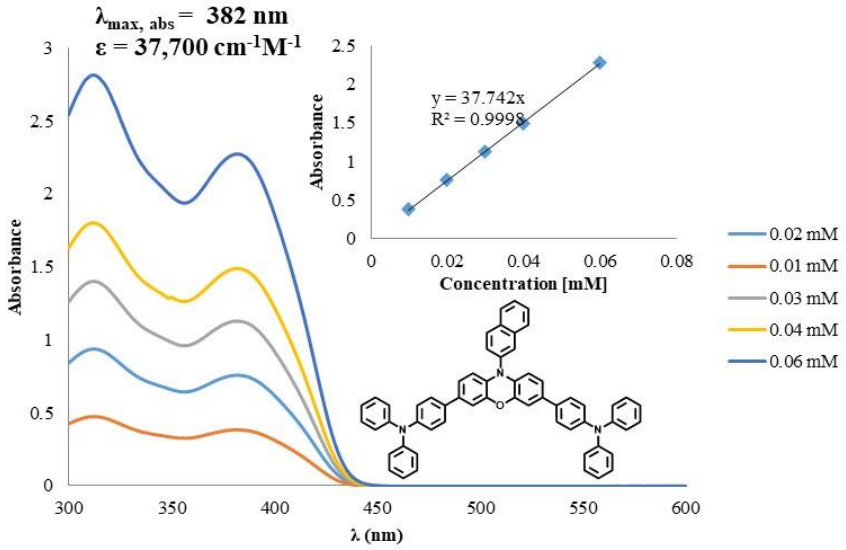

Figure 3.76. *UV-vis spectrum of* ***14*** *at different concentrations in DMAc with a path length of 1 cm. Graph in the upper right hand corner demonstrates adherence to the Beer-Lambert law at the maximum wavelength of absorption.*

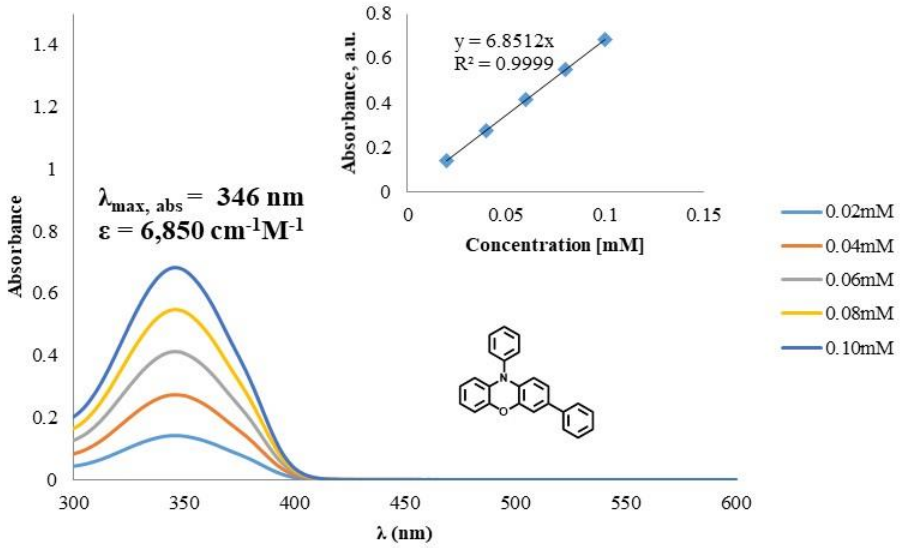

Figure 3.78. *UV-vis spectrum of* ***7*** *at different concentrations in DMAc with a path length of 1 cm. Graph in the upper right hand corner demonstrates adherence to the Beer-Lambert law at the maximum wavelength of absorption.*

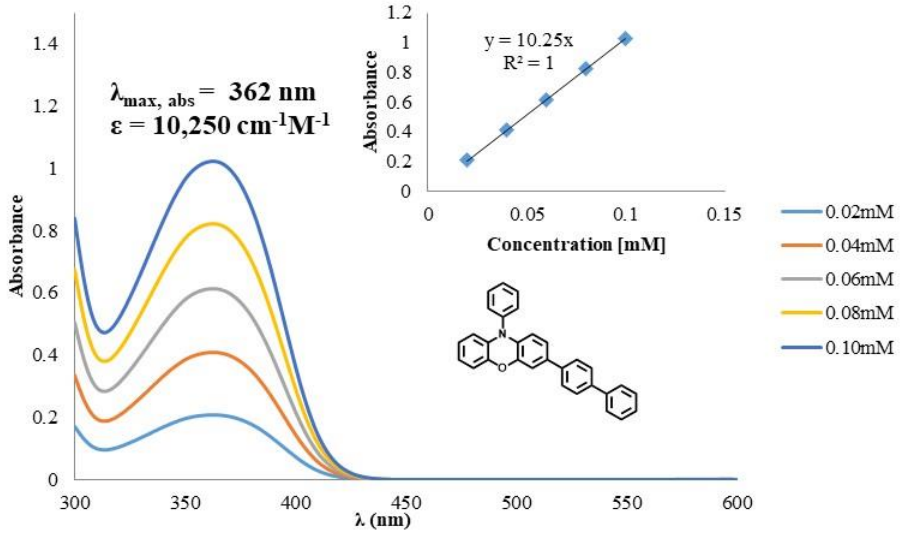

Figure 3.79. *UV-vis spectrum of* ***8*** *at different concentrations in DMAc with a path length of 1 cm. Graph in the upper right hand corner demonstrates adherence to the Beer-Lambert law at the maximum wavelength of absorption.*

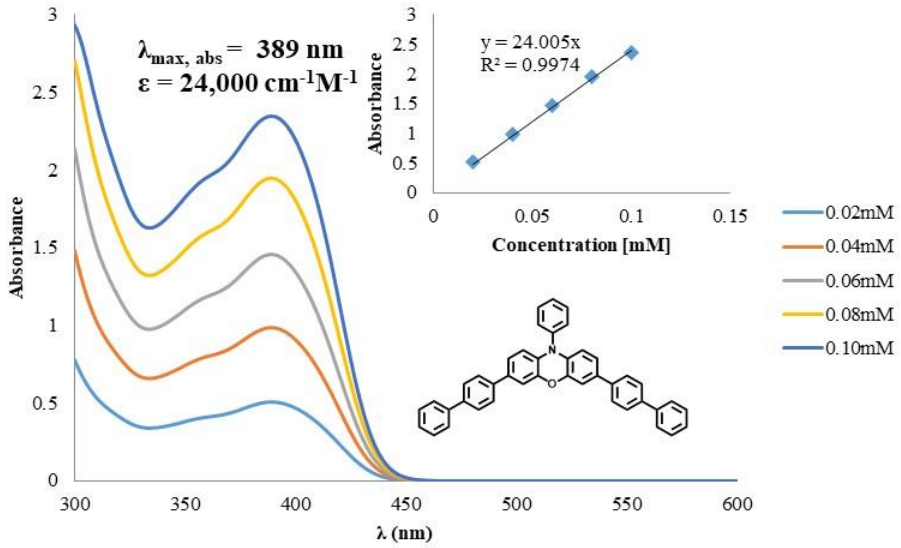

Figure 3.80. *UV-vis spectrum of* ***9*** *at different concentrations in DMAc with a path length of 1 cm. Graph in the upper right hand corner demonstrates adherence to the Beer-Lambert law at the maximum wavelength of absorption.*

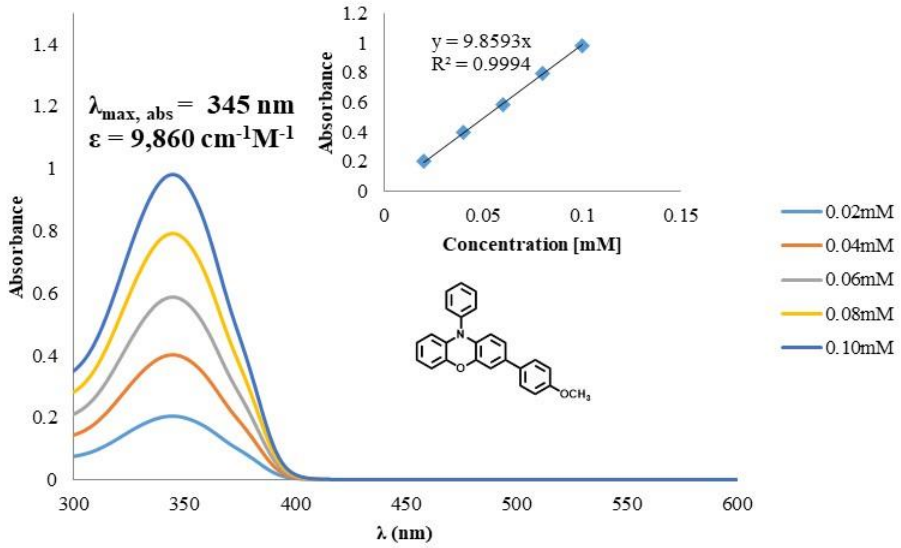

Figure 3.81. *UV-vis spectrum of* ***18*** *at different concentrations in DMAc with a path length of 1 cm. Graph in the upper right hand corner demonstrates adherence to the Beer-Lambert law at the maximum wavelength of absorption.*

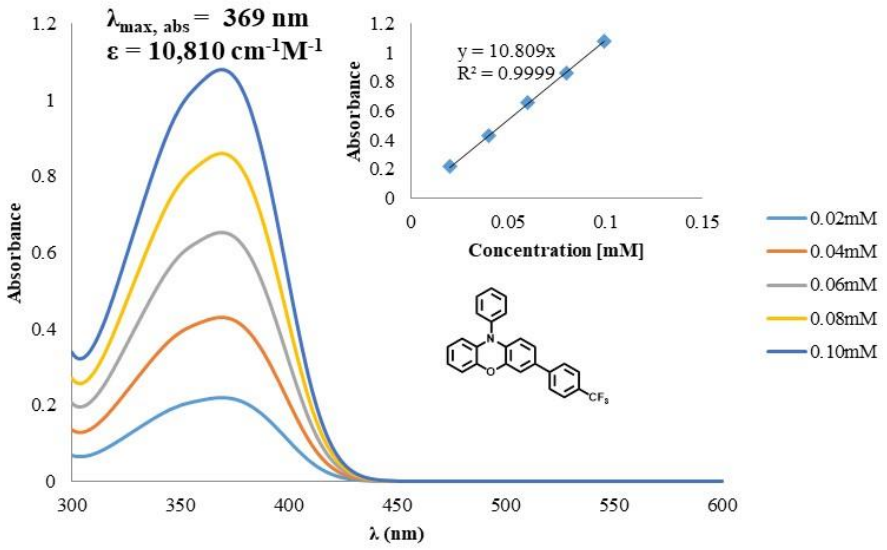

Figure 3.82. *UV-vis spectrum of* ***19*** *at different concentrations in DMAc with a path length of 1 cm. Graph in the upper right hand corner demonstrates adherence to the Beer-Lambert law at the maximum wavelength of absorption.*

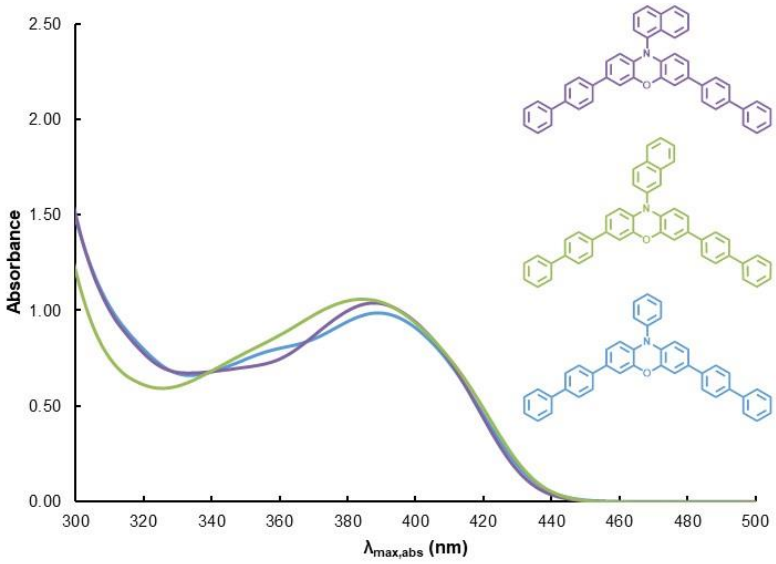

Figure 3.83. *UV-vis spectra of* ***1***, ***5***, *and* ***9*** *at 0.04 mM in DMAc with a path length of 1 cm.*

Fluorescence Spectroscopy

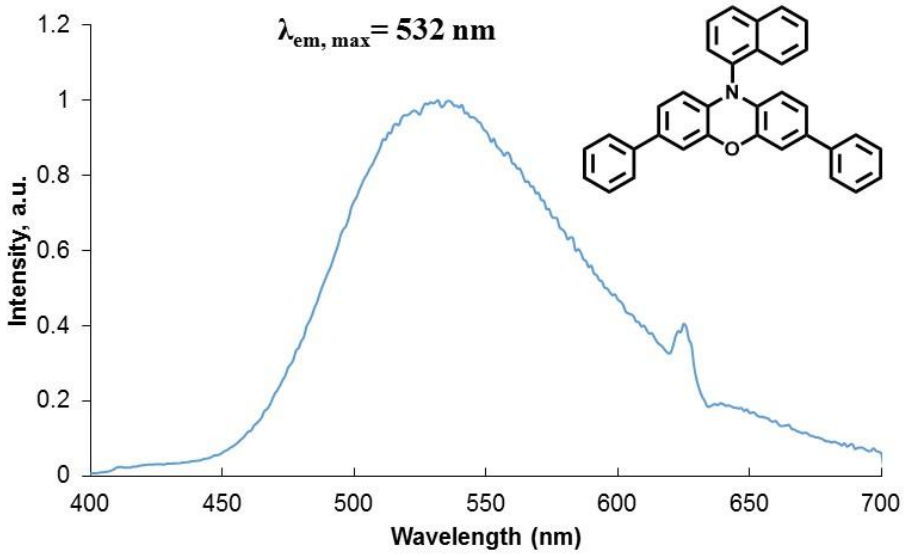

Figure 3.84. *Fluorescence spectrum of* ***10*** *in DMAc was scanned from 400 to 700 nm after excitation at 360 nm. The spectrum is an average of 3 scans with an integration time of 0.25 s.*

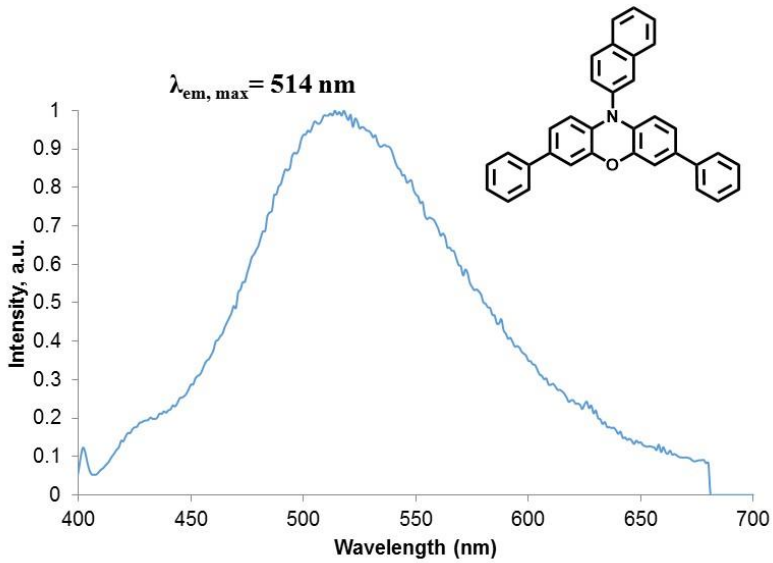

Figure 3.85. *Fluorescence spectrum of* ***4*** *in DMAc was scanned from 400 to 700 nm after excitation at 360 nm. The spectrum is an average of 3 scans with an integration time of 0.25 s.*

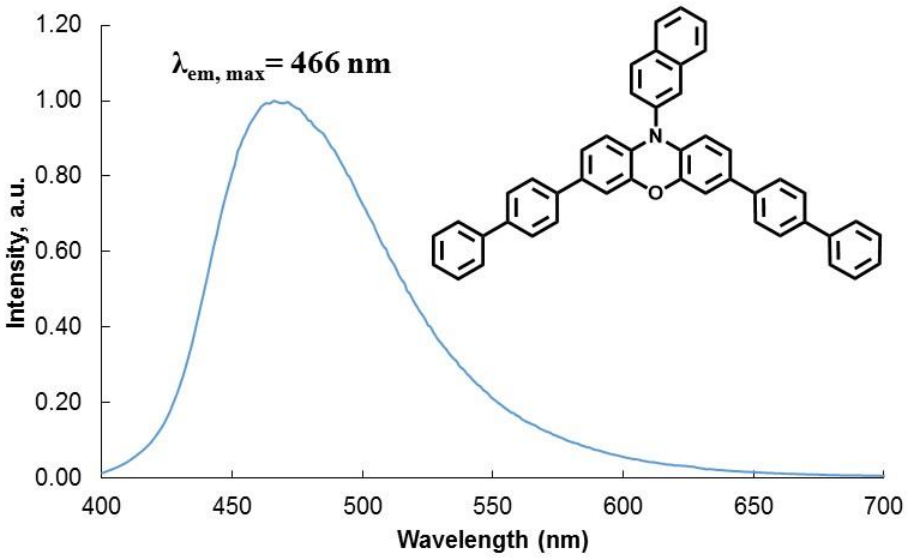

Figure 3.86. *Fluorescence spectrum of* ***5*** *in DMAc was scanned from 400 to 700 nm after excitation at 380 nm. The spectrum is an average of 3 scans with an integration time of 0.5 s.*

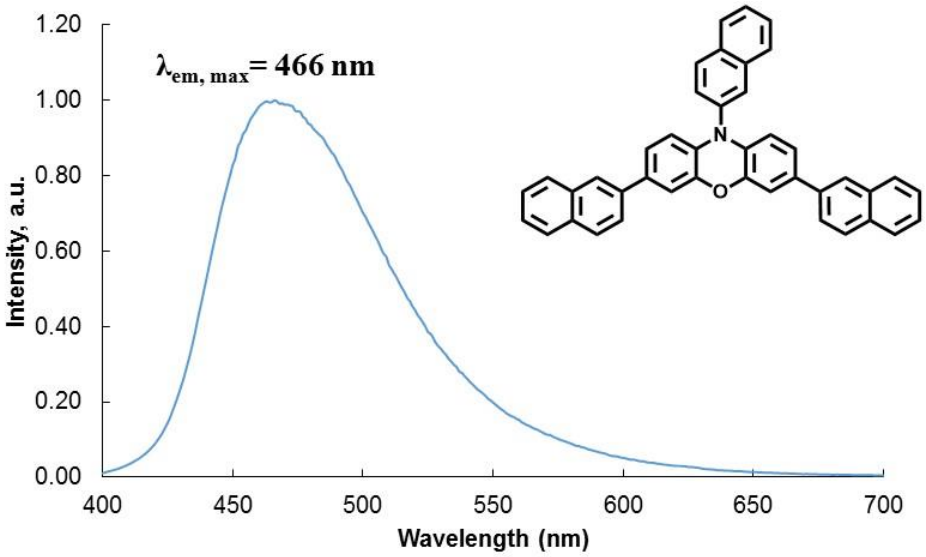

Figure 3.87. *Fluorescence spectrum of* ***17*** *in DMAc was scanned from 400 to 700 nm after excitation at 380 nm. The spectrum is an average of 3 scans with an integration time of 0.5 s.*

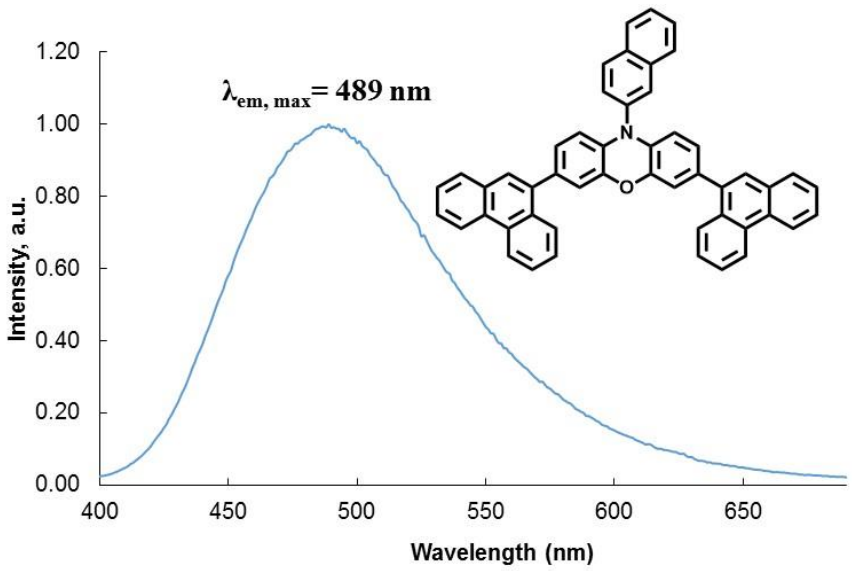

Figure 3.88. *Fluorescence spectrum of* ***15*** *in DMAc was scanned from 400 to 700 nm after excitation at 350 nm. The spectrum is an average of 3 scans with an integration time of 0.5 s.*

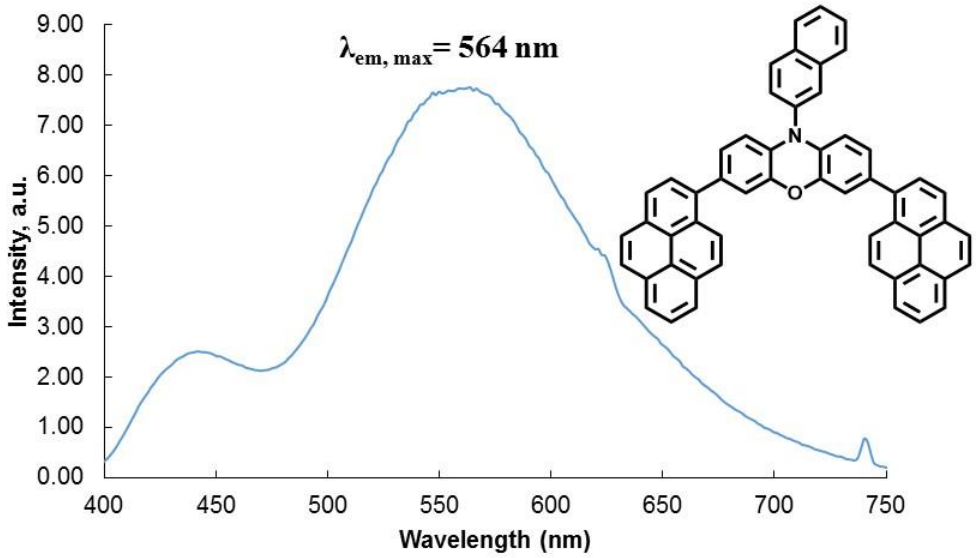

Figure 3.89. *Fluorescence spectrum of* ***16*** *in DMAc was scanned from 400 to 700 nm after excitation at 370 nm. The spectrum is an average of 3 scans with an integration time of 0.5 s.*

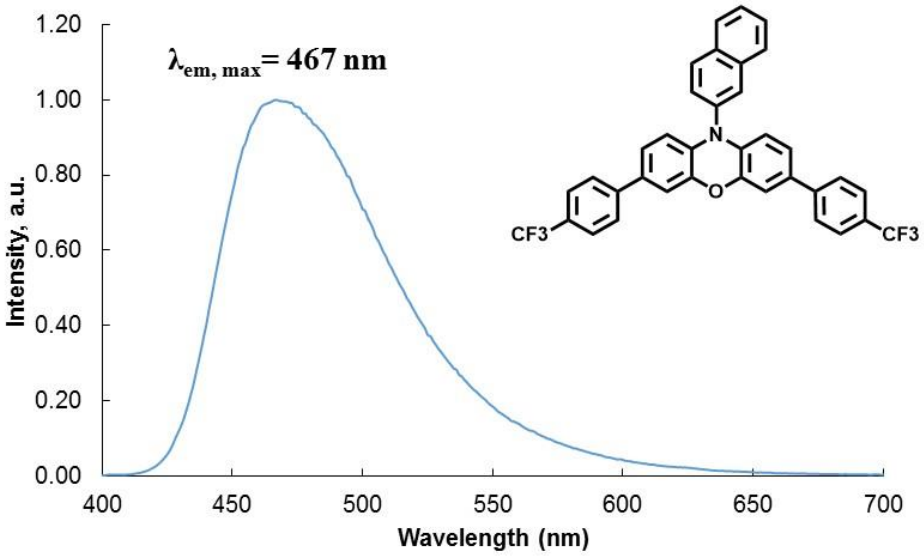

Figure 3.90. *Fluorescence spectrum of* ***13*** *in DMAc was scanned from 400 to 700 nm after excitation at 380 nm. The spectrum is an average of 3 scans an integration time of 0.5 s.*

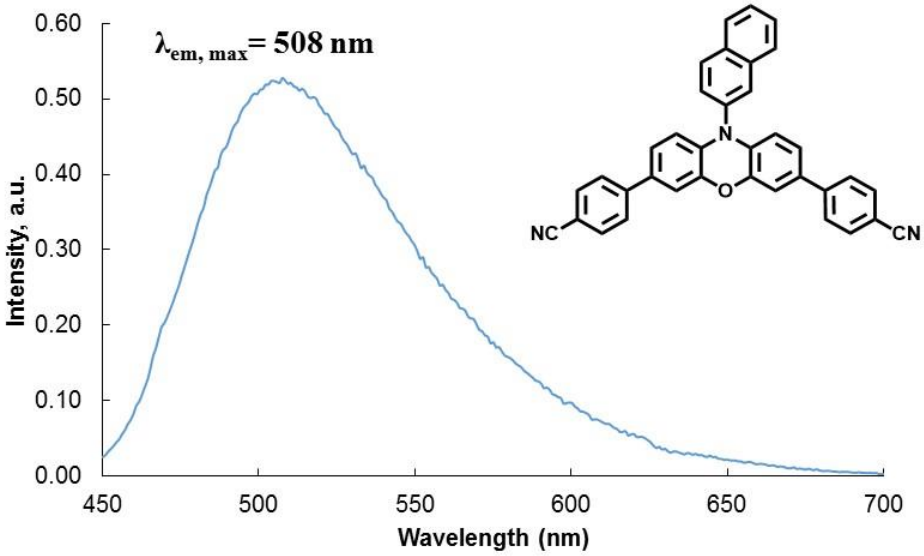

Figure 3.91. *Fluorescence spectrum of* ***12*** *in DMAc was scanned from 450 to 700 nm after excitation at 411 nm. The spectrum is an average of 3 scans with an integration time of 0.5 s.*

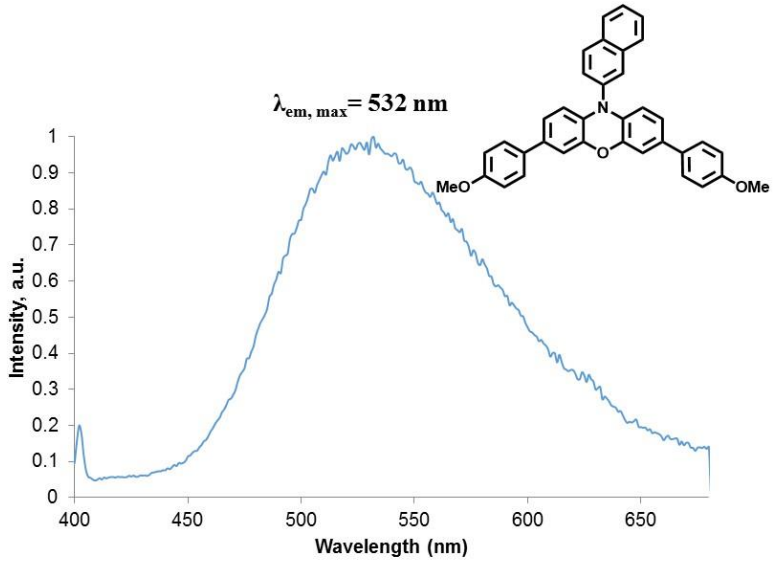

Figure 3.92. *Fluorescence spectrum of* ***11*** *in DMAc was scanned from 400 to 700 nm after excitation at 360 nm. The spectrum is an average of 3 scans with an integration time of 0.5 s.*

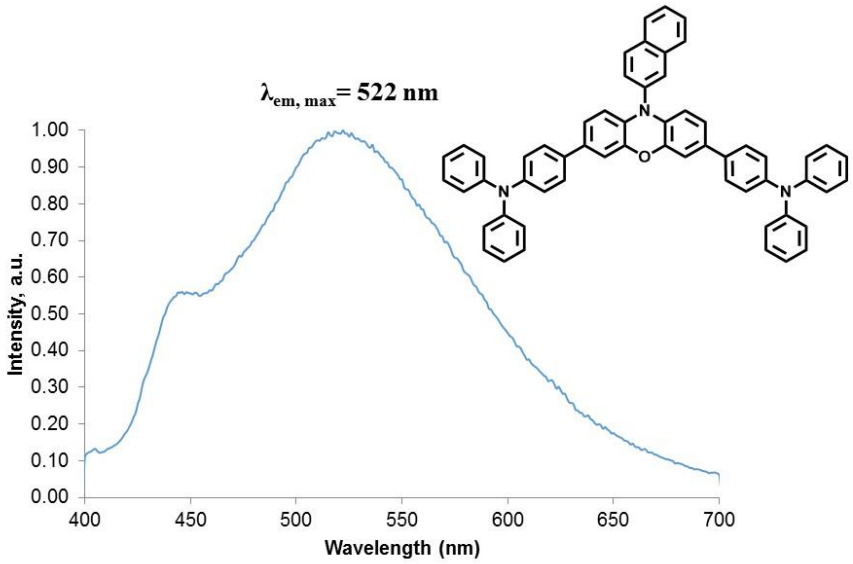

Figure 3.93. *Fluorescence spectrum of* ***14*** *in DMAc was scanned from 400 to 700 nm after excitation at 380 nm. The spectrum is an average of 3 scans with an integration time of 0.5 s.*

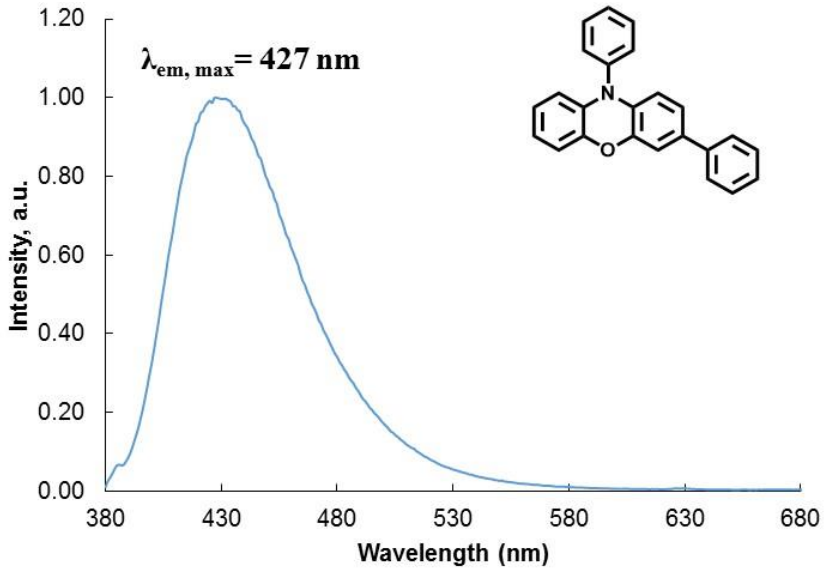

Figure 3.94. *Fluorescence spectrum of* ***7*** *in DMAc was scanned from 380 to 680 nm after excitation at 346 nm. The spectrum is an average of 3 scans with an integration time of 0.5 s.*

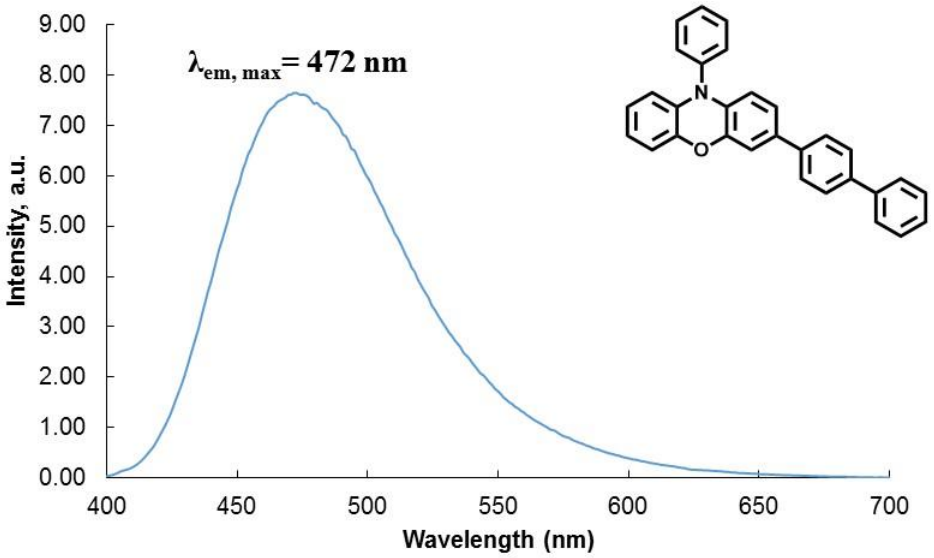

Figure 3.95. *Fluorescence spectrum of* ***8*** *in DMAc was scanned from 375 to 700 nm after excitation at 363 nm. The spectrum is an average of 3 scans with an integration time of 0.5 s.*

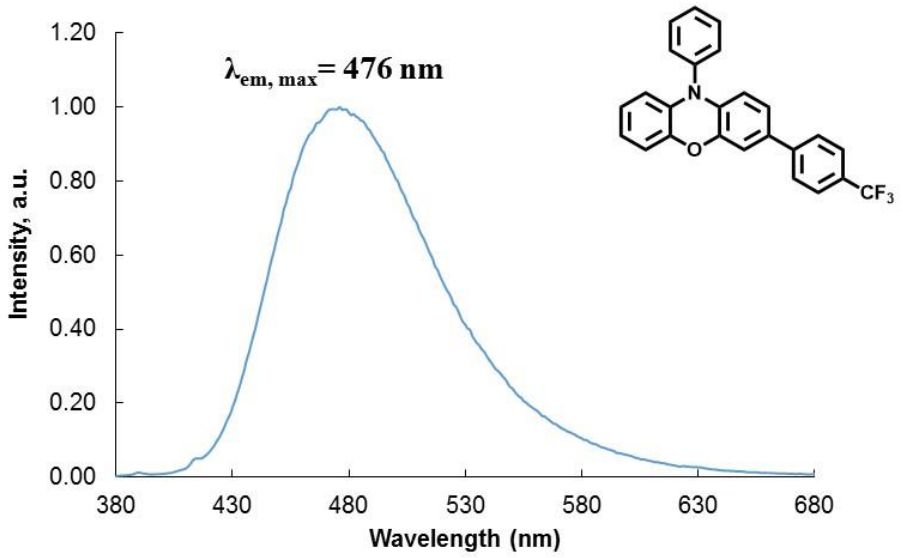

Figure 3.96. *Fluorescence spectrum of* ***19*** *in DMAc was scanned from 380 to 680 nm after excitation at 369 nm. The spectrum is an average of 3 scans with an integration time of 0.5 s.*

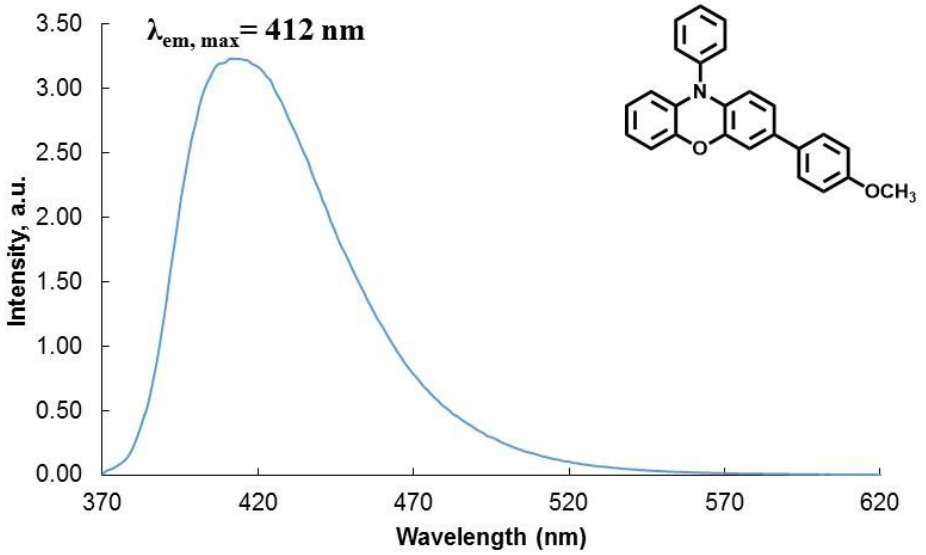

Figure 3.97. *Fluorescence spectrum of* ***18*** *in DMAc was scanned from 370 to 730 nm after excitation at 344 nm. The spectrum is an average of 3 scans with an integration time of 0.5 s.*

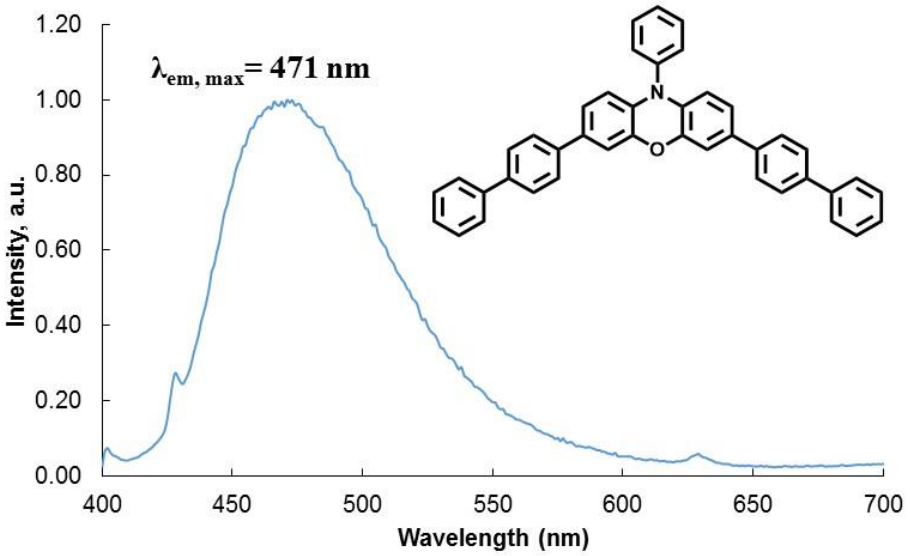

Figure 3.98. *Fluorescence spectrum of* ***9*** *in DMAc was scanned from 400 to 700 nm after excitation at 380 nm. The spectrum is an average of 3 scans with an integration time of 0.5 s.*

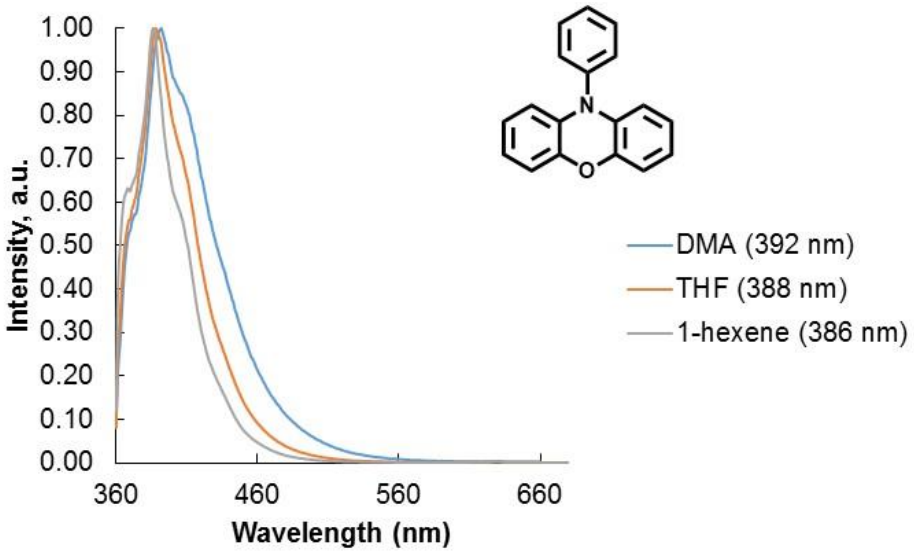

Figure 3.99. *Fluorescence spectra of* ***6*** *in DMAc (blue), THF (orange), and 1-hexene (grey) are shown. Each spectrum is an average of 3 scans with an integration time of 0.5 s.*

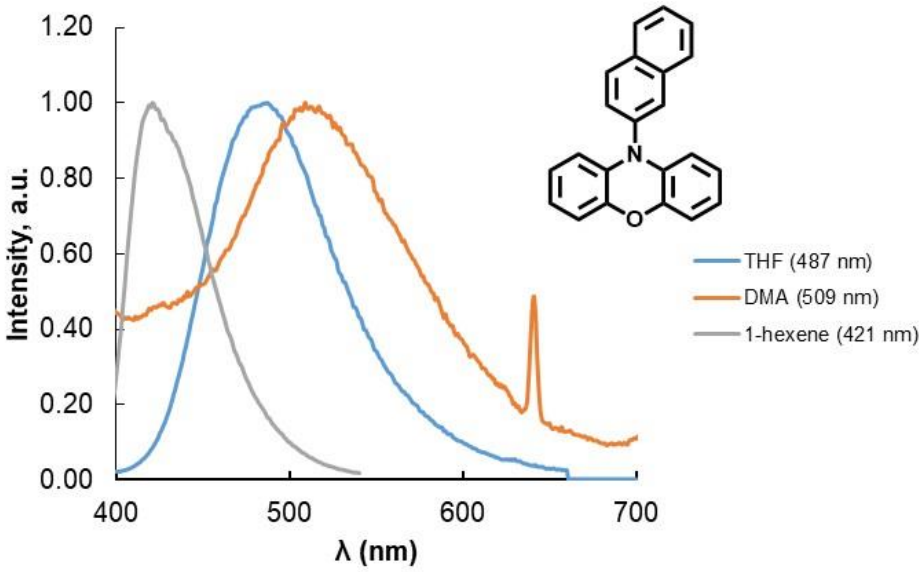

Figure 3.100. *Fluorescence spectra of* ***3*** *in DMAc (orange) and THF (blue) are shown. Each spectrum is an average of 3 scans with an integration time of 0.5 s.*

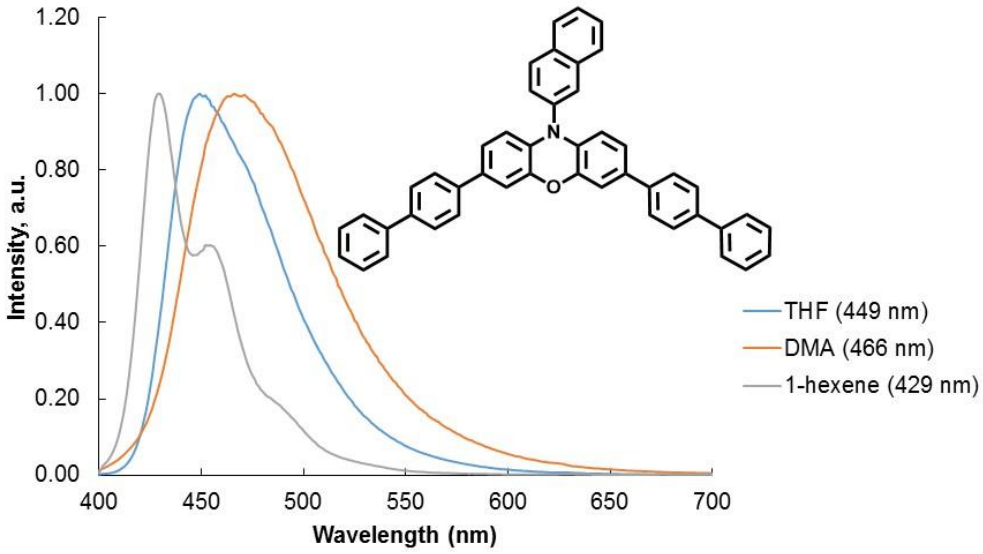

Figure 3.101. *Fluorescence spectra of* ***5*** *in DMAc (blue), THF (orange), and 1-hexene (grey) are shown. Each spectrum is an average of 3 scans with an integration time of 0.5 s.*

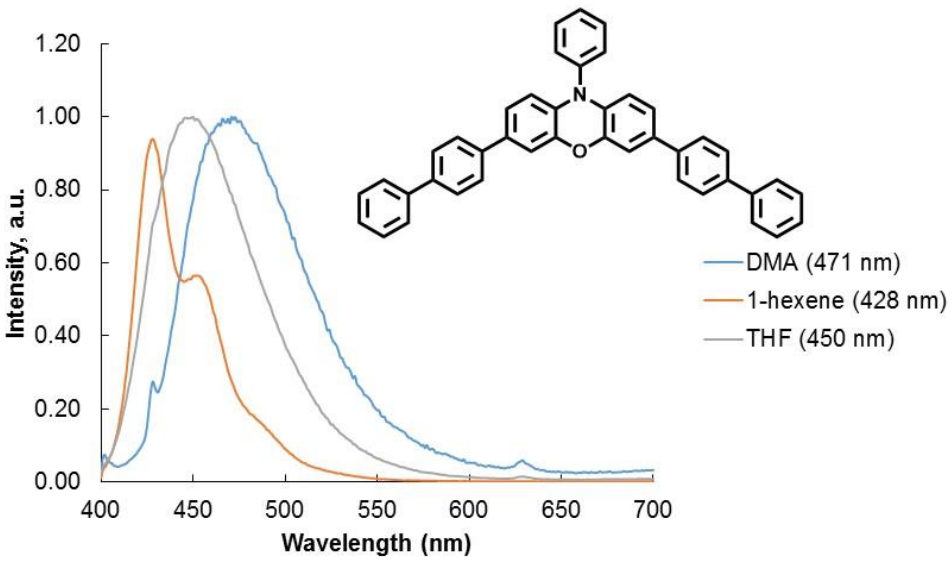

Figure 3.102. *Fluorescence spectrum of* ***9*** *in DMAc (blue), THF (grey), and 1-hexene (orange) are shown. Each spectrum is an average of 3 scans with an integration time of 0.5 s.*

Tables of Emission Data and Solvatochromic Shifts

Table 3.6. *Emission data acquired in DMAc.*

PC	$\lambda_{max, em}$ (nm)
6	392
2	524
10	532
1	506
3	509
4	514
5	466
17	466
15	489
16	564
13	467
12	508
11	532
14	522
7	427
8	472
9	471
18	412
19	476

Table 3.7. *Emission of PCs in DMAc and the shift in emission wavelength relative to DMAc in other solvents.*

PC	Solvent	em λ_{max} (nm)	Blue-Shift from DMAc (nm)
6	DMAc	392	N/A
	THF	388	4
	1-hexene	386	6
5	DMAc	466	N/A
	THF	449	17
	1-hexene	429	37
9	DMAc	471	N/A
	THF	450	21
	1-hexene	428	43

7. Computational Modeling of SOMOs and ESP Maps

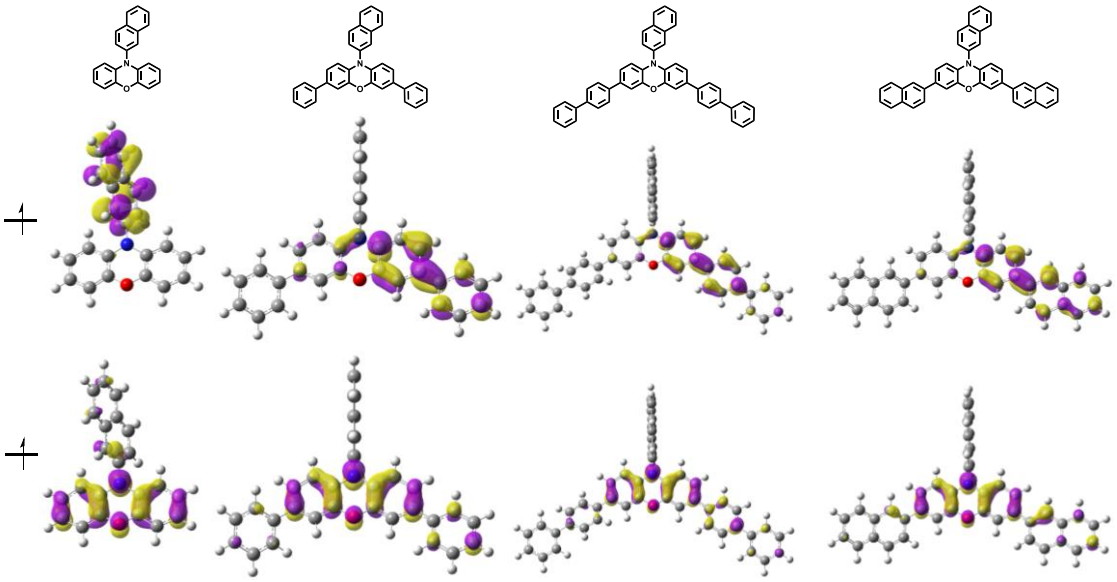

Figure 3.103. *Computational modeling of the singularly occupied molecular orbitals (SOMOs) for PCs* ***3****,* ***4****,* ***5****, and* ***17*** *(from left to right); the lower lying SOMO (bottom) and higher lying SOMO (top) for each PC in the triplet excited state are shown.*

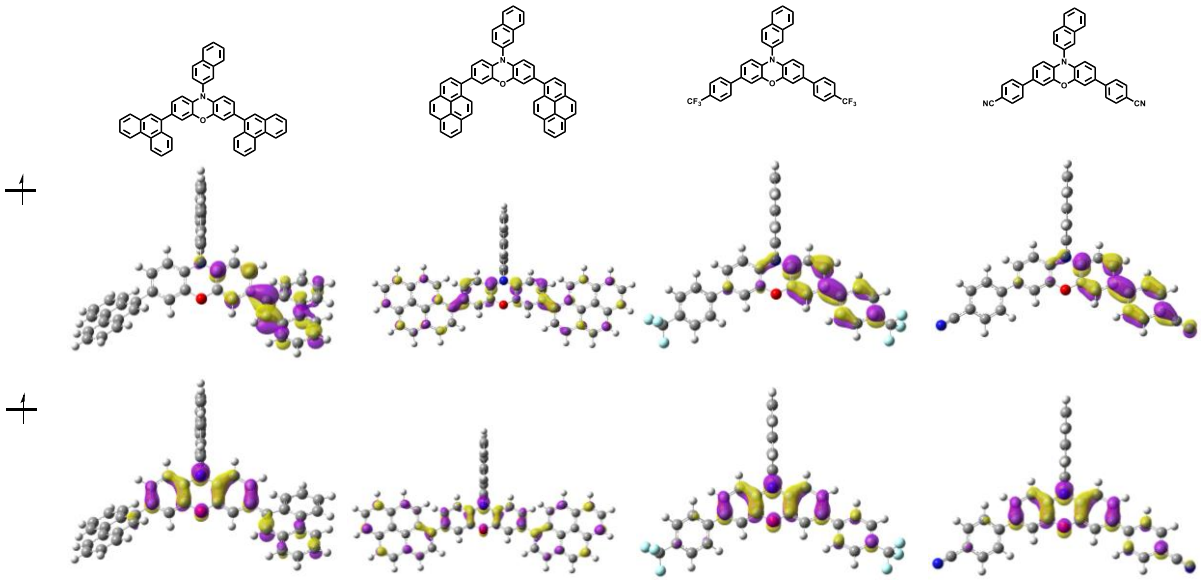

Figure 3.104. *Computational modeling of the singularly occupied molecular orbitals (SOMOs) for PCs* ***15****,* ***16****,* ***13****, and* ***12*** *(from left to right); the lower lying SOMO (bottom) and higher lying SOMO (top) for each PC in the triplet excited state are shown.*

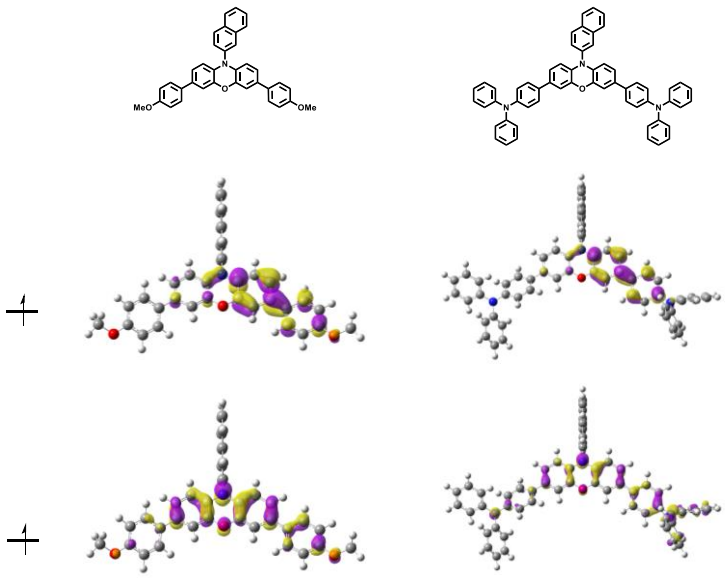

Figure 3.105. *Computational modeling of the singularly occupied molecular orbitals (SOMOs) for PCs* ***11*** *and* ***14*** *(from left to right); the lower lying SOMO (bottom) and higher lying SOMO (top) for each PC in the triplet excited state are shown.*

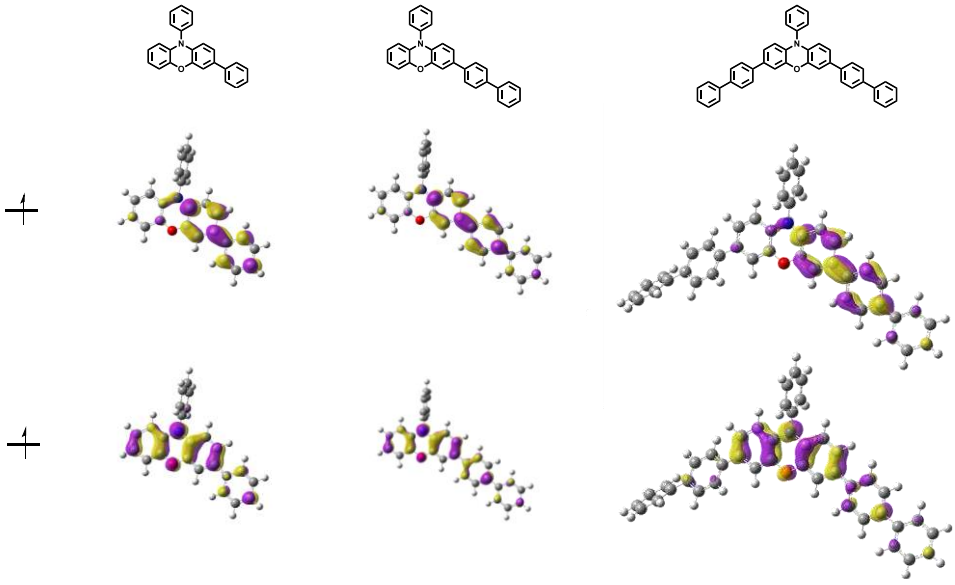

Figure 3.106. *Computational modeling of the singularly occupied molecular orbitals (SOMOs) for PCs* ***7****,* ***8****, and* ***9*** *(from left to right); the lower lying SOMO (bottom) and higher lying SOMO (top) for each PC in the triplet excited state are shown.*

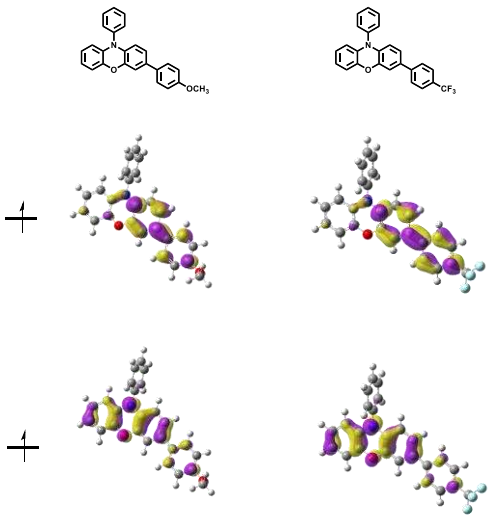

Figure 3.107. *Computational modeling of the singularly occupied molecular orbitals (SOMOs) for PCs* ***18*** *and* ***19*** *(from left to right); the lower lying SOMO (bottom) and higher lying SOMO (top) for each PC in the triplet excited state are shown.*

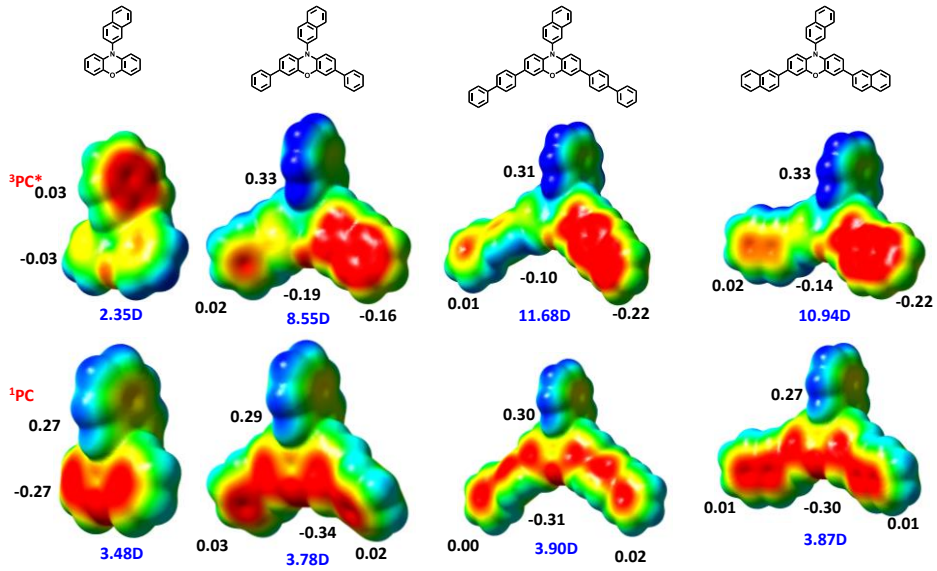

Figure 3.108. *Electrostatic potential (ESP) mapped electron density for PCs* ***3***, ***4***, ***5***, *and* ***17*** *(from left to right) in the ground state (bottom) and triplet excited state (top) are shown. Red color represents electron rich regions and blue color represents electron deficient regions; the computed dipole moment (μ) for each PC in units of Debye (D) are shown in dark blue.*

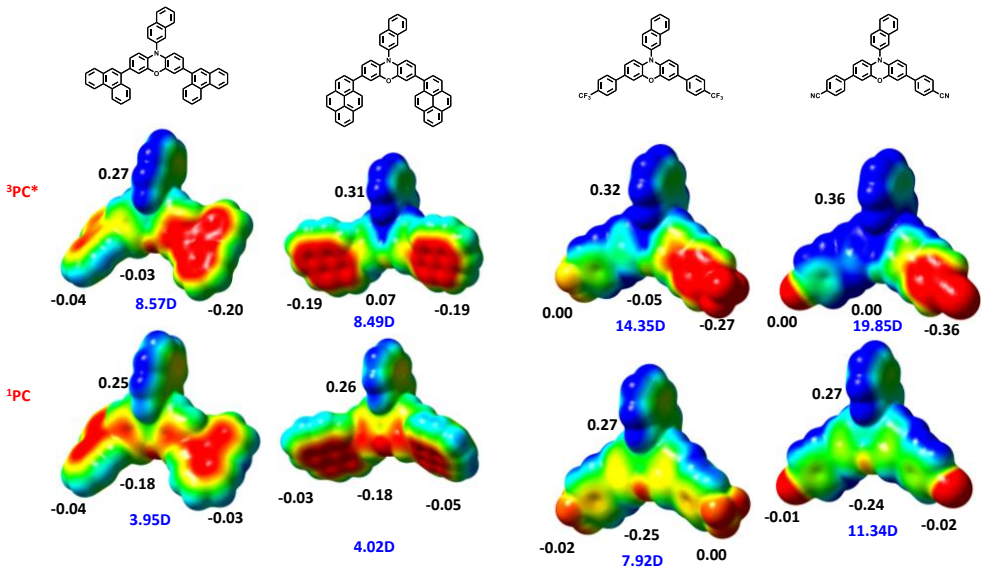

Figure 3.109. *Electrostatic potential (ESP) mapped electron density for PCs* ***15****,* ***16****,* ***13****, and* ***12*** *(from left to right) in the ground state (bottom) and triplet excited state (top) are shown. Red color represents electron rich regions and blue color represents electron deficient regions; the computed dipole moment (μ) for each PC in units of Debye (D) are shown in dark blue.*

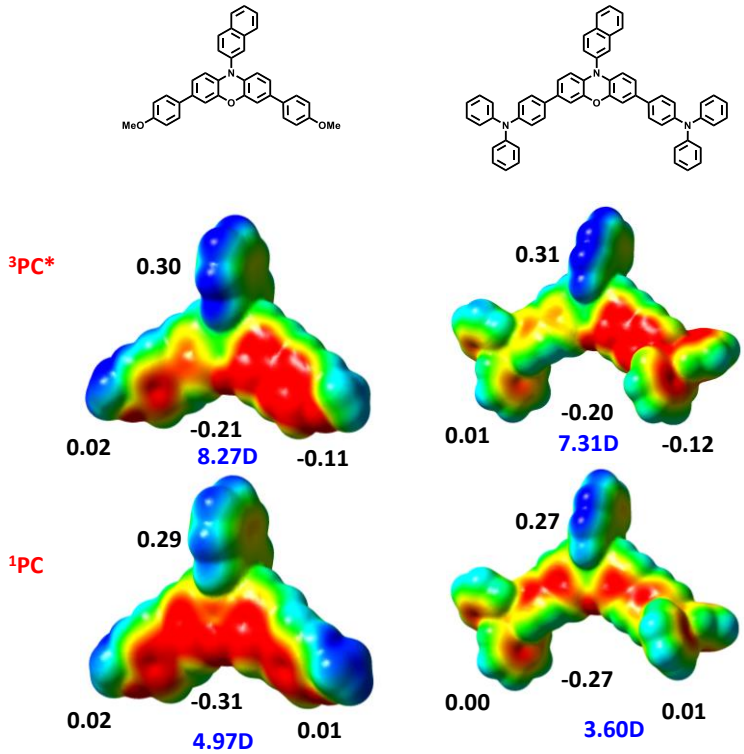

Figure 3.110. *Electrostatic potential (ESP) mapped electron density for PCs* ***11*** *and* ***14*** *(from left to right) in the ground state (bottom) and triplet excited state (top) are shown. Red color represents*

electron rich regions and blue color represents electron deficient regions; the computed dipole moment (μ) for each PC in units of Debye (D) are shown in dark blue.

8. Additional Polymerization Data

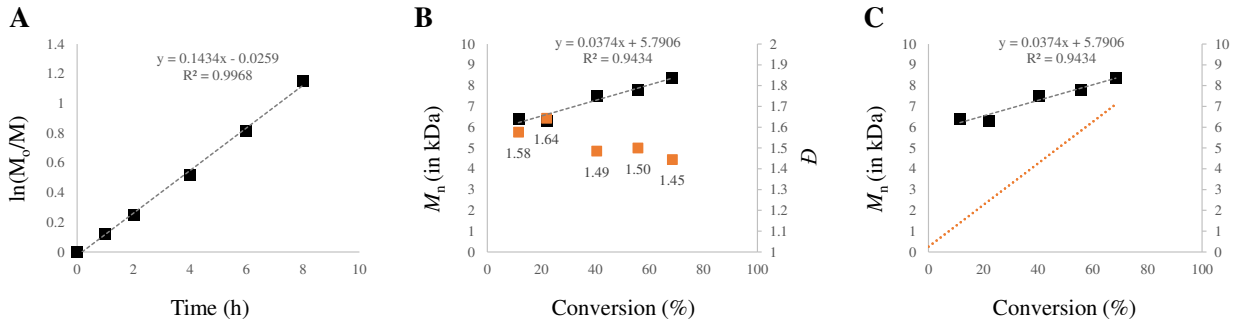

Figure 3.111. *Polymerization of methyl methacrylate performed according to the general polymerization procedure using photoredox catalyst **4** in a white-light LED beaker. A) plot of the natural log of monomer consumption as a function of time B) plot of growth of molecular weight (black squares) and dispersity (orange squares) as a function of conversion C) plot of growth of molecular weight versus conversion (black squares, grey line is line of best fit) compared to the theoretical growth of molecular weight versus conversion (orange line)*

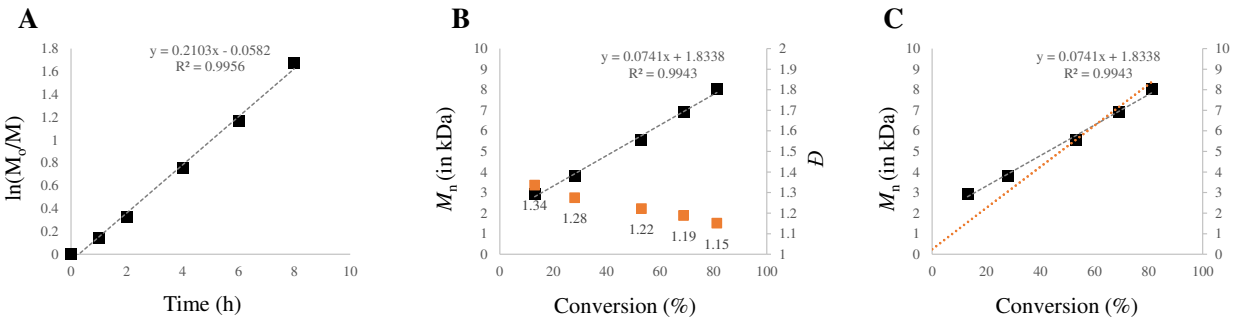

Figure 3.112. *Polymerization of methyl methacrylate performed according to the general polymerization procedure using photoredox catalyst **5** in a white-light LED beaker. A) plot of the natural log of monomer consumption as a function of time B) plot of growth of molecular weight (black squares) and dispersity (orange squares) as a function of conversion C) plot of growth of molecular weight versus conversion (black squares, grey line is line of best fit) compared to the theoretical growth of molecular weight versus conversion (orange line)*

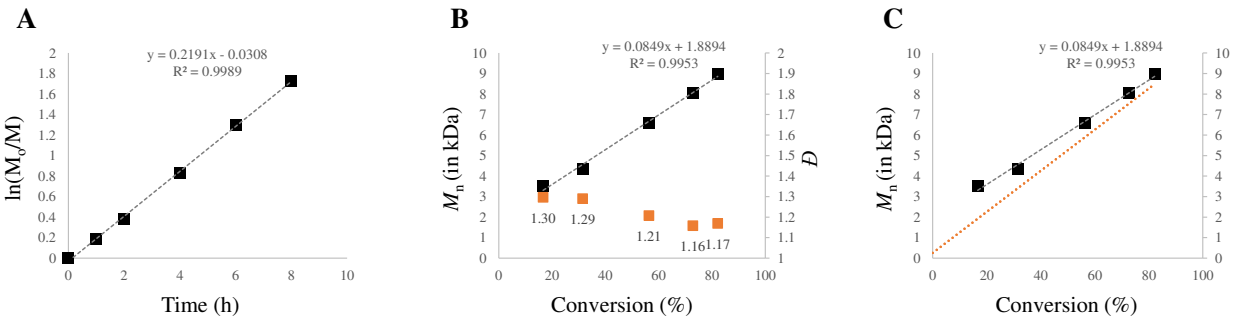

Figure 3.113. *Polymerization of methyl methacrylate performed according to the general polymerization procedure using photoredox catalyst* ***17*** *in a white-light LED beaker. A) plot of the natural log of monomer consumption as a function of time B) plot of growth of molecular weight (black squares) and dispersity (orange squares) as a function of conversion C) plot of growth of molecular weight versus conversion (black squares, grey line is line of best fit) compared to the theoretical growth of molecular weight versus conversion (orange line)*

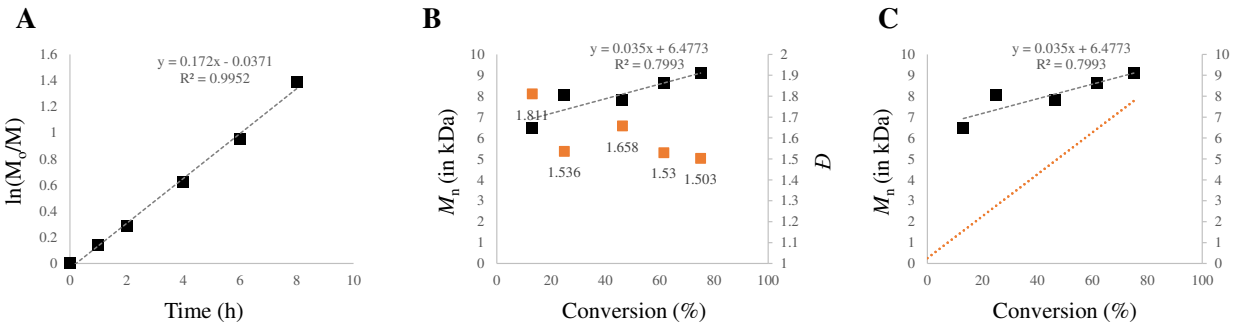

Figure 3.114. *Polymerization of methyl methacrylate performed according to the general polymerization procedure using photoredox catalyst* ***15*** *in a white-light LED beaker. A) plot of the natural log of monomer consumption as a function of time B) plot of growth of molecular weight (black squares) and dispersity (orange squares) as a function of conversion C) plot of growth of molecular weight versus conversion (black squares, grey line is line of best fit) compared to the theoretical growth of molecular weight versus conversion (orange line).*

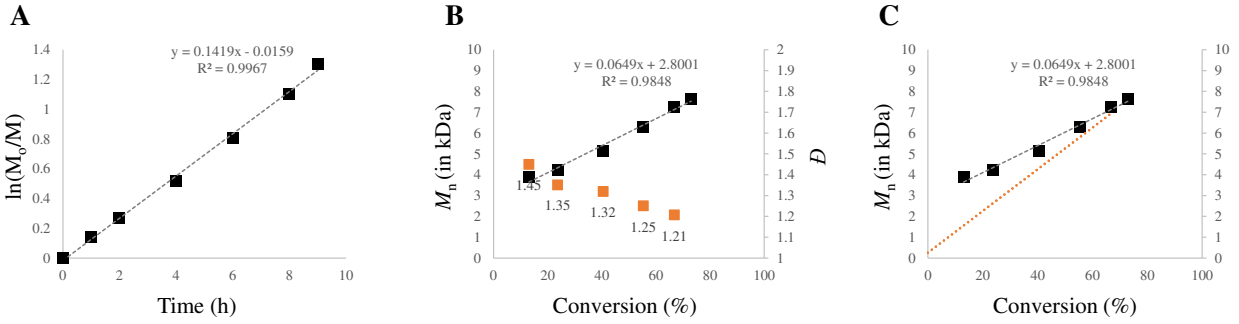

Figure 3.115. *Polymerization of methyl methacrylate performed according to the general polymerization procedure using photoredox catalyst* ***16*** *in a white-light LED beaker. A) plot of the*

natural log of monomer consumption as a function of time B) plot of growth of molecular weight (black squares) and dispersity (orange squares) as a function of conversion C) plot of growth of molecular weight versus conversion (black squares, grey line is line of best fit) compared to the theoretical growth of molecular weight versus conversion (orange line)

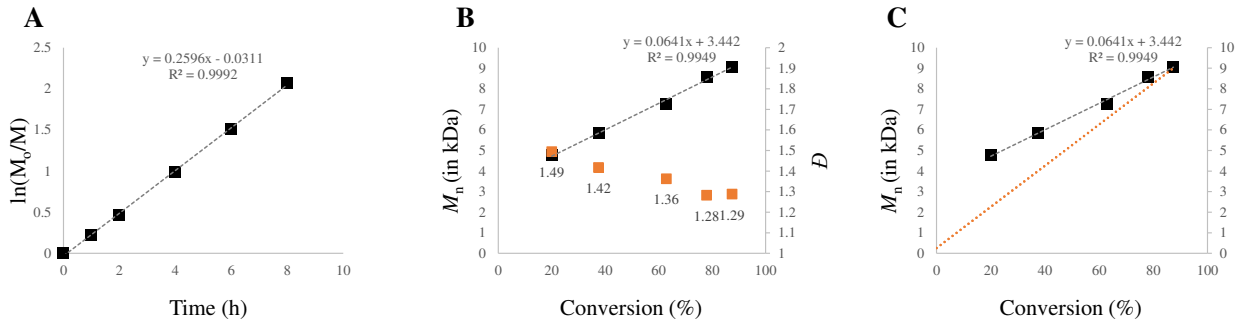

Figure 3.116. *Polymerization of methyl methacrylate performed according to the general polymerization procedure using photoredox catalyst* ***13*** *in a white-light LED beaker. A) plot of the natural log of monomer consumption as a function of time B) plot of growth of molecular weight (black squares) and dispersity (orange squares) as a function of conversion C) plot of growth of molecular weight versus conversion (black squares, grey line is line of best fit) compared to the theoretical growth of molecular weight versus conversion (orange line)*

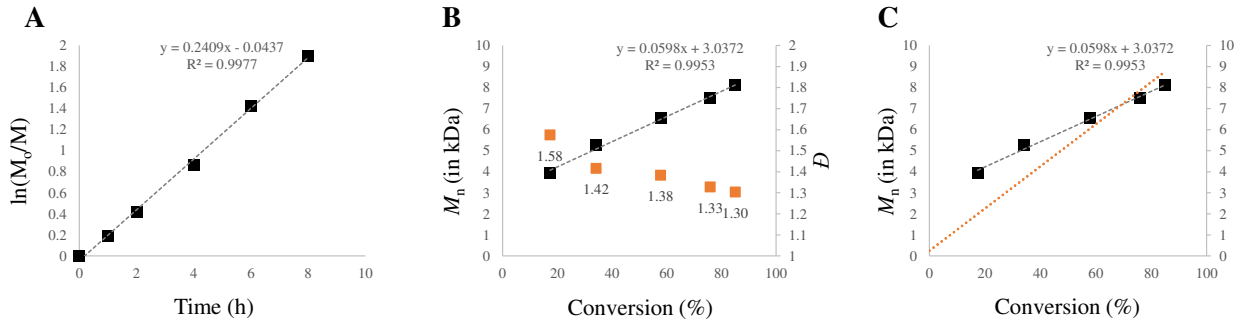

Figure 3.117. *Polymerization of methyl methacrylate performed according to the general polymerization procedure using photoredox catalyst* ***12*** *in a white-light LED beaker. A) plot of the natural log of monomer consumption as a function of time B) plot of growth of molecular weight (black squares) and dispersity (orange squares) as a function of conversion C) plot of growth of molecular weight versus conversion (black squares, grey line is line of best fit) compared to the theoretical growth of molecular weight versus conversion (orange line)*

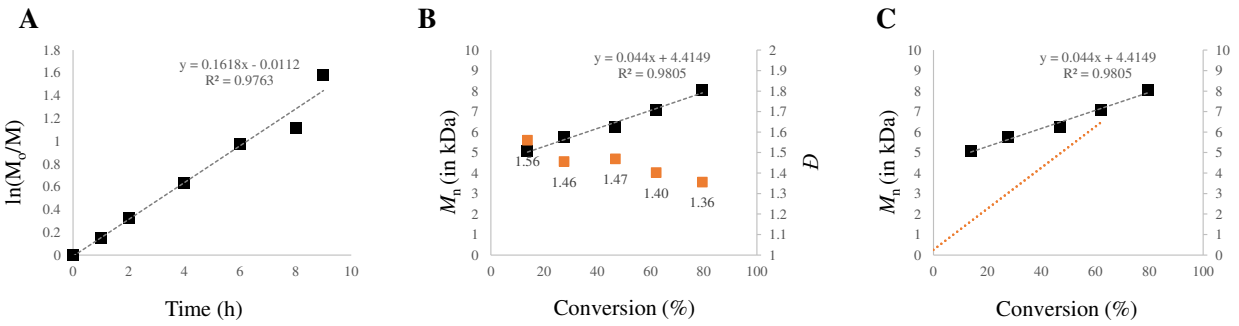

Figure 3.118. *Polymerization of methyl methacrylate performed according to the general polymerization procedure using photoredox catalyst* ***11*** *in a white-light LED beaker. A) plot of the natural log of monomer consumption as a function of time B) plot of growth of molecular weight (black squares) and dispersity (orange squares) as a function of conversion C) plot of growth of molecular weight versus conversion (black squares, grey line is line of best fit) compared to the theoretical growth of molecular weight versus conversion (orange line)*

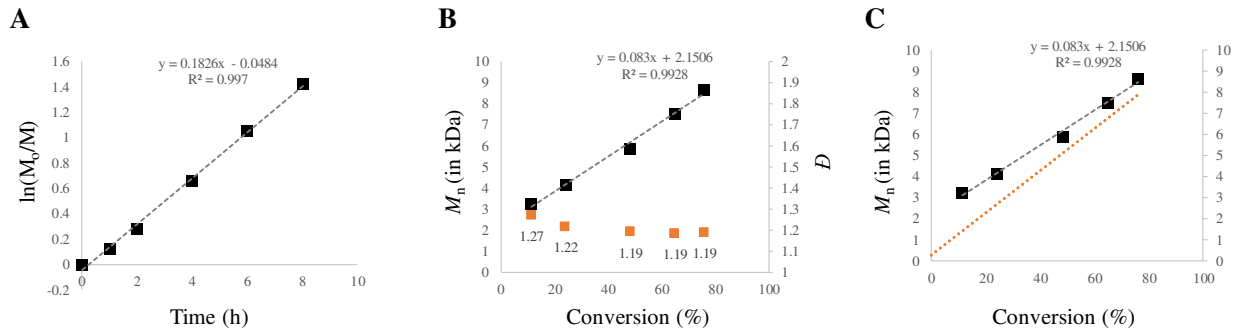

Figure 3.119. *Polymerization of methyl methacrylate performed according to the general polymerization procedure using photoredox catalyst* ***14*** *in a white-light LED beaker. A) plot of the natural log of monomer consumption as a function of time B) plot of growth of molecular weight (black squares) and dispersity (orange squares) as a function of conversion C) plot of growth of molecular weight versus conversion (black squares, grey line is line of best fit) compared to the theoretical growth of molecular weight versus conversion (orange line)*

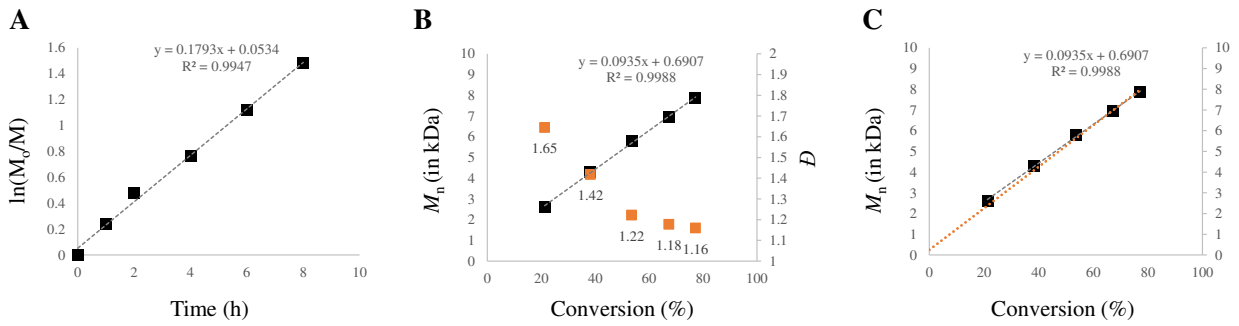

Figure 3.120. *Polymerization of methyl methacrylate performed according to the general polymerization procedure using photoredox catalyst* ***9*** *in a white-light LED beaker. A) plot of the natural log of monomer consumption as a function of time B) plot of growth of molecular weight (black squares) and dispersity (orange squares) as a function of conversion C) plot of growth of molecular weight versus conversion (black squares, grey line is line of best fit) compared to the theoretical growth of molecular weight versus conversion (orange line)*

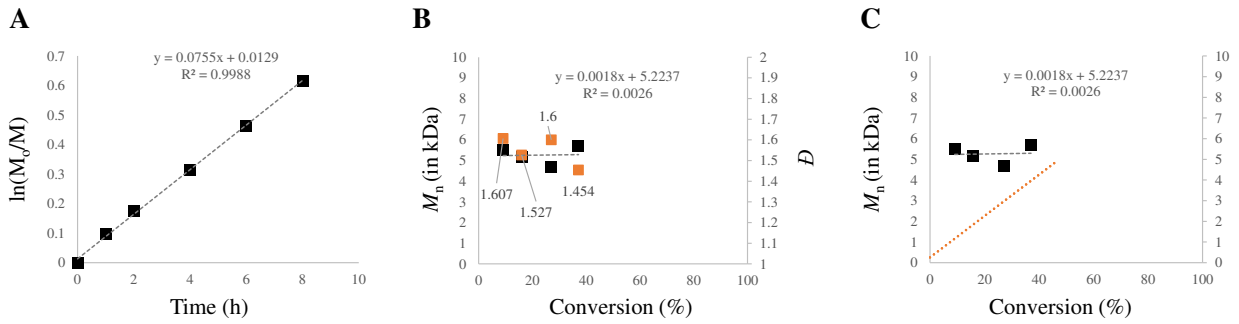

Figure 3.121. *Polymerization of methyl methacrylate performed according to the general polymerization procedure using photoredox catalyst* ***8*** *in a white-light LED beaker. A) plot of the natural log of monomer consumption as a function of time B) plot of growth of molecular weight (black squares) and dispersity (orange squares) as a function of conversion C) plot of growth of molecular weight versus conversion (black squares, grey line is line of best fit) compared to the theoretical growth of molecular weight versus conversion (orange line)*

9. Computational Details Part I

All calculations were performed using computational chemistry software package Gaussian 09 ver. D01.[24] We acknowledge the use of computational resource provided by XSEDE - Comet supercomputer.

a) Reduction Potentials

Standard reduction potentials (E^0) were calculated following previously reported procedures.[25–28] A value of -100.5 kcal/mol was assumed for the reduction free energy of the standard hydrogen electrode (SHE). Thus, E^0 = (-100.5 - ΔG_{red})/23.06 (V vs. SHE); for E^0 ($^2PC^{\bullet+}/^3PC^*$), ΔG_{red} = G($^3PC^*$) - G($^2PC^{\bullet+}$) while for E^0 ($^2PC^{\bullet+}/^1PC$), ΔG_{red} = G(^1PC) - G($^2PC^{\bullet+}$).

The Gibbs free energies of $^3PC^*$, $^2PC^{\bullet+}$, and ^1PC were calculated at the unrestricted M06/6-311+G** level of theory in CPCM-H_2O solvent (single point energy) using geometries optimized at unrestricted M06/6-31+G** level of theory in CPCM-H_2O solvent. For PC 14, 15 and 16 with extensive structures, frequency calculations were performed at unrestricted M06/6-31G** level of theory. The triple zeta basis set (6-311+G**) generally improves the E^0 ($^2PC^{\bullet+}/^1PC$) by ~0.1V relative to 6-31+G**, while the triplet energy is invariant for these two basis sets.

To reference to the Saturated Calomel Electrode (SCE), E^0 (vs. SHE) is converted to E^0 (vs. SCE) using E^0 (vs. SCE) = E^0 (vs. SHE) - 0.24 V. Triplet energies (in eV) of PCs were obtained by [G($^3PC^*$) - G(^1PC), in kcal/mol]/23.06.

Based on the comparison of our large experimental and computational data set, the choice of CPCM solvation model is justified as the computed reduction potential closely approximates the experimental values. For example, the computed ground state oxidation potentials between the $^2PC^{\bullet+}/^1PC$ redox couple is typically within ~0.2 to 0.3 V from the experimental values.

b) Excited State Calculation

Using optimized ground state geometries, single point time dependent density functional theory (TD-DFT) calculations were performed using the rCAM-B3LYP/6-31+G(d,p)/CPCM-DMA level of theory.[29] rCAM-B3LYP was chosen because it gave better λ_{max} predictions that are

closer to experimental values in comparison to rωB97xd level of theory; however, both of these methods gave similar results in terms of contributions of local excitation (LE) and charge transfer (CT) in the initial photoexcitation. TD-DFT calculations (with our chosen CAM-B3LYP method) corroborate experimental observations that UV-vis absorption becomes increasingly red-shifted with higher molar absorptivity as the aryl conjugation at the phenoxazine core position is increased (see Figure 3.3).

c) Electrostatic Potential (ESP) Calculation

At optimized geometries (ground state singlet and excited triplet states), single point energy calculations with CHELPG[30] ESP population analysis were performed at uM06/6-31G(d,p)/CPCM-DMA level of theory. Total electron density of ^{1}PC and ^{3}PC* were first plotted and then were mapped with ESP derived charges to show distribution of charges on the phenoxazine derivatives.

REFERENCES

(1) (a) Tucker, J. W.; Stephenson, C. R. J. *J. Org. Chem.* **2012**, *77*, 1617–1622. (b) Prier, C. K.; Rankic, D. A.; Macmillan, D. W. C. *Chem. Rev.* **2013**, *113*, 5322–5363. (c) Schultz, D. M.; Yoon, T. P. *Science* **2014**, *343*, 985. (d) Yoon, T. P.; Stephenson, C. R. J. *Adv. Synth. Catal.* **2014**, *356*, 2739. (e) Corrigan, N.; Shaanmugam, S.; Xu, J.; Boyer, C. *Chem. Soc. Rev.* **2016**, *45*, 6165−6212. (f) Chen, M.; Zhong, M.; Johnson, J. A. *Chem. Rev.* **2016**, *116*, 10167−10211. (g) Shaw, M. H.; Twilton, J.; MacMillan, D. W. C.; *J. Org. Chem.* **2016**, *81*, 6898−6926. (h) Michaudel, Q.; Kottisch, V.; Fors, B. P. *Angew. Chem. Int. Ed.* **2017**, *56*, 9760–9679.

(2) (a) Hedstrand, D. M.; Kruizinga, W. M.; Kellogg, R. M. *Tetrahedron Lett.* **1978**, *19*, 1255−1258. (b) van Bergen, T. J.; Hedstrand, D. M.; Kruizinga, W. H.; Kellogg, R. M. *J. Org. Chem.* **1979**, *44*, 4953−4962. (c) Soc, C.; Narayanam, J. M. R.; Stephenson, C. R. J. *Chem. Soc. Rev.* **2011**, *40*, 102–113.

(3) (a) Sauvage, J.-C.; Collin, J.-P. Chambron, J.-C.; Guillerez, S.; Coudret, C. *Chem. Rev.* **1994**, *94*, 993–1019. (b) Damrauer, N. H.; Cerullo, G.; Yeh, A.; Boussie, T. R.; Shank, C. V; McCusker, J. K. *Science* **1997**, *275*, 54–57.

(4) (a) Higgins, R. F.; Fatur, S. M.; Shepard, S. G.; Stevenson, S. M.; Boston, D. J.; Ferreira, E. M.; Damrauer, N. H.; Rappé A.K.; Shores, M. P. *J. Am. Chem. Soc.* **2016**, *138*, 5451–5464. (b) Kainz, Q. M.; Matier, C. D.; Bartoszewicz, A.; Zultanski, S. L.; Peters, J. C.; Fu, G. C. *Science*, **2016**, *351*, 681–684. (c) Romero, N. A.; Nicewicz, D. A. *Chem. Rev.* **2016**, *116*, 10075–10166. (d) Joshi-Pangu, A.; Levesque, F.; Roth, H. G.; Oliver, S. F.; Campeau, L-C.; Nicewicz, D.; DiRocco, D. A. *J. Org. Chem.* **2016**, *81*, 7244–7249.

(5) (a) Poelma, S. O.; Burnett, G. L.; Discekici, E. H.; Mattson, K. M.; Treat, N. J.; Luo, Y.; Hudson, Z. M.; Shankel, S. L.; Clark, P. G.; Kramer, J. W.; Hawker, C. J.; Read de Alaniz, J. *J.*

Org. Chem. **2016**, *81*, 7155–7160. (b) Treat, N. J.; Sprafke, H.; Kramer, J. W.; Clark, P. G.; Barton, B. E.; Alaniz, J. R. De; Fors, B. P.; Hawker, C. J. *J. Am. Chem. Soc.* **2014**, *136*, 16096–16101. (c) Hudson, Z. M.; Luo, Y.; Hawker, J.; Read, J.; Alaniz, D. A *Chem Commun.* **2015**, *51*, 11705–11708. (d) Pan, X.; Fang, C.; Fantin, M.; Malhotra, N.; So, W. Y. Peteanu, L. A.; Isse, A. A.; Gennaro, A.; Liu, P.; Matyjaszewski, K. *J. Am. Chem. Soc.* **2016**, *138*, 2411–2425. (e) Miyake, G. M.; Theriot, J. C. *Macromolecules* **2014**, *47*, 8255–8261. (f) Theriot, J. C.; Lim, C.; Yang, H.; Ryan, M. D.; Musgrave, C. B.; Garret, M. *Science* **2016**, *352*, 1082–1086. (g) Pearson, R. M.; Lim, C.; McCarthy, B. G.; Musgrave, C. B.; Miyake, G. M. *J. Am. Chem. Soc.* **2016**, *138*, 11399–11407.

(6) (a)Fors, B. P.; Hawker, C. J. *Angew. Chem. Int. Ed.* **2012**, *51*, 8850–8853. (b) Treat, N. J.; Fors, B. P.; Kramer, J. W.; Christianson, M.; Chiu, C-Y.; Read de Alaniz, J.; Hawker, C. J. *ACS Macro Lett.* **2014**, *3*, 580–584.

(7) (a) Lim, C.; Ryan, M. D.; McCarthy, B. G.; Theriot, J. C.; Sartor, S. M.; Damrauer, N. H.; Musgrave, C. B.; Miyake, G. M. *J. Am. Chem. Soc.* **2017**, *139*, 348–355. (b) Ryan, M. D.; Theriot, J.C., Lim, C-H.; Yang, H.; Lockwood, A.G.; Garrison, N. G.; Lincoln, S. R.; Musgrave, C. B.; Miyake, G.M. *J. Polym. Sci. A.* **2017**, *55*, 3017–3027.

(8) (a) Frick, E.; Anastasaki, A.; Haddleton, D. M.; Barner-Kowollik, C. *J. Am. Chem. Soc.* **2015**, *137*, 6889−6896. (b) Ribelli, G. G.; Konkolewicz, D.; Bernhard, S.; Matyjaszewski, K. *J. Am. Chem. Soc.* **2014**, *136*, 13303−13312.

(9) (a) Zhu, Y.; Babel, A.; Jenekhe, S. A. *Macromolecules* **2005**, *38*, 7983–7991. (b) Zhu, Y.; Kulkarni, A. P.; Wu, P.; Jenekhe, S. A. *Chem. Mater.* **2008**, *20*, 4200–4211.

(10) Ramsey, B. L.; Pearson, R. M.; Beck, L. R.; Miyake, G. M. *Macromolecules*, **2017**, *50*, 2668–2674.

(11) Ryan, M. D.; Pearson, R. M.; French, T. A.; Miyake, G. M. *Macromolecules* **2017**, *50*, 4616–4622.

(12) Du, Y.; Pearson, R. M.; Lim, C.; Sartor, S. M.; Ryan, M. D.; Yang, H.; Damrauer, N. H.; Miyake, G. M. *Chem. Eur. J.* **2017**, *23*, 10962–10968.

(13) (a) Sullivan, B. P.; Nagle, J. K. *J. Am. Chem. Soc.* **1979**, *101*, 4816–4824. (b) Springer: Berlin Heidelberg, *Top. Curr. Chem.* **2007**, *281*. (c) Dixon, I. M.; Collin, J.; Sauvage, J.; Flamigni, L.; Collin, J.; Sauvage, I. D. *J. Chem. Soc. Rev.* **2000**, *29*, 385–391.

(14) Arias-rotondo, D. M.; McCusker, J. K. *Chem. Soc. Rev.* **2016**, *45*, 5803–5820.

(15) (a) Benniston, A. C.; Harriman, A.; Li, P.; Rostron, J. P.; Ramesdonk, H. J. Van; Groeneveld, M. M.; Zhang, H.; Verhoeven, J. W. *J. Am. Chem. Soc.* **2005**, *127*, 16054–16064. (b) Tanaka, H.; Shizu, K.; Nakanotani, H.; Adachi, C. *Chem Mater*. **2013**, *25*, 3766–3771. (c) Fukuzumi, S.; Kotani, H.; Ohkubo, K.; Ogo, S.; Tkachenko, N. V.; Lemmetyinene, H. *J. Am. Chem. Soc.* **2004**, *126*, 1600–1601.

(16) (a) Zhao, Y.; Gong, H.; Jiang, K.; Yan, S.; Lin, J.; Chen, M. *Macromolecules* **2018**, *51*, 938–946. (b) Gong, H.; Zhao, Y.; Shen, X.; Lin, J.; Chen, M.; *Angew. Chem. Int. Ed.* **2018**, *57*, 333–337.

(17) Reichardt, C. *Chem. Rev.* **1994**, *94*, 2319–2358.

(18) (a) Lee, J.; Shizu, K.; Tanaka, H.; Nakanotani, H.; Yasuda, T.; Kaji, H.; Adachi, C. *J. Mater. Chem. C* **2015**, *3*, 2175–2181. (b) Uoyama, H.; Goushi, K.; Shizu, K.; Nomura, H.; Adachi, C. *Nature* **2012**, *492*, 234–238. (c) Tao, Y.; Yuan, K.; Chen, T.; Xu, P.; Li, H.; Chen, R.; Zheng, C.; Zhange, L.; Huang, W. *Adv Mater.* **2014**, *26*, 7931–7958.

(19) Roth, H. G.; Romero, N. A.; Nicewicz, D. A. *Synlett* **2016**, *27*, 714–723.

(20) (a) Theriot, J. C.; McCarthy, B. G.; Lim, C-H.; Miyake, G. M. *Macromol. Rapid Commun.* **2017**, *38*, 1700040. (b) Pan, X.; Fang, C.; Fantin, M.; Malhotra, N.; So, W. Y.; Peteanu, L. A.; Isse, A. A.; Gennaro, A.; Liu, P.; Matyjaszewski, K. *J. Am. Chem. Soc.* **2016**, *138*, 2411–2425.

(21) Isse, A. A.; Lin, C. Y.; Coote, M. L.; Gennaro, A. *J. Phys. Chem. B* **2011**, *115*, 678–684.

(22) (a) Matyjaszewski, K.; Xia, J.; *Chem. Rev.* **2001**, *101*, 2921–2990. b) Coessens, V.; Pintauer, T.; Matyjaszewski, K.; *Prog. Polym. Sci.* **2001**, *26*, 337–377. c) Ouchi, M.; Terashima, T.; Sawamoto, M. *Chem. Rev.* **2009**, *109*, 4963–5050.

(23) (a) Matyjaszewski, K. *Macromolecules* **2012**, *45*, 4015–4039. (b) Nicolas, J.; Guillaneuf, Y.; Lefay, C.; Bertin, D.; Gigmes, D.; Charleux B. *Prog. Polym. Sci.* **2013**, *38*, 63–235. (c) Moad, G.; Rizzardo, E.; Thang, S. *Polymer* **2005**, *46*, 8458–8468. (d) Kamigaito, M.; Ando, T.; Sawamoto, M. *J. Am. Chem. Soc.* **2001**, *101*, 3689–3746.

(24) Gaussian 09, R. D., Frisch, M. J.; Trucks, G. W.; Schlegel, H. B.; Scuseria, G. E.; Robb, M. A.; Cheeseman, J. R.; Scalmani, G.; Barone, V.; Mennucci, B.; Petersson, G. A.; Nakatsuji, H.; Caricato, M.; Li, X.; Hratchian, H. P.; Izmaylov, A. F.; Bloino, J.; Zheng, G.; Sonnenberg, J. L.; Hada, M.; Ehara, M.; Toyota, K.; Fukuda, R.; Hasegawa, J.; Ishida, M.; Nakajima, T.; Honda, Y.; Kitao, O.; Nakai, H.; Vreven, T.; Montgomery, J. A., Jr.; Peralta, J. E.; Ogliaro, F.; Bearpark, M.; Heyd, J. J.; Brothers, E.; Kudin, K. N.; Staroverov, V. N.; Kobayashi, R.; Normand, J.; Raghavachari, K.; Rendell, A.; Burant, J. C.; Iyengar, S. S.; Tomasi, J.; Cossi, M.; Rega, N.; Millam, J. M.; Klene, M.; Knox, J. E.; Cross, J. B.; Bakken, V.; Adamo, C.; Jaramillo, J.; Gomperts, R.; Stratmann, R. E.; Yazyev, O.; Austin, A. J.; Cammi, R.; Pomelli, C.; Ochterski, J. W.; Martin, R. L.; Morokuma, K.; Zakrzewski, V. G.; Voth, G. A.; Salvador, P.; Dannenberg, J. J.; Dapprich, S.; Daniels, A. D.; Farkas, Ö.; Foresman, J. B.; Ortiz, J. V.; Cioslowski, J.; Fox, D. J. Gaussian, Inc., Wallingford CT, 2009.

(25) He, H.; Zapol, P.; Curtiss, L. A. *J. Phys. Chem. C,* **2010**, *114*, 21474–21481.

(26) Tossell, J. A. *Comput. Theor. Chem.* **2011**, *977*, 123–27.

(27) Winget, P.; Cramer, C. J.; Truhlar, D. G. *Theor. Chem. Acc.* **2004**, *112*, 217–227.

(28) Zhao, Y.; Truhlar, D. *Theor. Chem. Acc.* **2008**, *120*, 215–241.

(29) Yanai, T.; Tew, D. P.; Handy, N. C. *Chem. Phys. Lett.* **2004**, *393*, 51–57.

(30) Spackman, M. A. *J. Comput. Chem.* **1996**, *17*, 1–18.

CHAPTER 4 – ORGANOCATALYZED ATOM TRANSFER RADICAL POLYMERIZATION CATALYZED BY CORE MODIFIED *N*-ARYL PHENOXAZINES PERFORMED UNDER AIR

Overview

Organocatalyzed atom transfer radical polymerization (O-ATRP) was performed under air using core modified *N*-aryl phenoxazines as photoredox catalysts (PCs) to synthesize poly(methyl methacrylate) in a controlled fashion with initiator efficiency ($I^* = M_{n,theo}/M_n \times 100$) ranging from 84 to 99% and dispersity being ~1.2−1.3. Reduction of the reaction vial headspace was key for enabling the polymerization to proceed in a controlled fashion, as has been observed in Cu-catalyzed controlled radical polymerizations. The ability to synthesize block copolymers and turn the polymerization on and off via manipulation of the light source was demonstrated. Six core modified *N*-aryl phenoxazines were able to catalyze O-ATRP under air, albeit with most PCs achieving I^*s ~ 5% lower under air compared to when the reaction was performed under nitrogen.

Introduction

Controlled radical polymerization (CRP) methods mediated by photoredox catalysis have enabled the synthesis of polymeric materials with complex functionality and architecture under mild conditions that can be controlled through the manipulation of a light source.[1,2] The ability to control the polymerization spatially and temporally using a light source enables the application of these methods for photolithography and 3D-printing.[3,4] One barrier hindering the potential of photoredox catalyzed CRPs is the inability to perform these reactions under air. This challenge arises because oxygen (~20% of air) can quench propagating radical species[5] and is a triplet in the

ground state which can engage in triplet−triplet annihilation with other triplet species, in particular photoredox catalysts (PCs) that operate from a triplet excited state.[6]

Significant advances have been made in the development of oxygen tolerant photoredox catalyzed CRPs, but the majority of this work has focused on derivatives of reversible addition−fragmentation chain transfer polymerization.[7] Less attention has been paid to photoredox catalyzed variants of atom transfer radical polymerization (ATRP). Our interest in photoredox catalyzed variants of ATRP originated from our work on the development of organocatalyzed atom transfer radical polymerization (O-ATRP). Our group has investigated visible-light driven O-ATRP systems using organic dyes including perylene,[8] *N*,*N*-diaryl dihydrophenazines,[9−12] and *N*-aryl phenoxazines[13−15] as PCs. Despite the progress of our group and others[16−24] developing O-ATRP systems,[25,26] little progress has been made developing oxygen tolerant variants.

In copper catalyzed ATRP, oxygen tolerance has been achieved through a variety of methods which often involve regeneration of the activating Cu(I)/Cu(0) catalyst after it has been oxidized to form Cu(II)/Cu(I) by oxygen.[7] More recently, it has been suggested that the initiator also plays a role in oxygen consumption.[27] In addition to regenerating the catalyst through addition of exogenous reagents or the use of external stimuli, the volume of air available to the reaction mixture has also been identified as a key parameter. For example, increasing the volume of headspace of air in the reaction vessel for Cu-catalyzed ATRP slowed the polymerization such that performing the reaction in a flask open to air inhibited the reaction.[28] Similarly, in Cu-catalyzed reversible deactivation radical polymerizations performed under air, decreasing the reaction vessel headspace increased the rate of polymerization while retaining controlled characteristics such that elimination of vial headspace led to the most rapid controlled polymerization.[27] The decrease in

polymerization kinetics with increasing headspace volume was attributed to the increased amount of oxygen available to oxidize the activating species.

Results and Discussion

In our previous work we observed that the O-ATRP of methyl methacrylate (MMA) catalyzed by perylene, *N*,*N*-diaryldihydrophenazines, *N*-aryl phenoxazines, or core modified *N*-aryl phenoxazines (such as PC 1, Table 4.1) performed under air resulted in an uncontrolled polymerization or no polymerization.[8,9,13] However, these reactions were performed in 20 mL scintillation vials with ~18 mL of headspace of air. Inspired by previous ATRP reports demonstrating the beneficial effects of reducing the volume of reaction vial headspace for polymerizations performed under air,[27,28] we sought to determine if this would have a similar effect on O-ATRP systems. To study the effect of air on O-ATRP, the O-ATRP of MMA catalyzed by 1 was chosen as a model system since PC 1 was previously shown to catalyze O-ATRP under a variety of conditions[13,29,30] for the synthesis of polymers with complex composition[31] and architecture.[32] Minimal reagent purification was performed to enable saturation of air in the reaction mixtures (see *Experimental* section for more details).

Table 4.1. Results of the O-ATRP of MMA with Varied Reaction Vial Headspace[a]

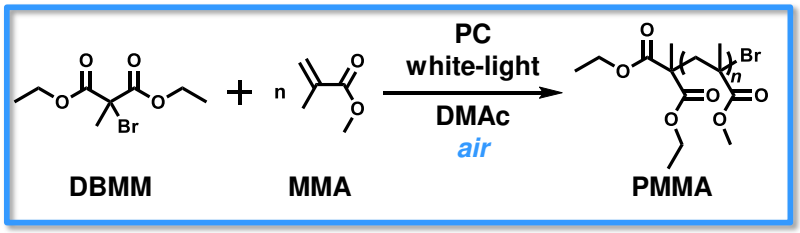

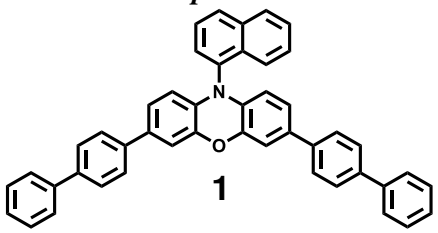

Run No.	Vial headspace of air (mL)	time (h)	conv. (%)	$M_{n,th}$ (kDa)	M_n (kDa)	M_w (kDa)	$Đ$ (M_w/M_n)	I^* ($M_{n,th}/M_n \times 100$)
1	18.2	24	36	3.9	7.6	14.5	1.90	50
2	5.55	24	69	7.1	9.4	11.8	1.25	75
3	3.71	24	77	8.0	10.5	12.8	1.22	76
4	1.86	8	53	5.5	7.3	8.8	1.21	76
5	0	8	68	7.0	8.1	9.8	1.22	87
6	0	26	95	9.8	11.3	13.2	1.18	87
7[b]	0	24	7	0.9	-	-	-	-
8[c]	0	24	0	0	-	-	-	-
9[d]	0	8	36	3.9	49.5	84.8	1.71	8

[a]*Reaction scheme for the O-ATRP of MMA performed under air (blue box) and structure of PC* ***1*** *(top right). The O-ATRP was performed with a [1000]:[10]:[1] ratio of MMA: diethyl 2-bromo-2-methylmalonate (DBMM): PC* ***1*** *(see Supporting Information for more details).* [b]*Reaction performed without PC.* [c]*Reaction performed without light.* [d]*Reaction performed without initiator.*

Performing the O-ATRP of MMA under air in a 20 mL scintillation vial (18.2 mL of headspace) led to only 36% monomer conversion after 24 h (Table 4.1, run 1). In accordance with our previous results,[13] the poly(methyl methacrylate) (PMMA) synthesized exhibited high dispersity, $Đ$, ($Đ$ = 1.90) a number-average molecular weight (M_n) which deviated appreciably from the theoretical value as indicated by a low initiator efficiency, I^*, ($I^* = M_{n,theo}/M_n \times 100$) of 50%, and a broad and asymmetric gel-permeation chromatography (GPC) trace (Figure 4.14), demonstrating that the polymerization was uncontrolled. Reducing the volume of air in the reaction vial had a drastic effect on the polymerization (Table 4.1, runs 1 and 2). The O-ATRP performed with reduced vial headspace (5.55 mL instead of 18.2 mL) proceeded more rapidly, reaching 69% conversion in 24 h (run 2) rather than 36% conversion (run 1), and exhibited characteristics of a controlled polymerization, producing PMMA with $Đ$ = 1.25 and I^* = 75%. Further reduction of

the reaction vial headspace continued to increase the rate of polymerization and the O-ATRP performed in a vial with no headspace reached 68% conversion in 8 h (run 5). All polymerizations performed exposed to 5.55 mL of headspace or less (runs 2−5) led to the synthesis of PMMA with moderate $Đ$ ($Đ \sim 1.2$) and I^* ranging from 75−87%, with the reaction performed in a vial with no headspace (run 5) exhibiting the best overall combination of low $Đ$ ($Đ = 1.22$) and high I^* ($I^* =$ 87%). Moreover, by performing the polymerization in a vial with no headspace for 26 h high monomer conversion was achieved (95%) while exhibiting controlled characteristics (PMMA $Đ$ = 1.18 and I^* = 87%). Omission of PC (run 7), light (run 8), or initiator (run 9) led to no polymerization or an uncontrolled polymerization.

To further explore the effect of air on the O-ATRP of MMA, polymerizations were performed with no vial headspace under air or under nitrogen for comparison and monitored over time (Figure 4.1). Given that 0.5 dram vials allowed for the reactions to be performed on a reasonable scale (8.60 mmol) with no vial headspace, a modified photoreactor was employed, which allowed for efficient stirring of these vials while employing the same light source used to investigate the effect of vial headspace on the reaction (see Supporting Information for more details). For the O-ATRP of MMA performed under air, pseudo first order kinetics were observed for monomer consumption over time (Figure 4.1A, left) and analysis of the of PMMA synthesized revealed linear growth of polymer molecular weight as a function of monomer conversion with measured M_n values in agreement with theoretical values (Figure 4.1A, right) and polymer $Đ \sim$ 1.2−1.3.

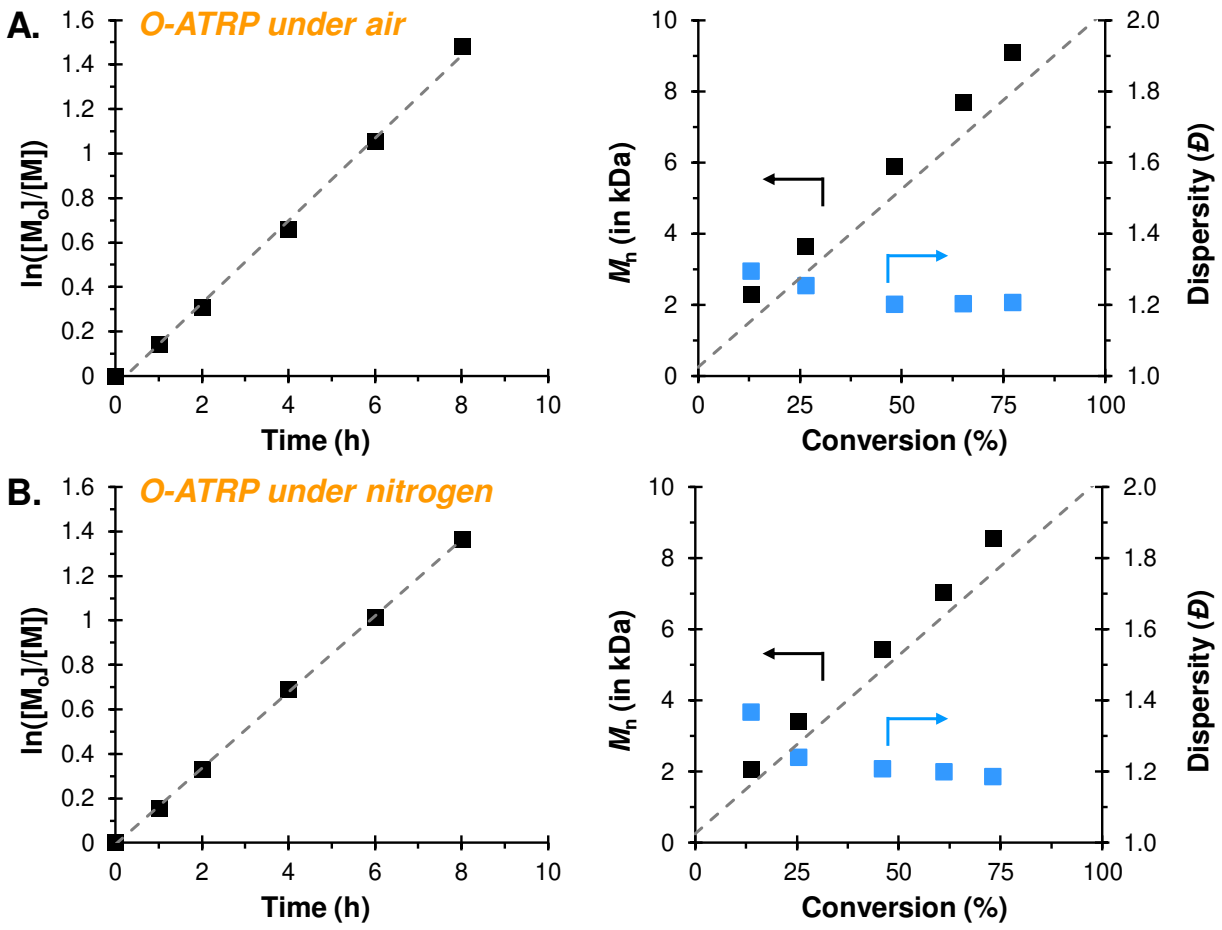

Figure 4.1. *Plots of the natural log of monomer consumption as a function of time (left) for the O-ATRP of MMA mediated by* ***1*** *under air (A) or under nitrogen (B) with a [1000]:[10]:[1] ratio of MMA: DBMM: PC* ***1****. Plots of growth of the experimentally measured M_n as a function of monomer conversion (right, black squares) with theoretical values (grey, dashed line). Dispersity of the PMMA at each M_n is shown (blue squares).*

Conducting the O-ATRP of MMA under nitrogen using PC 1 and reagents which were purified rigorously to exclude air yielded similar results to the O-ATRP performed under air (Figure 4.1B). In particular, the polymerization performed under nitrogen proceeded with a similar rate (O-ATRP under air reached 77% conversion in 8 h while the reaction under nitrogen reached 74% conversion) and synthesized PMMA exhibiting similar $Đ$ ($Đ \sim 1.2$). However, performing the reaction under nitrogen led to better control over polymer M_n, as evidenced by a higher I^* of 94% (compared to the reaction performed under air which exhibited $I^* = 88\%$). Proton NMR

analysis of precipitated PMMA synthesized under air or under nitrogen revealed no significant differences in polymer structure (Figures 4.10 and 4.11 of the *Experimental* section).

Temporal control was investigated for the O-ATRP of MMA performed under air using a pulsed irradiation experiment over the course of several days (Figure 4.2). Monomer conversion was only observed during irradiation periods (Figure 4.2A) accompanied by a linear increase in polymer M_n as a function of conversion with polymer $Đ$ remaining ~1.2 (Figures 4.2B, C). Removal of the light source halted the polymerization (for up to 22 h) with no further monomer conversion (Figure 4.2A), growth of polymer M_n (Figure 4.2B), or shift in the retention times of polymer GPC traces (Figure 4.2C). Comparison of polymer M_n, $Đ$, and GPC traces before and after dark periods revealed marginal differences in these data, indicating that air had no deleterious effects on the ability of PC 1 to (re)activate polymer chains in the presence of light (Figures 4.2A,B). Moreover, PC 1 was able to resume the polymerization after removing the light source for an extended period of time (16 h), suggesting that the PC exhibits some stability in the presence of air, albeit in the absence of light.

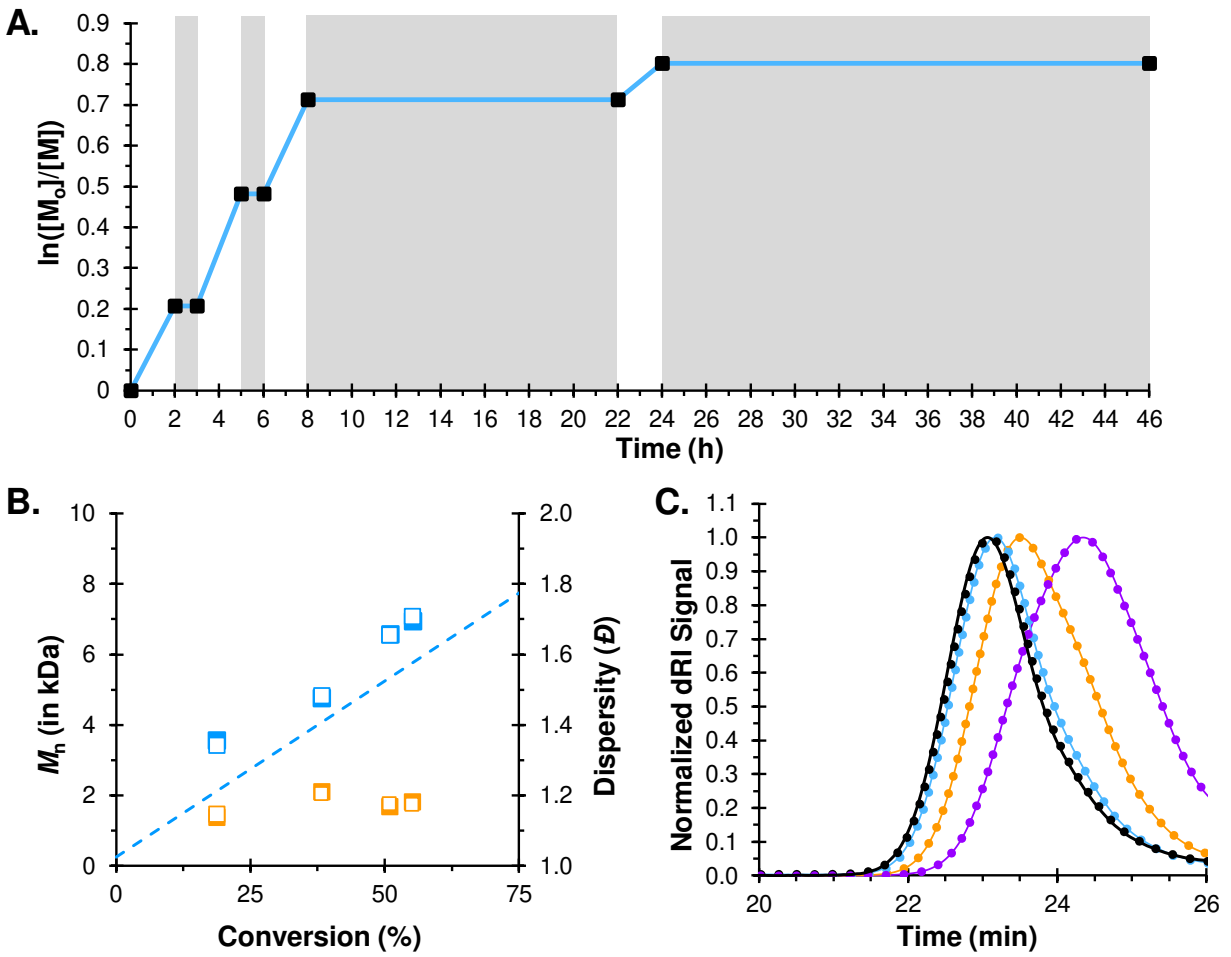

Figure 4.2. *Plot of growth of the natural log of monomer consumption as a function of time for a pulsed irradiation experiment conducted under air (A). Plot of growth of the experimentally measured M_n as a function of monomer conversion with theoretical M_n values (B, filled, blue squares are M_n values directly after irradiation while open markers are data directly after dark periods; blue dashed line shows theoretical M_n values). Dispersity of the PMMA at each M_n are shown (filled, orange squares are data directly after irradiation while open markers are data directly after dark periods). Gel permeation chromatography traces of PMMA synthesized during the pulsed irradiation experiment (C, traces with dotted lines are after each irradiation period and traces with bold lines are after dark periods).*

The reversible deactivation equilibrium established in O-ATRP enables the synthesis of polymers with high chain end group fidelity which can initiate subsequent polymerizations allowing for the synthesis of polymers with complex composition and architecture. To explore this feature in O-ATRP systems performed under air, matrix-assisted laser desorption/ ionization time-of-flight (MALDI−TOF) analysis (Figure 4.25 of the *Experimental* section) was performed on a

PMMA macroinitiator synthesized under air (Table 4.5 of the *Experimental* section). Peaks in the MALDI−TOF spectrum were assigned to polymer with a DBMM-derived α-end group and either a bromide or hydrogen ω-end group. Presence of the bromide end group supports the reversible-deactivation mechanism, while presence of the polymers with hydrogen terminal groups indicates the occurrence of termination events involving hydrogen abstraction. To gain insight into the proportion of polymer chains bearing alkyl bromide chain end groups, the PMMA macroinitiator was introduced to either additional MMA or benzyl methacrylate (BnMA) using O-ATRP conditions (Figure 4.3A). Shorter retention times were observed for the GPC trace of the chain-extended PMMA compared to the PMMA macroinitiator (Figure 4.3B) accompanied by a higher measured M_n value (M_n = 8.2 kDa for the macroinitiator and M_n = 20.6 kDa after chain extension with MMA) and high I^* (I^* = 89%), indicating good bromide chain end group fidelity of the macroinitiator. Addition of BnMA to the PMMA macroinitiator using O-ATRP conditions under air allowed for the synthesis of a poly(MMA-b-BnMA) copolymer with high I^* (I^* = 89%), and $Đ$ = 1.50, demonstrating control over the polymerization even at high conversion (94% conversion).

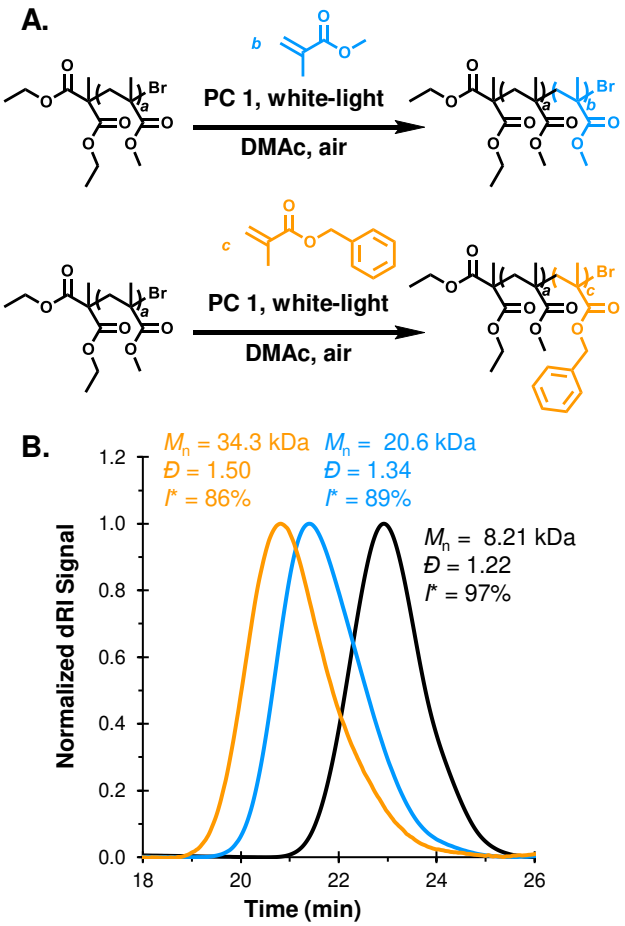

Figure 4.3. *Chain extension polymerizations with MMA (A, top) or BnMA (A, bottom) performed under air from a PMMA macroinitiator synthesized via O-ATRP under air. GPC traces of the PMMA macroinitiator synthesized under air before (B, black trace) and after addition of MMA (B, blue trace) or BnMA (B, orange trace).*

To gain further insight into the catalytic performance of core modified N-aryl phenoxazines in O-ATRP performed under air, five additional PCs (Table 4.2, PCs 2−6) exhibiting a range of photophysical and redox properties (Tables 4.3 and 4.4 of the *Experimental* section) were investigated. In accordance with our previous results,13 performing the O-ATRP of MMA under nitrogen using the modified photoreactor revealed that the PCs that exhibit stronger visible light absorption and more strongly reducing excited states (PCs 1−4) synthesized PMMA with lower *Đ* and higher I^* than the other PCs explored (Table 4.2, runs 9−16, odd numbered runs). The evaluation of success for this trend is based on the linearity of growth of polymer M_n as a function

of conversion and the ability of each PC to synthesize polymer with low $Đ$ and high I^* throughout the polymerization. PCs 1−6 were able to mediate the O-ATRP of MMA under air in a controlled fashion as demonstrated by the linear growth of polymer M_n as a function of monomer conversion (Figures 4.15, 4.17, 4.19, 4.21, and 4.23) and the synthesis of PMMA with high I^* = 84−88% and $Đ \sim$ 1.2−1.3 (runs 9−20, even numbered runs). However, I^* was lower for the polymerizations performed under air compared to those performed under nitrogen for all PCs except 5 (on average I^* was ~5% lower for the O-ATRP performed under air and catalyzed by 1−4 and 6), suggesting the presence of side reactions during the polymerizations performed under air.

Table 4.2. Results of the O-ATRP of MMA under Air or Nitrogen Mediated by PCs 1-6[a]

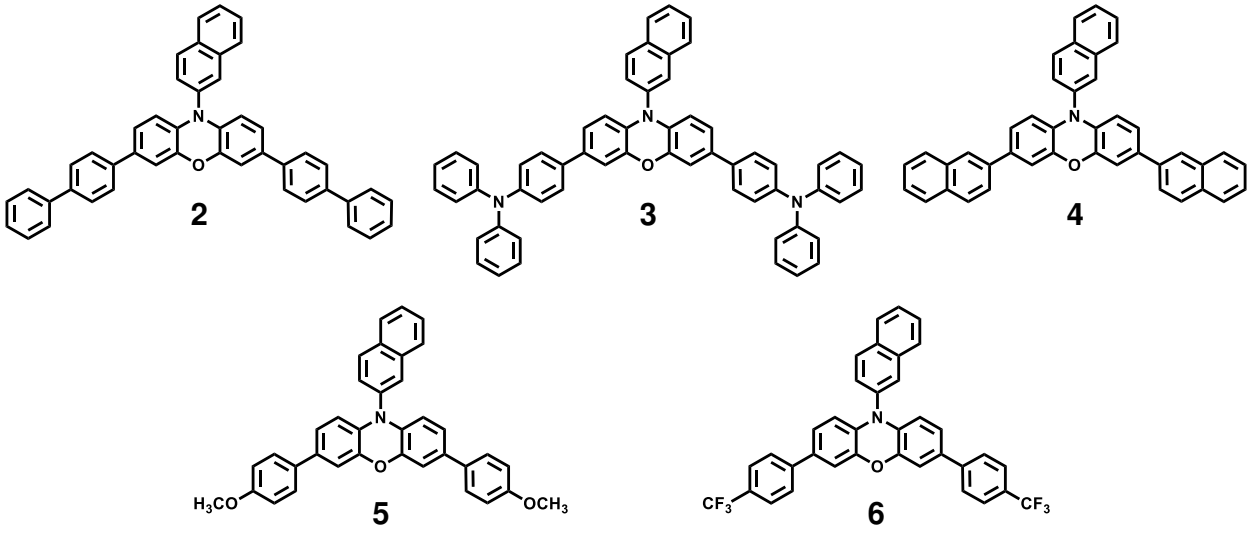

Run No.	PC	Atmosphere	time (h)	conv. (%)	$M_{n,th}$ (kDa)	M_n (kDa)	M_w (kDa)	$Đ$ (M_w/M_n)	I^* ($M_{n,th}/M_n \times 100$)
9	**1**	N_2	8	74	7.7	8.2	9.8	1.19	94
10	**1**	air	8	77	8.0	9.1	11.0	1.21	88
11	**2**	N_2	8	63	6.6	6.8	8.7	1.29	97
12	**2**	air	8	73	7.6	8.6	10.2	1.19	88
13	**3**	N_2	8	64	6.7	7.6	9.2	1.20	87
14	**3**	air	8	52	5.5	6.5	7.6	1.16	84
15	**4**	N_2	8	60	6.2	6.7	8.3	1.24	93
16	**4**	air	8	63	6.6	7.9	9.5	1.21	84
17	**5**	N_2	8	60	6.3	7.3	9.4	1.28	86
18	**5**	air	8	69	7.2	7.7	10.3	1.33	93
19	**6**	N_2	8	67	6.9	7.0	8.6	1.22	99
20	**6**	air	8	71	7.4	8.2	10.1	1.23	89

[a]The O-ATRP of MMA was performed with a [1000]:[10]:[1] ratio of MMA:DBMM:PC in 1:1 of MMA:DMAc v/v with 0.92 mL (8.60 mmol) of MMA in a 0.5 dram vial. See Supporting Information for more details.

Conclusion

In conclusion, O-ATRP performed under air and catalyzed by core modified N-aryl phenoxazines was found to proceed in a controlled fashion despite the potential deleterious effects of oxygen. Control over the polymerization using PC 1 was demonstrated by a linear growth of polymer M_n as a function of monomer conversion, the synthesis of PMMA with high I^* (I^* = 88%

after 8 h) and $Đ \sim 1.2$, and the synthesis of block copolymers. Temporal control over O-ATRP performed under air was demonstrated using a pulsed-irradiation experiment carried out over the course of multiple days. In accordance with reports on the effects of air on Cu catalyzed ATRP systems, reduction of the volume of air in the reaction vial headspace was critical to the success of this procedure such that elimination of vial headspace led to the synthesis of polymeric material with the highest I^*. Investigation of five other PCs (2−6) in O-ATRP performed under air revealed that control over the polymerization under these conditions is not exclusive to PC 1. In particular, all PCs explored were able to synthesize PMMA with $Đ \sim 1.2$−1.3 and $I^* = 84$−99%. Trends in PC performance for O-ATRP performed under air followed those for the polymerizations performed under nitrogen with PC 1 exhibiting the best overall performance. In the O-ATRP reactions performed under air, I^* was consistently lower than the reactions performed under nitrogen for most of the PCs (1−4 and 6), suggesting the presence of additional side reactions in the presence of air. Future work is aimed at understanding the mechanisms enabling these O-ATRP reactions to proceed in a controlled fashion under air without the addition of exogenous reagents.

Experimental

1. Materials and Methods

Purchased Chemicals and Experimental Equipment

Photocatalyst Synthesis

Buchwald Coupling: Phenoxazine was purchased from Beantown Chemical and used as received. Phenazine was purchased from Sigma Aldrich and used as received. 2-bromonaphthylene and 1-bromonaphthylene were purchased from VWR. Bis(dibenzylideneacetone) palladium(0) and 1.0 M solution of tri-*tert*-butylphosphine in toluene

were purchased from Sigma Aldrich and used as received. Dicyclohexylphosphino-2,6-diisopropoxybiphenyl (RuPhos) and chloro-(2-dicyclohexylphosphino-2,6-diisopropoxy-1,1-biphenyl) [2-(2-aminoethyl)phenyl] palladium(II) - methyl-t-butyl ether adduct (RuPhos precatalyst) were purchased from Sigma Aldrich and used as received. Sodium tert-butoxide was purchased from Sigma Aldrich and used as received. Dioxane and toluene were purified using an mBraun MB-SPS-800 solvent purification system and kept under nitrogen atmosphere.

Bromination: N-Bromosuccinimide was purchased from VWR and used as received.

Suzuki Coupling: Tetrakis(triphenyl phosphine) palladium (0) was purchased from Sigma Aldrich. Potassium carbonate was purchased from VWR. The boronic acid coupling partners were purchased from the following vendors and used as received:

4-biphenylboronic acid: TCI America

2-naphthylboronic acid: Sigma Aldrich

pyrene-1-boronic acid: Alfa Aesar

4-(trifluoromethyl)phenylboronic acid: Sigma Aldrich

4-methoxyphenylboronic acid: Sigma Aldrich

4-(diphenylamino)phenylboronic acid: TCI America

Polymer Synthesis

Methyl methacrylate (MMA), *N*,*N*-dimethyl acetamide (DMAc), and diethyl 2-bromo-2-methyl malonate (DBMM) were purchased from Sigma Aldrich. Benzyl methacrylate (BnMA) was purchased from TCI. For chemical preparation and storage, please see the following section on page four of the supporting information titled “Chemical Preparation and Storage”. The caps used for the 1 dram and 1.5 dram vials are assembled screw caps with hole with PTFE/silicone septum from Sigma Aldrich (product number: SU860078). Similarly, the caps used for the 0.5

dram vials are assembled screw caps with hole with PTFE/silicone septum from Sigma Aldrich (product number: 27262 Supelco).

Light Source Materials

Light Source: Double-density white-light LEDs were purchased from Creative Lighting Solutions (item no. CL-FRS1210-5M-12V-WH) and used in both of the photoreactors described herein. The emission profile of the light source is shown in Figure 4.7 of the *Experimental* section.

Connectors: solderless power connectors (Creative Lighting Solutions, product code: CL-FRS1210-2WPWER) are directly connected to the LED strips by cutting the plastic covering the first LED on the strip and pulling it back to reveal the copper soldering pads which are inserted into the power connector. The other end of the power connector is connected to a male JST connector (creative lighting solutions, product code: CL-JSTCONNECTOR-10PK).

Chemical Preparation and Storage

Polymerizations conducted under air:

Chemical Preparation: Methyl methacrylate was purified by passing it through a plug of aluminum oxide (activated, basic, Brockman grade I, 58 angstrom, purchased from Thermo Fisher Scientific) to remove the inhibitor. The initiator, DBMM, was dried over calcium hydride and distilled, but stored in air. DMAc was used as received (no SureSeal on the bottle so that it was stored under air).

Chemical Storage: Methyl methacrylate and DBMM were stored in a freezer at -25ºC.

Polymerizations conducted under nitrogen:

Chemical Preparation: Methyl methacrylate and DBMM were purified by drying over calcium hydride overnight followed by distillation under reduced pressure. Anhydrous DMAc stored under argon was purchased from VWR and brought into a nitrogen-filled glovebox.

Chemical Storage: Methyl methacrylate and DBMM were stored in the freezer of a nitrogen-filled glovebox. DMAc was stored on the shelf of a nitrogen-filled glovebox.

Instrumentation

Nuclear magnetic resonance spectra were recorded on a Bruker 400 MHz NMR Spectrometer to analyze polymerization conversion and precipitated polymer. All ^{1}H NMR experiments are reported in δ units, parts per million (ppm), and were measured relative to the signals for residual chloroform (7.26 ppm) in the deuterated solvent. Analysis of polymer molecular weights was performed via gel permeation chromatography (GPC) coupled with multi-angle light scattering (MALS), using an Agilent HPLC fitted with one guard column, three PLgel 5 μm MIXED-C gel permeation columns, a Wyatt Technology TrEX differential refractometer, and a Wyatt Technology miniDAWN TREOS light scattering detector, using tetrahydrofuran (THF) as the eluent at a flow rate of 1.0 mL/min. The dn/dc value used for PMMA was 0.084 and all other polymers were analyzed using a known concentration (2.00 mg/mL) assuming 100% mass recovery. MALDI-TOF analysis was performed on a Bruker Microflex LRF equipped with a nitrogen laser operating at 337 nm.

2. Procedures

Synthesis of Photocatalysts (PCs)

Syntheses of PCs **1**–**6** were performed using previously reported procedures.[13,14]

Polymerization Procedures

The polymerization reactions described herein were carried out in two types of photoreactor setups to accommodate for reaction vial size and allow for rapid screening of reaction conditions. The photoreactor used for larger vials (anything above 0.5 dram) was a beaker and the photoreactor used for 0.5 dram vials was a 3D-printed part, both of which are described in the following sections along with the polymerization procedures used for each. The same white-light LEDs were used to construct both photoreactors, the emission profile of which is shown in Figure 4.7 of the *Experimental* section.

Polymerization Procedure 1.0: Data for Table 4.1 (except controls)

A 20 mL scintillation vial was charged with 5.3 mg of PC **1** (8.6×10^{-6} mol, 1.0 equiv.) to which a stir bar, 0.92 mL of DMAc (1:1 v/v of DMAc: MMA), and 0.92 mL of the monomer, MMA, (8.6×10^{-3} mol, 1000 equiv.) were added. Then, 16.4 µL of the initiator, DBMM, (8.60×10^{-5} mol, 10.0 equiv.) was delivered using a Hamilton syringe. A 24/40 septum cap was placed upside down over the vial and wrapped with electrical tape (see Figures 4.4 and 4.5 of the *Experimental* section). The reaction vial was then placed in the dark while a white-light LED beaker (Figure 4.6 of the *Experimental* section) was turned on. The reaction vial was then introduced to the white-light LED beaker at which point the polymerization was considered to start (t = 0 for kinetic plots). Two cooling fans and compressed air were used to keep the reaction vials at room temperature.

The same general procedure described above was also performed using vials of the following sizes: 0.5 dram (1.85 mL, 0 mL of air headspace), 1 dram (3.70 mL, 1.86 mL of air headspace), 1.5 dram (5.55 mL, 3.71 mL of air headspace), and 2 dram (7.39 mL, 5.55 mL of air headspace). The caps for the vials were varied to fit each corresponding vial and allow for aliquots

to be removed without introducing additional air. As such, the following caps were used for each vial:

20 mL scintillation vial: 24/40 septum stopper upside down, wrapped with electrical tape

2 dram vial: 14/20 septum stopper upside down, wrapped with electrical tape

1.5 dram, 1 dram, and 0.5 dram: PP caps with PTFE/Silicone centers (see materials section for more details), wrapped with electrical tape

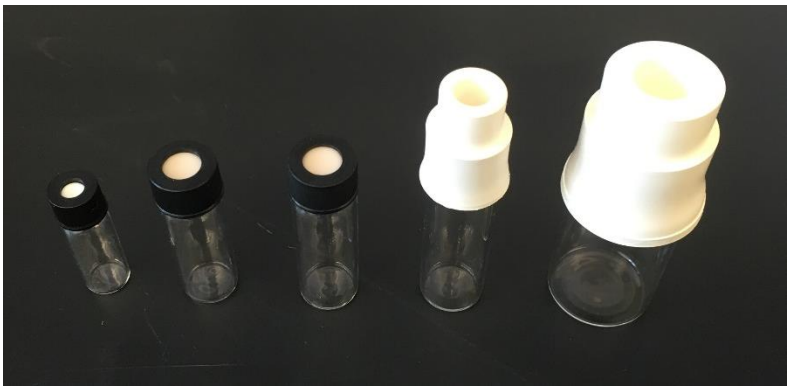

Figure 4.4. *Reaction vials used to study the effect the amount of headspace of air on the polymerization of MMA via O-ATRP.*

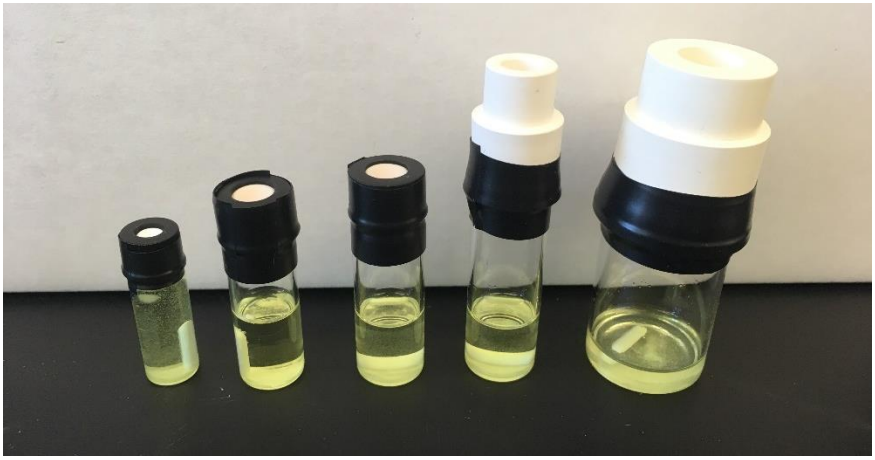

Figure 4.5. *Prepared reaction vials used to study the effect the amount of headspace of air on the polymerization of MMA via O-ATRP.*

Figure 4.6. *White-light LED beaker used as the light source for Polymerization Procedure 1.0 (see above). The beaker was prepared by wrapping a 400 mL beaker in aluminum foil (see left). Inside the beaker a 16-inch strip of white-light LEDs (27 lights) from Creative Lighting Solutions (item no. CL-FRS1210-5M-12V-WH) was wrapped along the inside. The end of the LED strip was connected to one end of a solderless power connector (Creative Lighting Solutions, product code: CL-FRS1210-2WPWER), the other end of which is connected to a male JST connector (Creative Lighting Solutions, product code: CL-JSTCONNECTOR-10PK). The power connector is wrapped in a piece of electrical tape to keep it firmly closed and to cover the first LED of the strip (26 available LEDs).*

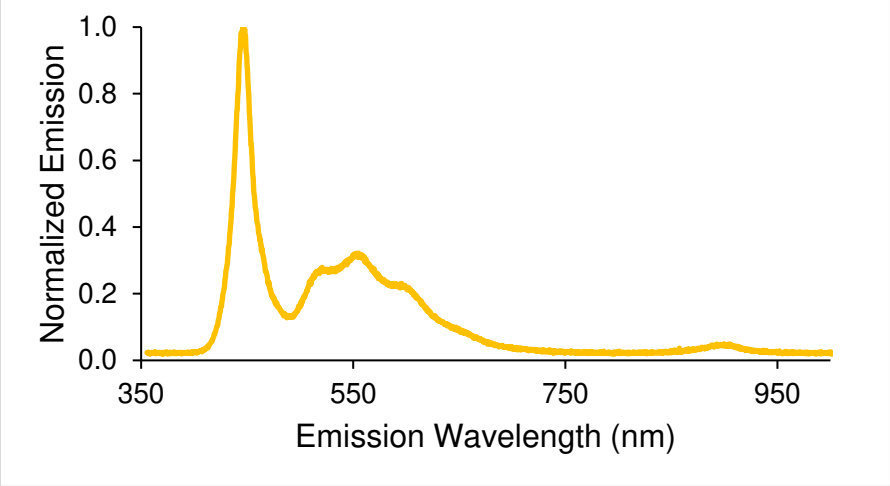

Figure 4.7. *Plot of the normalized emission of the white-light LEDs used to construct the two photoreactor setups described herein.*

Procedure for PMMA Macroinitiator Synthesis (Figure 4.3)

To scale up the polymerization while maintaining no headspace in the reaction vial, a 1.50 dram vial was used which required the use of a white-light LED beaker as the photoreactor. A 1.50 dram vial was equipped with a stir bar and charged with 15.8 mg of PC **1** (25.7×10^{-6} mol, 1 equiv.) to which 2.75 mL of DMAc (1:1 v/v of DMAc:MMA), 2.75 mL of MMA (25.7×10^{-3} mol,

1000 equiv.), and 49.1 µL of DBMM (25.7×10^{-5} mol, 1 equiv.) were added sequentially. The vial was capped with a PTFE/Silicon screw cap, which was then wrapped in parafilm. The vial was allowed to stir in a white-light LED beaker (described above) for 7 hours before an aliquot was removed and quenched with BHT chloroform to determine conversion by NMR (conversion = 77% by NMR, see procedure for polymerization kinetics and polymer analysis below). The polymerization mixture was then loaded into a syringe and slowly added to 450 mL of stirring methanol in a dry ice/acetone bath (approximately -78ºC). After stirring for an hour, the polymer was collected via vacuum filtration and dried in a vacuum oven at 50ºC overnight to yield 1.018 g of polymer (40% yield) with M_n = 8.21 kDa (see Table 4.6 of the *Experimental* section for more details). This macroinitiator was then used for chain extension and block copolymerization experiments (see procedures below).

Polymerization Procedure 2.0: Data for Table 4.2 and Figure 4.2

A 0.5 dram (1.85 mL) glass vial was charged with 5.3 mg of PC 1 (8.6×10^{-6} mol, 1.0 equiv.) to which a stir bar, 0.92 mL of DMAc (1:1 v/v of DMAc: MMA), and 0.92 mL of the monomer, MMA, (8.6×10^{-3} mol, 1000 equiv.) were added. Then, 16.4 µL of the initiator, DBMM, (8.60×10^{-5} mol, 10.0 equiv.) was delivered using a Hamilton syringe. A PTFE/Silicon septum cap was used to seal the vial and a small piece of electrical tape was wrapped around the edge of the cap. The reaction vial was then placed in the dark while the white-light LEDs on the 3D-printed photoreactor were turned on (Figure 4.8 of the *Experimental* section). The reaction vial was then introduced to the white-light LEDs at which point the polymerization was considered to start (t = 0 for kinetic plots). Two cooling fans and compressed air were used to keep the reaction vials at room temperature (see "temperature control" section below for more details).

The photoreactor setup used for these polymerizations was 3D-printed using high-impact polystyrene (HIPS) on a flashforge 3D-printer lined with two 16-inch strips of white-light LEDs which exhibit the emission profile shown in Figure 4.7 of the *Experimental* section. The photoreactor setup was constructed to allow for rapid screening of reaction conditions while keeping stirring and light intensity across reaction vials uniform. This is achieved since the photoreactor is designed with slots to hold 0.5 dram vials in place allowing the reactions to stir efficiently without falling over and ensuring that each vial is placed directly next to four LEDs (see Figure 4.8 of the *Experimental* section). Reaction vials were placed in every other slot to keep the temperature of the reactions that of room temperature (see "temperature control" section for more details).

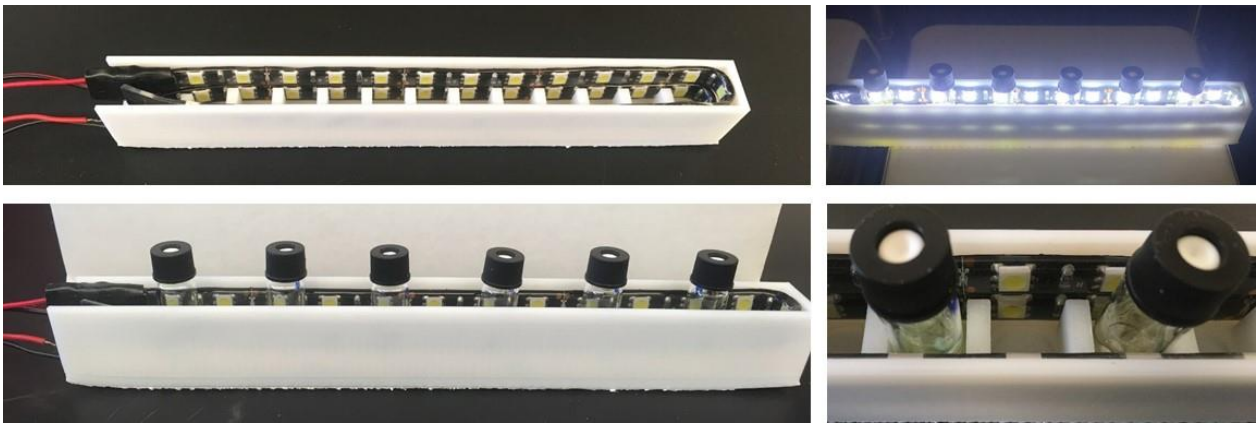

Figure 4.8. *The 3D-printed photoreactor used for polymerizations in 0.5 dram vials is lined with two 16-inch strips of white-light LEDs (top left). The end of each of the white-light LED strips is connected to one end of a solderless power connector (Creative Lighting Solutions, product code: CL-FRS1210-2WPWER), the other end of which is connected to a male JST connector (Creative Lighting Solutions, product code: CL-JSTCONNECTOR-10PK). The power connector is wrapped in a piece of electrical tape to keep it firmly closed and to cover the first LED of the strip. Reaction vials are placed in the holders in every other slot since this configuration was found to be necessary to ensure efficient cooling (bottom left). Reactions running in the photoreactor on a standard stir plate (top right). Each reaction vial is situated directly next to four LEDs (bottom right).*

Polymerization Procedure for On/Off Experiment (Figure 4.3)

The same general procedure as "Polymerization Procedure 2.0" was followed except that in "dark" periods, the reaction flask was wrapped entirely with aluminum foil.

Polymerization Procedure for Chain Extension from PMMA Macroinitiator (Figure 4.3)

A 0.5 dram vial was equipped with a stir bar and charged with 2.7 mg of PC **1** (4.4×10^{-6} mol, 1.0 equiv.) and 0.300 g of the PMMA macroinitiator described above (M_n = 8.21 kDa, 3.65×10^{-5}, 8.40 equiv.) which were dissolved in 1.15 mL of DMAc (1.89:1 of DMAc: MMA) using a vortex mixer. Then 0.61 mL of MMA were added (5.7×10^{-3} mol, 1,310 equiv.), the vial was capped with a PTFE/Silicon screw cap, a piece of parafilm was wrapped over the cap, and the vial was introduced to the 3D-printed photoreactor with white-light LEDs for 14 hours. After 14 hours, the reaction mixture as loaded into a syringe and slowly dripped into room temperature methanol to precipitate the polymer. After stirring for an hour, the polymer was collected via vacuum filtration and dried in a vacuum oven at 50ºC overnight to yield 0.870 g of polymer (77% conversion by gravimetric analysis). The resulting chain extended PMMA was found to have M_n = 20.6 kDa, $Đ$ = 1.34, and I^* = 89% (See Table 4.5 of the *Experimental* section for more details). We note that the stoichiometry was odd for this reaction (1310: 8.4: 1 of MMA: macroinitiator: PC) in order to use enough solvent to dissolve the macroinitiator and eliminate vial headspace in the 0.5 dram vial.

Block Copolymerization from PMMA Macroinitiator (Figure 4.3)

A 0.5 dram vial was equipped with a stir bar and charged with 1.8 mg of PC 1 (2.9×10^{-6} mol, 1.0 equiv.) and 0.200 g of the PMMA macroinitiator described above (M_n = 8.21 kDa, 2.44×10^{-5}, 8.40 equiv.) which were dissolved in 1.27 mL of DMAc (1.5:1 of DMAc: MMA) using a vortex mixer. Then 0.64 mL of BnMA were added (3.7×10^{-3} mol, 1,300 equiv.), the vial was capped with a PTFE/Silicon screw cap, a piece of parafilm was wrapped over the cap, and the vial

was introduced to the 3D-printed photoreactor with white-light LEDs for 14.5 hours. After 14.5 hours, an aliquot as taken for analysis by NMR and the rest of the reaction mixture as loaded into a syringe and slowly dripped into room temperature methanol to precipitate the polymer. After stirring for an hour, the polymer was collected via vacuum filtration and dried in a vacuum oven at 50ºC overnight to yield 0.632 g of polymer (74% yield). The resulting p(MMA-b-BnMA) copolymer was found to have M_n = 34.3 kDa, $Đ$ = 1.50, and I^* = 86% (see Table 4.5 of the *Experimental* section for more details).

Temperature Control

A 0.5 dram scintillation vial equipped with a stir bar was charged with 1.00 mL of DMAc and capped with a PTFE/Silicone septum cap. A hole was punctured through the top of the cap with a needle and the probe of a hand-held thermocouple was inserted into the solution of DMAc. The vial was place in the 3D-printed photoreactor with the white-light LEDs turned on. Two small fans and compressed air were used to cool the reaction vial to maintain room temperature. We note that the temperature of our laboratory typically fluctuates between 23ºC and 27ºC throughout the day and we observed that the temperature measured using the hand-held probe does fluctuate in accordance with the fluctuations of the temperature of the room. However, the maximum temperature recorded using the probe was found to be 26.8ºC (Figure 4.9 of the *Experimental* section), allowing us to confirm that no significant heating of the reactions is caused by the photoreactor.

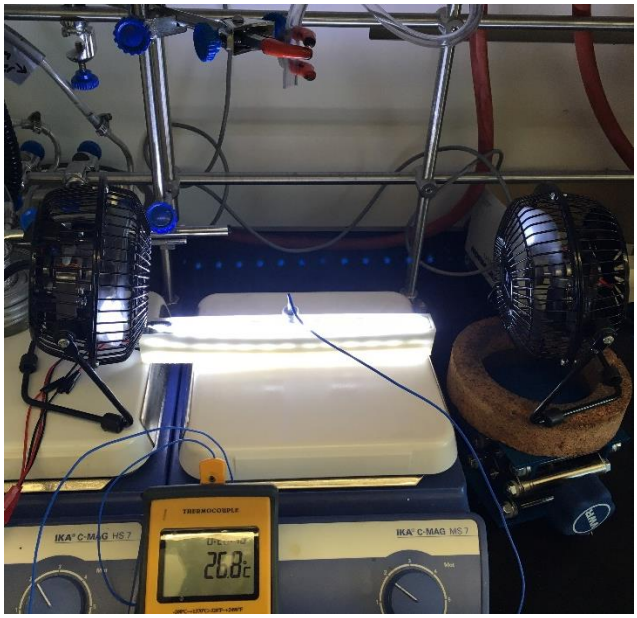

Figure 4.9. *Apparatus used to approximate the temperature of polymerization reactions.*

Procedure for Polymerization Kinetics and Polymer Analysis

To evaluate the kinetics and growth of polymer molecular weight as a function of conversion for each reaction, an aliquot of 0.15 to 0.20 mL of reaction mixture was taken using a nitrogen-purged needle and injected into a solution of deuterated chloroform containing the radical inhibitor, butylated hydroxyl toluene (BHT, 250 ppm), at predetermined times after the start of the polymerization (when the reaction mixture was exposed to light). Specifically, the needle of a 1.00 mL syringe is purged with nitrogen by drawing nitrogen from a sacrificial flask three to five times while dispensing in between. On the last iteration, the nitrogen is dispensed from the syringe (plunger is fully depressed) and the needle is used to puncture the septum cap of the reaction flask from which the aliquot is drawn. Finally, after each aliquot is removed, parafilm is immediately used to cover the cap of the reaction vial. Aliquots are taken in this manner to ensure no further introduction of air throughout the polymerization and no accidental injection of nitrogen into the reaction vial during the polymerization. The ^{1}H NMR spectrum of the aliquot is immediately

acquired to determine the percent conversion of monomer at that time. After NMR analysis, the sample is dried using compressed air, re-dissolved in HPLC grade, unstabilized tetrahydrofuran and analyzed by GPC.

Procedure for Polymer Analysis by MALDI-TOF

MALDI-TOF spectra were acquired on a Bruker Microflex LRF equipped with a nitrogen laser operating at 337 nm using linear positive ion mode. The PMMA macroinitiator synthesized according to the procedure on page S9 was dissolved in THF to make a 1.0 mg/mL stock solution. Ten microliters of the polymer stock solution was mixed with 10 µL of a solution of dihydroxybenzoic acid, DHB, (matrix) in THF (20.0 mg/mL) to which 1.5 µL of sodium trifluoroacetate was added (cationization agent). The solution was vortexed, centrifuged, and 0.5 µL was withdrawn and dispensed on the target plate. Each polymer sample was analyzed in triplicate. The samples were externally calibrated using a protein mixture (Protein Calibration Standard I, containing Insulin, Ubiquitin I, Cyctochrom C and Myoglobin, Bruker Daltonics Part No. 8206355) for calibration with analytes ranging from 4 kDa to 20 kDa.

Control Experiments

Control experiments were conducted according to “Polymerization Procedure 2.0” except either the initiator (DBMM), light, or the photocatalyst was omitted. For the reaction run in the absence of light, the reaction vial was wrapped in aluminum foil and still placed in the photoreactor on a stir plate. The outcomes of these experiments are described in Table 4.1.

3. Properties of Photoredox Catalysts

Table 4.3. *Absorption properties of the PCs explored in this work*

PC	abs λ_{max} (nm)[a]	$\varepsilon_{\lambda max, abs}$ ($M^{-1}cm^{-1}$)[a]	Ref.
1	388	26,600	13
2	384	25,900	14
3	363	22,000	14
4	388	21,100	14
5	382	37,700	14
6	379	20,600	14
7	384	25,300	14

[a]*Spectra acquired in DMAc.*

Table 4.4. *Redox Properties of the PCs explored in this work*

PC	em λ_{max} (nm)	$E_{S1, exp}$ (eV)	$E_{T1, calc}$ (eV)	$E_{1/2}$ ($^2PC^{\bullet+}/^1PC$) (V vs. SCE)	E^0_{ox} ($^2PC^{\bullet+}/^1PC$) (V vs. SCE)	$E^{0*}_{S1, exp}$ ($^2PC^{\bullet+}/^1PC^*$) (V vs. SCE)	$E^{0*}_{T1, calc}$ ($^2PC^{\bullet+}/^3PC^*$) (V vs. SCE)	Ref.
1	506	2.45	2.11	0.65	0.42	-1.80	-1.70	13
2	466	2.66	2.13	0.63	0.43	-2.03	-1.70	14
3	532	2.33	2.28	0.52	0.37	-1.81	-1.91	14
4	467	2.65	2.16	0.72	0.58	-1.93	-1.58	14
5	522	2.37	2.18	0.54	0.30	-1.83	-1.88	14
6	564	2.20	2.30	0.66	0.45	-1.54	-1.85	14
7	466	2.66	2.09	0.63	0.40	-2.03	-1.69	14

4. Additional Polymerization Data

NMR Spectra of Precipitated Polymers

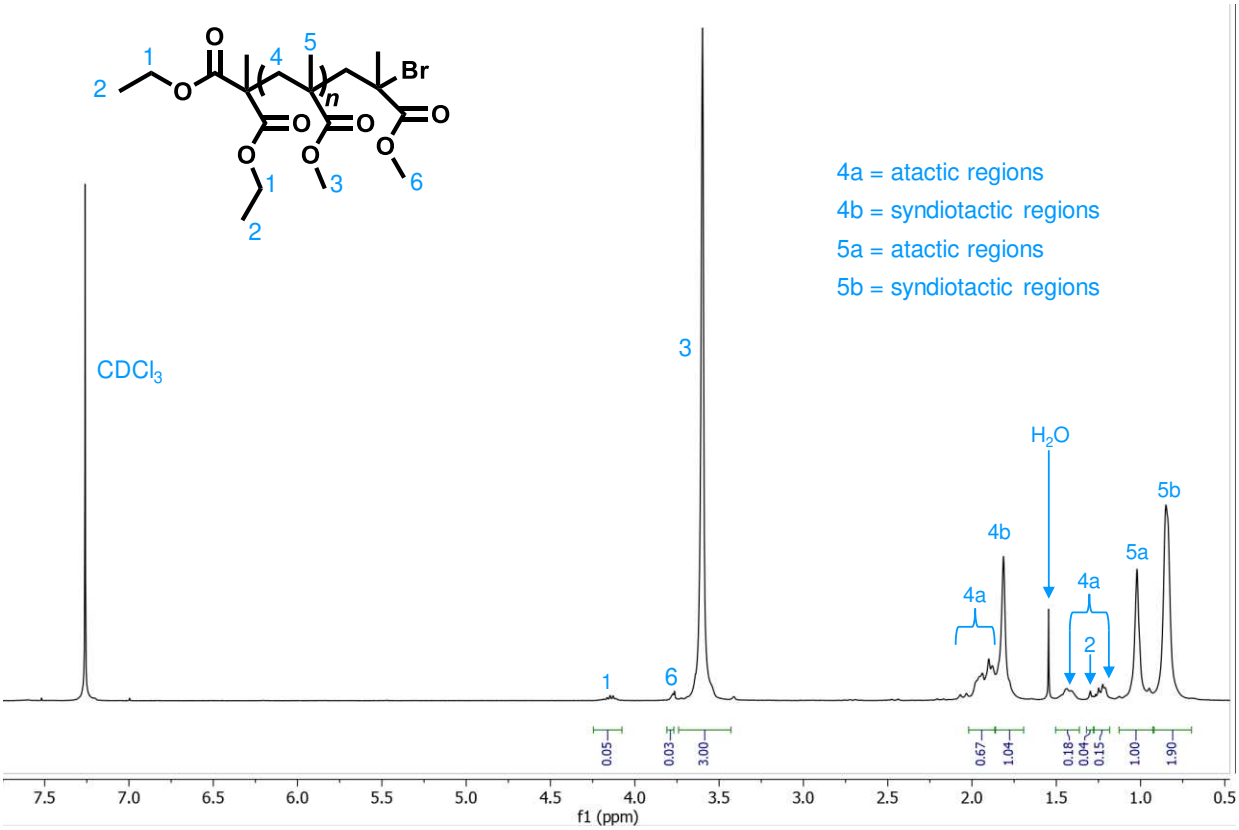

Figure 4.10. *^{1}H NMR of PMMA synthesized under nitrogen ($CDCl_3$, 400 MHz, PMMA DP = 80, $M_{n(NMR)}$ = 8.26 kDa).*

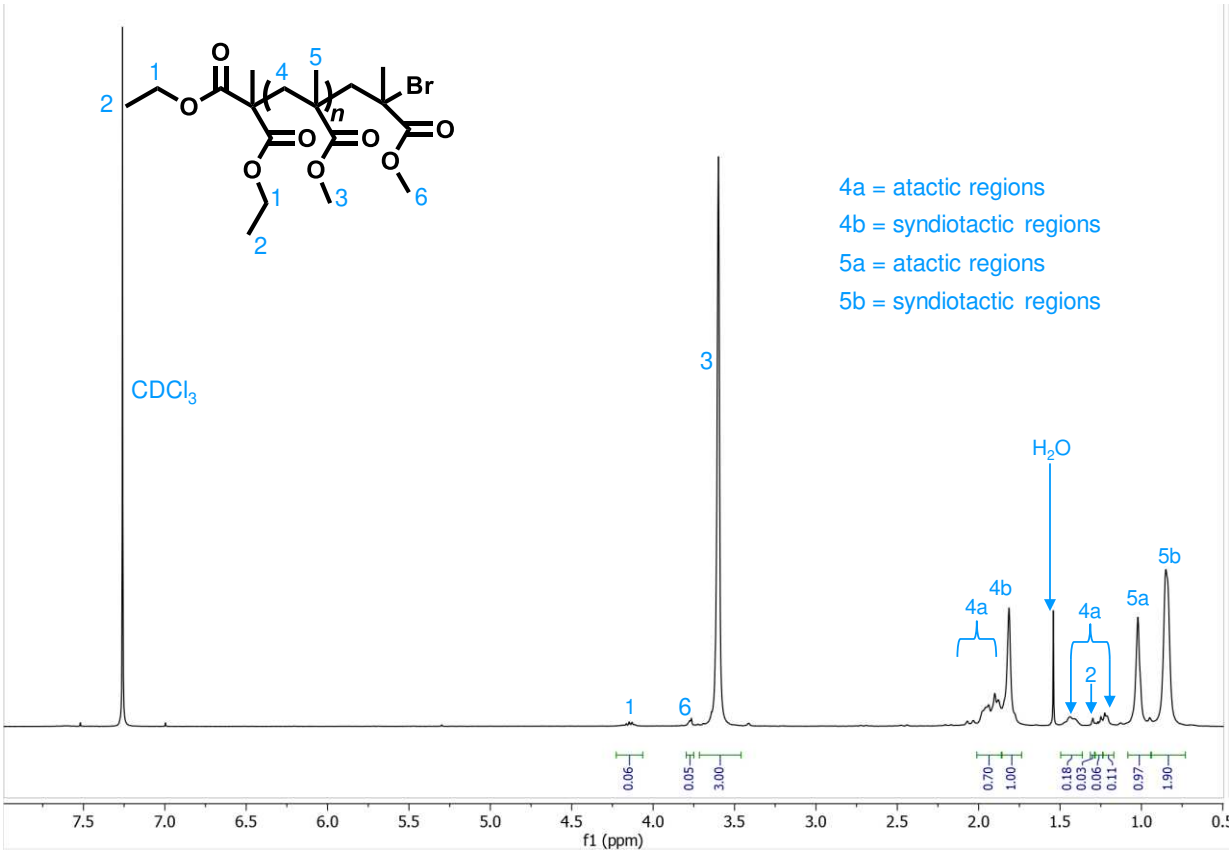

Figure 4.11. *^{1}H NMR of PMMA synthesized under air ($CDCl_3$, 400 MHz, PMMA DP = 67, $M_{n(NMR)}$ = 6.92 kDa).*

Gel-Permeation Chromatography Traces

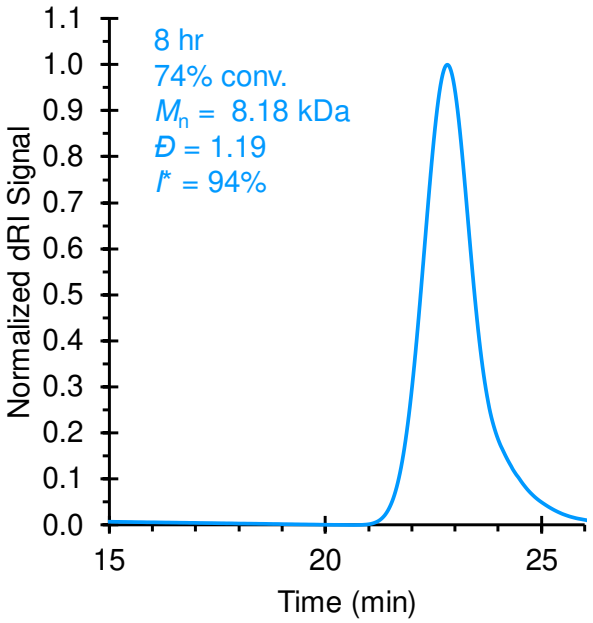

Figure 4.12. *GPC trace of PMMA synthesized under nitrogen using PC **1**.*

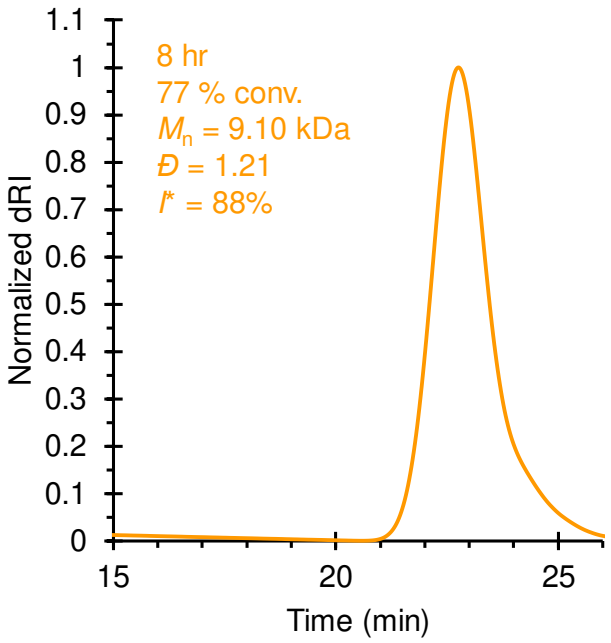

Figure 4.13. *GPC trace of PMMA synthesized under air using PC* ***1****.*

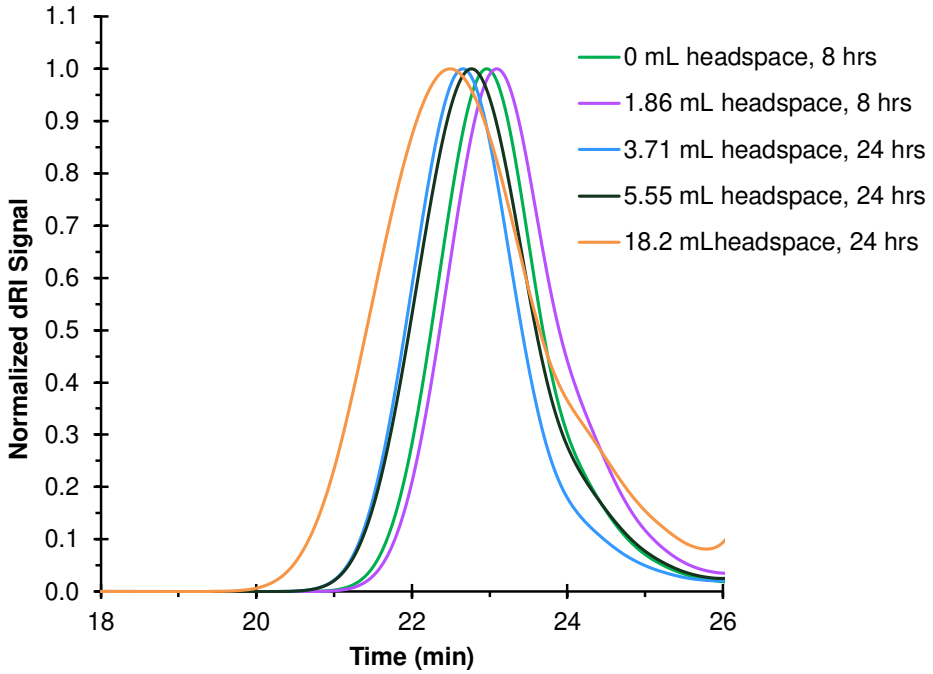

Figure 4.14. *GPC traces of PMMA synthesized in vials of different sizes using PC* ***1****. The corresponding molecular weight and dispersity data are presented in Table 4.1.*

Kinetic Data and Polymer Molecular Weight Growth

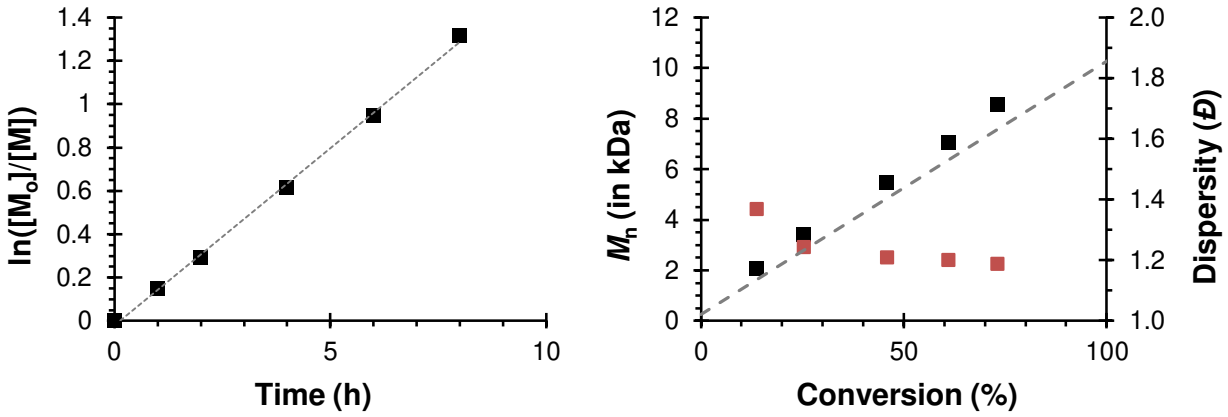

Figure 4.15. *Plot of the natural log of monomer consumption as a function of time (left) for the O-ATRP of MMA mediated by PC* ***2*** *under air. Plot of growth of the experimentally measured number average molecular weight (M_n) as a function of monomer conversion (right graph, black squares) with theoretical values (grey dashed line). Dispersity of the PMMA at each molecular weight are shown (red squares, secondary y-axis).*

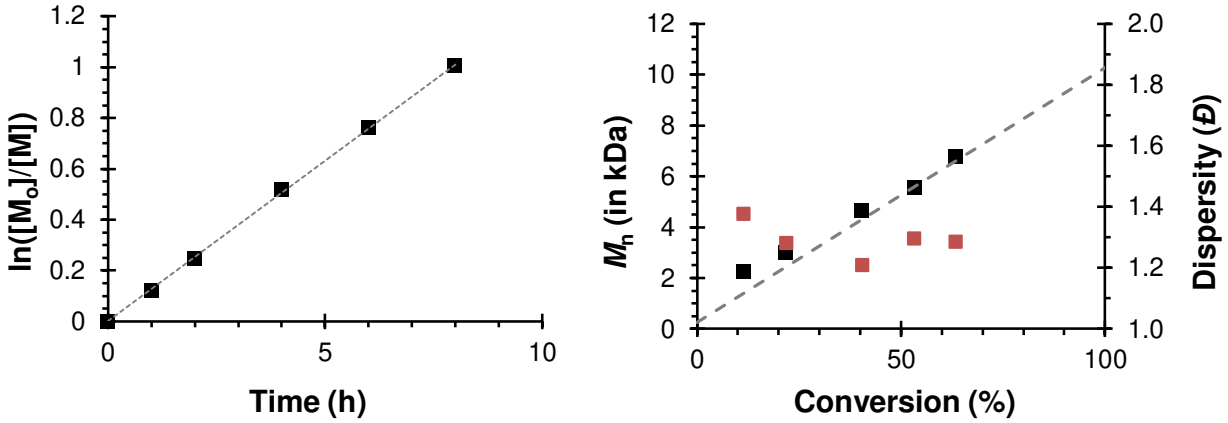

Figure 4.16. *Plot of the natural log of monomer consumption as a function of time (left) for the O-ATRP of MMA mediated by PC* ***2*** *under nitrogen. Plot of growth of the experimentally measured number average molecular weight (M_n) as a function of monomer conversion (right graph, black squares) with theoretical values (grey dashed line). Dispersity of the PMMA at each molecular weight are shown (red squares, secondary y-axis).*

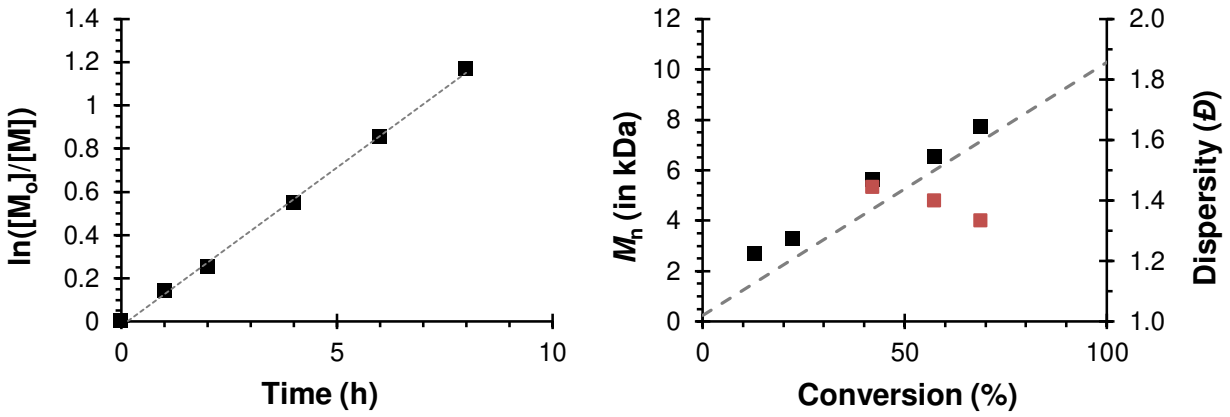

Figure 4.17. *Plot of the natural log of monomer consumption as a function of time (left) for the O-ATRP of MMA mediated by PC* ***3*** *under air. Plot of growth of the experimentally measured number average molecular weight (M_n) as a function of monomer conversion (right graph, black squares) with theoretical values (grey dashed line). Dispersity of the PMMA at each molecular weight are shown (red squares, secondary y-axis, low conversion values were greater than 2.0).*

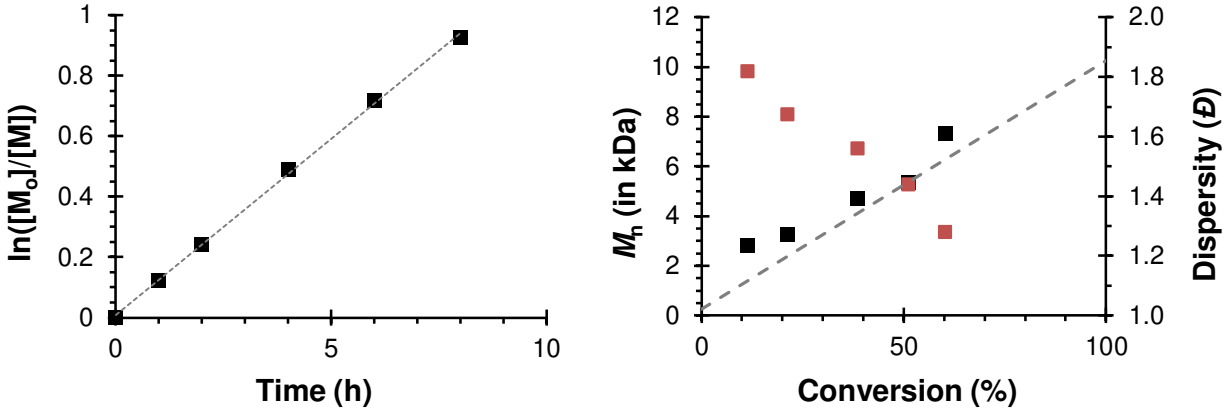

Figure 4.18. *Plot of the natural log of monomer consumption as a function of time (left) for the O-ATRP of MMA mediated by PC* ***3*** *under nitrogen. Plot of growth of the experimentally measured number average molecular weight (M_n) as a function of monomer conversion (right graph, black squares) with theoretical values (grey dashed line). Dispersity of the PMMA at each molecular weight are shown (red squares, secondary y-axis).*

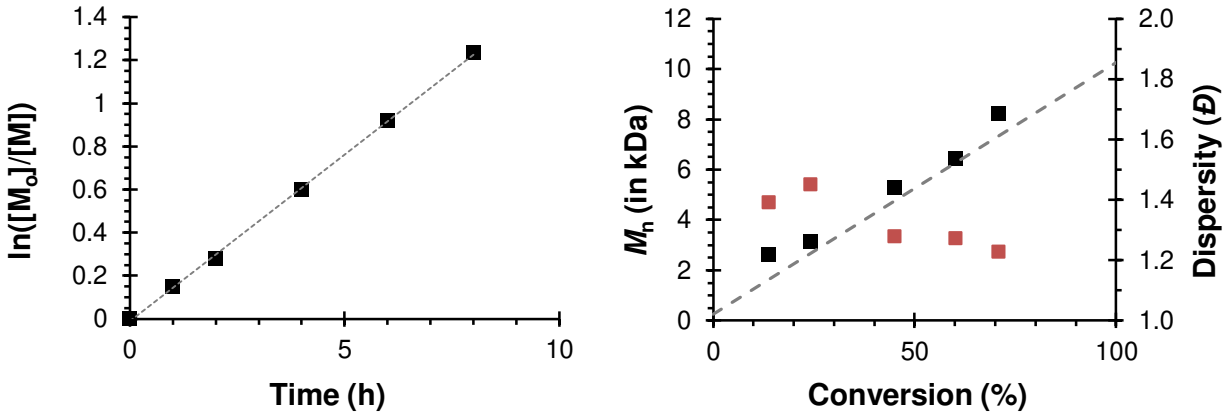

Figure 4.19. *Plot of the natural log of monomer consumption as a function of time (left) for the O-ATRP of MMA mediated by PC* ***4*** *under air. Plot of growth of the experimentally measured number average molecular weight (M_n) as a function of monomer conversion (right graph, black squares) with theoretical values (grey dashed line). Dispersity of the PMMA at each molecular weight are shown (red squares, secondary y-axis).*

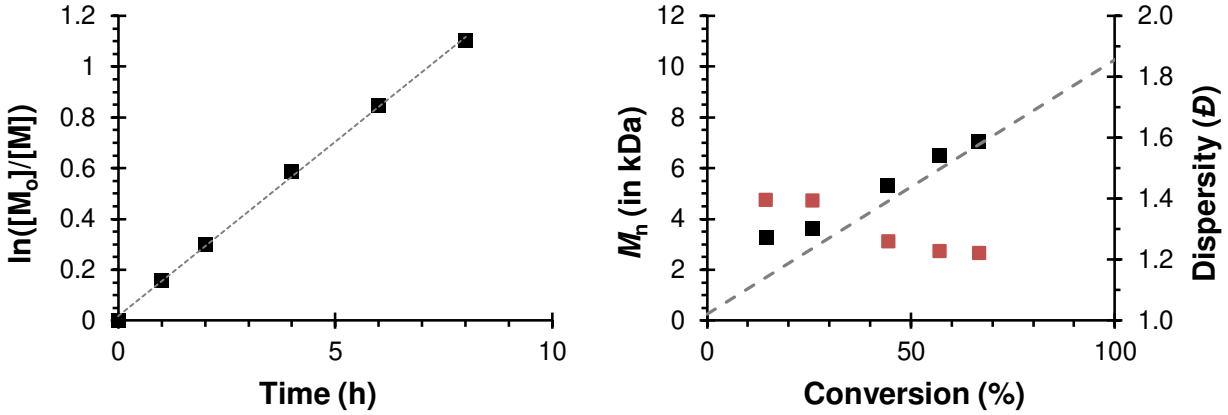

Figure 4.20. *Plot of the natural log of monomer consumption as a function of time (left) for the O-ATRP of MMA mediated by PC* ***4*** *under nitrogen. Plot of growth of the experimentally measured number average molecular weight (M_n) as a function of monomer conversion (right graph, black squares) with theoretical values (grey dashed line). Dispersity of the PMMA at each molecular weight are shown (red squares, secondary y-axis).*

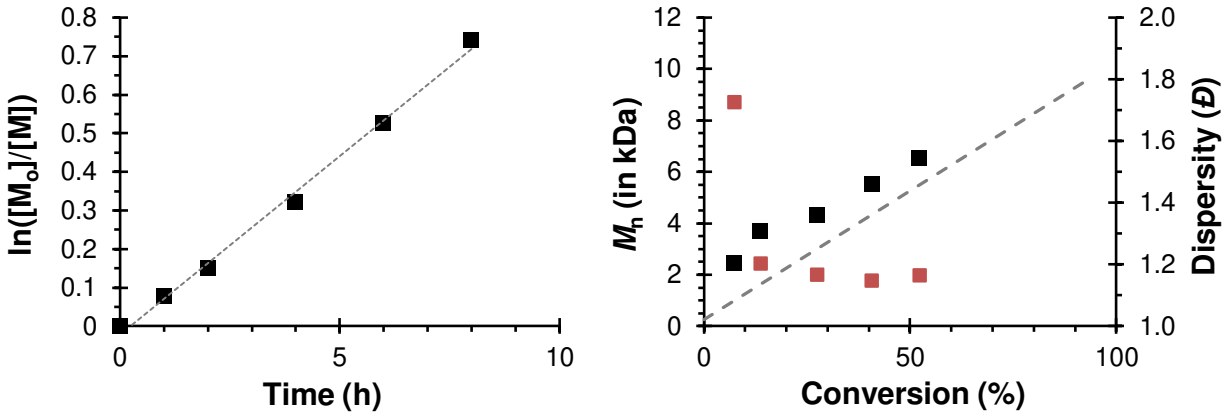

Figure 4.21. *Plot of the natural log of monomer consumption as a function of time (left) for the O-ATRP of MMA mediated by PC* ***5*** *under air. Plot of growth of the experimentally measured number average molecular weight (M_n) as a function of monomer conversion (right graph, black squares) with theoretical values (grey dashed line). Dispersity of the PMMA at each molecular weight are shown (red squares, secondary y-axis).*

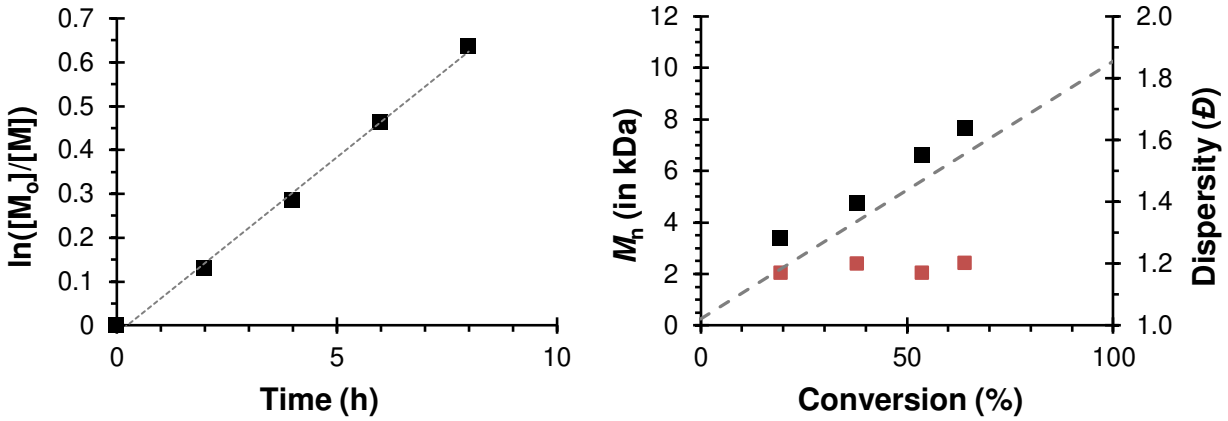

Figure 4.22. *Plot of the natural log of monomer consumption as a function of time (left) for the O-ATRP of MMA mediated by PC* ***5*** *under nitrogen. Plot of growth of the experimentally measured number average molecular weight (M_n) as a function of monomer conversion (right graph, black squares) with theoretical values (grey dashed line). Dispersity of the PMMA at each molecular weight are shown (red squares, secondary y-axis).*

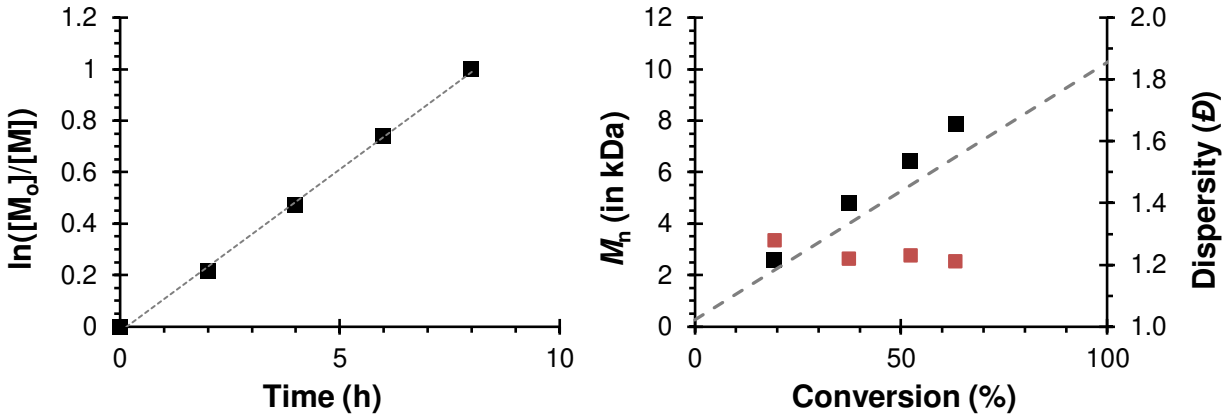

Figure 4.23. *Plot of the natural log of monomer consumption as a function of time (left) for the O-ATRP of MMA mediated by PC **7** under air. Plot of growth of the experimentally measured number average molecular weight (M_n) as a function of monomer conversion (right graph, black squares) with theoretical values (grey dashed line). Dispersity of the PMMA at each molecular weight are shown (red squares, secondary y-axis).*

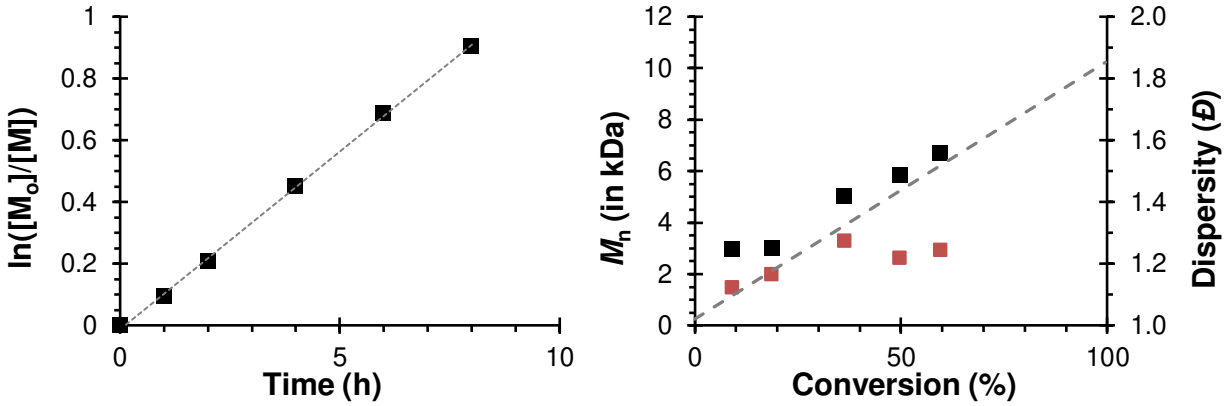

Figure 4.24. *Plot of the natural log of monomer consumption as a function of time (left) for the O-ATRP of MMA mediated by PC **7** under nitrogen. Plot of growth of the experimentally measured number average molecular weight (M_n) as a function of monomer conversion (right graph, black squares) with theoretical values (grey dashed line). Dispersity of the PMMA at each molecular weight are shown (red squares, secondary y-axis).*

MALDI-TOF Analysis of Polymer Synthesized under Air

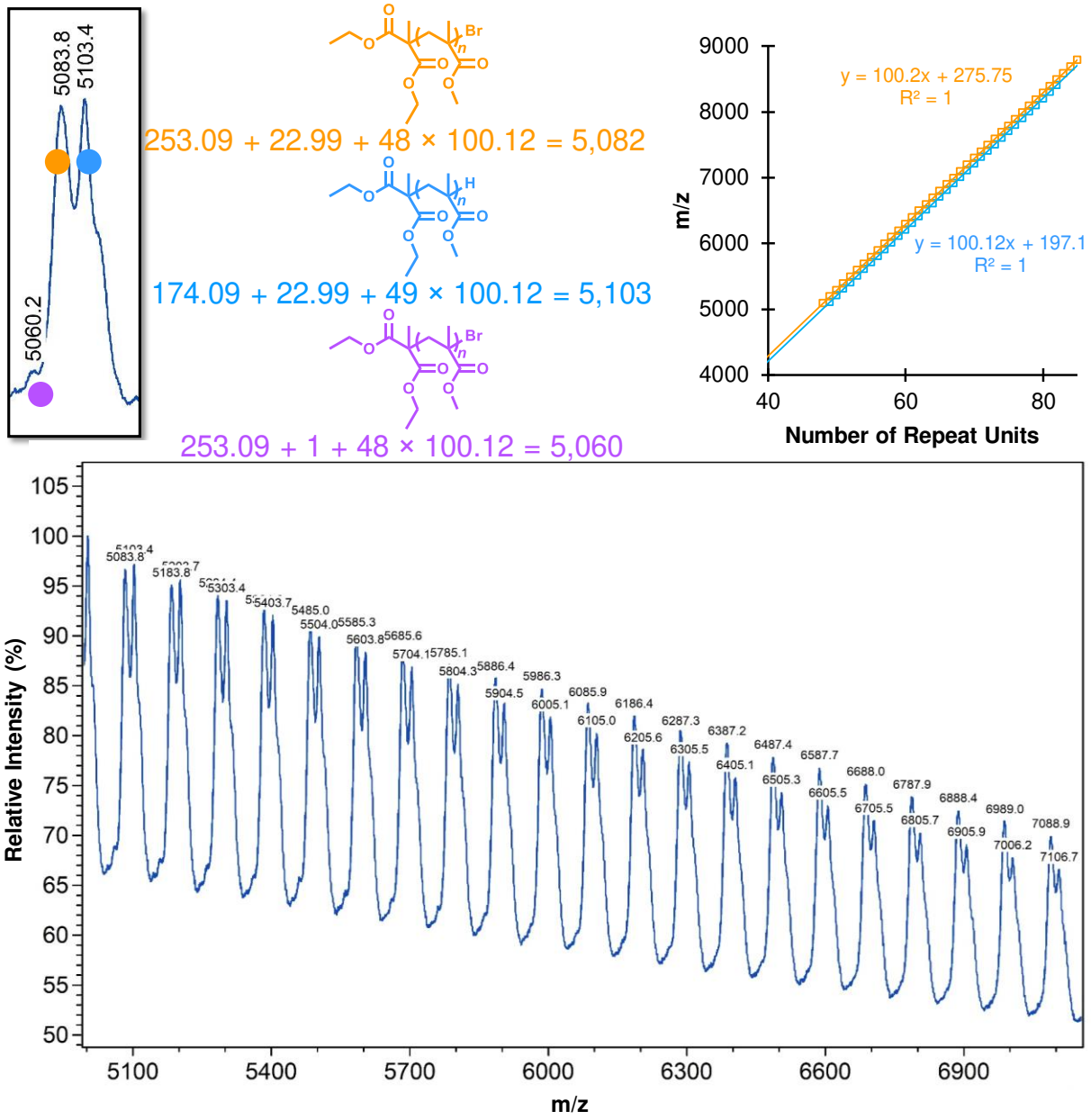

Figure 4.25. *Matrix-assisted laser desorption/ionization time of flight (MALDI-TOF) analysis of PMMA synthesized under air (M_n = 8.2 kDa). Two peaks were assigned to polymer chains with alkyl bromide (orange) or hydrogen (blue) terminal groups and the cationization agent, sodium (top left). A third peak was observed corresponding to protonation of alkyl bromide terminated polymer (purple). A plot of the mass-to-charge (m/z) ratio as a function of number of MMA repeat units (MW = 100.12 g/mol) was used to confirm these assignments (top right). However, analysis of the peaks corresponding to protonation (purple) was not performed because only three peaks were resolved.*

Additional Chain Extension and Block Copolymerization Data

Table 4.5. *Results for the Chain Extension and Block Copolymerization Performed under Air.*

Experiment	PC	time (h)	conv. (%)	$M_{n,th}$ (kDa)	M_n (kDa)	M_w (kDa)	$Đ$ (M_w/M_n)	I^* ($M_{n,th}/M_n \times 100$)
PMMA Macroinitiator	1	7	77	8.0	8.2	10.0	1.22	97
Chain Extended PMMA	1	14	77	18.3	20.6	27.6	1.34	89
P(MMA-b-BnMA) Copolymer	1	14.5	94	29.7	34.3	51.3	1.50	86

REFERENCES

(1) Chen, M.; Zhong, M.; Johnson, J. A.. *Chem. Rev.* **2016**, *116*, 10167–10211.

(2) Corrigan, N.; Shanmugam, S.; Xu, J.; Boyer, C. *Chem. Soc. Rev.* **2016**, *45*, 6165–6212.

(3) Discekici, E. H.; Pester, C. W.; Treat, N. J.; Lawrence, J.; Mattson, K. M.; Narupai, B.; Toumayan, E. P.; Luo, Y.; McGrath, A. J; Clark, P. G.; Read de Alaniz, J.; Hawker, C. J. *ACS Macro Lett.* **2016**, *5*, 258–262.

(4) Ligon, S. C.; Husár, B.; Wutzel, H.; Holman, R.; Liska, R. *Chem. Rev.* **2014**, *114*, 557–589.

(5) Flory, P. J. In *Principles of Polymer Chemistry*; Cornell University Press: New York, 1995; p 168.

(6) Turro, N.J.; Ramamurthy, V.; Scaiano, J.C. In *Modern Molecular Photochemistry of Organic Molecules*; University Science Books: California, 2010; p 1001.

(7) Yeow, J.; Chapman, R.; Gormly, A. J.; Boyer, C. *Chem. Soc. Rev.* **2018**, *47*, 4357–4387.

(8) Miyake G.M.; Theriot, J. C. *Macromolecules* **2014**, *47*, 8255–8261.

(9) Theriot, J. C.; Lim, C-H.; Yang, H.; Ryan, M. D.; Musgrave, C. B.; Miyake, G. M. *Science* **2016**, *352*, 1082–1086.

(10) Ryan, M. D.; Jordan, J. C.; Lim, C-H.; Yang, H.; Lockwood, A. G.; Garrison, N. G.; Lincoln, S. R.; Musgrave, C. B.; Miyake, G. M. *J. Polym. Sci., Part A; Polym. Chem.* **2017**, *55*, 3017–3027.

(11) Lim, C-H.; Ryan, M. D.; McCarthy, B. G.; Theriot, J. C.; Sartor, S. M.; Damrauer, N. H.; Musgrave, C. B.; Miyake, G. M. *J. Am. Chem. Soc.* **2017**, *139*, 348 –355.

(12) Theriot, J.C.; Miyake, G. M.; Boyer, C. A. *ACS Macro Lett.* **2018**, *7*, 662–666.

(13) Pearson, R. M.; Lim, C-H.; McCarthy, B. G.; Musgrave, C. B.; Miyake, G. M. *J. Am. Chem. Soc.* **2016**, *138*, 11399–11407.

(14) McCarthy, B. G.; Pearson, R. M.; Lim, C-H.; Sartor, S. M.; Damrauer, N. H.; Miyake, G. M. *J. Am. Chem. Soc.* **2018**, *140*, 5088–5101.

(15) Sartor, S. M.; McCarthy, B. G.; Pearson, R. M.; Miyake, G. M.; Damrauer, N. H. *J. Am. Chem. Soc.* **2018**, *140*, 4778–4781.

(6) Treat, N. J.; Sprafke, H.; Kramer, J. W.; Clark, P. G.; Barton, B. E.; Read de Alaniz, J.; Fors, B. P.; Hawker, C. J. *J. Am. Chem. Soc.* **2014**, *136*, 16096−16101.

(7) Pan, X.; Lamson, M.; Yan, J.; Matyjaszewski, K. *ACS MacroLett.* **2015**, *4*, 192–196.

(8) Pan, X.; Fang, C.; Fantin, M.; Malhotra, N.; So, W. Y.; Peteanu, L. A.; Isse, A. A.; Gennaro, A.; Liu, P.; Matyjaszewsk, K. *J. Am. Chem. Soc.* **2016**, *138*, 2411–2425.

(9) Liu, X.; Zhang, L.; Cheng, Z.; Zhu, X. *Polym. Chem.* **2016**, *7*, 689–700.

(20) Kutahy, C.; Aykac, F. S.; Yilmaz, G.; Yagci, Y. *Polym. Chem.* **2016**, *7*, 6094–6098.

(2) Allushi, A.; Jockusch, S.; Yilmaz, G.; Yagci, Y. *Macromolecules* **2016**, *49*, 7785–7792.

(22) Allushi, A.; Kutahya, C.; Aydogan, C.; Kreutzer, J.; Yilmaz, G.; Yagci, Y. *Polym. Chem.* **2017**, *8*, 1972–1977.

(23) Kutahya, C.; Allushi, A.; Isci, R.; Kreutzer, J.; Ozturk, T.; Yilmaz, G.; Yagci, Y.. *Macromolecules* **2017**, *50*, 6903–6910.

(24) Huang, Z.; Gu, Y.; Liu, X.; Zhang, L.; Cheng, Z.; Zhu, X. *Macromol. Rapid Commun.* **2017***, 38,* 1600461.

(25) Theriot, J. C.; McCarthy, B. G.; Lim, C-H.; Miyake, G. M. *Macromol. Rapid. Commun.* **2017**, *38*, 1700040.

(26) Pan, X.; Fantin, M.; Yuan, F.; Matyjaszewski, K. *Chem. Soc. Rev.* **2018**, *47*, 5447–5490.

(27) Liarou, E.; Whitfield, R.; Anastasaki, A.; Engelis, N. G.; Jones, G. R.; Velonia, K.; Haddleton, D.M. *Angew. Chem. Int. Ed.* **2018**, 57, 8998–9002.

(28) Matyjaszewski, K.; Coca, S.; Gaynor, S. G.; Wei, M.; Woodworth, B. E. *Macromolecules* **1998**, *31*, 5967–5969.

(29) Ryan, M. D.; Pearson, R. M.; French, T. A.; Miyake, G. M. *Macromolecules* **2017**, *50*, 4616–4622.

(30) Ramsey, B. L.; Pearson, R. M.; Beck, Logan, R.; Miyake, G. M. *Macromolecules* **2017**, *50*, 2668–2674.

(3) Discekici, E. H.; St. Amant, A. H.; Nguyen, S. N.; Lee, I-H.; Hawker, C. J.; Read de Alaniz, J. *J. Am. Chem. Soc.* **2018**, *140*, 5009–5013.

(32) Buss, B. L.; Beck, L. R.; Miyake, G. M. *Polym. Chem.* **2018**, *9*, 1658–1665.

CHAPTER 5 – EXPLOITING CHARGE TRANSFER STATES FOR MAXIMIZING INTERSYSTEM CROSSING YIELDS IN ORGANIC PHOTOREDOX CATALYSTS

Overview

A key feature of prominent transition-metal- containing photoredox catalysts (PCs) is high quantum yield access to long-lived excited states characterized by a change in spin multiplicity. For organic PCs, challenges emerge for promoting excited-state intersystem crossing (ISC), particularly when potent excited-state reductants are desired. Herein, we report a design exploiting orthogonal π-systems and an intermediate- energy charge-transfer excited state to maximize ISC yields (Φ_{ISC}) in a highly reducing (E^{0*} = −1.7 V vs SCE), visible-light-absorbing phenoxazine-based PC. Simple substitution of N-phenyl for N-naphthyl is shown to dramatically increase ΦISC from 0.11 to 0.91 without altering catalytically important properties, such as E^{0*}.

Introduction

The recent resurgence of photoredox catalysis was facilitated by discrete photoredox catalysts (PCs) whose lowest energy excited states are formed in significant yields and are sufficiently long-lived to efficiently engage in outer-sphere electron transfer in competition with inner-sphere decay processes.[1] This property can confer distinct benefits for photoredox catalysis: making possible high conversion efficiencies, allowing for conditions employing small co-catalyst concentrations, making feasible catalysis via activated electron transfer, and decreasing catalyst loading.[2] Because long lifetimes are commonly enabled by spin interconversion in the excited state, initial PCs were chromophores incorporating transition metals (e.g., Ru or Ir) where Φ_{ISC} (where ISC refers to intersystem crossing) is approximately unity due to the heavy atom effect.[3]

The scarcity of Ru and Ir has motivated exploration of PCs built from abundant materials. Those incorporating first row transition metals similarly exploit the heavy-atom effect for lifetime extension.[4] Organic PCs (OPCs) are attractive by way of extending reaction scope[5] and alleviate metal contamination concerns.6 However, unlike metal-containing PCs, optimization of Φ_{ISC} in OPCs must be tied to design. For excited-state oxidants, high Φ_{ISC} can be achieved using carbonyls[5] or by incorporation of heavy halogens.[7] Unfortunately, these strategies are often impractical for highly reducing chromophores[6,8] due to the electron withdrawing character of these functional groups which can lessen the reducing power of the OPC or impact its chemical stability.[2c,9]

Recently, we reported a highly reducing, phenoxazine-based OPC (**2**) which possesses a notably high Φ_{ISC} = 0.91 and a triplet lifetime of 480 μs at room temperature (RT) in *N*,*N*-dimethylacetamide (DMAc).[10] It was soon thereafter noted that high Φ_{ISC} is not shared by all structurally similar PCs. In particular, replacement of *N*-naphthyl with *N*-phenyl (**1**) results in Φ_{ISC} = 0.11. This is surprising since the *N*-substituent does not impact the initial and final excited states in both compounds (*vide infra*), nor does it alter the reduction potential from the long-lived triplet, which has been reported as −1.70 and −1.72 V vs SCE for **1** and **2**.[10,11] Notably, these reduction potentials are potent even by comparison to well-known Ir(III) complexes such as fac-Ir(ppy)$_3$ (−1.73 V vs SCE). The current work seeks to uncover the photophysical mechanism for this stark discrepancy in Φ_{ISC}, such that it may be exploited in comparable OPC systems.

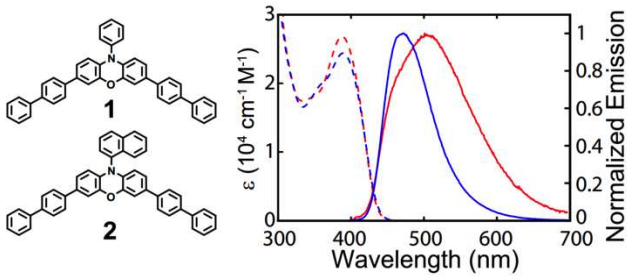

Figure 5.1. *Absorption (dashed)*[10-11] *and emission (solid) of* ***1*** *(blue) and* ***2*** *(red) in deaerated RT DMAc.*

Results and Discussion

Figure 5.1 shows electronic absorption for **1** and **2** in DMAc. The spectra are highly similar, possessing comparable λmax and molar extinction. These data were modeled using TD-DFT (see *Experimental* section) which reveals that the prominent lowest-energy feature at 388 nm for both PCs is almost completely described as a single interorbital transition originating in a phenoxazine-localized HOMO. The acceptor orbitals (LUMO for 1 and LUMO+1 for **2**) are qualitatively the same and indicate wave function delocalization over the phenoxazine plus the adjacent rings of both biphenyl substituents (Figure 5.10 of the *Experimental* section). Neither involves the nearly perpendicular *N*-aryl substituent. We next consider the catalytically relevant lowest-energy excited states. Figure 5.2A,B shows selected nanosecond transient absorption (NSTA) spectra for **1** and **2**. The long and strongly oxygen sensitive lifetimes (1200 μs (**1**) and 480 μs (**2**)[12]) are highly suggestive that the lowest-energy excited state in these systems is a triplet.

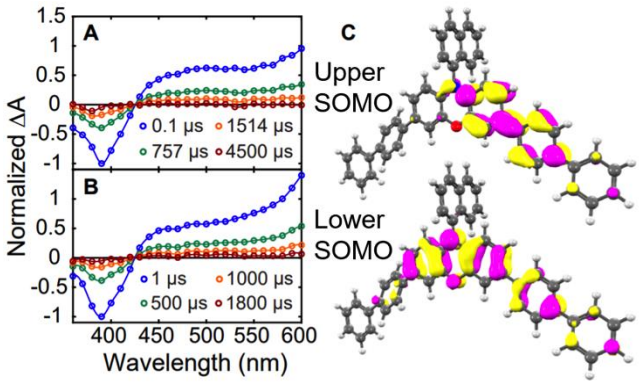

Figure 5.2. *Selected spectra from NSTA of **1** (A) and **2** (B)[10] in deaerated RT DMAc. (C) Triplet SOMOs of **2** (cam-b3lyp/6-31g(d,p)/CPCM-DMA level of theory).*

Both compounds possess similar NSTA spectra, consisting of a prominent ground-state bleach and a largely unfeatured excited-state absorption (ESA). DFT calculations within the triplet manifold offer additional insight. Figure 5.2C shows the singly occupied molecular orbitals (SOMOs) determined for the geometry-optimized lowest-energy triplet of **2**. The SOMOs for **1** are highly similar (Figure 5.11 of the *Experimental* section). For both PCs, the lower SOMO is dominated by phenoxazine π character which strongly resembles the ground-state (GS) HOMO (Figure 5.10 of the *Experimental* section). In contrast, the higher SOMO (in both molecules) shows π character shifted asymmetrically, including one outer ring of the phenoxazine plus the adjacent ring from a single biphenyl substituent. This SOMO is suggestive of double-bond character between these two rings on one side of the PC, a point that is strongly supported by structural changes on that side of the molecule (shortening of the first inter-ring C−C bond concomitant with the decreasing of the inter-ring dihedral angle) noted in the comparison between the optimized triplet and GS geometries (see *Experimental*). With SOMOs in mind, the lowest triplet of **1** and **2** is interpreted as charge transfer (CT), involving a shift of electron density from the phenoxazine toward one of the biphenyl substituents (denoted TCT-Biph). We note that this symmetry-breaking CT is typical of acceptor− donor−acceptor complexes possessing relatively low quadrupolar moments, particularly in polar solvents (e.g., DMAc).[13] Drawing on computational and NSTA results, **1** and **2** have highly similar lowest triplets. Notwithstanding, the measured Φ_{ISC}s for **1** and **2** are highly divergent. Whereas Φ_{ISC} for **2** is 91%,[10] this sharply contrasts with 11% reported here for **1**, as determined using a triplet−triplet energy-transfer method.[10] These observations motivate a more extensive photophysical characterization.

Emission spectra (Figure 5.1) originate within the singlet manifold, an assignment supported by time-resolved measurements and their insensitivity to ambient oxygen (see *Experimental*). No triplet emission is observed for either compound. Both species exhibit a high degree of solvatochromism,[10,11] indicating CT character in their emissive states. However, their spectral profiles are clearly distinct. Whereas that of **1** is unremarkable, that of **2** is broader and red-shifted with a shoulder at ~460 nm. Importantly, there are also substantial emission quantum yield differences: Φ_{em}(**1**) = 80% while Φ_{em}(**2**) = 2.3% (Table 5.1 of the *Experimental* section).

An initial effort to characterize dynamics involved time-correlated singlet photon counting (TCSPC). In addition to kinetic information, time evolution of spectral features can be assessed (see *Experimental*). **1** is again unremarkable. Under certain pump polarization conditions, a 350 ps rotational diffusion contribution is observed, but under no circumstances are profile changes seen (see Figures 5.14 and 5.16 of the *Experimental* section). The spectrum decays to baseline with a time constant of 2.87 ns, assigned to the lifetime of the S_1 (Table 5.1 of the *Experimental* section).

Given the aforementioned fluorescence solvatochromism for **1**, we anticipate that the emitting state has symmetry-breaking CT character involving the phenoxazine and a single biphenyl substituent. This assignment is strongly supported by measurements of a chemical analogue possessing only one biphenyl substituent but is otherwise identical (called **1a**; see *Experimental*). Notably, while these compounds possess quite different absorption profiles,[11] the emission profiles of **1** and **1a** are remarkably similar (Figure 5.19 of the *Experimental* section), corroborating the symmetry breaking CT assignment of the S_1 in **1**. We refer to it hereafter as $S_{CT\text{-}Biph}$.

In contrast to **1**, TCSPC data for **2** show marked spectral evolution. We have extracted 20 ps and 5.2 ns speciesassociated spectra (Figure 5.3). Interestingly, the early-time spectrum of **2** peaks at 460 nm, a value very similar to $\lambda_{max,em}$ for **1**. This is compelling evidence that **2** initially explores an emissive singlet similar to SCT-Biph in **1**. At later times, emission in **2** changes dramatically, culminating in the broad spectrum centered at 505 nm that is responsible for the red shift in Figure 5.1. Consideration of the only substitutional difference hints at participation by the *N*-naphthyl moiety.

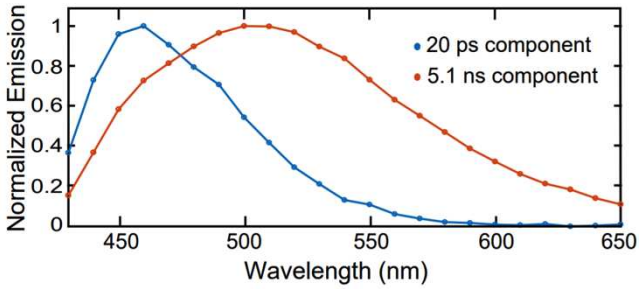

Figure 5.3. *Species-associated emission spectra for 2 in deaerated RT DMAc generated by a globally fit bi-exponential model of the TCSPC data.[14] See experimental for details.*

Using Φ_{em} and TCSPC lifetimes, a radiative rate constant (k_r) can be quantified see Table 5.1 of the *Experimental* section for equations). **1** is straightforward, given only one emissive state. In **2**, early S_n emission (Figure 5.3) makes a minor contribution (~3.7%) and can be ignored. As seen in Table 5.1 of the *Experimental* section S_1, k_r for **1** is a factor of 70 larger than in **2**. Further, using Φ_{ISC} along with the observed emission lifetime, k_{ISC} can be isolated from other nonradiative pathways (k_{nr}). Notably, k_{ISC} for **2** is 4.5 times greater than for **1**.

These molecule-specific k_r and k_{ISC} values have a marked impact on catalytically important properties. To better understand their origins, femtosecond transient absorption (FSTA) experiments (400 nm pump) were conducted. In **1** (Figure 5.4A), the data reveal early processes that complete within ~10 ps. The remaining spectral features (see *Experimental* for discussion) decay uniformly with a longer component (>2 ns) that cannot be fully resolved. This includes the

620 nm ESA, which is expected to involve $\pi^* \leftarrow \pi^*$ originating in excess charge density on the biphenyl. Given the TCSPC lifetime as well as spectral assignments (see *Experimental*), these latter TA features are assigned to $S_{CT\text{-}Biph}$.

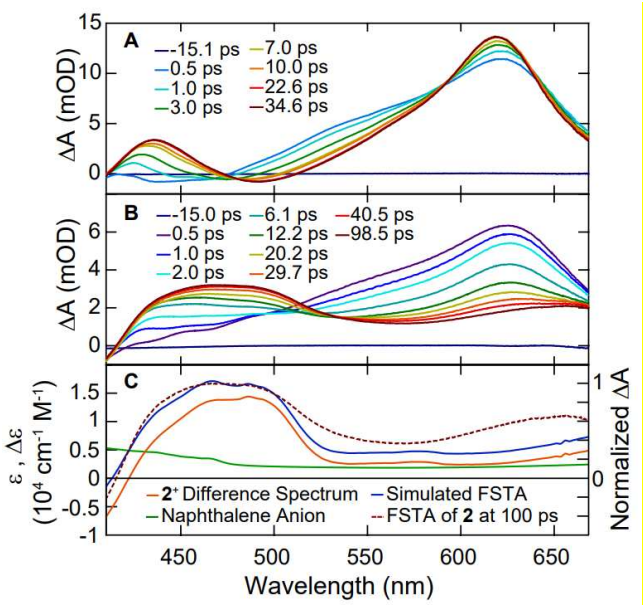

Figure 5.4. *Selected spectra for **1** (A) and **2** (B) from FSTA in deaerated RT DMAc. (C) A late-time TA spectrum of **2** (dashed, right axis) and the simulated spectrum with relevant redox-derived data (solid, left axis).*

We next turn to **2** (Figure 5.4B). At early times the spectrum is very similar to that of **1**, consistent with the GS absorption commonality. However, striking evolution follows, including the emergence of a broad ESA (~470 nm) over ~20 ps that then remains for the experiment duration. This evolution corroborates TCSPC evidence that **2** initially occupies a state analogous to $S_{CT\text{-}Biph}$ in **1** but then rapidly relaxes to an S1 unique to **2**. Interestingly, beginnings of evolution on the nanosecond time scale are observable (Figure 5.20 of the *Experimental* section), corresponding to the emergence of features seen in longer time NSTA data (Figure 5.2). This is consistent with triplet-state formation.

The low degree of electronic coupling between the naphthyl substituent that is ~90° (GS geometry) relative to the phenoxazine enables assignment of this unique S_1 in **2** using absorption

spectra of respective ions in a redox pair. The spectrum and molar extinction of the cation (~14 400 M−1 cm−1 at 490 nm) was determined by spectroelectrochemical bulk electrolysis of **2** (see SI). The anionic spectrum was produced by chemical reduction of naphthalene using sodium,15 and the molar extinction ε(λ) was estimated using relevant literature[16] (~3500 M−1 cm−1 at 465 nm) (see *Experimental*). The sum of these redox-derived data is used to simulate a FSTA spectrum, which is compared with a long-time FSTA spectrum of **2** in Figure 5.4C. These data agree well, particularly with respect to the ~475 nm ESA. The S_1 of **2** is thus assigned and denoted as $S_{CT\text{-}Naph}$.

An energy level diagram is presented in Figure 5.5. In **1**, excitation to the Franck−Condon singlet (SFC) is followed by solvent reorganization and inter-ring conformational relaxation as $S_{CT\text{-}Biph}$ is formed and thermalized on a <10 ps time scale. That state can undergo ISC, but ISC is in competition with efficient photoluminescence driven by a large k_r. The result is a high Φ_{em} concurrent with low Φ_{ISC}.

For **2** there is an important difference inasmuch as $S_{CT\text{-}Biph}$ is only transiently populated prior to formation of an intermediate $S_{CT\text{-}Naph}$. This has significant consequences that are, we believe, inherent to the geometry of $S_{CT\text{-}Naph}$ which resembles a radical pair. First, the perpendicular anion and cation π-systems significantly decrease k_r connecting $S_{CT\text{-}Naph}$ with the GS. This phenomenon is seen in compounds like 9,9-bianthryl.[17] The second consequence concerns the overall reaction $S_{CT\text{-}Naph} \rightarrow T_{CT\text{-}Biph}$, which competes effectively against k_r and k_{nr}.

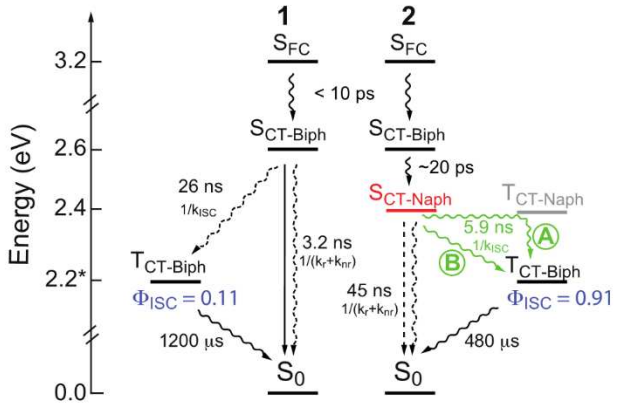

Figure 5.5. *Energy level diagram with alternative ISC pathways (A) and (B) shown for* ***2****. Dashed lines reflect less likely pathways. Time constants (after formation of the lowest-energy singlet) are derived from coefficients tabulated in Table 5.1 of the Experimental section as described there. Generally, energies are derived from the absorption or emission* λ_{max}*.* $T_{CT\text{-}Naph}$ *(grey) is not observed, and its energy is approximated. The y-axis* * *indicates energies determined computationally.*

Here, there are two ISC pathways (denoted (A) and (B) in Figure 5.5) which cannot be definitely distinguished without further magnetic-field dependent measurements. For (A), the rate-limiting step is $S_{CT\text{-}Naph} \rightarrow T_{CT\text{-}Naph}$ ISC. These states should have comparable energies as the orthogonal orbital systems limit direct exchange interactions between the unpaired electrons. While spin−orbit coupling between SCT-Naph and TCT-Biph is not expected to be large given the common orbitals, the near-degeneracy could increase coupling via hyperfine interactions.[18] In (B), ISC directly couples $S_{CT\text{-}Naph}$ with the long-lived $T_{CT\text{-}Biph}$. To understand why this might be fast, we draw on literature showing that CT states with perpendicular geometries have greatly enhanced k_{ISC} to a locally excited triplet[19] because the large change in orbital angular momentum facilitates spin−orbit coupling between states. Due to the high degree of spatial separation of SOMOs generally required to facilitate ISC via (A),[20] (B) is considered to be the more likely pathway.

Conclusion

These findings show that the introduction of a CT state with perpendicular geometry at an appropriate energy can dramatically improve Φ_{ISC} for phenoxazine-based OPCs, and, importantly, this state has minimal impact on other photophysical parameters key to photocatalysis.

Experimental

1. Materials and Methods

Compounds **1** and **2** were synthesized according to a previously published procedures[7g,11]. Anhydrous *N*,*N*-dimethylacetamide (DMAc), anhydrous dimethoxyethane, tetrahydrofuran (THF), and sodium lumps were purchased from Sigma-Aldrich. Naphthalene crystals were purchased from Fisher Scientific.

2. Photophysical Characterization

For steady state emission, TCSPC, and NSTA experiments, all samples were prepared in 1 cm x 1 cm quartz cuvettes with optical densities near or below 0.1 at the excitation wavelength. All samples used anhydrous DMAc (with the exception of Figure 5.19 of the *Experimental* section, in which THF was also used as a solvent) and were degassed prior to experiments by bubbling argon for at least 15 minutes. All reported lifetimes and quantum yields are the average of at least three independent measurements, and the reported percent error is 2 times the standard deviation of a set of measurements.

Absorption and Emission Spectra and Emission Quantum Yield

Absorption spectra were measured using an Agilent Cary 5000 UV-Vis-NIR Spectrophotometer. Emission spectra were measured using an SLM 8000C Spectrofluorometer

with the appropriate wavelength-dependent correction applied to the raw data. The quantum yield of emission was determined by the comparative method, using Coumarin 460 in ethanol as the reference for **1** and Coumarin 500 in methanol as the reference for **2**.

Time-Correlated Single Photon Counting (TCSPC)

A continuous wave diode laser (Millennia Xs Pro, Spectra Physics) pumped a mode-locked femtosecond Ti:Sapphire oscillator (Tsunami, Spectra Physics) producing pulsed 800 +/- 5 nm light at a repetition rate of 82 MHz and width of ~100 fs. The pulses were passed through a pulse-picker (NEOS technologies) utilizing an acousto-optic modulator (Bragg cell) to lower the repetition rate to 4.1 MHz. The deflected output beam was passed through a β-barium borate (BBO) crystal to generate the second harmonic of the fundamental centered at 400 nm. The output was filtered to remove any of the unconverted fundamental. The remaining 400 nm beam was measured to have a power of ~ 100 μW and was attenuated with neutral density filters as needed to avoid saturation of the detector. The emitted light was collected at 90° relative to the direction of excitation, focused, and passed a polarizer set at magic angle relative the polarization of the excitation before passing through a monochrometer. Since horizontally polarized light was used for excitation, observation at magic angle does not necessarily prevent observation of a time-dependent rise in emission intensity which can result from rotational diffusion of the excited compound. Detection was achieved using a water-cooled microchannel plate PMT (Hamamatsu, R3809U-50) negatively biased at −2900 V. The instrument response function was recorded with the use of a dilute scattering solution ($CaCO_3$ in water) and observing 400 nm light.

Emission traces were fit to model of exponentials convoluted with a Gaussian fit of the instrument response function, with the lowest number of exponentials used that would give a reasonable fit. In addition to kinetic information at individual wavelengths, spectrally resolved

time-dependent emission data was generated by collected emission traces at several individual wavelengths and then normalizing the area of each individual trace to the steady-state emission intensity at that particular wavelength. This spectrally resolved TCSPC data was then globally fit to gaussian-convoluted exponential decays, yielding species-associated spectra.

Nanosecond Transient Absorption (TA)

Nanosecond to millisecond TA measurements were made using a previously described home-built setup[10]. All samples were excited at 355 nm in generating spectra and excited state lifetimes. Spectra were constructed using single-wavelength kinetics collected every 10 nm that were subsequently fit using a global single exponential decay model. Φ_{ISC} was measured using a triplet-triplet energy transfer (TETT) method described previously[10], with *fac*-Ir(ppy)$_3$ as the sensitizer.

FSTA

Femtosecond transient absorption data were collected using a previously described home-built setup.[21] Samples were prepared in anhydrous DMAc and degassed by purging with argon for 20 minutes prior to being sealed in a quartz cuvette with a path length of 0.2 cm. Samples were excited at 400 nm and were prepared to have a low optical density (~0.2) at that wavelength.

Spectroelectrochemical Measurements

Spectroelectrochemistry experiments were conducted using a home-built glass optically transparent thin layer electrode cell with a 0.2 cm path length and a Pt mesh working electrode, a Pt wire counter electrode, and a freshly prepared 0.01 M Ag/$AgNO_3$ reference electrode which used anhydrous DMAc for the solvent. 0.1 M tetrabutylammonium hexafluorophosphate ($TBAPF_6$) was used as the electrolyte. The sample was dissolved in anhydrous DMAc, degassed with Ar, then blanketed with Ar for the duration of the experiment. Bulk electrolysis of the sample was performed using an electrochemical analyzer (CH Instruments 601C), and electronic

absorption spectra were acquired using a Hewlett Packard diode array UV-vis spectrophotometer (HP8452A). Cyclic voltammetry measurements using the freshly prepared 0.01M $Ag/AgNO_3$ reference electrode were conducted in order to determine potentials for bulk electrolysis.

3. Key Photophysical Parameters

Table 5.1. *Summary of Photophysical Data Acquired in DMAc at 298K.*

PC	$\lambda_{max,abs}$ (nm)	$\lambda_{max,em}$ (nm)	τ_{S1} (ns)	Φ_{em}	τ_{T1} (μs)	Φ_{ISC}	k_r[a] (s^{-1})	k_{nr}[a,c] (s^{-1})	k_{ISC} (s^{-1})
1	388	472	2.87 ± 0.04	0.8 ± 0.1	1200 ± 200	0.11 ± 0.02	2.8×10 ± 0.4×10^8	3×10^7 ± 4×10^7	3.8×10 ± 0.7×10^7
2	388	505	5.2 ± 0.1	0.023 ± 0.006	480 ± 50[b]	0.91 ± 0.09[b]	4×10^6 ± 1×10^6	1×10^7 ± 2×10^7	1.7×10 ± 0.2×10^8

[a]Rate constants for $S_1 \rightarrow GS$.
[b]Values from reference 3.
[c]This value is calculated via the following equation:

$$k_{nr} = \tau_{S1}^{-1} - k_r - k_{ISC}$$

Propagation of error from k_r and k_{ISC} results in an error calculated for k_{nr} which exceeds the value of k_{nr} itself, for both **1** and **2**.

4. Computational Data and Methods

All calculations utilized the GAUSSIAN 09 version D01 computational chemistry package.[22] All coordinates in Tables S6 – S9 are reported in Angstrom in the XYZ format. Energy is reported in parentheses as follows: E_{0k} (not ZPE and thermally corrected), H (298 K) and G (298 K) stated in units of Hartree.

Ground and triplet state geometries of compounds **1** and **2** were obtained using similar methods to references **1** and **2**, computed at the uM06/6-31+g(d,p)/CPCM-n,n-dimethylacetamide level of theory. Using this geometry, vibrational calculations were performed at the uM06/6-311+g(d,p)/CPCM-n,n-dimethylacetamide, and frequency calculations were performed at the uM06/6-31+g(d,p)/CPCM-n,n-dimethylacetamide level of theory, due to the extensive structure, to achieve the Gibbs free energies.

These geometries were then used to perform a single point time dependent density functional theory (TD-DFT) calculation using cam-b3lyp/6-31+g(d,p)/CPCM-n,n-dimethylacetamide, molecular orbitals were obtained and visualized with cam-b3lyp/6-31g(d,p)/CPCM-n,n-dimethylacetamide.[23] The first 8 excited states of a total of 20 calculated for compound **1** and **2** are reported below. Dominant transitions involved in excitation within strong oscillator strengths (high f value) are denoted in the predicted absorption spectrum figures with the $S_1 \leftarrow S_o$ transition highlighted in red.

TD-DFT of Ground State Absorption

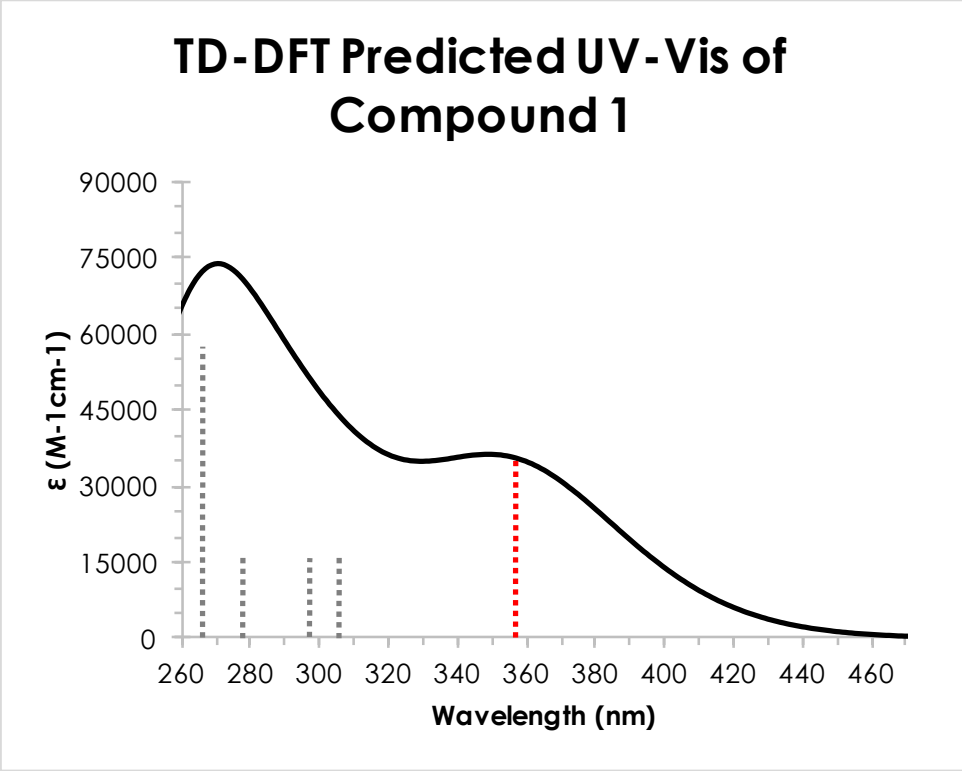

Figure 5.6. *UV-Vis stick spectrum for* ***1****, which shows the lowest energy transition of significant oscillator strength in red. The spectrum in black assumes a Gaussian band shape with a standard deviation of 0.4 eV for each transition. Note that the TD-DFT method used commonly overestimates transition energies.*[24]

Table 5.2. *Computed molecular orbital origins for the lowest-energy absorption transition in PC* ***1****.*

Orbital Transition	Percent Contribution
HOMO → LUMO	77%
HOMO → LUMO + 7	11%
HOMO - 1 → LUMO + 1	3%
HOMO → LUMO + 2	2%

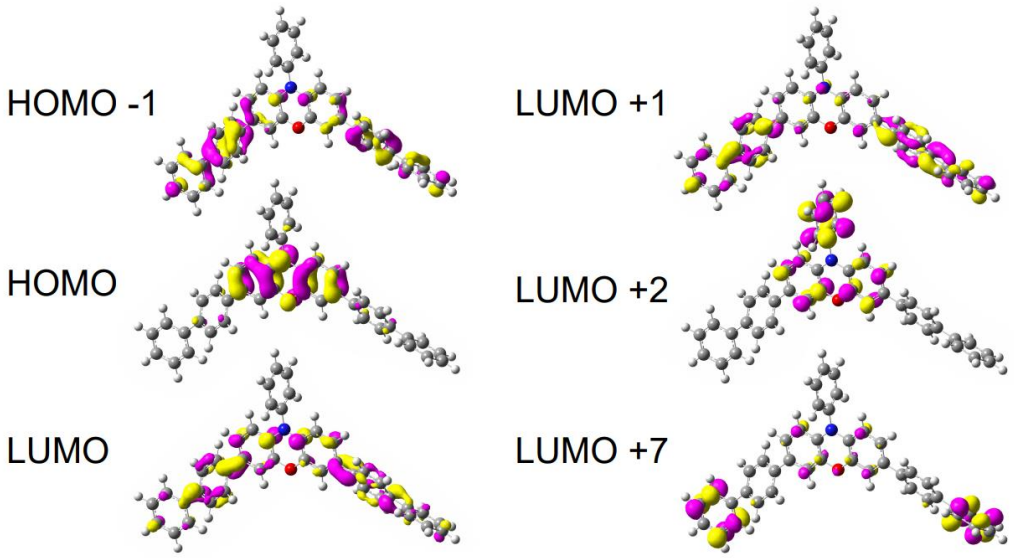

Figure 5.7. *Visualizations of the molecular orbitals involved in the calculated lowest energy excitation of* ***1****.*

Table 5.3. *The eight lowest-energy excitations computed for compound* ***1****.*

Excited State 1: Singlet 3.4725 eV 357.05 nm f=0.8128 <S**2>=0.000	
147 ->150 (π_{HOMO-1}->π_{LUMO+1})	-0.11829
148 ->149 (π_{HOMO}->π_{LUMO})	0.62092
148 ->151 (π_{HOMO}->π_{LUMO+2})	-0.1057
148 ->156 (π_{HOMO}->π_{LUMO+7})	-0.23079
Excited State 2: Singlet 4.0616 eV 305.26 nm f=0.3740 <S**2>=0.000	
145 ->149	0.10005
148 ->151	0.60349
148 ->162	0.23831
Excited State 3: Singlet 4.1519 eV 298.62 nm f=0.3586 <S**2>=0.000	
147 ->149	-0.17482
148 ->150	0.52358
148 ->154	-0.17263
148 ->157	0.20312
148 ->159	-0.21329
Excited State 4: Singlet 4.2835 eV 289.45 nm f=0.0024 <S**2>=0.000	
145 ->152	-0.10735
148 ->152	0.67223
Excited State 5: Singlet 4.4456 eV 278.89 nm f=0.3776 <S**2>=0.000	
146 ->150	0.18797
147 ->149	0.27951
148 ->150	-0.26703
148 ->154	-0.26613
148 ->157	0.25598
148 ->159	-0.21613
148 ->165	0.19613
Excited State 6: Singlet 4.6324 eV 267.64 nm f=0.0094 <S**2>=0.000	
148 ->153	0.47181
148 ->154	0.13865
148 ->155	0.26075
148 ->158	-0.12056
148 ->159	-0.14197
148 ->163	0.17159
148 ->164	0.10567
148 ->168	-0.17104
Excited State 7: Singlet 4.6690 eV 265.55 nm f=1.3102 <S**2>=0.000	
146 ->149	0.43993
147 ->150	0.37122
148 ->156	-0.28175
Excited State 8: Singlet 4.7776 eV 259.51 nm f=0.0001 <S**2>=0.000	
146 ->149	0.10631

147 ->154	0.10064
148 ->151	-0.245
148 ->153	-0.14575
148 ->155	0.23661
148 ->156	0.18664
148 ->157	0.11905
148 ->158	-0.23506
148 ->160	-0.1704
148 ->162	0.37219

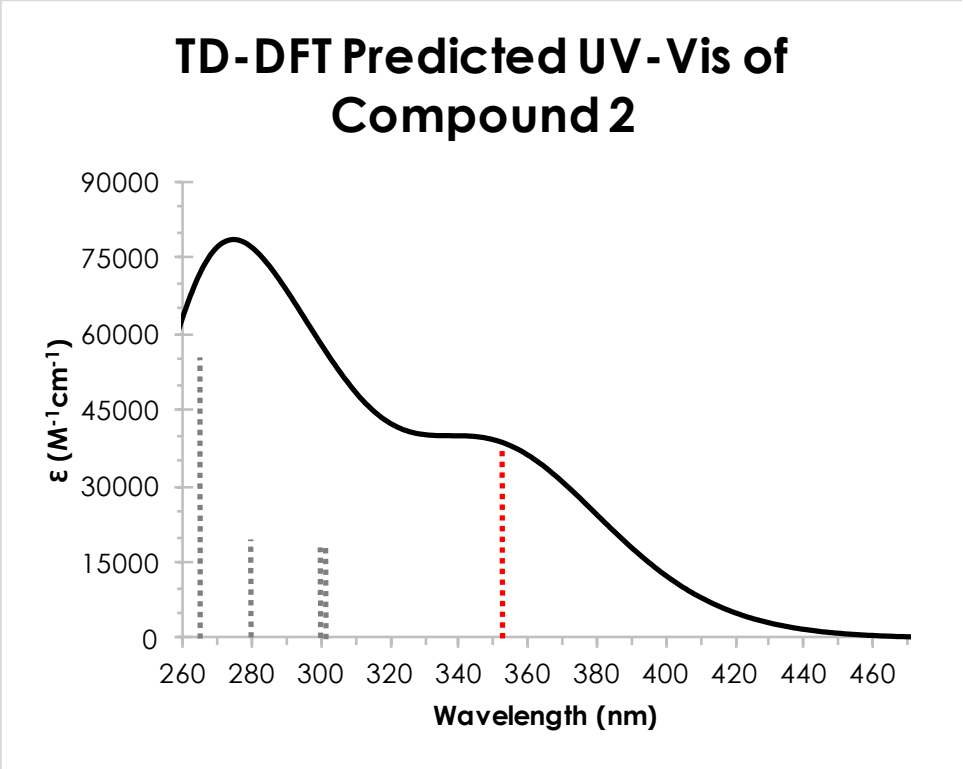

Figure 5.7*. UV-Vis stick spectrum for* ***2****, which shows the lowest energy transition of significant oscillator strength in red. The spectrum in black assumes a Gaussian band shape with a standard deviation of 0.4 eV for each transition. Note that the TD-DFT method used commonly overestimates transition energies.*[24]

Table 5.4. *Computed molecular orbital transitions for the lowest-energy absorption of PC* ***2****.*

Transition	Percent Contribution
HOMO → LUMO + 1	77%
HOMO → LUMO + 6	5%
HOMO → LUMO + 7	4%
HOMO - 1 → LUMO + 2	3%
HOMO → LUMO + 8	3%

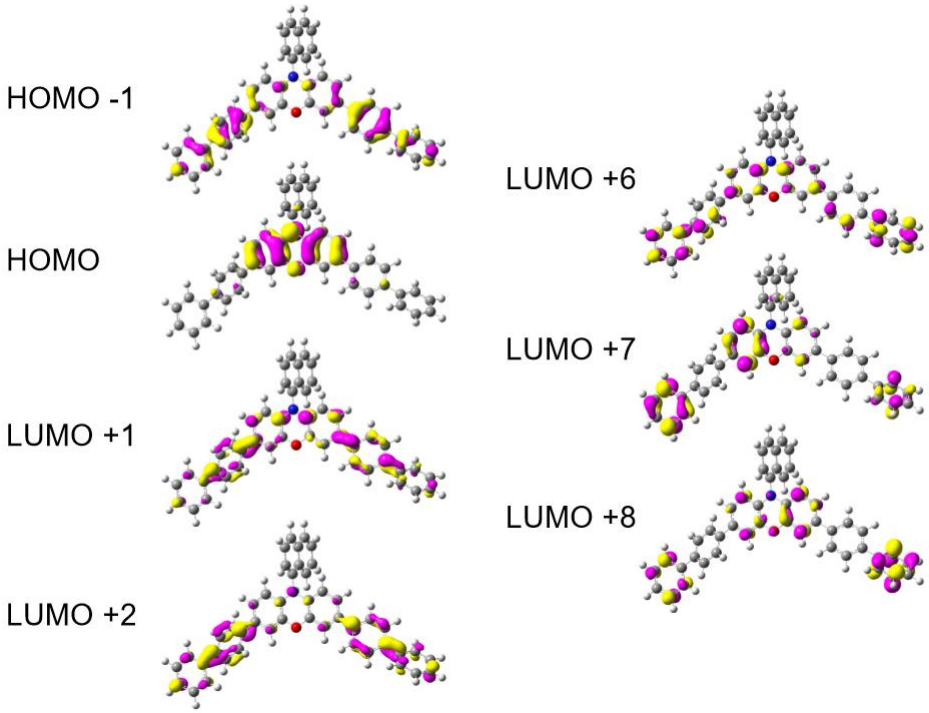

Figure 5.8. *Visualizations of the molecular orbitals involved in the calculated lowest energy excitation of* ***2****.*

Table 5.5. *The eight lowest-energy excitations computed for compound* ***2****.*

Excited State 1: Singlet 3.5098 eV 353.25 nm f=0.8585 <S**2>=0.000	
160 -> 164 (π_{HOMO-1}->π_{LUMO+3})	-0.12887
161 -> 163 (π_{HOMO}->π_{LUMO+1})	0.62232
161 -> 168 (π_{HOMO}->π_{LUMO+6})	0.1533
161 -> 169 (π_{HOMO}->π_{LUMO+7})	-0.14429
161 -> 170 (π_{HOMO}->π_{LUMO+8})	0.13225
Excited State 2: Singlet 3.6335 eV 341.22 nm f=0.0058 <S**2>=0.000	
161 -> 162	0.68022
Excited State 3: Singlet 4.1179 eV 301.08 nm f=0.4221 <S**2>=0.000	
160 -> 163	-0.14426
161 -> 164	0.41164
161 -> 165	0.31883
161 -> 166	-0.19593
161 -> 171	0.24118
161 -> 172	-0.12285
Excited State 4: Singlet 4.1275 eV 300.38 nm f=0.4074 <S**2>=0.000	
160 -> 163	0.11381
161 -> 164	-0.3154
161 -> 165	0.40498
161 -> 167	-0.13714
161 -> 168	-0.1933
161 -> 170	0.1156
161 -> 173	0.24211
Excited State 5: Singlet 4.4203 eV 280.49 nm f=0.4454 <S**2>=0.000	
158 -> 164	-0.18977
159 -> 162	-0.1352
160 -> 163	-0.28073
161 -> 164	0.22283
161 -> 166	0.31512
161 -> 168	-0.20198
161 -> 170	0.15187
161 -> 171	-0.15422
161 -> 172	0.11573
161 -> 177	-0.17181
Excited State 6: Singlet 4.5424 eV 272.95 nm f=0.0407 <S**2>=0.000	
156 -> 162	-0.115
156 -> 165	-0.12468
159 -> 162	0.63618
161 -> 164	0.13536
Excited State 7: Singlet 4.5760 eV 270.95 nm f=0.0025 <S**2>=0.000	
156 -> 162	0.47583
159 -> 162	0.14334

159 -> 165	0.4118
159 -> 167	0.11582
Excited State 8: Singlet 4.6497 eV 266.65 nm f=1.2526 <S**2>=0.000	
158 -> 163	0.44844
160 -> 164	0.37603
161 -> 168	0.15086
161 -> 169	-0.1619
161 -> 170	0.15326

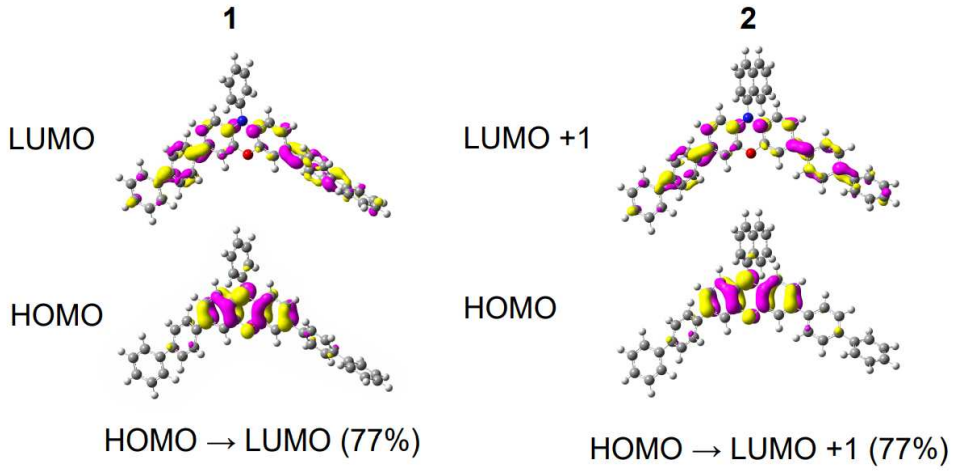

Figure 5.9. *Visualization of the molecular orbitals which comprise the majority of the orbital transition (percent contribution shown in parentheses) in the lowest energy excitation* ***1*** *and* ***2*** *(shown in red in Figs. S1 and S3). Note the similarity between* ***1*** *and* ***2****.*

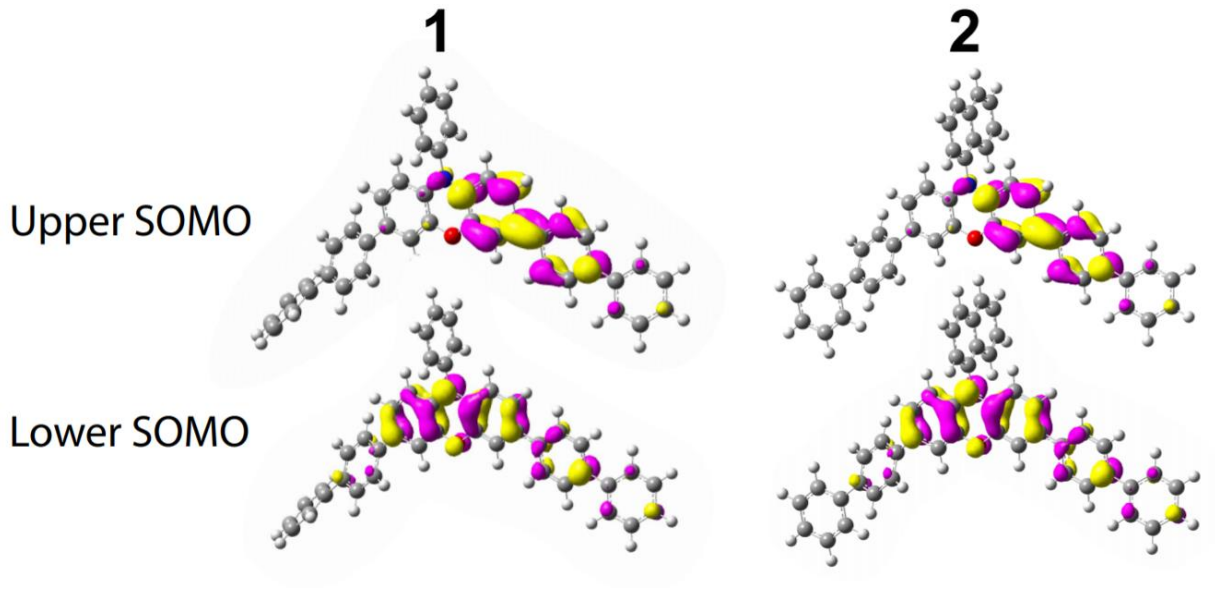

Figure 5.10. *Computed singly occupied molecular orbitals (SOMOs) of the lowest energy triplet state for* ***1*** *and* ***2****. The "Upper SOMO" and "Lower SOMO" refer to the higher energy SOMO and the lower energy SOMO, respectively.*

Geometry Changes between S_0 and T_1 for ***1*** *and* ***2***

For both molecules, in the calculated lowest-energy triplet geometry, the C–C bond which joins the phenoxazine moiety to the biphenyl substituent (particularly, the biphenyl substituent which possesses excess electron density in the upper triplet SOMO) decreases in length by 0.06 Å relative to the calculated ground state singlet geometry. Further, the related inter-ring dihedral angle which contains this C-C bond decreases by more than 30 degrees. These geometric changes are strongly suggestive of double-bond character between the carbon atoms joining these two aryl systems.

6. Oxygen Sensitivity of Steady State Emission

In order to assess the O_2 sensitivity of the emission of **1** and **2** in DMAc, emission spectra of both species were measured first under ambient conditions and then after the solution had been purged with argon for at least 20 minutes. The results are shown in Figures 5.10 and 5.11 of the *Experimental* section. As the figures show, the presence of O_2 has a quite limited impact on the intensity of emission of both species and the emission profiles of both species are entirely unchanged. These findings, in corroboration with the short lifetime of the emissive excited state as measured by TCSPC, indicate that the measured steady state emission of **1** and **2** originates from the singlet manifold, and the slight loss of intensity observed under ambient conditions is interpreted as the diffusion-limited quenching of the singlet excited state by O_2.

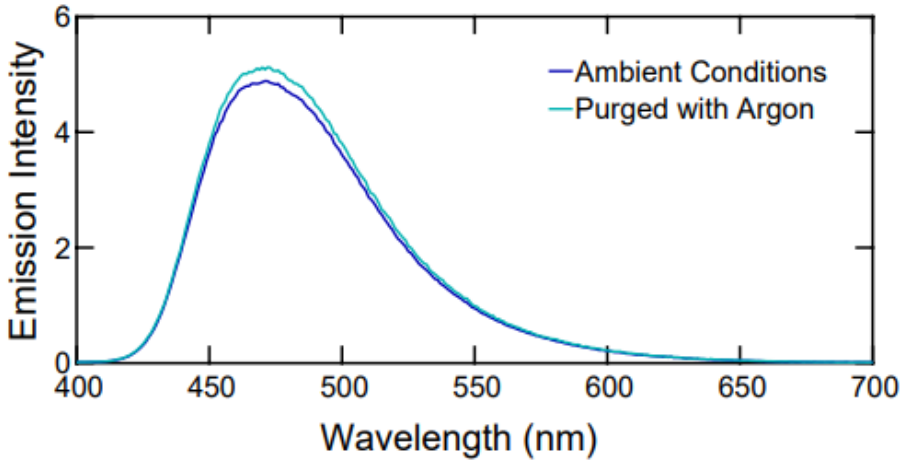

Figure 5.11. *The steady state emission of **1** under ambient conditions and after purging with argon, at 20 °C and using 360 nm excitation.*

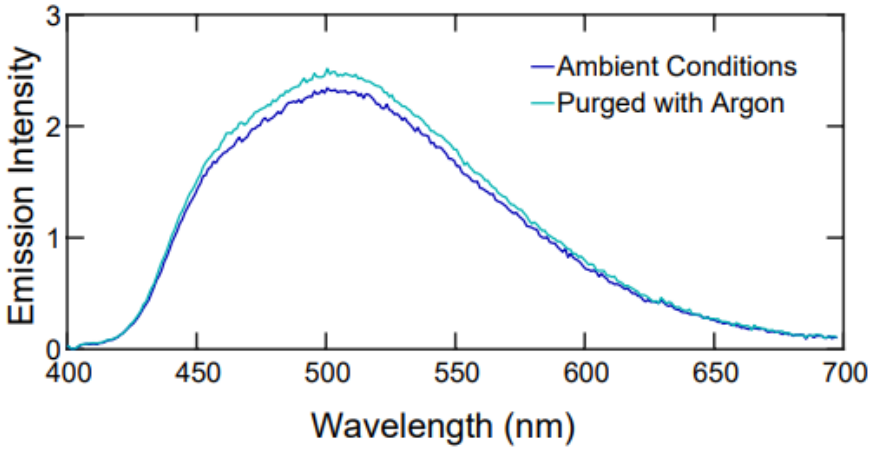

Figure 5.12. *The steady state emission of* ***2*** *under ambient conditions and after purging with argon, at 20 °C and using 360 nm excitation.*

7. TCSPC

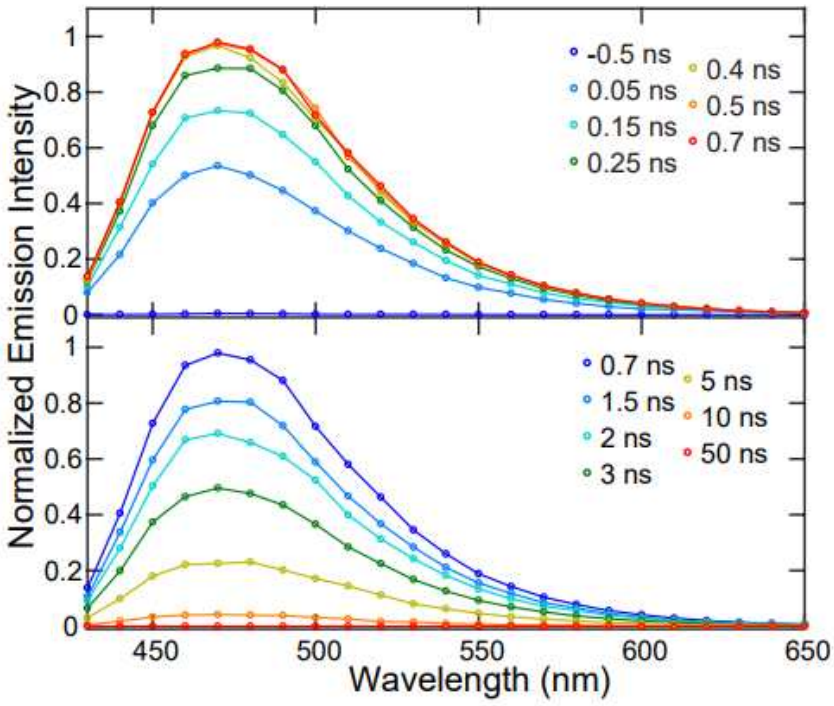

Figure 5.13. *Time-dependent emission spectra of* ***1*** *at selected timepoints at early times (upper) and later times (lower), taken at room temperature.*

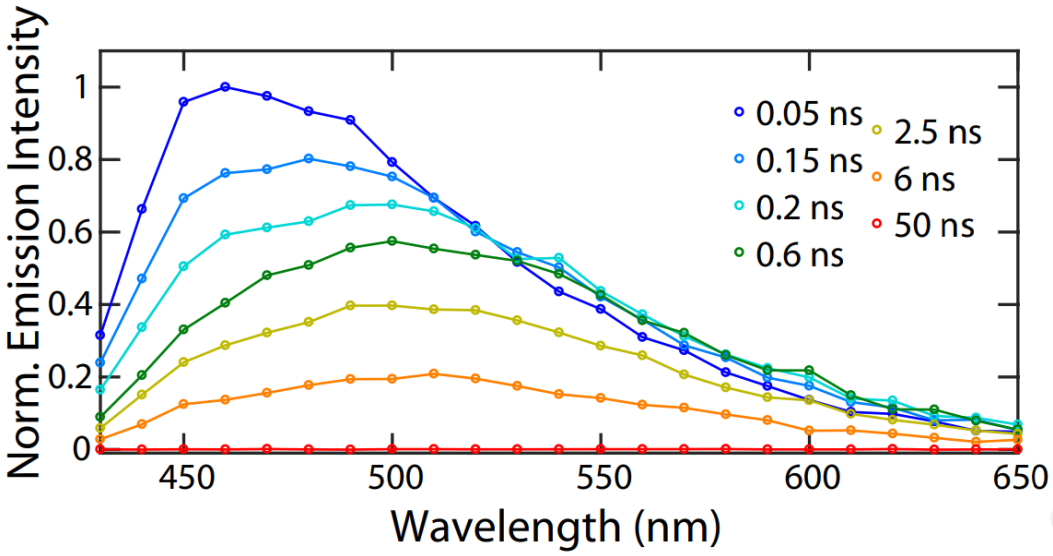

Figure 5.14. *Time-dependent emission spectra of* ***2*** *at selected timepoints. The early emission component (centered at ~ 460 nm) persists for much longer than its fit lifetime (~ 20 ps) due to convolution with the IRF. Data were acquired at room temperature.*

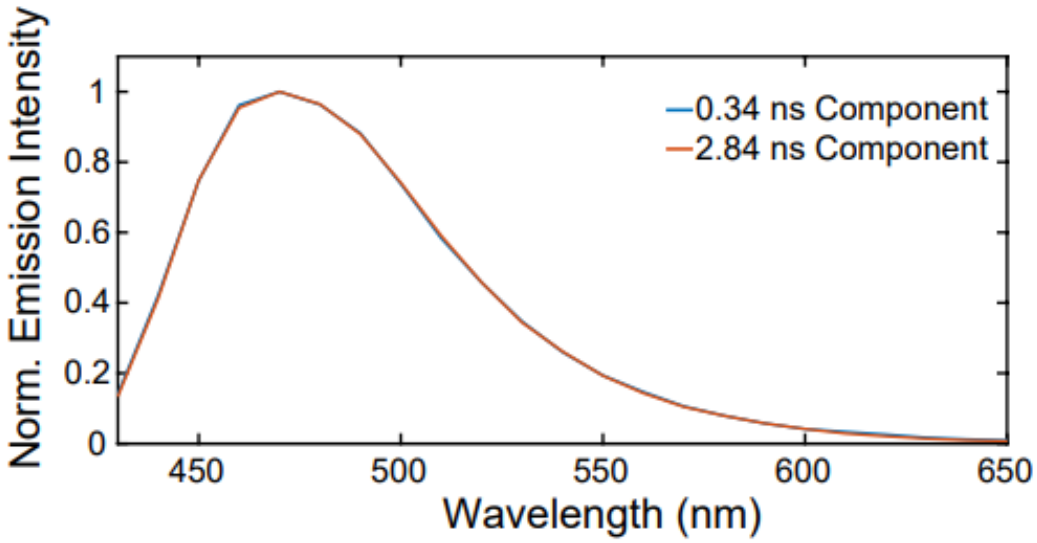

Figure 5.15. *Species associated emission spectra for* ***1*** *in DMAc generated by a global fit of the TCSPC data with a bi-exponential decay model. Note that no spectral evolution is observed, as the early component does not arise from electronic relaxation but rather arises from rotational diffusion.*

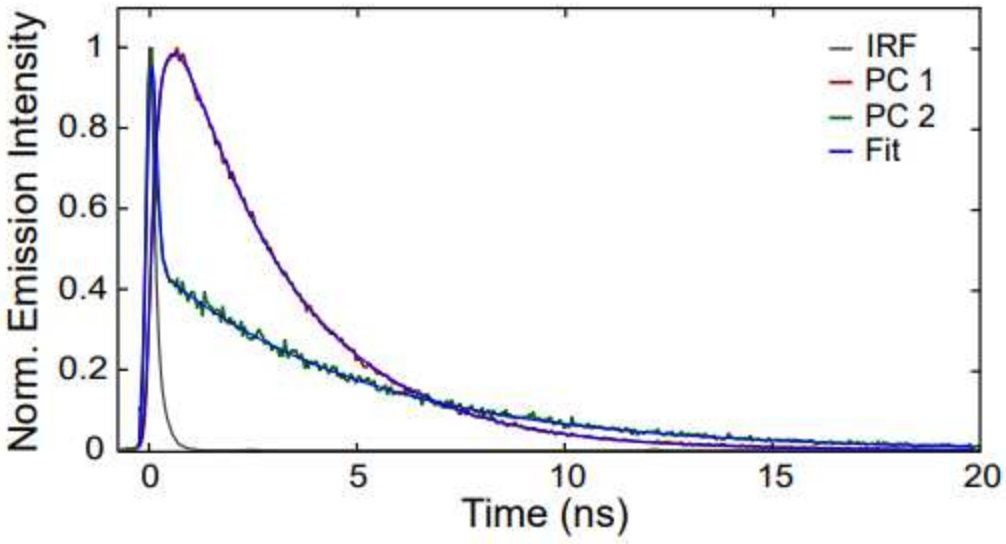

Figure 5.16. *TCPSC traces of* ***1*** *and* ***2*** *collected at 460 nm and their fits to a biexponential decay convoluted with a gaussian. The fits used in the above are 340 ps and 2.84 ns for* ***1*** *and 20 ps and 5.10 ns for* ***2****, with a gaussian with FWHM = 298 ps used for both. The IRF was acquired by monitoring a scattering chalk solution at 400 nm. Data were acquired at room temperature.*

8. Emission of "Monomer" Analogue to 1

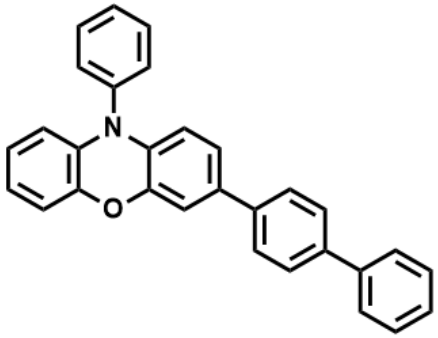

Figure 5.17. *Structure of 3-biphenyl,10-phenyl phenoxazine (**1a**).*

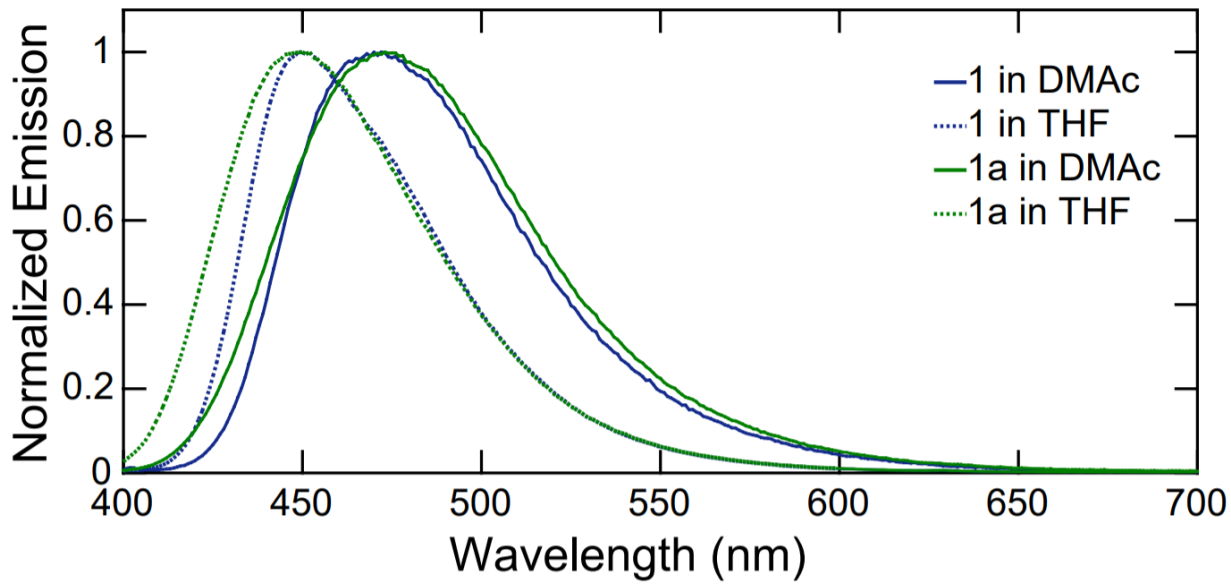

Figure 5.18. *The emission spectra of **1** and **1a** in DMAc and THF using 360 nm excitation taken at 20 °C.*

9. FSTA of 1

Within the late-time FSTA spectrum (> 10 ps) of **1**, the ground state bleach is only a minor contributor but is observable at the high-energy edge. Stimulated emission is seen most prominently at 490 nm, a point that deserves comment: due to spectral contamination of this feature with excited state absorption (ESA) at higher energy (430 nm), we do not expect the peak of this feature to match the emission profile observed in steady state emission experiments. As mentioned in the main text, the S_1 of **1** exhibits a prominent ESA at 620 nm, which is expected to be related to $\pi^* \leftarrow \pi^*$ originating in the excess charge density that has moved towards the biphenyl arm in the formation of this S_1 state with CT state character.

We point out salient features of the dynamics in **1**. Of note, the stimulated emission peak shifts from ~ 450 nm to 490 nm in the first ~ 10 ps, an observation that is consistent with dynamic solvation events. Furthermore, the observation of an isosbestic point at 590 nm indicates a concomitant electronic conversion from the initially excited state to a lower-lying, electronically distinct singlet. Given expectations that S_1 is CT in nature and given the computational observations regarding the T_1 state, we anticipate that inter-ring conformational changes constitute a key nuclear coordinate in these early dynamics.

10. FSTA of 2 at Long Time Delays

At long time delays in the FSTA of **2**, the beginnings of further spectral evolution are observable. This evolution describes the decay of the 475 nm ESA and the concomitant rise of a broad ESA at redder wavelengths, with an associated isosbestic point at 520 nm (Figure 5.20 of the *Experimental* section). Due to the long timescale (> 2 ns) and the similarity of the emerging feature with the NSTA spectrum of **2**, this process is understood as accompanying ISC from S_1 to T_1 directly, or via T_n where that state is short-lived and not observed.

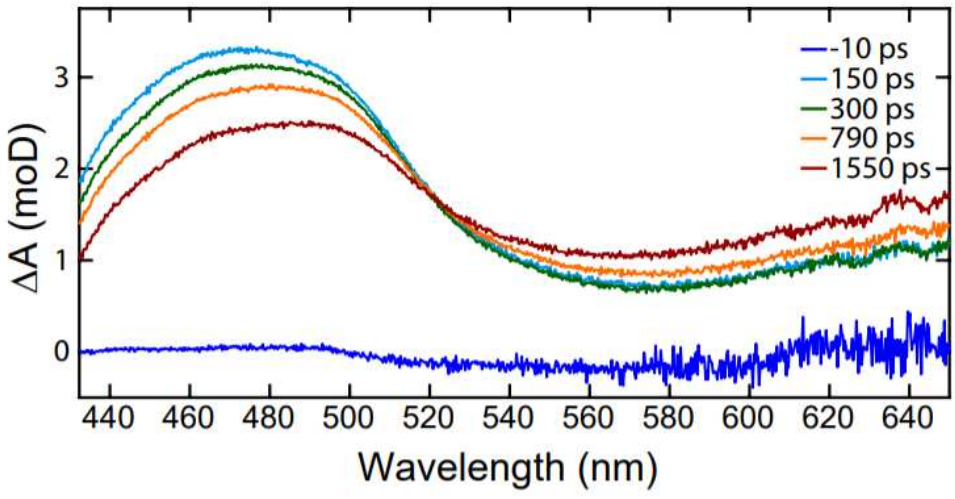

Figure 5.19. *FSTA spectra of* ***2*** *at late time delays, showing the decay of the lowest energy singlet and the concomitant rise of a new feature, attributed to the transient absorption of the* T_1*. Data were acquired at room temperature.*

11. Synthesis and Absorption Spectrum of Naphthalene Anion

40 mg (1.7 mol, 2.5 eq.) of sodium metal and 85 mg (0.66 mol, 1.0 eq.) of naphthalene were placed in a round-bottom flask, and the atmosphere was purged and replaced with N_2 several times. Excess sodium metal was used since, at such a small scale, a significant fraction of the sodium is expected to react with residual water and O_2. Then ~ 15 mL of degassed anhydrous dimethoxyethane were introduced via cannula transfer. The solution was kept under positive N_2 pressure and stirred for 30 minutes. No reaction was observed. Next, the reaction flask was sonicated for 30 minutes, and a dramatic color change (from colorless to dark green) was observed. The resulting solution was immediately brought into a nitrogen-filled glovebox for storage and preparation for UV-Vis measurements (using an Agilent Cary 5000 UV-Vis-NIR Spectrophotometer). The sample for absorption measurement was prepared by adding several drops of concentrated naphthalene anion solution into a quartz cuvette (path length: 0.2 cm) containing anhydrous, degassed DMAc. The absorption spectrum is shown in Figure 5.18 of the *Experimental* section.

In order to simulate the TA spectrum of **2** in the $S_{CT\text{-}Naph}$ state, the molar absorptivity of the naphthalene anion must be known in addition the absorption profile. However, due to the difficulty of maintaining a known concentration of naphthalene anion under our conditions, a molar absorptivity was not measured in our lab. Instead the molar absorptivity was acquired from a literature source.[25] We note that while the conditions under which the molar absorptivity of the naphthalene anion was measured (77 K in 2-methyl-tetrahydrofuran glass) differ substantially from the conditions of our experiments (room temperature in DMAc solution), we consider the literature value (~ 3,500 M^{-1} cm^{-1} at 465 nm) a reasonable approximation which, in light of the ~

14,400 M^{-1} cm^{-1} molar absorptivity of the radical cation, establishes the naphthalene anion as a relatively minor contributor to the TA spectrum of **2** in the $S_{CT\text{-}Naph}$ state.

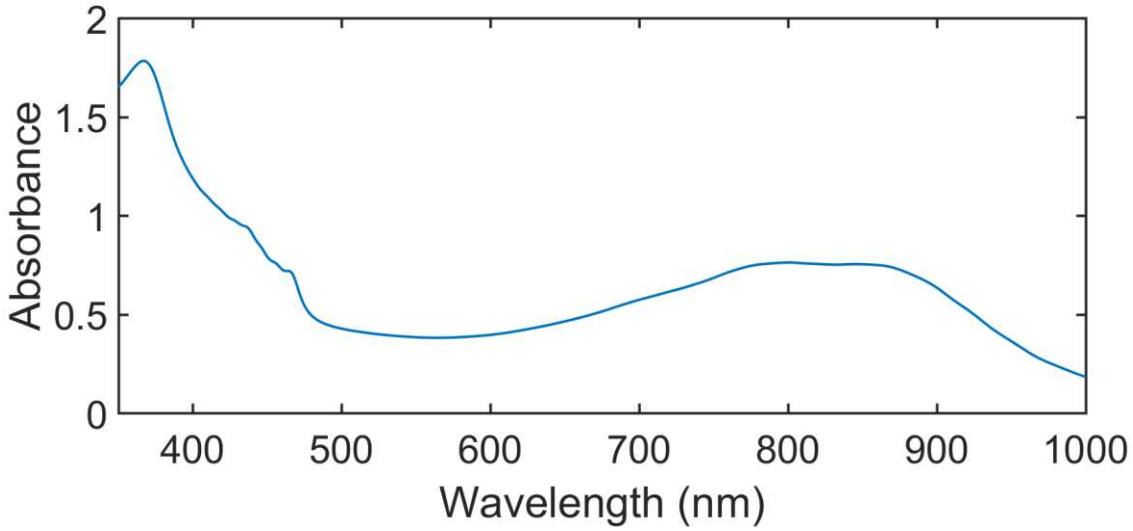

Figure 5.20. *The absorption spectrum of sodium naphthalenide in DMAc taken at room temperature.*

12. Spectroelectrochemistry

Oxidative spectroelectrochemistry was conducted for **1** and **2** in anhydrous DMAc. Bulk electrolysis of both compounds was achieved by holding the potential well above the measure oxidation potential of both catalysts, which, for both **1** and **2** was measured to be ~ 0.37 V against the 0.01 M $Ag/AgNO_3$ reference electrode in anhydrous DMAc. The experiment was run until significant spectral changes in the absorption of each compound were no longer observed (~ 30 minutes). Due to the large overpotential used, it is assumed that at late times bulk electrolysis has gone to completion and that remaining absorption signal arises solely from the oxidized species.

Figure 5.20 shows the time-dependent absorption spectra acquired during the spectroelectrochemical experiment, and Figure 5.11 shows the oxidative difference spectra generated by subtracting the ground state absorption from the spectrum acquired at the latest time

delay. We note that the similarity of the difference spectra of **1** and **2** strongly suggests that the n-aryl substituent plays little to no role in the absorption spectrum of the radical cation of either species.

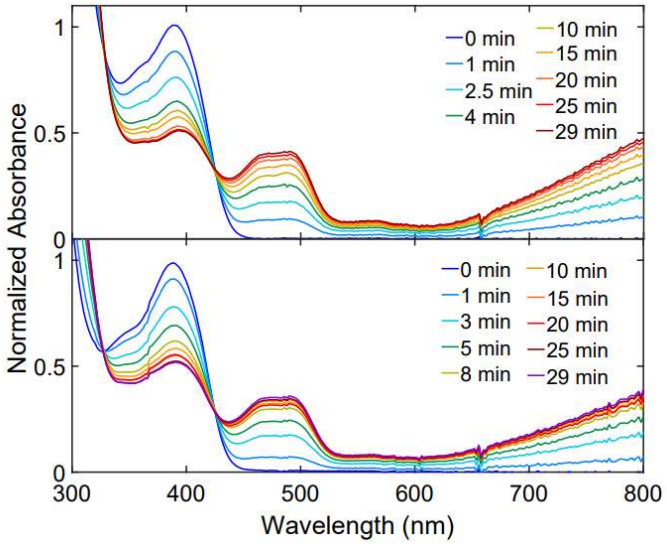

Figure 5.21. *Spectroelectrochemical data of* ***1*** *(upper) and* ***2*** *(lower) at various time delays from the onset of bulk electrolysis.* ***1*** *was held at a potential of 0.5 V vs 0.01 M Ag/AgNO*$_3$*, and* ***2*** *was held at 0.45 V vs 0.01 M Ag/AgNO*$_3$*. Data were acquired at room temperature.*

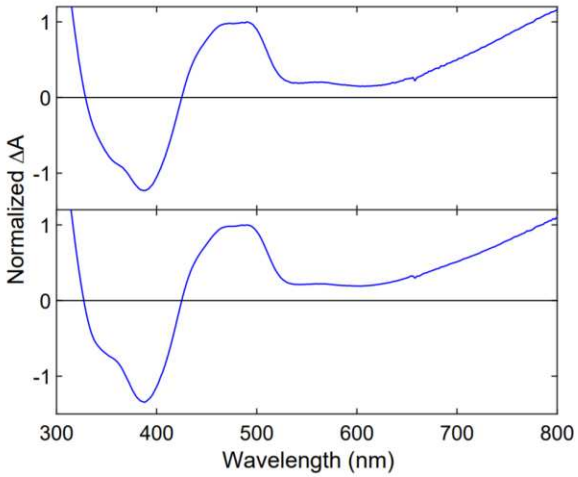

Figure 5.22. *Normalized oxidative difference spectra of* ***1*** *(upper) and* ***2*** *(lower).*

In addition to the oxidative difference spectrum of **2** and the absorption spectrum of the naphthalene radical anion, the molar absorptivity of both species is needed in order to inform the

weights with which to combine the two spectra in simulating the TA spectrum in the $S_{CT\text{-}Naph}$ state of **2**. Since bulk electrolysis has led to complete conversion of **2** to $\mathbf{2}^{\bullet+}$, and since the molar absorptivity of the neutral species is known, the concentration of oxidized species can be calculated using Beer's law. With this known, the molar absorptivity of $\mathbf{2}^{\bullet+}$ can be calculated with another application of Beer's law, using the absorbance at late times in the spectroelectrochemical experiment. This gives a molar absorptivity of 14,400 M^{-1} cm^{-1} at 490 nm.

REFERENCES

(1) (a) Zeitler, K., *Angew. Chem., Int. Ed.* **2009,** *48*, 9785–9789. (b) Yoon, T. P.; Ischay, M. A.; Du, J. *Nat. Chem.* **2010,** *2*, 527–532. (c) Nicewicz, D. A.; MacMillan, D. W. C. *Science* **2008**, *322*, 77–80. (d) Narayanam, J. M.; Tucker, J. W.; Stephenson, C. R. *J. Am. Chem. Soc.* **2009**, *131*, 8756–8757. (e) Prier, C. K.; Rankic, D. A.; MacMillan, D. W. C. *Chem. Rev.* **2013**, *113*, 5322–5363.

(2) (a) Low catalyst loading was observed by Ref 2b and was attributed to efficient ISC by Ref 2c. (b) Fors, B. P.; Hawker, C. J. *Angew. Chem., Int. Ed.* **2012**, *51*, 8850–8853. (c) Koyama, D.; Dale, H. J. A.; Orr-Ewing, A. J. *J. Am. Chem. Soc.* **2018**, *140*, 1285–1293. (d) Ramsey, B. L.; Pearson, R. M.; Beck, L. R.; Miyake, G. M. *Macromolecules* **2017**, *50*, 2668–2674.

(3) Juris, A.; Balzani, V.; Barigelletti, F.; Campagna, S.; Belser, P.; von Zelewsky, A. *Coord. Chem. Rev.* **1988**, *84*, 85–277.

(4) (a) Reiser, O. *Acc. Chem. Res.* **2016**, *49*, 1990–1996. (b) Hernandez-Perez, A. C.; Collins, S. K. *Acc. Chem. Res.* **2016**, *49*, 1557–1565. (c) Larsen, C. B.; Wenger, O. S. *Chemistry* **2018**, *24*, 2039–2058. (d) Higgins, R. F.; Fatur, S. M.; Shepard, S. G.; Stevenson, S. M.; Boston, D. J.; Ferreira, E. M.; Damrauer, N. H.; Rappé, A. K.; Shores, M. P. *J. Am. Chem. Soc.* **2016**, *138*, 5451–5464.

(5) Romero, N. A.; Nicewicz, D. A. *Chem. Rev.* **2016**, *116*, 10075–10166.

(6) Treat, N. J.; Sprafke, H.; Kramer, J. W.; Clark, P. G.; Barton, B. E.; Read de Alaniz, J.; Fors, B. P.; Hawker, C. J. *J. Am. Chem. Soc.* **2014**, *136*, 16096–16101.

(7) Fleming, G. R.; Knight, A. W. E.; Morris, J. M.; Morrison, R. J. S.; Robinson, G. W. *J. Am. Chem. Soc.* **1977**, *99*, 4306–4311.

(8) (a) Theriot, J. C.; Lim, C.-H.; Yang, H.; Ryan, M. D.; Musgrave, C. B.; Miyake, G. M. *Science* **2016**, *352*, 1082–1086. (b) Pearson, R. M.; Lim, C.-H.; McCarthy, B. G.; Musgrave, C. B.; Miyake, G. M. *J. Am. Chem. Soc.* **2016**, *138*, 11399–11407.

(9) (a) Poelma, S. O.; Burnett, G. L.; Discekici, E. H.; Mattson, K. M.; Treat, N. J.; Luo, Y.; Hudson, Z. M.; Shankel, S. L.; Clark, P. G.; Kramer, J. W.; Hawker, C. J.; Read de Alaniz, J. *J. Org. Chem.* **2016**, *81*, 7155–7160. (b) Koyama, D.; Dale, H. J. A.; Orr-Ewing, A. J. *J. Am. Chem. Soc.* **2018**, *140*, 1285–1293.

(10) Du, Y.; Pearson, R. M.; Lim, C.-H.; Sartor, S. M.; Ryan, M. D.; Yang, H.; Damrauer, N. H.; Miyake, G. M. *Chem. Euro. J.* **2017**, *23*, 10962–10968.

(11) McCarthy, B. G.; Pearson, R. M.; Lim, C.-H.; Sartor, S. M.; Damrauer, N. H.; Miyake, G. M. *J. Am. Chem. Soc.* **2018**, *140*, 5088–5101.

(12) Because triplet energetics and solvation are expected to be very similar for these two molecules (*vide infra*), this 2.5 difference in lifetime may indicate participation by other excited states in determining electronic coupling for non-radiative decay.

(13) Terenziani, F.; Painelli, A.; Katan, C.; Charlot, M.; Blanchard-Desce, M. *J. Am. Chem. Soc.* **2006**, *128*, 15742–15755.

(14) Note that the reported time constants in this Figure arise from the fit of a single measurement, whereas the values in Table 5.1 originate in the average of multiple measurements.

(15) DMAc and other solvents considered (e.g. dimethoxyethane) possess a solvent window that precludes the use of electrochemical techniques.

(16) Shida, T.; Iwata, S. *J. Am. Chem. Soc.* **1973**, *95*, 3473–3483.

(17) (a) Nakashima, N.; Murakawa, M.; Mataga, N. *Bull. Chem. Soc. Jpn.* **1976**, *49*, 854–858. (b) Becker, H. D.; Langer, V.; Sieler, J.; Becker, H. C. *J. Org. Chem.* **1992**, *57*, 1883–1887.

(18) (a) Levanon, H.; Norris, J. R., *Chem. Rev.* **1978**, *78*, 185–198. (b) Dance, Z. E.; Mi, Q.; McCamant, D. W.; Ahrens, M. J.; Ratner, M. A.; Wasielewski, M. R. *J. Phys. Chem. B* **2006**, *110*, 25163–73.

(19) (a) vanWilligen, H.; Jones, G.; Farahat, M. S. *J. Phys. Chem.* **1996**, *100*, 3312–3316. (b) Dance, Z. E. X.; Mickley, S. M.; Wilson, T. M.; Ricks, A. B.; Scott, A. M.; Ratner, M. A.; Wasielewski, M. R. *J. Phys. Chem. A* **2008**, *112*, 4194–4201. (c) Benniston, A. C.; Harriman, A.; Li, P.; Rostron, J. P.; van Ramesdonk, H. J.; Groeneveld, M. M.; Zhang, H.; Verhoeven, J. W. *J. Am. Chem. Soc.* **2005**, *127*, 16054–16064.

(20) (a) Weller, A.; Staerk, H.; Treichel, R. *Farad. Discuss.* **1984**, *78*, 271–278. (b) Weiss, E. A.; Ratner, M. A.; Wasielewski, M. R. *J. Phys. Chem. A* **2003**, *107*, 3639–3647.

(21) Shepard, S. G.; Fatur, S. M.; Rappé, A. K.; Damrauer, N. H. *J. Am. Chem. Soc.* **2016**, *138*, 2949–2952.

(22) M. J. Frisch, G. W. T., H. B. Schlegel, G. E. Scuseria,; M. A. Robb, J. R. C., G. Scalmani, V. Barone, B. Mennucci,; G. A. Petersson, H. N., M. Caricato, X. Li, H. P. Hratchian,; A. F. Izmaylov, J. B., G. Zheng, J. L. Sonnenberg, M. Hada,; M. Ehara, K. T., R. Fukuda, J. Hasegawa, M. Ishida, T. Nakajima,; Y. Honda, O. K., H. Nakai, T. Vreven, J. A. Montgomery, Jr.,; J. E. Peralta, F. O., M. Bearpark, J. J. Heyd, E. Brothers,; K. N. Kudin, V. N. S., T. Keith, R. Kobayashi, J. Normand,; K. Raghavachari, A. R., J. C. Burant, S. S. Iyengar, J. Tomasi,; M. Cossi, N. R., J. M. Millam, M. Klene, J. E. Knox, J. B. Cross,; V. Bakken, C. A., J. Jaramillo, R. Gomperts, R. E. Stratmann,; O. Yazyev, A. J. A., R. Cammi, C. Pomelli, J. W. Ochterski,; R. L. Martin, K. M., V. G. Zakrzewski, G. A. Voth,; P. Salvador, J. J. D., S. Dapprich, A. D. Daniels,; O. Farkas, J. B. F., J. V. Ortiz, J. Cioslowski,; and D. J. Fox *Gaussian 09, Revision D.01*, Gaussian, Inc. : Wallingford, CT, 2009.

(23) Spackman, M. A. *J. Comp. Chem.* **1996**, *17*, 1–18.

(24) Jacquemin, D.; Wathelet, V.; Perpete, E. A.; Adamo, C. *J. Chem. Theory Comput.* **2009**, *5*, 2420–2435.

(25) Shida, T.; Iwata, S. *J. Am. Chem. Soc.* **1973**, *95*, 3473–3483.

CHAPTER 6 – SUMMARY

Through this work, *N*-aryl phenoxazines were developed as strongly reducing organic photoredox catalysts for O-ATRP and other synthetic transformations. Modification of the *N*-aryl and core substituents on phenoxazine yielded organic photocatalysts with varied photophysical and redox properties (i.e. with excited state reduction potentials ranging from -1.42 V to -2.11 V vs. SCE), contributing fundamental knowledge to the fields of photoredox catalysis and photophysical chemistry. By studying the catalytic performance of these phenoxazines in O-ATRP, eight catalyst design principles were identified and catalysts with superior performance were developed (Figure 6.1).

Since our initial report on *N*-aryl phenoxazines as PCs, our group has continued to explore the utility of these catalysts for O-ATRP to synthesize well-defined polymers with different composition[1] and architecture[2] while demonstrating the tolerance of these systems to varied lighting conditions[3] and the presence of impurities such as oxygen (Chapter 4). Moreover, this work has inspired application of the phenoxazine catalytic platform for other light-driven polymerizations and small molecule transformations by our group[4–6] and others[7–12]. To enable continued study and application of phenoxazine PCs by the broader chemistry community, a start-up company that originated from our group, New Iridium, has commercialized one phenoxazine PC through MilliporeSigma. We envision that the fundamental studies described herein coupled with the commercialization of these catalysts will open new avenues for the development of sustainable, photoredox-catalyzed methods for the synthesis of polymers, agrochemicals, pharmaceuticals, and more.

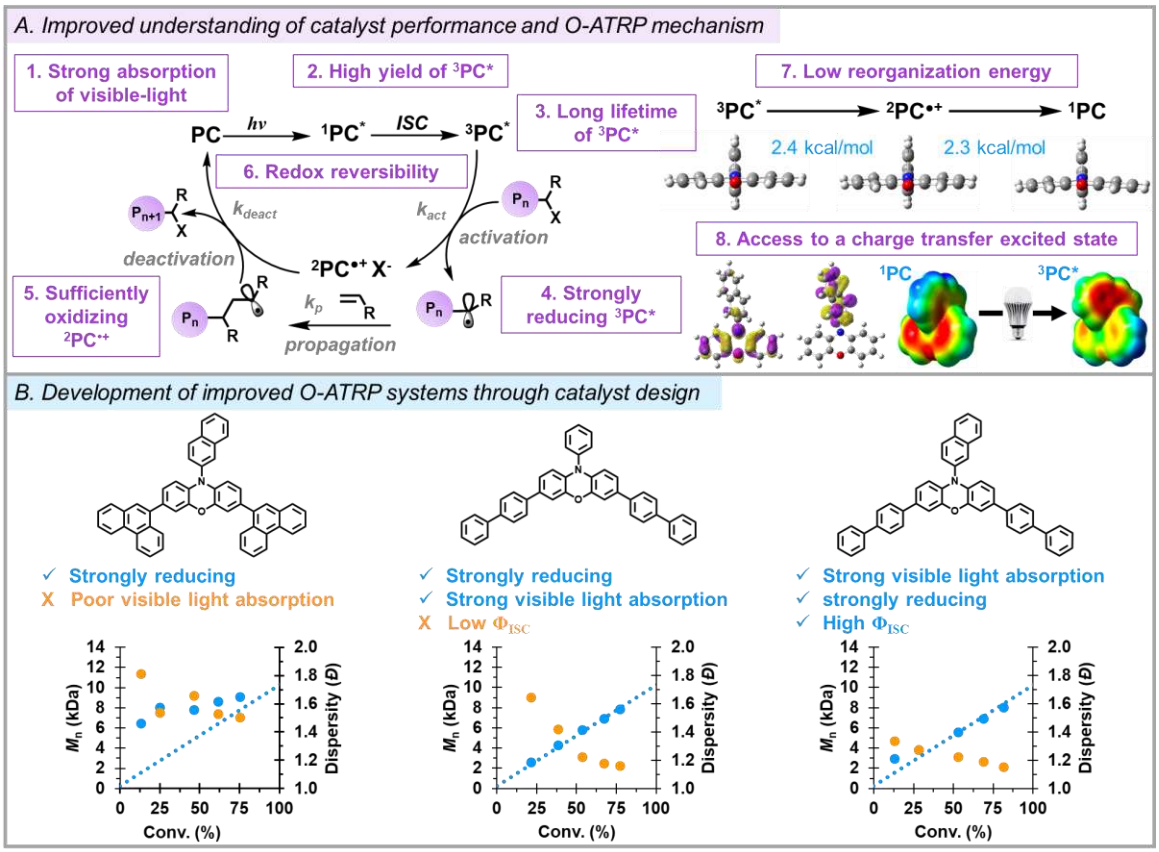

Figure 6.1. *Summary of the contributions of this research to the development of O-ATRP.* ***A.****) O-ATRP mechanism highlighting the eight key catalyst design principles established through this work.* ***B.****) Example of how improved understanding of catalyst properties has enabled the development of improved O-ATRP systems. Each PC structure is shown above a plot of polymer M_n as a function of monomer conversion for the O-ATRP of MMA mediated by that PC. Measured M_n values (blue circles), theoretical M_n values (blue dotted line), and Đ values (orange circles) are shown for each plot. A brief description of PC properties is below each PC structure.*

REFERENCES

(1) Ramsey, B.; Pearson, R.; Beck, L.; Miyake, G. *Macromolecules* **2017**, *50*, 2668–2674.

(2) Buss, B.; Beck, B.; Miyake, G. *Polym. Chem.* **2018**, *9*, 1658–1665.

(3) Ryan, M. D.; Pearson, R. M.; French, T. A.; Miyake, G. M. *Macromolecules* **2017**, *50*, 4616–4622.

(4) Du, Y.[†]; Pearson, R[†]; Lim, C.[†]; Sartor, S.; Ryan, M.; Yang, H.; Damrauer, N.; Miyake, G. M. *Chem. Euro. J.,* **2017**, *23*, 1–8. ([†]authors contributed equally)

(5) Kudisch, M.; Lim, C.-H.; Thordarson, P.; Miyake, G. M. *J. Am. Chem. Soc.* **2019**, *141*, 19479–19486.

(6) Rao, H.; Lim, C.; Bonin, J.; Miyake, G. M.; Robert, M. *J. Am. Chem. Soc.* **2018**, *140*, 17830–17834.

(7) Berger, A. L.; Donabauer, K.; Konig, B. *Chem. Sci.* **2018**, *9*, 7230–7235.

(8) Discekici, E. H.; St. Amant, A. H.; Nguyen, S. N.; Lee, I-H.; Hawker, C. J.; Read de Alaniz, J. *J. Am. Chem. Soc.* **2018**, *140*, 5009–5013.

(9) Park, G. S.; Back, J.; Choi, E. M.; Lee, E.; Son, K.-S. *Eur. Polym. J.* **2019**, *117*, 347–352.

(10) Vogt, D. B.; Seath, C. P.; Wang, H.; Jui, N. T. *J. Am. Chem. Soc.* **2019**, *141*, 13203–13211.

(11) Lewis, S. E.; Wilhelmy, B. E.; Leibfarth, F. A. *Polym. Chem.* **2020**, DOI: 10.1039/C9PY01884K.

(12) Shibutani, S.; Kodo, T.; Takeda, M.; Nagao, K.; Tokunaga, N.; Sasake, Y.; Ohmiya, H. *J. Am. Chem. Soc.* **2020**, *142*, 1211–1216.